# Attitude Control Subsystem Design of the Stable and Highly Accurate Pointing Earth-imager

A MSc Thesis

By David Ju

in partial fulfillment of the requirements for the degree of

**Master of Science**
in Aerospace Engineering

at the Delft University of Technology
Department of Space Engineering

5th October 2017

TU Delft

| | |
|---|---|
| Supervisor | Dr.ir. J.M. Kuiper |
| Committee Members | Dr. A. Cervone |
| | ir. B.C. Root |

# Abbreviations

| | |
|---|---|
| ACS | Attitude Control Subsystem |
| ADCS | Attitude Determination and Control Subsystem |
| ARE | Algebraic Ricatti Equation |
| ATS | Attitude Thruster Subsystem |
| CMG | Control Moment Gyro |
| ConOps | Concept of Operations |
| COTS | Commercial off the shelf |
| EO | Earth Observation |
| FMS1 | Full Major Spinup |
| FMS2 | Full Minor Spinup |
| FOV | Field of View |
| IAGA | International Association of Geomagnetism and Aeronomy |
| IFOV | Instantaneous Field of View |
| IGRF12 | International Geomagnetic Reference Field 12th generation |
| LEO | Low Earth Orbit |
| LQR | Linear Quadratic Regulator |
| MEMS | microelectromechanical system |
| MSAFE | Marshall Solar Activity Future Estimates (Model) |
| MSFC | Marshall Space Flight Center |
| MT | Magnetorquer |
| MTF | Modulation Transfer Function |
| MW | Momentum Wheel |
| MWTS | Momentum Wheel Torquing Subsystem |
| NASA | National Aeronautics and Space Administration |
| NRLMSISE00 | Naval Research Laboratory Mass Spectrometer and Incoherent Scatter radar Exosphere (2001 Model) |
| PPL | Precession Phase Lock |
| PS | Partial Spinup |
| RW | Reaction Wheel |
| SHAPE | Stable and Highly Accurate Pointing Earth-imager |
| SMC | Sliding Mode Control |
| SMCS | Sliding Mode Control Spinup |
| SSO | Sun Synchronous Orbit |

| | |
|---|---|
| TBD | To Be Determined |
| UTC | Coordinated Universal Time |
| VLEO | Very Low Earth Orbit |

# Nomenclature

| | |
|---|---|
| $\eta$ | Nutation Angle [deg] |
| $\lambda$ | Longitude [deg] |
| $\mu$ | Pointing Error [rad] |
| $\mu_0$ | Vacuum Magnetic Permeability [$4\,\pi \cdot 10^{-7}$ T m $A^{-1}$] |
| $\mu_E$ | Gravitational Parameter of Earth [398 600 $km^3$ $s^{-2}$] |
| $\boldsymbol{\omega}$ | Angular Body Rate Column Vector [rad $s^{-1}$] |
| $\Omega_p$ | Precession Frequency [rad/s] |
| $\omega_s$ | Relative Rotor Angular Velocity Around the Spin Axis [rad $s^{-1}$] |
| $\phi$ | Latitude [deg] |
| $\rho$ | Total Air Mass Density [kg $m^{-3}$] |
| $\rho_m$ | Material Density [kg $m^{-3}$] |
| $\boldsymbol{\tau}$ | External Torque [Nm] |
| $\xi$ | Damper Displacement [m] |
| $A$ | Wetted Surface Area [$m^2$] |
| $a$ | Semi-major Axis [km] |
| $\mathbf{B}$ | Magnetic Flux Density [T] |
| $\mathbf{b}$ | Initial Damper Mass Location to Center of Mass Column Vector [m] |
| $c_d$ | Damping Coefficient [kg s $m^{-1}$] |
| $C_D$ | Drag Coefficient [-] |
| $F_T$ | Thrust [N] |
| $g_a$ | Spinup Torque [Nm] |
| $h$ | Altitude [km] |
| $\mathbf{H}$ | Angular Momentum Column Vector [N m s] |
| $H_s$ | Rotor Angular Momentum [N m s] |
| $\mathbf{I}$ | Mass Moment of Inertia Matrix [kg $m^2$] |
| $I_s$ | Rotor Moment of Inertia Around the Spin Axis [kg $m^2$] |
| $k_d$ | Spring Stiffness [kg $m^{-1}$] |

| | |
|---|---|
| $m$ | Mass [kg] |
| $\mathbf{M}_A$ | Dipole Moment Vector of the Magnetorquers [A $m^2$] |
| $\mathbf{M}_E$ | Earth's Magnetic Moment Vector [$8 \cdot 10^{22}$ A $m^2$] |
| $\mathbf{M}_M$ | Spacecraft Magnetic Moment Vector [A $m^2$] |
| $m_d$ | Damper Mass [kg] |
| $n$ | Mean Motion [rad $s^{-1}$] |
| $\mathbf{n}$ | Spin Axis Column Vector [-] |
| $\mathbf{p}$ | Linear Momentum Vector [kg m $s^{-1}$] |
| $p_n$ | Linear Momentum of Damper Mass [kg m $s^{-1}$] |
| $T$ | Rotational Kinetic Energy [J] |
| $t_m$ | Maintenance Operation Time [s] |
| $t_n$ | Nominal Operation Time [s] |

# Abstract

As technology improves, increasingly higher resolution payload can be achieved using Cubesats for Earth observation. The diffraction limit prevents the resolution to up to a few meters for these missions and are confined to Very Low Earth Orbits (VLEO). At these altitudes, strong disturbances act on the system, limiting its lifetime and the pointing capabilities of CubeSats. As a solution, the Department of Space Engineering at the Delft University of Technology has proposed a 6 unit CubeSat named the Stable and Highly Accurate Pointing Earth-imager (SHAPE) orbiting at a Sun synchronous VLEO which uses a momentum wheel to passively stabilize the system against the external environment within a competitive cost of less than 500 000 €. By utilizing the dual-spin stabilization concept, composed of a stable platform and a spinning rotor, it is expected to perform pointing missions of less than 1 degree.

In this thesis, the SHAPE concept has been revisited and further developed based on the work of Kuiper and Dolkens to conduct whether these types of missions are feasible within the aspect of the Attitude Determination and Control Subsystem (ADCS). This thesis covers the base of this subsystem approached from a top-down methodology; designed from the final nominal mission mode to the detumbling mode on a system level.

The ADCS design will consist of a momentum wheel which has been determined to have an angular momentum of 1 Nms. This value is based on a prediction of the worst-case atmospheric density of the next solar cycle. The design point, at which the momentum wheel has been sized, has been taken at 90% of SHAPE's lifetime after several design iterations. Hereby, the last 10% of the mission has been partially forfeited with degraded performances due to the exponential increase in disturbances acting on the spacecraft at lower altitudes. As therefore, the mass and size of the momentum wheel has been reduced with 41% and 20%, respectively. To re-align the angular momentum vector within the 1 degree pointing requirement, a set of magnetorquers with a dipole moment of 0.5 $Am^2$ has been chosen due to their low power consumption, mass, cost, and high reliability while capable of producing sufficient torque. Also, a damper is to be integrated as it provides the system asymptotic reduction of the transverse momenta, thus increasing the image quality without expenditure of additional power.

To reach the nominal mission observation state, several momentum wheel spinup strategies have been investigated. Based on a trade-off between three spinup concepts, it was concluded that the major axis spinup is most suited. This type is initiated after the spacecraft as a whole has attained an angular momentum equivalent to that of the desired end value of the momentum wheel. Then, a constant rotor torque is applied, providing a momentum transfer from the platform to the rotor. The disadvantage of this spinup procedure is that the system's solar panels are aligned parallel to the orbital plane, meaning that power cannot be generated and batteries are required during the spinup. Despite this, it was found that after completing the spinup, the transverse angular momenta was minimized to marginal values in contrast to the other spins. The inclusion of the passive damper during the major axis spin further improves the ability of reducing the transverse momentum as the damper's dissipative energy property adds an asymptotic attraction at the point of lowest energy, located at the spin axis near the end of the spinup.

The all-spun state is achieved using a set of thrusters. This choice was taken as the magnetorquers was found not to deliver sufficient torque. From the detumbling analysis, it was concluded that the magnetorquers are able to reduce the tumbling rates with magnitudes of up to 35 deg/s to mean motion values in less than an orbit using a static gain B-dot controller.

Imperfections in the momentum wheel can cause static and dynamic imbalance, imparting internal disturbances to the system which affects the image quality detrimentally. Therefore, isolators are to be integrated within the momentum wheel suspension subsystem. If these disturbances can be negated using isolators, it can be expected that the pointing error will stay within one degree and attitude stability can be achieved at least until the design altitude of 280 km. However, the analysis and design of the isolators have yet to be done and thus the attainability of the pointing and image quality requirements are still inconclusive.

*"Life is the sum of all your choices."*

*- Albert Camus*

# Preface

From my youth, I was always fascinated in rockets, planets and the universe (and also insects for which my curiosity to it has vanished). Pursuing science was very obvious. The interest of space and pursue to it were not during my lifetime. At my final years of high school, my carrier decision had to be made and was divided into either medicine or aerospace engineering; to help people or go into the direction of my own interest. This decision was tough, but I decided to pursue in aerospace engineering at Delft University of Technology mainly as a challenge. Halfway though my bachelor studies, aerospace engineering had not been motivating for me and pursuing this seemed to have been disappointing. Doubt was in my mind. This changed at the design synthesis exercise. Focusing more on the space and especially on the attitude control system of the spacecraft has awoken my fascination in space and has enlightened me to further pursue to do my master's degree in space engineering.

To *keep* thinking about what to do and what would have been if I have chosen a different path is a thought of futility as life is continuous and flowing in a single direction. Or as Albert Camus, a philosopher of the Absurd, has said; "*You will never be happy if you continue to search for what happiness consists of. You will never live if you are looking for the meaning of life.*"

I would like to thank my supervisor Hans Kuiper for the subject of SHAPE and his pragmatic approach towards engineering. This subject has greatly introduced me to spinning spacecraft (which I thought to be obsolete for satellites) and its intriguing complex rotational motions. Furthermore, I am especially grateful for my parents and brother for supporting me throughout my academic life with their love for which I dedicate this thesis to.

# Contents

# List of Tables

# List of Figures

# Chapter 1

# Introduction

The trend toward smaller spacecraft has been growing over the past decade. With these growth, more effort have been spent into miniaturization of small and low power instruments, subsystems and components. The CubeSat is a new standardized form of a spacecraft class classified within the nano satellites (Engberg et al. 1995). This standardization has been led by Stanford's University's Space Systems Development Lab and its use has been continued to be developed by universities and industries worldwide. As the miniaturization of technology improves, Earth Observation (EO) missions with high resolution are increasingly more feasible and can serve in important EO missions such as in the areas of environmental studies, defense, disaster response etc. The size of the spacecraft however limits resolutions in the order of a few meters at Very Low Earth Orbits (VLEO) due to the maximum aperture of 10 cm dimension imposed by the CubeSat standardization.

Currently, spacecraft classified from micro and larger apply three axis control stabilization to allow high pointing accuracies of orders a few arcseconds. For nano-satellites and smaller, this is still difficult to achieve at VLEO due to miniaturization problems of attitude control hardware, causing unwanted vibrations to the system. In addition, achieving high resolution at VLEO is also restrained due to the dense atmospheric particles of Earth, exponentially increasing at lower altitudes. To solve this problem, a solution has been proposed by the Department of Space Engineering at the Delft University of Technology called the Stable and Highly Accurate Pointing Earth-Imager (SHAPE) (Kuiper & Dolkens 2016). This design utilizes a high spinning momentum wheel, providing the spacecraft resistance against the atmospheric disturbance. This concept also known as dual-spin stabilization is an antiquated form of stabilization which had been used prevalently in the early decades of the space age.

An inherent problem with a single-spinning spinning is that its instrument rotates as well. The development of dual-spin spacecraft also called dual spinners have allowed the separation of the spacecraft (as the name implies) into two components. One of which is the platform providing Earth pointing capabilities and a spinning part called the rotor which gives the spacecraft its spin stabilization. This dual-spin concept in which SHAPE is based on, can provide its survival in the dense atmosphere while allowing its high pointing accuracy of 1 degree and high resolution EO mission.

**Research Objective**

The SHAPE concept currently is still not major system design driven. The previously mentioned challenges impose hard requirements and constraints and therefore the Attitude Determination and Control Subsystem (ADCS) is one of its key aspects to its success. An initial system design has already proposed by Kuiper & Dolkens (2016) for which this MSc thesis will be based upon and will continue as a feasibility study to form a possible ADCS design. Hereby, two factors are important; the pointing accuracy of at least 1 degree and the attitude stability imposed by the image quality (moreover in the next chapter). As such, a research objective is set up as follows;

*The research objective is to come to a feasible spacecraft design with recommendations for SHAPE's Attitude Determination and Control Subsystem to achieve a pointing accuracy of at least 1 degree and attitude stability imposed by the payload of SHAPE.*

In this thesis, the system design based on Kuiper & Dolkens (2016) are revisited with regard to the attitude dynamics.

The analysis is to be broken down in multiple design steps throughout SHAPE's mission phases producing a possible solution.

**Structure**

This feasibility study will first look at the case study presented by Kuiper and Dolkens as SHAPE in the first chapter. Hereby, requirements and constraints will be re-stated and further divided into different spacecraft system phases. Furthermore, it will provide with a design methodology for a feasible attitude system design. The third chapter will give a brief explanation of the background knowledge of spacecraft rotational dynamics and stability theory. Chapter 4 gives the momentum wheel design based on a prediction of the atmospheric condition, estimated disturbances and numerical simulations under mission operation conditions. This will be followed by the analysis on how the spacecraft reach this condition based on a spinup procedure of the momentum wheel. Hereby several different options will be analyzed and an optimal solution will be selected. Chapter 6 gives a brief analysis whether the current design can reduce rotation rates to tolerable values imparted by the disconnection from a launcher's upper stage. In Chapter 7, the design specification are given based on previous analyses. This thesis is then finalized with the conclusions and recommendations in Chapter 8.

# Chapter 2

# System Objective

A spacecraft consists of subsystems with interlinked designs. A simple generalization of the design process cannot be made and iterations are required for an optimized system in terms of performance factors such as mass, volume and cost. The CubeSat is a relative new standard for spacecraft with 'semi'-fixed dimensions developed by California Polytechnic State University and Stanford University's Space Systems Development Lab (Heidt et al. 2000). With the use of this concept, spacecraft can be developed with lesser resources albeit with degraded performance in contrast to the larger counterparts. Although, SHAPE's ADCS is partly based on early spacecraft designs from the 1960s and 1970s, application to VLEO CubeSat designs have yet to be realized. To limit the scope of the research within the timeframe of this thesis, the SHAPE concept will focus on the ADCS on a system level within the specification given by Kuiper & Dolkens (2016). This chapter starts off by stating the case study SHAPE, followed by the system requirements. In Section 2.3, the control modes with the corresponding requirements are given with respect to the ADCS. The outline of the design process is then stated in Section 2.4. The chapter is finalized with the concept of operations.

## 2.1 Case Study

SHAPE performs its EO mission with the ANT-2A which is a plug-and-play camera design for CubeSats and is currently in development by the Delft University of Technology (Kuiper & Dolkens 2016). With this instrument, a spatial resolution of 4 meters is to be achieved at an altitude of approximately 350 km for Earth observation in the visible spectrum. The size of the payload is expected to be 10 x 10 x 30 cm or equivalent to a 3 unit (3U) CubeSat with each unit having a volume of 1 L. To accommodate the remaining subsystems an additional 3U CubeSat has been added. For symmetry purposes, both 3U modules are decided to be placed 5 cm away from the momentum wheel as shown in Figure 2.1. The total mass of the system including the momentum wheel had been estimated to be approximately 8 kg for which the Attitude Control Subsystem (ACS) has been attributed a mass budget of 800 g and approximately 500 g for the momentum wheel. Additionally, power budgets of 6 W and 11 W have been appointed to the ADCS subsystem for nominal and non-nominal mission operations, respectively. The cost of the ADCS have been estimated at 22% of the total budget. SHAPE's orbit will be a noon-midnight sun-synchronous with an altitude of 380 to 230 km. From this preliminary point, the attitude control system is designed in a top-down fashion.

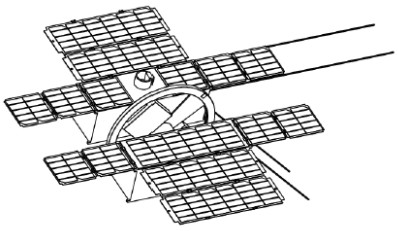

Figure 2.1: Preliminary Design of SHAPE (Kuiper & Dolkens 2016)

## 2.2 System Requirements

In this section, the system requirements are listed in Table 2.1 and briefly elaborated on its rationale whereas necessary. Note that the definition of system in this context is regarded as the attitude system.

Table 2.1: Key Attitude Requirements and Constraints

| Code | Requirements | Rationale |
|---|---|---|
| S.1 | The system shall have a pointing accuracy better than 1.0°. | Targeting, small overlapping coverage and technology demonstration |
| S.2 | The system shall operate between 380 to 230 km altitude. | Minimal lifetime of 6 months and payload resolution |
| S.3 | The momentum wheel shall use magnetic bearings. | Sustained rotation of the momentum wheel throughout its mission |
| S.4 | The momentum wheel shall be spun up with TU Delft resistojets. | Technology demonstration |
| S.5 | The system shall be in a noon/midnight SSO orbit. | Power requirement and payload requirement of wavelength of 450-650 nm |
| S.6 | The Modulation Transfer Function shall be above 52% at the Nyquist frequency. | Image quality requirement |
| S.7 | The maximum radius of the momentum wheel shall be less than 14 cm. | To fit the design within two CubeSat units including a margin for an adjusted P-POD design. |
| S.8 | The system shall have no single point of failure. | |
| S.9 | The system shall have peak power of 11 W during non-mission operation modes. | Allocated power budget |
| S.10 | The system shall have peak power of 6 W during mission operation modes. | Allocated power budget |
| S.11 | The momentum wheel shall have a maximum mass of 500 g. | Allocated mass budget |

The first requirement (S.1) is the main objective for the momentum wheel design. There are multiple methods in which the pointing accuracy requirement can be derived. This can either be related to solar panel pointing or orbit manoeuvres, but in general this is raised from the requirement related to the main payload (Larson & Wertz 1999). There are three reasons for the pointing accuracy regarding this payload. One is to position the target within the Field of View (FOV). To observe a target with certainty, the pointing error should be less than the FOV. For example, if one has a pointing error of 0.7° with $3\sigma$ certainty, a four times FOV of 2.8° yield that the target will be with $6\sigma$ certainty. SHAPE will not have this certainty, but with 1 degree it will approach it closely. The second is to reduce overlapping coverage. If the pointing angle is larger than the FOV, the sensor might be directed outside the desired location. This can result that overlap can occur with a previously imaged location. The third reason is to demonstrate high pointing performance for CubeSat missions.

The operational altitude range defined in requirement (S.2) is determined from the orbital decay. To sustain approximately 6 months of mission operation, a CubeSat should initiate its mission at around 380 km. This is due to the high atmospheric drag present at LEOs which shows an exponential drop in altitude. Furthermore, this altitude is required for a high spatial resolution of less than 4 meters. To have a sustained momentum wheel rotation, the wheel is spun upon magnetic bearings to minimize friction throughout its lifetime (S.3). The momentum wheel will be spun once with a set of TU Delft resistojets for technology demonstration (S.4) (Cervone et al. 2017). The magnetic bearings requires a minimum of 5000 rpm of the momentum wheel to function, a value of 6000 to 7000 rpm is expected to sustain a value above the minimum velocity throughout the lifetime.

The Modulation Transfer Function MTF is a often used measure in optical engineering. This function defines the image contrast and thus the image quality at a defined spatial frequency with a value of 100% being the highest and thus can be used as an assessment tool for the performance of the optical system. The overall MTF value is the product of

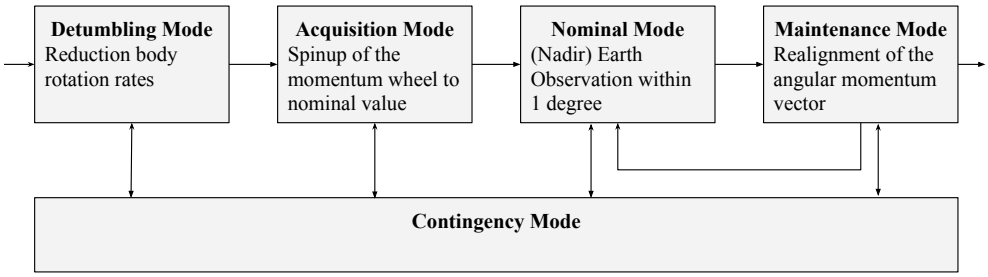


Figure 2.2: Control Mode Sequence

several sub-MTFs consisting of a list of factors such as scattering due to aerosols, detector dimensions, and movement (Joseph 2015). One of the limiting factors of MTF is the detector dimension. Assuming a square size, the MTF due to the detector is equivalent to 63% at the Nyquist frequency. To minimize further loss of image quality, attitude control requirements have been set up for high random frequency angular deviations known as jitter, sinusoidal motion, and linear motion in the direction of orbital velocity. The attitude stability requirement will be based on this important measure.

Requirement (S.7) has been established to allow for a compact adjusted P-POD design (Riki Munakata 2009). Taking a maximum radius of 14 cm allows the system to account for an extra margin of 1 cm on both sides for protection. A momentum wheel larger than 15 cm means that additional CubeSats will be harder to be fit into a CubeSat deployer.

## 2.3 Control Modes

A spacecraft has multiple phases during its lifetime which are given a specific type of functions. Related to this research, four main modes are considered. These include the detumbling, acquisition, nominal, maintenance and contingency modes. In this section, a short description including main functions is given for each of these modes in the field of attitude control for which a diagram is shown in Figure 2.2. These modes are then used to construct the design process as given in the following section.

**Detumbling Mode**

After ejection from the upper stage module, the spacecraft will be subjected to a so-called tumbling rate. This rotation of the spacecraft is in most cases unwanted and the spacecraft is therefore to be detumbled to reduce this effect. During this phase, some of the subsystem's functions are limited due to the loss in power as a result of misalignment of the solar panels to the Sun and inability to deploy all solar panels due to high rotational rates. Besides, the battery has limited capacity within the confound of the system and therefore the detumbling should be done within a specific time.

**Acquisition Mode**

After a spacecraft is successfully detumbled, the acquisition mode is followed. This mode may include various tasks such as establishment of communication with the ground station and deployment of the solar panels. For this study, this mode will be defined as the mission time in which the spacecraft transitions from the detumbling phase to the nominal phase. This includes at least the spinup of the momentum wheel to its nominal value which can include the use of actuators and other attitude related instruments. Like during the detumbling mode, limitations regarding power may be the case. These depend on the spinup strategy taken which is discussed in Chapter 5.

**Nominal Mode**

The spacecraft is then to be capable of executing its main mission. As stated before, SHAPE shall be observing the Earth. During this period, the spacecraft shall be pointing nadir and slewing operations will not be performed. In terms of a single rotor dual-spin spacecraft, one actuator will be continuously operated on the spin axis. The other two axes are gyroscopically stiffened as explained in Chapter 3 and do not require continuous correction.

**Maintenance Mode**

The spacecraft requires maintenance after some period of continuous operation. This "maintenance" differs for actuators used. If one uses reaction wheels, these have to be desaturated periodically as saturated wheels are not capable of producing torque if the maximum angular velocity is reached. Other needs for a maintenance mode of a spinning spacecraft is to re-adjust its angular momentum vector in inertial frame (see Chapter 4).

**Contingency Mode**

In the event of a critical anomaly for which the on-board system cannot correct, the spacecraft is set to the contingency mode. The system's vital functions are then only activated to ensure its survivability. These include such as attitude control for power generation (solar pointing), thermal control, and ground communication.

### 2.3.1 Control Mode Requirements

By having defined the various control modes, a subdivision can be made of the system requirements depending on each mode's functions and their limitations. These requirement are given to be used for constraints to other subsystems or attitude related soft- and hardware. In Table 2.2 to 2.5, the sub-requirements and the associated rationale are listed.

Table 2.2: Detumbling Mode Requirements

| Code | Requirement | Rationale |
|---|---|---|
| S-DM.1 | The angular momentum vector in inertial space shall be aligned perpendicular to the orbital plane within ±<TBD°>. | Section 7.6 |
| S-DM.2 | Transverse rotation rates shall be reduced to less than ten times the mean motion. | Allow coarse pointing and steering |
| S-DM.3 | The magnitude of the angular momentum shall be increased to at least <TBD> Nms. | TBD to be resolved after pre-acquistion analysis for spin stabilization (Section 6.4). |
| S-DM.4 | The detumbling shall be completed within one orbit. | Minimize energy consumption and thus limit battery size. |
| S-DM.5 | The axis of spin stabilization shall be the major axis. | Section 5.7 |
| S-DM.6 | The peak power consumption shall be less than 11 W. | Requirement (S.9) |

Table 2.3: Acquisition Mode Requirements

| Code | Requirement | Rationale |
|---|---|---|
| S-AQ.1 | The momentum transfer from the platform to the rotor shall be done at a constant rate of $1.6 \cdot 10^{-4}$ Nm. | Estimated from a 8 cm wheel radius and two 1 mN resistojets (Section 4.4) |
| S-AQ.2 | The momentum transfer shall be completed within 1.5 orbits. | Spinup time including a margin |
| S-AQ.3 | The momentum wheel shall be spun up to 7000 rpm. | Requirement (S.3) and 2000 rpm added for rotational energy loss over lifetime |
| S-AQ.4 | The magnetic bearings shall be deployed at 5000 rpm. | Requirement (S.3) |
| S-AQ.5 | The acquisition mode shall lead to the nominal mode conditions. | Functional |
| S-AQ.6 | The peak power consumption shall be less than 11 W. | Requirement (S.10) |

Table 2.4: Nominal Mode Requirements

| Code | Requirement | Rationale |
|---|---|---|
| S-NM.1 | The angular momentum vector in inertial space shall be aligned parallel to the orbital rotational axis within a maximum margin of 1 degree. | Part of requirement (S.1) and Section 4.1 |
| S-NM.2 | The system shall be able to monitor the Earth continuously within 1.0° pointing accuracy for at least 1/2 orbit. | Requirement (S.5) |
| S-NM.3 | The nutation angle shall be contained within at least 0.3 degree | Requirement (S.1) and Section 4.7.4 |
| S-NM.4 | The payload platform shall rotate at a rate equivalent to the orbital rate. | Nadir Earth observation, Requirement (S.1) and see Section 4.1 |
| S-NM.5 | The angular velocity shall be contained within 5.5 mrad/s (target) / 3.8 mrad/s (desired) for all axes. | Requirement (S.6) and Section 2.3.2. Note that this is the attitude stability requirement. |

Table 2.5: Maintenance Mode Requirements

| Code | Requirement | Rationale |
|---|---|---|
| S-MM.1 | The maintenance mode shall take place after the pointing angle from nadir has exceeded 1.0°. | Requirement (S.1) |
| S-MM.2 | The angular momentum vector in inertial frame shall be repositioned within 1/2 orbit. | Requirement (S.5) |

### 2.3.2 Modulation Transfer Function Requirement

To elaborate more on requirement (S-NM.5), the effects of linear and sinusoidal motion, and jitter on the MTF have to be determined to comply with requirement (S.6). While the sensor is activated for measurement, linear motion can cause a smear on the image as the spacecraft is traveling along the Earth's surface. This direction can be assumed to be aligned to the spacecraft's orbital velocity. In general, rotational motion of the Earth contributes to a small transverse motion which is negligible. Sinusoidal motion are associated with periodic disturbances such as nutational or resonance motion, yielding in image blurring. Similarly, random high frequency motion can cause reduction of image quality. The frequency and amplitude of the jitter are however superimposed and a probabilistic approach is usually taken to determine the MTF. The MTF for the three cases are defined by Sandau (2009) as

$$\mathrm{MTF}_{\mathrm{smear}} = \frac{\sin\left(\pi V_{\mathrm{sub}} t_{\mathrm{int}} f\right)}{\pi V_g t_{\mathrm{int}} f} \qquad \mathrm{MTF}_{\mathrm{sin}} = J_0(2\pi A f) \qquad \mathrm{MTF}_{\mathrm{jitter}} = e^{-2\pi^2 \sigma_J^2 f^2} \tag{2.1}$$

where $V_{\mathrm{sub}}$ is the sub-satellite velocity (velocity at the intersection between the Earth's surface and the nadir.), $t_{\mathrm{int}}$ the integration time of the sensor, $f$ the spatial frequency, $A$ the amplitude of the sine wave, and $\sigma_j$ the root mean square value of the amplitude of the jitter. $J_0(x)$ is here the $0^{\mathrm{th}}$-order Bessel function of the first kind. The sub-satellite velocity can be computed using

$$V_{\mathrm{sub}} = \frac{R_E}{R_E + h} V_O \tag{2.2}$$

where $R_E$ is the radius of the Earth, $h$ the altitude, and $V_O = \sqrt{\mu_E/(R_E + h)}$ the orbital velocity. For the integration time, usually the dwell time is taken. This is the time span, the detector is exposed to a single ground resolution;

$$t_d = \frac{x_{\mathrm{IFOV}}}{V_{\mathrm{sub}}} \tag{2.3}$$

with $x_{\mathrm{IFOV}}$ the ground distance of Instantaneous Field of View (IFOV) which is equivalent to the ground resolution. In Figure 2.3, the normalized frequency is plotted against the MTF. This normalization is applied with respect to the spatial cutoff frequency of $1/x_{\mathrm{IFOV}}$ given in px/m and the variables $k_s$, $k_{\mathrm{sin}}$, and $k_j$ are defined as follows

$$k_s = \frac{V_{\mathrm{sub}} t_d}{x_{\mathrm{IFOV}}}, \qquad k_{\mathrm{sin}} = \frac{A}{x_{\mathrm{IFOV}}}, \qquad k_j = \frac{\sigma_j}{x_{\mathrm{IFOV}}} \tag{2.4}$$

Note that these are convenient expressions with respect to $x_{\mathrm{IFOV}}$. For example a $k_s$ of 0.1 yields in a $V_{\mathrm{sub}} t_d$ equal to 10% of $x_{\mathrm{IFOV}}$. Next to the payload's loss in MTF of at most 52%, there are other contributions which impacts the image quality besides the three previously related losses. These include such as the effects of particles in the atmosphere which are harder to estimate. Instead, the requirement value of MTF contributed by the ADCS has been approximated based on two reference optical payloads; Hyperion (Nelson & Barry 2001) and GeoEye-1 (GeoEye 2009). At visible wavelengths, the Hyperion payload has been given a requirement value of at least 0.2 and pre-flight measurement values showed a MTF from 0.22 to 0.29 depending on the wavelength and field of view angle. For GeoEye-1, the system MTF has been found to be 0.14. For SHAPE, a system target value has thus been taken for 15% and a desired value of 20%. The 52% payload value is relatively high as the square sensors takes a minimum of 63% MTF. To ensure that uncertainties are within specification, an additional 50% MTF has been taken on top of the payload MTF. Using Equation 2.1 and Equation 2.4, the target and desired MTF values for the attitude system have been estimated at 58% and 77%, respectively.

In Figure 2.4, the combined MTF is given for a frequency $k$ normalized with respect to $x_{\mathrm{IFOV}}$. Two horizontal lines are also depicted to represent the target and desired MTF values. The values for in-track and cross track motions have been found to be deviating within 5% of each other and thus the more strict value has been taken for all three axes. For the target and desired MTF values, the system is expected to be stable if $k$ is within 26% and 18% of the pixel size.

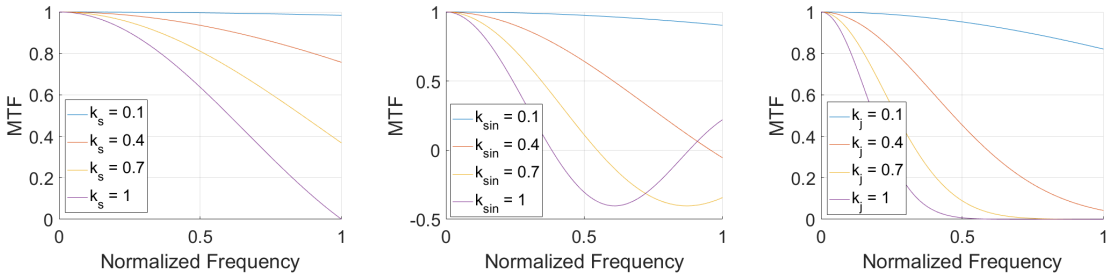


(a) Linear Motion (b) Sinusoidal Motion (c) Jitter

Figure 2.3: Attitude Related MTFs against the Normalized Spatial Frequency

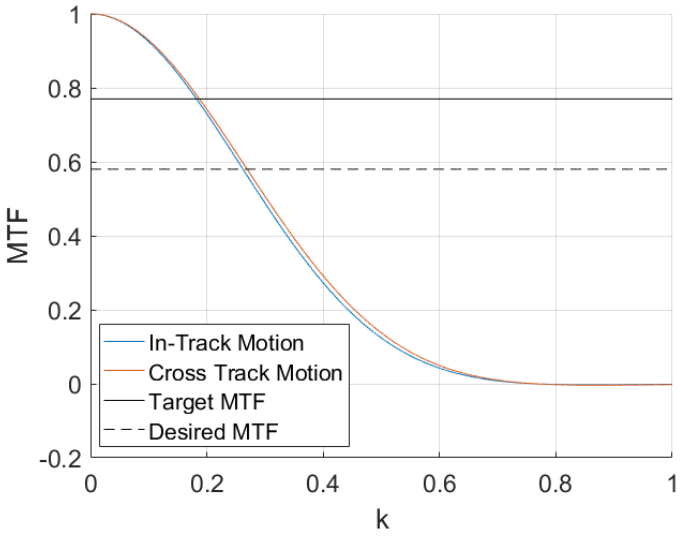


Figure 2.4: Combined Attitude MTF at Nyquist Frequency versus $k$

As the payload is primarily designed at an altitude of 350 km, the integration time has been set equivalent to the dwell time of 0.55 ms. The maximum allowable angle is approximated by dividing $kx_{\text{IFOV}}$ with the height at 350 km; $\theta_{\text{MTF}} = kx_{\text{IFOV}}/h = 3.0$ $\mu$rad for the target value. Dividing by the dwell time, the maximum allowable angular velocity can be determined; $\omega_{\text{max}} = 5.5$ mrad/s. Similarly for the desired value, $\theta_{\text{MTF}} = 2.1$ $\mu$rad and $\omega_{\text{max}} = 3.8$ mrad/s. It should be again noted that this value corresponds to the pitch axis (in-track direction) as the MTF due to linear motion is not applicable to the other two axes. The difference however is less than 5% and therefore for all axes the maximum allowable pitch angular velocity is taken as the general angular velocity constraint.

## 2.4 Design Methodology

Although the concept of dual-spin stabilization has been superseded by 3-axis stabilization, developing 3-axis attitude control system of CubeSats is difficult to achieve with current technology. The "outdated" dual-spin stabilization technique may provide an adequate solution for LEO CubeSats. As the application is not yet applied for VLEO CubeSat, an investigation is performed whether it is feasible. Hereby, a multi-pronged approach is used; a top-down and a bottom-up design. In this thesis, the top-down method is utilized which starts from the end solution while refining the solution to component level throughout the process. Here, the level is limited with respect to the attitude system and two main objectives are to be realized.

The first goal is to revisit the work by Kuiper & Dolkens (2016) and resize the momentum wheel based on predicted conditions during the nominal and maintenance modes within the upcoming decade. The momentum wheel was designed to have an axial moment of inertia value of 1.3 g $m^2$. At a rotational velocity of 7000 rpm, the angular momentum produced by the wheel is approximately 1 Nms which does not match with the given momentum value of 14 mNm in their study. Therefore the first part of this thesis is devoted to resize the momentum wheel if it is found to be necessary. The sizing of the wheel is an important aspect as the stability of the system affects the performance of SHAPE during its lifetime. Achieving the mission operational state is the second objective of this thesis and thus on *how* the spacecraft can attain the dual-spin configuration. This is done by analyzing the possible options of the acquisition mode and select the most suitable option based on evaluation criteria.

These objectives are applied into a design iteration process. The concept is still in its infancy and an accurate prediction of the mission conditions are not yet possible. This thesis will be an initial iteration to verify the possibility of a VLEO high resolution CubeSat EO mission. The design process is started from the point of Earth observation mission and thus the nominal and maintenance design points. The outputs are then used to determine the design for the acquisition mode with respect to the given requirements. This is also applied to the detumbling mode. The whole procedure is then iterated until a feasible design can be found fulfilling requirements and constraints. This is illustrated schematically in Figure 2.5.

The priority of any decision made is given from high for the nominal and maintenance modes and low to the detumbling mode. Design choices of the nominal and maintenance modes are placed at a higher priority due to the importance of the system's main performance and observation mission during these modes. This initial design is not definite and a second analysis should be performed as project planning and budgets are realized.

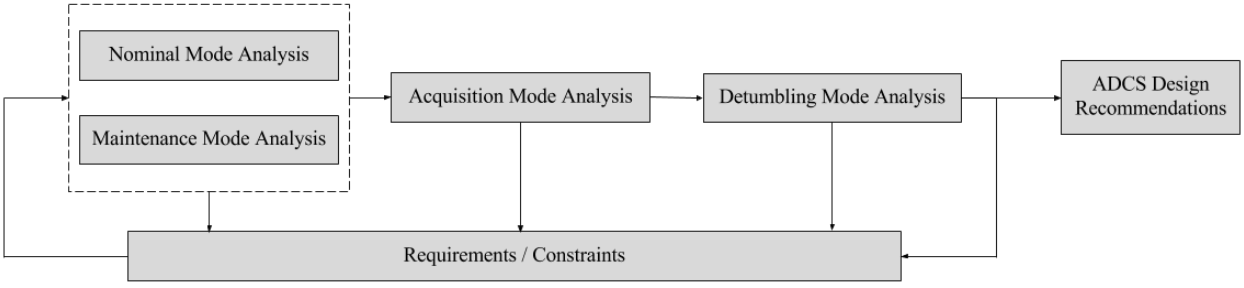


Figure 2.5: Design Analysis Iteration

## 2.5 Concept of Operations

The design presented in this thesis is preliminary and not representable as the design has been based on worst-case assumptions. To design the ACS, a guide line is given in the form of a Concept of Operations (ConOps) as shown in Figure 2.6. The first block (1) requires only a single iteration if the project planning and launch windows are set. The second block (2) contains several subsystems which can affect the ADCS and therefore continuous iterations are expected and red double-headed arrows are used for depiction. Note that the ConOps is given with respect to the system level design of the ADCS and not of the overall system. If at one point in the ConOps an adjustment is applied, an iteration should be followed to optimize the system. In this work, the launch window has been taken at a point of worst-case condition. The next design iteration can be based on a launch window dependent on the project planning and a more optimal condition as given in Chapter 4.

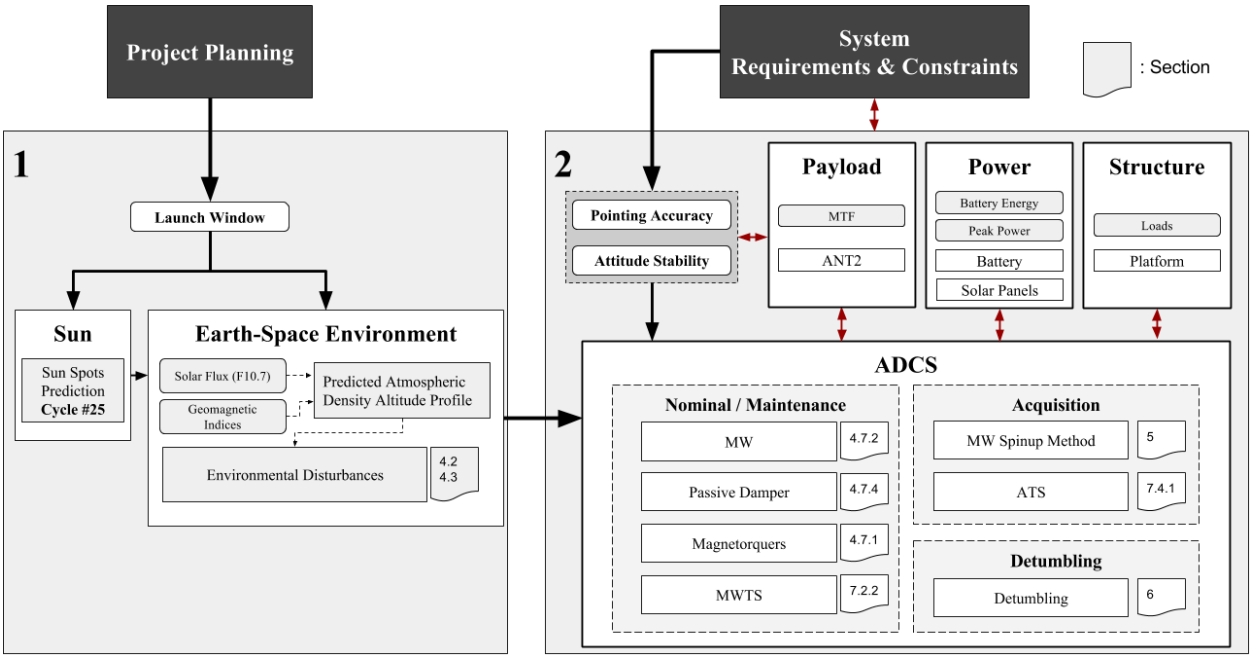


Figure 2.6: Concept of Operations

# Chapter 3

# Background Theory

Before diving into the sizing of the momentum wheel and the selection of the spinup strategy, it is important to understand the rotational kinematics, dynamics of spinning bodies and the concept of the dual-spin spacecraft. This chapter will first give a brief section over the mathematical notations used throughout this work. This is followed by a list of reference frames used which are core to the study of rotational kinematics. In Section 3.4, the resulting motion of a body due to interactions with internal or external physical factors are described. Section 3.5 gives the definition of stability, a nonlinear stability analysis tool, implications of spin stabilization, and the impact of energy dissipation. Then, an important geometric tool for spacecraft motion is given. This chapter closes with a brief description of the dual-spin spacecraft concept.

## 3.1 Mathematical Notation

In this section, some mathematical notations are explained used throughout this thesis. Scalar values are denoted using unbolded letters. Vector notations are given as an overhead arrow, $\vec{\cdot}$. Matrix notations are bolded with lowercase letters representing column vectors and uppercase letters matrices. An exception is the skew symmetric matrix given with a lowercase letter with a cross as superscript;

$$\mathbf{a}^{\times} = \begin{bmatrix} 0 & -a_3 & a_2 \\ a_3 & 0 & -a_1 \\ -a_2 & a_1 & 0 \end{bmatrix} \tag{3.1}$$

The skew symmetric matrix is used to exchange the cross product in vector notation or

$$\mathbf{a}^{\times}\mathbf{b} = \vec{a} \times \vec{b}$$

The superscript of the letter $T$ is used to represent the transpose of the column vector or matrix. The inverse is stated using the superscript of negative one. The identity matrix of size $l$ is given as

$$\bar{\mathbf{1}}_l = \begin{bmatrix} 1 & 0 & 0 & \cdots & 0 \\ 0 & 1 & 0 & \cdots & 0 \\ 0 & 0 & 1 & \cdots & 0 \\ \vdots & \vdots & \vdots & \ddots & \vdots \\ 0 & 0 & 0 & \cdots & 1 \end{bmatrix} \quad \text{with size } \; l \times l \tag{3.2}$$

## 3.2 Reference Frames

Describing a single point, a system of points or a rigid body, requires the application of reference frames. These frames constitute of a set of three right-handed orthonormal vectors used to express directions of mathematical or physical


(a) Schematic Reference Frames $I$, $O$ and $B$

(b) Spacecraft Principal Body Frame $B$

Figure 3.1: Reference Frames

concepts. These can include the direction of the solar wind, Earth's magnetic field, or the orientations of bodies. A multitude of two or more reference frames can then be used to describe a body's orientation relative to each other.

To describe a motion in general, it is important to select an *inertially* fixed reference frame. An inertial reference frame, also called a Newtonian reference frame, is a frame in which Newton's first law can be applied, implying that a particle or body remains in either rest or linear constant motion (Wakker 2015). In the scale of our solar system, small perturbations caused by other galactic systems induces small accelerations to the 'inertial' reference systems in our solar system. By purposely neglecting these small perturbations, one can instead use a *pseudo*-inertial reference frame to describe the motions of bodies. For the remainder of this thesis, an inertial reference frame is referred to this pseudo-inertial frame. A list of reference frame used are listed below and shown in Figure 3.1.

- **Earth-Fixed Inertial Frame**, $N$, is an inertial frame used for Earth-orbiting satellites. An example of such inertial frame is the Non-Rotating Geocentric Equatorial Reference Frame (Wakker 2015). The XY-plane is given in Earth's equatorial plane with its origin centered at Earth's center of mass. The positive Z- and X-axes are directed along the north pole and the First Point of Aries, $\Upsilon$, respectively. The Y-axis is completed using the right-hand rule.

  In this thesis throughout Chapter 4 to Chapter 5, it has been assumed that the exact XY-plane and the directions of the axes are not important as the only bodies considered are the Earth and the spacecraft in her orbit.

- **Orbiting Reference Frame**, $O$, is a local vertical and local horizontal (LVLH) reference frame in which the spacecraft's center of mass is located at its origin. The positive X- and Z- axes are along the orbit direction and towards Earth (nadir), respectively. The Y-axis is directed perpendicular to the orbital plane with its positive axis determined by the right-hand rule.

- **Spacecraft Principal Body Frame**, $B$, is the spacecraft's reference frame in which the centre of mass is at the origin. The axes are aligned to the principal axes of the spacecraft in which the X-axis is aligned to the spin axis of the momentum wheel. The Y-axis is aligned to the principal axis corresponding to the maximum mass moment of inertia and the Z-axis to its minimum.

For the simulations, the angle $\boldsymbol{\theta}$ will be used to represent the rotation of the body frame $B$ with respect to the inertial frame $N$.

## 3.3 Rotational Kinematics

For the analysis of rotational motion, the kinematics gives the relative orientation of a reference frame with respect to another. To describe this orientation, several types of angular representations can be employed. Two commonly used angular parameters are Euler angles and quaternions, each having their own benefits and disadvantages. Here, a brief summary is given for the rotational kinematics in terms of direction cosines, Euler angles and quaternions.

### 3.3.1 Direction Cosine Matrix

Consider two orthogonal right-handed reference frames $A$ and $B$ with unit vectors $(\vec{a}_1, \vec{a}_2, \vec{a}_3)$ and $(\vec{b}_1, \vec{b}_2, \vec{b}_3)$, respectively. One can express the unit vectors of frame $B$ as

$$\begin{bmatrix} \vec{b}_1 \\ \vec{b}_2 \\ \vec{b}_3 \end{bmatrix} = \mathbf{C}^{B/A} \begin{bmatrix} \vec{a}_1 \\ \vec{a}_2 \\ \vec{a}_3 \end{bmatrix} \tag{3.3}$$

with the superscript $B/A$ denoting that the transformation is done from $A$ to $B$. The matrix $\mathbf{C}^{B/A}$ is called a direction cosine matrix as its elements are expressed in terms of cosines between the unit vectors of $A$ and $B$ or equivalently $C_{ij} = \vec{b}_j \cdot \vec{a}_i$. The computation of the reverse transformation (from $B$ to $A$) can be performed by taking the transpose of $\mathbf{C}$ as this is equivalent to its inverse due to the matrix' orthonormality. Another important property is that any vector in one of the reference frame can be expressed in the other using the direction cosine matrix. For the prove of these properties, one is referred to the textbook by Wie (1998).

The direction cosine matrix gives a direct transformation from one frame to another which seems convenient but requires the knowledge of 9 different angles. As a result, it is relatively computationally expensive compared to the other angular parameters.

### 3.3.2 Euler Angles

Instead one can use Euler angles. These angles describe a reference frame with respect to another using a series of three rotations requiring therefore only the knowledge of three angles. Any rotation is expressed using a set of three rotations for which the second and third rotation a different axis is used with respect to the previous. This results in a total of 12 different methods to represent a rotation. To illustrate its purpose, the $1 \leftarrow 2 \leftarrow 3$ set is taken.

Consider again two reference frames denoted by $A$ and $B$. In contrast to the direction cosine matrix, the transformation is not direct and two intermediate reference frames are used i.e. $B \leftarrow A'' \leftarrow A' \leftarrow A$. For the aforementioned rotation set, the first rotation is around the third body axis with a magnitude of $\theta_3$. This is subsequently followed by the second ($\theta_2$) and first ($\theta_1$), respectively. The rotation matrices are given below.

$$\begin{bmatrix} \vec{a}'_1 \\ \vec{a}'_2 \\ \vec{a}'_3 \end{bmatrix} = \mathbf{C}_3(\theta_3) \begin{bmatrix} \vec{a}_1 \\ \vec{a}_2 \\ \vec{a}_3 \end{bmatrix} = \begin{bmatrix} \cos\theta_3 & \sin\theta_3 & 0 \\ -\sin\theta_3 & \cos\theta_3 & 0 \\ 0 & 0 & 1 \end{bmatrix} \begin{bmatrix} \vec{a}_1 \\ \vec{a}_2 \\ \vec{a}_3 \end{bmatrix} \tag{3.4}$$

$$\begin{bmatrix} \vec{a}''_1 \\ \vec{a}''_2 \\ \vec{a}''_3 \end{bmatrix} = \mathbf{C}_2(\theta_2) \begin{bmatrix} \vec{a}'_1 \\ \vec{a}'_2 \\ \vec{a}'_3 \end{bmatrix} = \begin{bmatrix} \cos\theta_2 & 0 & -\sin\theta_2 \\ 0 & 1 & 0 \\ \sin\theta_2 & 0 & \cos\theta_2 \end{bmatrix} \begin{bmatrix} \vec{a}'_1 \\ \vec{a}'_2 \\ \vec{a}'_3 \end{bmatrix} \tag{3.5}$$

$$\begin{bmatrix} \vec{b}_1 \\ \vec{b}_2 \\ \vec{b}_3 \end{bmatrix} = \mathbf{C}_1(\theta_1) \begin{bmatrix} \vec{a}''_1 \\ \vec{a}''_2 \\ \vec{a}''_3 \end{bmatrix} = \begin{bmatrix} 1 & 0 & 0 \\ 0 & \cos\theta_1 & \sin\theta_1 \\ 0 & -\sin\theta_1 & \cos\theta_1 \end{bmatrix} \begin{bmatrix} \vec{a}''_1 \\ \vec{a}''_2 \\ \vec{a}''_3 \end{bmatrix} \tag{3.6}$$

The complete transformation is then simply given by multiplying the three rotations as

$$\begin{bmatrix} \vec{b}_1 \\ \vec{b}_2 \\ \vec{b}_3 \end{bmatrix} = \mathbf{C}_1(\theta_1)\mathbf{C}_2(\theta_2)\mathbf{C}_3(\theta_3) \begin{bmatrix} \vec{a}_1 \\ \vec{a}_2 \\ \vec{a}_3 \end{bmatrix} \tag{3.7}$$

The direction cosine matrix in terms of Euler angles can be computed using the following equation;

$$\mathbf{C}^{B/A} = \begin{bmatrix} \cos(\theta_2)\cos(\theta_3) & \cos(\theta_2)\sin(\theta_3) & -\sin\theta_2 \\ \sin\theta_1\sin\theta_2\cos\theta_3 - \cos\theta_1\sin\theta_3 & \sin\theta_1\sin\theta_2\sin\theta_3 + \cos\theta_1\cos\theta_3 & \sin\theta_1\cos\theta_2 \\ \cos\theta_1\sin\theta_2\cos\theta_3 + \sin\theta_1\sin\theta_3 & \cos\theta_1\sin\theta_2\sin\theta_3 - \sin\theta_1\cos\theta_3 & \cos\theta_1\cos\theta_3 \end{bmatrix} \tag{3.8}$$

### 3.3.3 Quaternions

According to Euler's rotation theorem, any rotation can be expressed with a magnitude and an axis fixed in the body reference frame. This allows a more compact but more abstract representation of rotation called quaternions which are defined as

$$q_1 = e_1 \sin(\theta/2) \tag{3.9}$$
$$q_2 = e_2 \sin(\theta/2) \tag{3.10}$$
$$q_3 = e_3 \sin(\theta/2) \tag{3.11}$$
$$q_4 = \cos(\theta/2) \tag{3.12}$$

with $e_i$ representing the vector elements of the rotation axis (also called the Euler axis) and $\theta$ the magnitude of the rotation. The quaternions have the following property;

$$q_1^2 + q_2^2 + q_3^2 + q_4^2 = 1 \tag{3.13}$$

Due to numerical errors, this constraint can be violated resulting in invalid rotations. Therefore, normalization should be routinely applied. Similar to Euler angles, the direction cosine matrix can be parametrized in terms of quaternions as

$$\mathbf{C}^{B/A} = \begin{bmatrix} 1-2(q_2^2+q_3^2) & 2(q_1q_2+q_3q_4) & 2(q_1q_3-q_2q_4) \\ 2(q_2q_1-q_3q_4) & 1-2(q_1^2+q_3^2) & 2(q_2q_3+q_1q_4) \\ 2(q_3q_1+q_2q_4) & 2(q_3q_2-q_1q_4) & 1-2(q_1^2+q_2^2) \end{bmatrix} \tag{3.14}$$

One reason of its abstractness is in its non-additive properties. Consider two successive rotations in terms of quaternions as $\mathbf{q}'$ and $\mathbf{q}''$ with $\mathbf{q}$ the quaternions associated with the combined rotation. The rotations can be added by using the so-called quaternion matrix multiplication rule given as

$$\begin{bmatrix} q_1 \\ q_2 \\ q_3 \\ q_4 \end{bmatrix} = \begin{bmatrix} q_4'' & q_3'' & -q_2'' & q_1'' \\ -q_3'' & q_4'' & q_1'' & q_2'' \\ q_2'' & -q_1'' & q_4'' & q_3'' \\ -q_1'' & -q_2'' & -q_3'' & q_4'' \end{bmatrix} \begin{bmatrix} q_1' \\ q_2' \\ q_3' \\ q_4' \end{bmatrix} \tag{3.15}$$

or

$$\begin{bmatrix} q_1 \\ q_2 \\ q_3 \\ q_4 \end{bmatrix} = \begin{bmatrix} q_4' & -q_3' & q_2' & q_1' \\ q_3' & q_4' & -q_1' & q_2' \\ -q_2' & q_1' & q_4' & q_3' \\ -q_1' & -q_2' & -q_3' & q_4' \end{bmatrix} \begin{bmatrix} q_1'' \\ q_2'' \\ q_3'' \\ q_4'' \end{bmatrix} \tag{3.16}$$

which the latter is called the quaternion transmuted matrix. Subtraction of rotations are done by taking the inverse of the matrix in Equation 3.16 and solve the equation for $\mathbf{q}''$;

$$\begin{bmatrix} q_{1e} \\ q_{2e} \\ q_{3e} \\ q_{4e} \end{bmatrix} = \begin{bmatrix} q_4' & q_3' & -q_2' & -q_1' \\ -q_3' & q_4' & q_1' & -q_2' \\ q_2' & -q_1' & q_4' & -q_3' \\ q_1' & q_2' & q_3' & q_4' \end{bmatrix} \begin{bmatrix} q_1 \\ q_2 \\ q_3 \\ q_4 \end{bmatrix} \tag{3.17}$$

Note that the inversion of the matrix is equivalent to its transpose due to its orthonormal property of the quaternions.

### 3.3.4 Kinematic Differential Equation

In the previous sections, it was shown how to express an orientation from one reference frame to another. A more elaborated case is when the orientation of reference frames are time-dependent to each other. For example, the orbiting reference frame rotates with respect to the inertial frame $N$ with a constant rotational speed equivalent to the mean motion, assuming a circular orbit. This time-dependency between the reference frames is called kinematic differential equations. The equations in terms of Euler angles and quaternions are respectively;

$$\begin{bmatrix} \dot{\theta}_1 \\ \dot{\theta}_2 \\ \dot{\theta}_3 \end{bmatrix} = \frac{1}{\cos\theta_2} \begin{bmatrix} \cos\theta_2 & \sin\theta_1\sin\theta_2 & \cos\theta_1\sin\theta_2 \\ 0 & \cos\theta_1\cos\theta_2 & -\sin\theta_1\cos\theta_2 \\ 0 & \sin\theta_1 & \cos\theta_1 \end{bmatrix} \begin{bmatrix} \omega_1 \\ \omega_2 \\ \omega_3 \end{bmatrix} \tag{3.18}$$

and

$$\begin{bmatrix}\dot{q}_1\\ \dot{q}_2\\ \dot{q}_3\\ \dot{q}_4\end{bmatrix} = \frac{1}{2}\begin{bmatrix}0 & \omega_3 & -\omega_2 & \omega_1\\ -\omega_3 & 0 & \omega_1 & \omega_2\\ \omega_2 & -\omega_1 & 0 & \omega_3\\ -\omega_1 & \omega_2 & -\omega_3 & 0\end{bmatrix}\begin{bmatrix}q_1\\ q_2\\ q_3\\ q_4\end{bmatrix} = \frac{1}{2}\begin{bmatrix}q_4 & -q_3 & q_2 & q_1\\ q_3 & q_4 & -q_1 & q_2\\ -q_2 & q_1 & q_4 & q_3\\ -q_1 & -q_2 & -q_3 & q_4\end{bmatrix}\begin{bmatrix}\omega_1\\ \omega_2\\ \omega_3\\ 0\end{bmatrix} \tag{3.19}$$

Here, $\omega_i$ are the elements of the rotational velocity vector $\vec{\omega}^{B/A}$ equivalent to the rotation rates of reference frame $B$ with respect to $A$. To describe the motion of a rigid body, $B$, in a circular orbit, $A$, in inertial space, $N$, the angular velocity from the body to the inertial frame, $\vec{\omega}^{B/N}$, has to be described. This is equivalent to

$$\vec{\omega}^{B/N} = \vec{\omega}^{B/A} + \vec{\omega}^{A/N} = \vec{\omega}^{B/A} - n\vec{a}_2 \tag{3.20}$$

Using Equation 3.18 and Equation 3.19, the kinematic differential equations in terms of Euler angles and quaternions can be derived, respectively as

$$\begin{bmatrix}\dot{\theta}_1\\ \dot{\theta}_2\\ \dot{\theta}_3\end{bmatrix} = \frac{1}{\cos\theta_2}\mathbf{A}\begin{bmatrix}\omega_1\\ \omega_2\\ \omega_3\end{bmatrix} + \frac{n}{\cos\theta_2}\mathbf{A}\begin{bmatrix}\cos\theta_2\cos\theta_3\\ \sin\theta_1\sin\theta_2\cos\theta_3 - \cos\theta_1\sin\theta_3\\ \cos\theta_1\sin\theta_2\cos\theta_3 + \sin\theta_1\sin\theta_3\end{bmatrix} \tag{3.21}$$

with

$$\mathbf{A} = \begin{bmatrix}\cos\theta_2 & \sin\theta_1\sin\theta_2 & \cos\theta_1\sin\theta_2\\ 0 & \cos\theta_1\cos\theta_2 & -\sin\theta_1\cos\theta_2\\ 0 & \sin\theta_1 & \cos\theta_1\end{bmatrix} \tag{3.22}$$

and

$$\begin{bmatrix}\dot{q}_1\\ \dot{q}_2\\ \dot{q}_3\\ \dot{q}_4\end{bmatrix} = \frac{1}{2}\begin{bmatrix}q_4 & -q_3 & q_2 & q_1\\ q_3 & q_4 & -q_1 & q_2\\ -q_2 & q_1 & q_4 & q_3\\ -q_1 & -q_2 & -q_3 & q_4\end{bmatrix}\begin{bmatrix}\omega_1\\ \omega_2\\ \omega_3\\ 0\end{bmatrix} + \frac{n}{2}\begin{bmatrix}q_4 & -q_3 & q_2 & q_1\\ q_3 & q_4 & -q_1 & q_2\\ -q_2 & q_1 & q_4 & q_3\\ -q_1 & -q_2 & -q_3 & q_4\end{bmatrix}\begin{bmatrix}C_{11}\\ C_{21}\\ C_{31}\\ 0\end{bmatrix} \tag{3.23}$$

Note that the first column of the direction cosine matrix is taken as the mean motion is given in the first axis.

Euler angles are used due to its ease of understanding rotational motions. However, it has an inherent flaw. At $\theta_2 = \pm\pi/2$ for this particular rotation set, the system is locked onto the second axis. This phenomena is also called gimbal lock and is a problem which might occur at large rotational manoeuvres. Despite the abstract description, quaternions does not contain trigonometric terms increasing the computational speed (Wie 1998) and therefore have been chosen to be implemented in the numerical simulations of this thesis.

### 3.3.5 Conversion of Angular Representations

Before continuing to the rotational dynamics, this section will be concluded with how one can convert from Euler angles to quaternions and vice versa. This has no other benefit than for its ease of visually understanding and for the conversion required for the initial conditions. The conversion from Euler angles to quaternions can be derived by considering each rotation of the set as a separate rotation with respect to quaternions. The rotation sequence $1 \leftarrow 2 \leftarrow 3$ is thus divided into a rotation on the third axis of magnitude $\theta_3$, the second axis with $\theta_2$ and as well for the first. A rotation through one of the axis is simply obtained by using the definition of quaternions as given in Equation 3.12. For example, a rotation through the third axis with magnitude $\theta_3$ has an equivalent eigenaxis of $\vec{e} = (0, 0, 1)$ and magnitude $\theta = \theta_3$ or in quaternions as

$$\begin{aligned} q_1 &= 0\\ q_2 &= 0\\ q_3 &= \sin\frac{\theta_3}{2}\\ q_4 &= \cos\frac{\theta_3}{2}\end{aligned}$$

In a similar manner, the other two axes can be defined in quaternions. To add these rotations together the quaternion matrix multiplication rule given in Equation 3.15 is used, giving the following relationship between Euler angles and

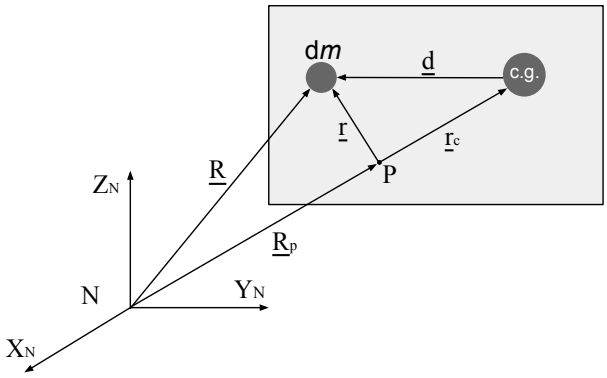


Figure 3.2: Schematic View of the Rigid Body in Inertial Reference Frame

quaternions

$$\begin{bmatrix} q_1 \\ q_2 \\ q_3 \\ q_4 \end{bmatrix} = \begin{bmatrix} \sin\frac{\theta_1}{2}\cos\frac{\theta_2}{2}\cos\frac{\theta_3}{2} - \cos\frac{\theta_1}{2}\sin\frac{\theta_2}{2}\sin\frac{\theta_3}{2} \\ \cos\frac{\theta_1}{2}\sin\frac{\theta_2}{2}\cos\frac{\theta_3}{2} + \sin\frac{\theta_1}{2}\cos\frac{\theta_2}{2}\sin\frac{\theta_3}{2} \\ \cos\frac{\theta_1}{2}\cos\frac{\theta_2}{2}\sin\frac{\theta_3}{2} - \sin\frac{\theta_1}{2}\sin\frac{\theta_2}{2}\cos\frac{\theta_3}{2} \\ \cos\frac{\theta_1}{2}\cos\frac{\theta_2}{2}\cos\frac{\theta_3}{2} + \sin\frac{\theta_1}{2}\sin\frac{\theta_2}{2}\sin\frac{\theta_3}{2} \end{bmatrix} \tag{3.24}$$

The inverse relationship is hard to compute from this equation. However, one can derive the inverse relation by using the elements of the direction cosine matrix in terms of Euler angles and quaternions. By dividing element $C_{23}$ with $C_{33}$ of Equation 3.8, one obtains

$$\frac{C_{23}}{C_{33}} = \frac{\sin\theta_1\cos\theta_2}{\cos\theta_1\cos\theta_2} = \tan\theta_1 \quad \rightarrow \quad \theta_1 = \tan^{-1}\frac{C_{23}}{C_{33}} \tag{3.25}$$

Similarly,

$$C_{13} = -\sin\theta - 2 \quad \rightarrow \quad \theta_2 = \sin^{-1} -C_{13} \tag{3.26}$$

$$\frac{C_{12}}{C_{11}} = \frac{\cos\theta_2\sin\theta_3}{\cos\theta_2\cos\theta_3} = \tan\theta_3 \quad \rightarrow \quad \theta_3 = \tan^{-1}\frac{C_{12}}{C_{11}} \tag{3.27}$$

The final relationships are obtained by substituting the direction cosine elements given in quaternions (Equation 3.14) into the equations above.

## 3.4 Rotational Dynamics

For the rotational dynamics several assumptions are used which have important implications in the motion of spinning bodies. Therefore in the following subsection, the derivation of the rotational dynamics, also known as Euler's rotational equations of motion, will be given. Additionally, several principles such as the conservation of angular momentum and the kinetic energy are derived.

### 3.4.1 Derivation of Euler's Rotational Equations of Motion

Assume a rigid body $\mathcal{R}$ in an inertial reference frame as shown in Figure 3.2. The rotation of $\mathcal{R}$ about an arbitrary point $P$ is given as

$$\int \vec{r} \times \ddot{\vec{R}}\, \mathrm{d}m = \vec{\tau}_P \tag{3.28}$$

where $\vec{r}$ denotes the position vector of a mass element $\mathrm{d}m$ relative to point $P$, $\vec{R}$ the position vector of the element with respect to the inertial frame, and $\vec{\tau}_P$ the external disturbance torque around point $P$. If the position vector of $P$ to $\mathcal{R}$'s

center of mass is given as $\vec{r}_c$, the following relations hold

$$\int \vec{r}\,\mathrm{d}m = m\vec{r}_c \qquad \int \vec{d}\,\mathrm{d}m = 0 \tag{3.29}$$

with $m$ the total mass of $\mathcal{R}$ and $\vec{d}$ the position vector of the mass element with respect to the center of mass. Using the vector relation $\vec{R} = \vec{R}_P + \vec{r}$ and applying Equation 3.29, to Equation 3.28 yields the following

$$\dot{\vec{H}}_{r,P} + m\vec{r}_c \times \ddot{\vec{R}}_P = \vec{\tau}_P \tag{3.30}$$

with

$$\vec{H}_{r,P} = \int \vec{r} \times \dot{\vec{r}}\,\mathrm{d}m \tag{3.31}$$

Here, $\vec{H}_{r,P}$ is defined as the relative angular momentum at point $P$. The derivative of the relative angular momentum equals;

$$\dot{\vec{h}}_P = \int \dot{\vec{r}} \times \dot{\vec{r}}\,\mathrm{d}m + \int \vec{r} \times \ddot{\vec{r}}\,\mathrm{d}m = 0 + \int \vec{r} \times \ddot{\vec{r}}\,\mathrm{d}m$$

Similarly, one can define the absolute angular momentum as

$$\vec{H}_P = \int \vec{r} \times \dot{\vec{R}}\,\mathrm{d}m \tag{3.32}$$

with its derivative;

$$\dot{\vec{H}}_P = \int \dot{\vec{r}} \times \dot{\vec{R}}\,\mathrm{d}m + \int \vec{r} \times \ddot{\vec{R}}\,\mathrm{d}m$$

Substitution into Equation 3.28 results in

$$\dot{\vec{H}}_P + \int \dot{\vec{R}} \times \dot{\vec{r}}\,\mathrm{d}m = \vec{\tau}_P$$

Substitution of $\vec{R} = \vec{R}_P + \vec{r}$ and the derivative of Equation 3.29 yields

$$\dot{\vec{H}}_P + m\dot{\vec{R}}_P \times \dot{\vec{r}}_c = \vec{\tau}_P \tag{3.33}$$

The absolute and relative angular momentum equalize when the point $P$ is inertially fixed or is located at the center of mass reducing the equation to

$$\dot{\vec{H}}_P = \dot{\vec{h}}_P = \vec{\tau}_P \tag{3.34}$$

Another important result from Equation 3.34 is that when no external torque acting on the rigid body, the total angular momentum of the system reduces to a constant value. This phenomena is also known as the *conservation of angular momentum* which has important implications (see Section 3.6).

Continuing from Equation 3.34 with the reference point now taken at the center of mass, the position vectors are now equivalent to $\vec{r}_c = 0$, $\vec{R}_P \triangleq \vec{R}_c$ and $\vec{r} = \vec{d}$. Substituting into the definition for the absolute angular momentum, using the vector position relation $\vec{R} = \vec{R}_c + \vec{d}$ and Equation 3.29, one can obtain

$$\vec{H} = \int \vec{d} \times \dot{\vec{R}}\,\mathrm{d}m = \int \vec{d} \times \dot{\vec{d}}\,\mathrm{d}m$$

Hereby, the subscript $P$ has been dropped to denote the absolute angular momentum with respect to the center of mass. The current time derivatives are given in the inertial frame $N$, to express $\dot{\vec{d}}$ in the body frame $B$ with respect to the inertial frame one can apply the transport theorem as

$$\dot{\vec{d}} = \left.\frac{\mathrm{d}\vec{d}}{\mathrm{d}t}\right|_N = \left.\frac{\mathrm{d}\vec{d}}{\mathrm{d}t}\right|_B + \vec{\omega} \times \vec{d} \tag{3.35}$$

with $\vec{\omega}$, the rotational velocity of the rigid body with respect to the inertial frame. Substitution yields in

$$\vec{H} = \int \vec{d} \times \left( \left.\frac{\mathrm{d}\vec{d}}{\mathrm{d}t}\right|_B + \vec{\omega} \times \vec{d} \right) \mathrm{d}m$$

The equation can be reduced using the assumption that $\mathcal{R}$ is a rigid body and thus the system's mass elements does not change in position throughout time; $\mathrm{d}\vec{d}/\mathrm{d}t \Big|_B = 0$. This leads to

$$\vec{H} = \int \vec{d} \times \left(\vec{\omega} \times \vec{d}\right) \mathrm{d}m \tag{3.36}$$

Express the position and angular velocity vector in the body frame $B$ as

$$\vec{d} = d_1\vec{b}_1 + d_2\vec{b}_2 + d_3\vec{b}_3 \qquad \vec{\omega} = \omega_1\vec{b}_1 + \omega_2\vec{b}_2 + \omega_3\vec{b}_3 \tag{3.37}$$

Equation 3.36 can then be solved as

$$\vec{H} = (I_{11}\omega_1 + I_{12}\omega_2 + I_{13}\omega_3)\vec{b}_1 + (I_{21}\omega_1 + I_{22}\omega_2 + I_{23}\omega_3)\vec{b}_2 + (I_{31}\omega_1 + I_{32}\omega_2 + I_{33}\omega_3)\vec{b}_3 \tag{3.38}$$

with

$$I_{ii} = \int (d_j^2 + d_k^2)\ \mathrm{d}m \qquad I_{ij} = -\int d_i d_k\ \mathrm{d}m$$

for $i = 1, 2, 3$, $j = 1, 2, 3$, $k = 1, 2, 3$ and $i \neq j \neq k$. These are called the moments of inertia and products of inertia, respectively. Expressing the components of the angular momentum vector in the body frame gives

$$H_1 = I_{11}\omega_1 + I_{12}\omega_2 + I_{13}\omega_3 \tag{3.39}$$

$$H_2 = I_{21}\omega_1 + I_{22}\omega_2 + I_{23}\omega_3 \tag{3.40}$$

$$H_3 = I_{31}\omega_1 + I_{32}\omega_2 + I_{33}\omega_3 \tag{3.41}$$

or in matrix notation as

$$\mathbf{H} = \mathbf{I}\boldsymbol{\omega} \tag{3.42}$$

An important integral of motion is the *rotational kinetic energy* which is defined as

$$T = \frac{1}{2}\int \dot{\vec{d}} \cdot \dot{\vec{d}}\ \mathrm{d}m \tag{3.43}$$

Using the transport theorem defined earlier and the rigidity assumption, the energy can be derived to

$$T = \frac{1}{2}\vec{\omega} \cdot \vec{H} \tag{3.44}$$

Starting back from Equation 3.29 and applying the transport theorem in matrix form yields

$$\dot{\mathbf{H}} = \left.\frac{\mathrm{d}\mathbf{H}}{\mathrm{d}t}\right|_B + \boldsymbol{\omega}^{\times}\mathbf{H} = \boldsymbol{\tau} \tag{3.45}$$

Substitution of Equation 3.42 into 3.45 gives

$$\boldsymbol{\tau} = \left.\frac{\mathrm{d}\,(\mathbf{I}\boldsymbol{\omega})}{\mathrm{d}t}\right|_B + \boldsymbol{\omega}^{\times}\mathbf{I}\boldsymbol{\omega} = \left.\frac{\mathrm{d}\mathbf{I}}{\mathrm{d}t}\right|_B \boldsymbol{\omega} + \mathbf{I}\left.\frac{\mathrm{d}\boldsymbol{\omega}}{\mathrm{d}t}\right|_B + \boldsymbol{\omega}^{\times}\mathbf{I}\boldsymbol{\omega}$$

As $\mathrm{d}\mathbf{I}/\mathrm{d}t = 0$ and $\mathrm{d}\boldsymbol{\omega}/\mathrm{d}t = \dot{\boldsymbol{\omega}}$, Euler's rotational equations of motion in matrix format is

$$\mathbf{I}\dot{\boldsymbol{\omega}} + \boldsymbol{\omega}^{\times}\mathbf{I}\boldsymbol{\omega} = \boldsymbol{\tau} \tag{3.46}$$

The last concept to derive is the principal moments of inertia. This is a special case where the product moment of inertia are reduced to zero. To find the values of the principal moments of inertia and the according axis in the body frame one can use the following

$$\left[\lambda\bar{\mathbf{I}}_3 - \mathbf{I}\right]\mathbf{e} = 0 \tag{3.47}$$

with $\lambda$, the eigenvalues, define the magnitude of the principal moments of inertia on the principal axes $e_i$. If the rigid body is given in the principal body frame, the rotational motion reduces to

$$I_1\dot{\omega}_1 - (I_2 - I_3)\omega_2\omega_3 = \tau_1 \tag{3.48}$$

$$I_2\dot{\omega}_2 - (I_3 - I_1)\omega_3\omega_1 = \tau_2 \tag{3.49}$$

$$I_3\dot{\omega}_3 - (I_1 - I_2)\omega_1\omega_2 = \tau_3 \tag{3.50}$$

This is a system of coupled, nonlinear ordinary differential equations.

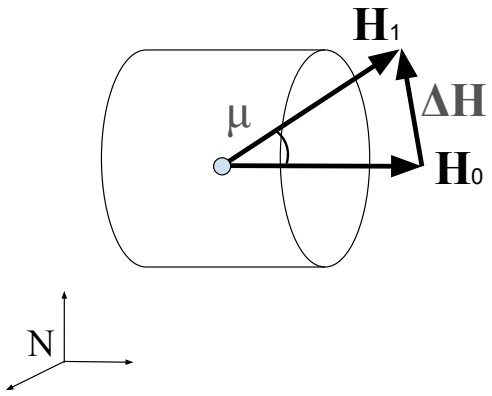


Figure 3.3: Change of Angular Position in Inertial Space

### 3.4.2 Gyroscopic Properties

The advantage of spinning spacecraft as mentioned in the introduction is the gyroscopic stiffness. The effect of this property can be understood using vectors in inertial space as depicted in Figure 3.3. Hereby, vector $\mathbf{H}_0$ represents the initial or desired angular momentum vector. Due to an external disturbance, a displacement of the vector $\Delta\mathbf{H}$ can occur, resulting in the final orientation of the angular momentum vector $\mathbf{H}_1$. Depending on the direction of this external disturbance, an attitude change of the spacecraft can be observed. If for one assumes that the disturbance is constant and acts perpendicular to the desired angular momentum vector, this angle can be approximated as

$$\mu \approx \frac{\|\Delta \boldsymbol{H}\|}{\|\boldsymbol{H}\|} = \frac{\tau t_n}{\|\boldsymbol{H}\|} \tag{3.51}$$

with $\tau$ the cross external disturbance torque and $t_n$ the time it acts upon the vector. Note that hereby small angles approximation has been assumed which should allow less than 0.015% error for cosine angles smaller than 1°. Following from this relation, it can be concluded that a higher angular momentum provides a stronger "stiffness" against external disturbance. To increase the angular momentum, one requires an increased inertia or angular velocity. Another property of spinning spacecraft is the added stability due to the spinning motion. This is handled in the next section.

## 3.5 Stability

Spin stabilization is as the name implies a technique used to stabilize a spacecraft by inducing a spin around an axis. To analyze how this phenomena arises, one is required to know the concept of stability theory. In this section, two concepts are briefly summarized; stability in the sense of Lyapunov and Lyapunov's direct method. This is followed with the stability of a spinning spacecraft and the effect of energy dissipation on the stability.

### 3.5.1 Stability in the Sense of Lyapunov

Stability of systems is considered to be either unstable, stable in the sense of Lyapunov (or Lyapunov stable) or asymptotically stable. The latter is also seen as a special case of stability in the sense of Lyapunov. A differential equation in the form

$$\dot{\mathbf{x}} = f(t, \mathbf{x}) \tag{3.52}$$

with an equilibrium point $f(t, 0) = 0$, is considered to be stable in the sense of Lyapunov if the solution $\mathbf{x}(t)$ with initial conditions of $(t_0, \mathbf{x}_0)$ stays near the solution $x = 0$ for $t > t_0$ and $x > x_0$. This system is considered unstable if the solution is not stable in the sense of Lyapunov and is said to be asymptotically stable if the solution is considered Lyapunov stable and converges to the equilibrium point. More formal definitions of these stability conditions can be found in the textbook by Verhulst (2006).

### 3.5.2 Lyapunov's Direct Method

A method to analyze whether nonlinear systems are globally or locally stable is Lyapunov's direct method (Verhulst 2006). Although there are different methods to analyze nonlinear systems, Lyapunov's direct method is used as a base for many sub-analysis such as in control theory. An important key concept herein is the Lyapunov's function.

Consider a function $V(t, x)$ which is assumed to be continuously differentiable for $t \leq t_0$ within a domain $D$ with $V(t, 0) = 0$. This function is said to be positive (semi)definite if it is larger than (or equal to) zero for $t \leq t_0$ and negative if is it smaller than (or equal to) zero. The system is Lyapunov stable if one can find a function $V(t, x)$ which is positive definite and its derivative negative (semi)definite, or

$$\dot{V}(t, x) = \frac{\partial V}{\partial t} + \frac{\partial V}{\partial x} f(t, x) \tag{3.53}$$

If the derivative is negative definite, the system is said to be asymptotic stable. If it is semidefinite, it coheres to Lyapunov stability. Depending on the domain $D$, the system given in Equation 3.52 can be globally stable. This is the case as $D$ surrounds the set for all possible $x$ and has the property that $V(t, x)$ satisfies the aforementioned conditions. For an autonomous system, the first partial derivative in Equation 3.53 is equal to zero. The function $V(t, x)$ which satisfies these conditions is then called a Lyapunov function. Lyapunov's direct method is a powerful tool for which the system can be verified for local or global stability, but requires the setup of Lyapunov functions. These might provoke some difficulty as devising a Lyapunov function requires in-depth understanding of the dynamics.

### 3.5.3 Spin Stability

To determine the attitude stability of spinning spacecraft, a technique called infinitesimal (linear stability) analysis can used Hughes (2004). By perturbing the system with small angles and angular velocities, and linearization of the rotational dynamics, one can analyze whether the system is stable (see Appendix A). The stability analysis are provided by Hughes and are therefore not given in this work and instead the reader is to be referred to Hughes' textbook.

Hughes concludes that the system defined by Equations 3.48 to 3.50 with $\tau_i = 0$ are unstable in terms of the attitude. By applying a small perturbation in the angular velocity on the axis of rotation, the system will not return to its original state. However, a different kind of stability does exist which is called directionally stability. These conditions have been found to be dependent on the ratios of inertias which are given as below assuming the rotation occurs in the second principal axis.

$$k_1 \triangleq \frac{I_2 - I_3}{I_1} \qquad k_3 \triangleq \frac{I_2 - I_1}{I_3} \tag{3.54}$$

The conditions for which the system is directionally stability are given as

$$1 + k_1 k_3 > 0 \tag{3.55}$$

$$k_1 k_3 > 0 \tag{3.56}$$

$$(1 - k_1 k_3)^2 > 0 \tag{3.57}$$

Directional stability implies that the system is stable against perturbations perpendicular to the angular momentum vector. Plotting the conditions for all possible values of $k_1$ and $k_3$ are shown in Figure 3.4. The difference between static and dynamic stability is based on different terms in the equations derived from the infinitesimal analysis which again one is referred to Hughes. In the figure, black represents unstable configurations while white and gray are directionally stable under the pretense of a *rigid* spacecraft.

### 3.5.4 Energy Dissipation

The first American spacecraft *Explorer 1*, a minor axis (prolate) spinner which has been assumed to be stable, became unstable over time (Likins 1986). This problem was first predicted by Bracewell & Garriott (1958) and analyzed by Mingori (1969). They concluded that energy dissipation by flexible structural elements caused the spacecraft to precess over time to a major axis spin. For the analysis of energy dissipation on spin stabilized bodies, two methods are given by Hughes (2004); the energy sink hypothesis and by approximation of non-rigidity using a discrete damper. The first uses a 'mathematical' reduction in the kinetic energy to describe energy dissipation. The rigid body including a discrete damper provides a more analytical result as the effects of non-rigidity are modeled in the form of a ball-in-tube

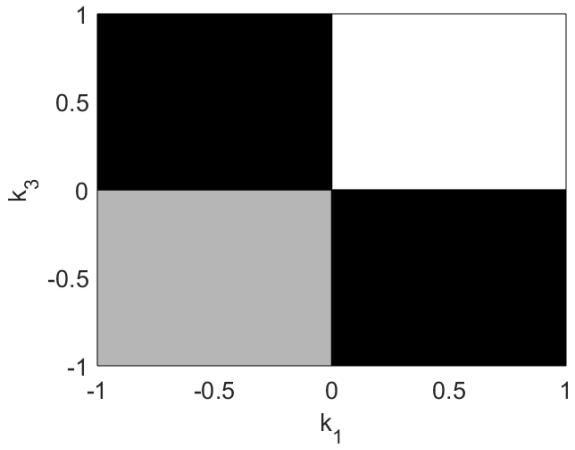


Figure 3.4: Smelt Diagram for a Rigid Spinning Spacecraft with White Depicting Static Stability, Gray Dynamically Stability and Black Instability

damper. Using again the infinitesimal analysis, Hughes provides conditions for which the system is directionally stable. The inertia ratios are now defined as

$$k_{1d} \triangleq k_1 \qquad k_{3d} \triangleq k_3 - \Xi \tag{3.58}$$

with $\Xi$ depicting the parameter associated with damping. This parameter relates to the ratio of the damper's inertia to the third principal axis of the body, frequency of the damper and the speed of the rotation. The resulting Smelt diagram is shown in Figure 3.5. The left bottom corner associated with a spacecraft spinning around its minor axis has become unstable compared to the case without energy dissipation.

Additionally, a small portion of the major inertia spin has become unstable (just above the $k_{d3} = 0$ line). The stability of this spin is besides being directionally stable, also asymptotically stable. A damping device therefore is beneficial for a major axis spinning spacecraft. From the results of energy dissipation arose the major axis rule for spinning spacecraft for which it is required to be more 'disk'-like (oblate) around its axis of rotation to ensure stability.

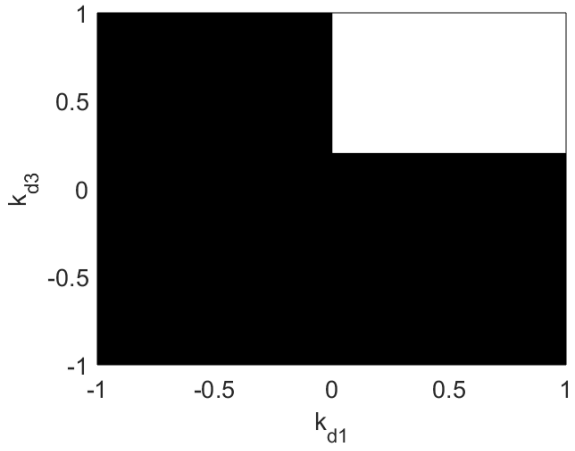


Figure 3.5: Smelt Diagram for a Rigid Spinning Spacecraft with a Point Mass Damper with White Depicting Asymptotically Directionally Stability and Black Instability

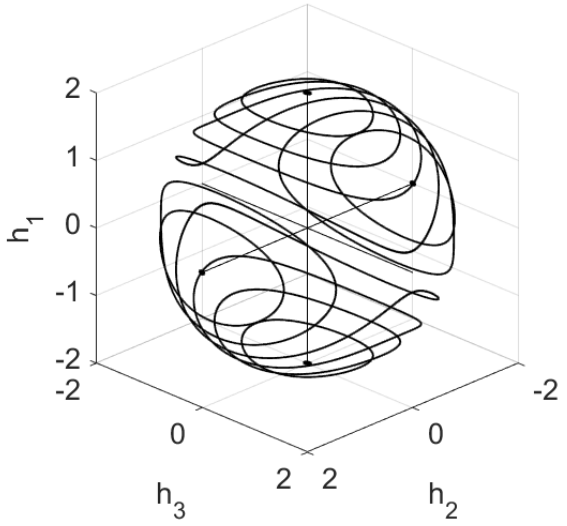


Figure 3.6: Rigid Spacecraft Momentum Sphere with SHAPE's Inertia with $\|\vec{H}\| = 2$ Nms

## 3.6 Momentum Sphere

The angular momentum conservation and rotational energy derived in Section 3.4.1 are two quantities which limit the possible range of rotational motions. The conservation of angular momentum states that the angular momentum for an external torque-free motion is constant. As the magnitude is constant the possible angular momentum in the body frame is limited on a so-called momentum sphere defined as

$$H^2 = H_1^2 + H_2^2 + H_3^2 \tag{3.59}$$

The energy is given in matrix form as

$$T = \frac{1}{2}\boldsymbol{\omega}^T \mathbf{H} \tag{3.60}$$

By substitution of Equation 4.15, the energy can be expressed in terms of angular momentum and the moment of inertia;

$$T = \frac{1}{2}\left(\frac{H_1^2}{I_1} + \frac{H_2^2}{I_2} + \frac{H_3^2}{I_3}\right) \tag{3.61}$$

The rotational energy represents geometrically an ellipsoid. The intersection between these two geometrical surfaces results in a range of possible motion of the spinning rigid spacecraft also called polhodes. In Figure 3.6, the polhodes projected on the momentum sphere are shown using SHAPE's moments of inertia with an angular momentum of 2 Nms. One can conclude from the definition of stability that the major and minor axes are directionally stable in the sense of Lyapunov as the polhodes are closed orbits staying near the axis. The intermediate axis does not show such behavior and is unstable as given in Section 3.5.3. The energy of the polhodes has the highest values at the positive or negative major axis and lowest at the minor axis. The effects of energy dissipation therefore can be derived from these spheres. As the energy reduces over time, the rotational motion of the spacecraft will develop towards one around the major axis.

## 3.7 Dual-Spin Spacecraft

The dual-spin spacecraft is the solution to the unstable prolate single spinning spacecraft described previously. Besides the possibility of a despun platform for sensors and payload, it has an added benefit that a prolate spacecraft is stable. The very first prolate dual-spinner TACSAT-1 was launched in 1969 which proved this concept (Likins 1986).

A dual-spacecraft can be divided into two characteristic components. One is a "stationary" body also called the platform ($\mathcal{P}$) which is stationary in the sense that it is rotating relatively slowly in contrast to the rotating body known as the wheel, rotor or gyro ($\mathcal{W}$). The platform either is inertially fixed or rotates depending on the mission. Even if the platform is designed to be stationary, the gyroscopic properties still holds for a dual-spin spacecraft. The combination of the platform and the rotor (gyro) is defined as a gyrostat. The rotational motion for a gyrostat is given as

$$\dot{\mathbf{H}} = -\boldsymbol{\omega}^{\times}\mathbf{H} + \boldsymbol{\tau} \tag{3.62}$$

with

$$\mathbf{H} = \mathbf{I}\boldsymbol{\omega} + I_s\omega_s\mathbf{a} \tag{3.63}$$

Substitution of Equation 3.63 into Equation 3.62 and describing the body in the principal body frame gives

$$I_1\dot{\omega}_1 = (I_2 - I_3)\omega_2\omega_3 + H_s(a_2\omega_3 - a_3\omega_2) + \tau_1 \tag{3.64}$$

$$I_2\dot{\omega}_2 = (I_3 - I_1)\omega_3\omega_1 + H_s(a_3\omega_1 - a_1\omega_3) + \tau_2 \tag{3.65}$$

$$I_3\dot{\omega}_3 = (I_1 - I_2)\omega_1\omega_2 + H_s(a_1\omega_2 - a_2\omega_1) + \tau_3 \tag{3.66}$$

In these equations, $H_s$ represents the angular momentum of the rotor equivalent to $I_s\omega_s$ with $\omega_s$ the relative angular velocity of the rotor and $a_i$ position vector elements of the spin axis of the rotor given in the principal axis frame. The gyroscopic coupling now is applied by the $H_s$ term which for example occurs with the first and third axes, if the spin axis is aligned to $\vec{a} = (0, 1, 0)^T$. The stiffness is still retained in the angular momentum stored in the rotor.

### 3.7.1 Stability

Similar to the stability analysis of the rigid spinning spacecraft, Hughes applies the infinitesimal analysis to the dual-spin spacecraft. The modified Smelt parameters $k_1$ and $k_3$ are given as

$$k_{1h} \triangleq k_1 + \Omega\sqrt{\frac{1-k_1}{1-k_3}} \qquad k_{3h} \triangleq k_3 + \Omega\sqrt{\frac{1-k_3}{1-k_1}} \tag{3.67}$$

with $\Omega$ a parameter affiliated with the angular momentum of the rotor, the transverse inertias and the angular velocity of the platform in the spin axis. The results are depicted in Figure 3.7. Similar to the rigid spacecraft without energy dissipation, the system has directional stability on the prolate axis. The dual-spin spacecraft is also able to stabilize the configuration on the intermediate axis, albeit only for a specific range of inertias. Increasing the angular momentum of the rotor however influences the system considerably. At values of $\Omega \geq 1$ and $\Omega \leq -1$, any configuration of inertias is directionally stable.

### 3.7.2 Momentum Sphere

The intersection of the energy ellipsoid with the momentum sphere for the dual-spin spacecraft is similar to that of the single spinner. While the angular momentum conservation remains the same, the energy equation is given as

$$T = \frac{1}{2}\left[\frac{(H_1 - h_s)^2}{I_1} + \frac{H_2^2}{I_2} + \frac{H_3^2}{I_3}\right] \tag{3.68}$$

The trajectories of motion, again applied to SHAPE, are given in Figure 3.8. The situation corresponds to the case where the rotor has absorbed all of the angular momentum. The rotational kinetic energy is lowest at the positive minor axis equivalent to zero as the platform is not rotating. The energy increases in the direction to the negative axis with the axis point itself having the maximum energy. The directional stability can be observed very clearly, given on the direction of minor axis.

### 3.7.3 Energy Dissipation

To confirm that the dual-spin spacecraft is indeed directionally stable in presence of energy dissipation, one can analyze the stability properties by adding a damper. Hughes gives the adjusted inertia parameters as

$$k_{1hd} \triangleq k_{1h} \qquad k_{3hd} \triangleq k_{3h} - \Xi \tag{3.69}$$

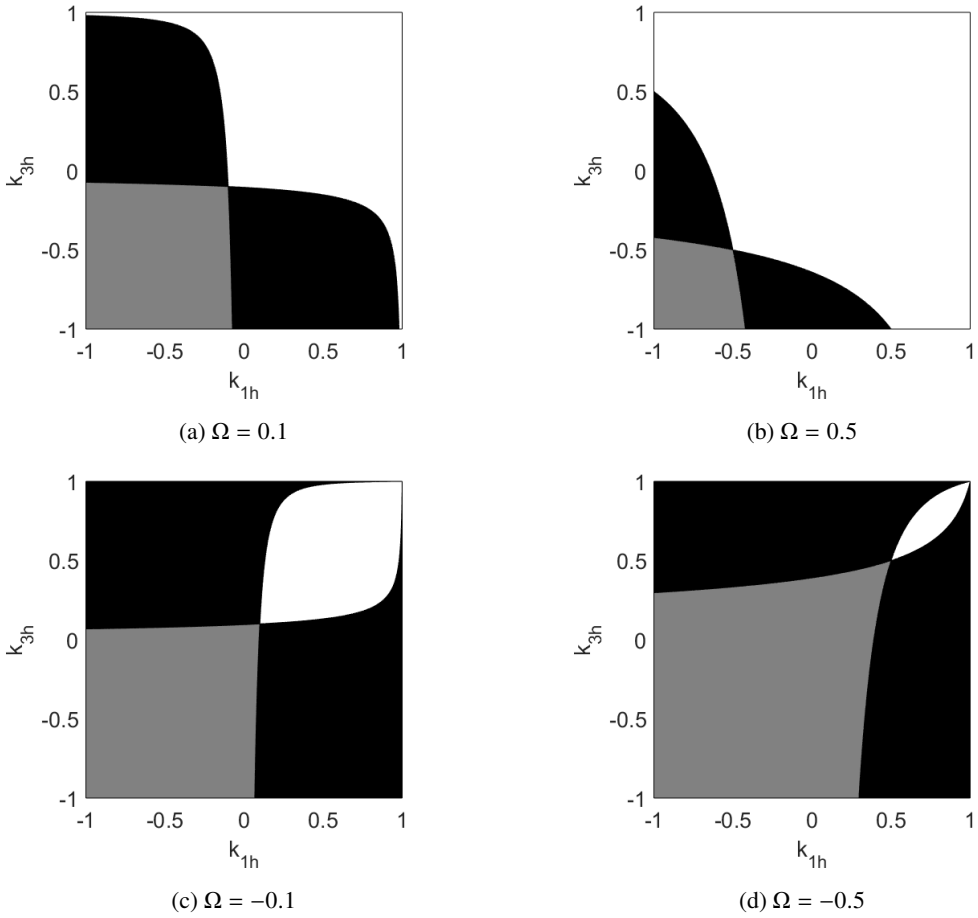


(a) $\Omega = 0.1$ (b) $\Omega = 0.5$

(c) $\Omega = -0.1$ (d) $\Omega = -0.5$

Figure 3.7: Smelt Diagram for a Dual-Spin Spacecraft with White Depicting Static Stability, Gray Dynamically Stability and Black Instability

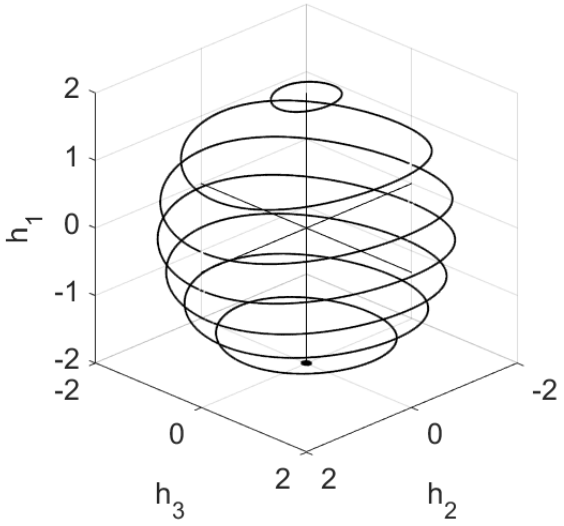


Figure 3.8: Dual-Spin Spacecraft Momentum Sphere with SHAPE's Inertia with $\|\vec{H}\| = 2$ Nms

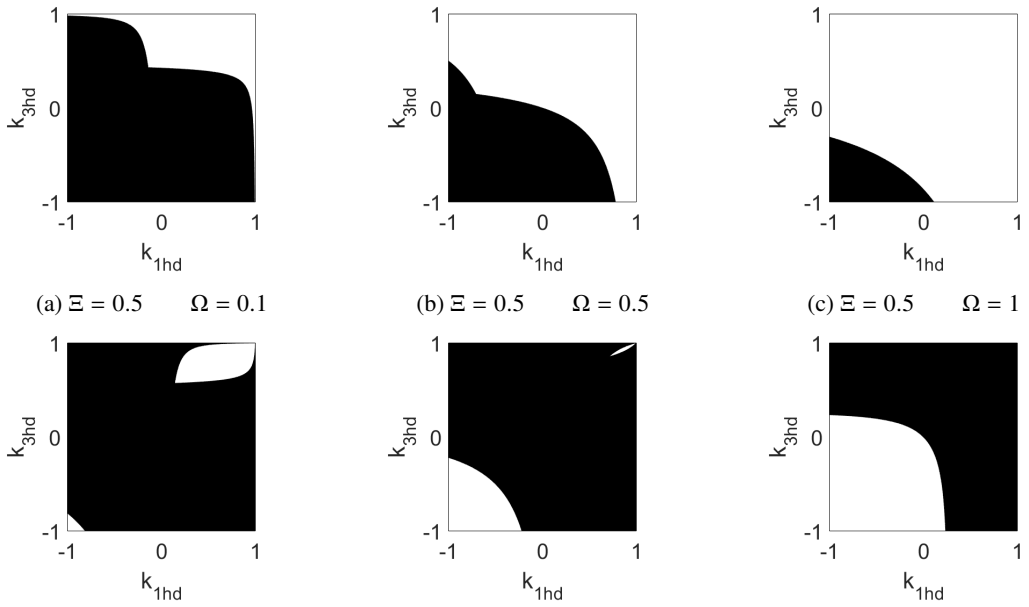


(a) $\Xi = 0.5$ $\Omega = 0.1$ (b) $\Xi = 0.5$ $\Omega = 0.5$ (c) $\Xi = 0.5$ $\Omega = 1$

(d) $\Xi = 0.5$ $\Omega = -0.1$ (e) $\Xi = 0.5$ $\Omega = -0.5$ (f) $\Xi = 0.5$ $\Omega = -1$

Figure 3.9: Smelt Diagram for a Dual-Spin Spacecraft Including a Point Mass Damper with White Depicting Asymptotic Directional stability and Black Instability

with its results shown in Figure 3.9. The effects of energy dissipation seem to be affecting prolate spacecraft considerably. However by having a sufficiently large angular momentum, one is able to design a stable spacecraft. Like the rigid spinning spacecraft with energy dissipation, the dual-spin spacecraft has asymptotic directional stability. Adding a damper should improve the stability performance of the spacecraft if the angular momentum is specified appropriately which of course comes at the price of additional mass and costs.

# Chapter 4

# Nominal and Maintenance Modes

Designing the spacecraft with respect to the attitude dynamics and control is an important aspect especially prevalent for the nominal phase as the system has to perform its high accuracy Earth observation mission. To do this, the spacecraft requires various sensors and actuators to provide the system stability and control. The main component to be considered is the momentum wheel which provides the system its gyroscopic stiffness to soften the external disturbances. In this chapter, the sizing of the momentum wheel and the selection of the required control actuators are discussed. In Section 4.1, the nominal orientation of SHAPE is given and the assumed mass moments of inertia. Next, the external disturbances torques are stated. Section 4.3 states the atmospheric density model and gives a prediction of the density in the upcoming solar cycle for which the momentum wheel is to be designed. Then, in Section 4.4, the design parameters are presented which are affected during the lifetime. To achieve the pointing requirement, the system is required to reposition during the maintenance mode. For this, a control scheme is required and is discussed in Section 4.5. This is followed with nutation damping in Section 4.6 and a final trade-off is given in Section 4.7. The chapter is finalized with a summary.

## 4.1 Nominal Orientation and Moment of Inertia

Pointed out in Section 3.7, the dual-spin spacecraft is directionally stable around the spin axis. The orientation of SHAPE as a dual-spinner should therefore be aligned in such a way that its platform can maintain its Earth-pointing capabilities with efficiency. Hereby, the reference frames as given in Section 3.2 plays an integral role. The nature of Earth-pointing missions yields in two requirements to be placed on the spacecraft.

The first requirement is that the satellite's angular momentum vector should be perpendicular to its orbital plane. This is established from the nadir pointing mission requirement in conjunction with the gyroscopic property of spinning spacecraft. If the momentum vector is not parallel to the rotation axis of the orbit, the spacecraft must either keep adjusting the momentum vector by actively torquing the spacecraft or requires a slewing mechanism for the payload within the platform. Both require additional constraints to the system; torquing the spacecraft against its gyroscopic stiffness will apply high demands for its actuators and a slewing mechanism will result in additional risks of failure.

An example is given in Figure 4.1. The angular momentum vector and therefore the body of the spacecraft is inertially fixed directed to the right. The rotational motion around Earth however yields that the spacecraft is not pointing nadir (the $\vec{b}_3$ axis) anymore until it arrives at its initial nadir pointing position. By directing the angular momentum vector perpendicular to the orbital plane, the orbiting motion on the pitch axis can be corrected by rotating the platform through the spin axis which is uncoupled from the transverse axes.

The second requirement emanating from the first is that the platform should be rotating with the rotation rate around Earth to fixate the platform with respect to the orbital reference frame $O_{xyz}$. The rotational rate of the platform is approximately equivalent to the mean motion $n$ (assuming circular orbit), or

$$n = \sqrt{\frac{\mu_E}{a^3}} \tag{4.1}$$

with $\mu_E$ the gravitational parameter of Earth and $a$ the semi-major axis.

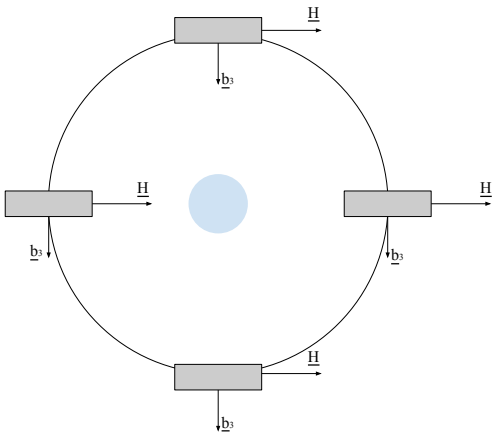


Figure 4.1: Angular Momentum Vector on the Orbital Plane

The mass moments of inertia of the spacecraft have been approximated by taking a uniform material density of the two 3U boxes. The inertia can be determined as follows

$$I_x = \frac{m}{12}\left(y^2 + z^2\right) + md_x^2, \quad I_y = \frac{m}{12}\left(x^2 + z^2\right) + md_y^2, \quad I_z = \frac{m}{12}\left(x^2 + y^2\right) + md_z^2 \tag{4.2}$$

where $d_i$ is the perpendicular distance from the box' center of mass to the spin axis located at the center of mass of the body. In Table 4.1, the mass moment of inertia of the 3U boxes are given with the reference body frame given in Section 3.2.

Table 4.1: SHAPE's Mass Moments of Inertia

| **Inertia** | **Value** [g m$^2$] |
|---|---|
| $I_x$ | 64 |
| $I_y$ | 146 |
| $I_z$ | 96 |

## 4.2 Environmental Disturbances

Many variants of disturbances are present in space. These include such as solar radiation, gravity gradient, atmospheric, and magnetic field, but can also be internally such as due to fuel sloshing. For the design of LEO spacecraft, in general the gravity gradient, the magnetic field, and atmospheric disturbances are the largest contributors due to their increasingly stronger influences in LEOs. In addition, the eddy-current torque is an important disturbance torque to be analyzed as it concerns the use of conductive rotational bodies. In this section, these disturbances disturbance torques are summarized.

### 4.2.1 Gravity Gradient Disturbance

In a uniform gravity field, the center of mass is equivalent to the center of gravity, resulting that no torque is produced due to this field for the body in consideration. In practice, a gravity field is not uniform and the imbalance of gravitational forces on mass elements of a rigid body causes a net torque around the center of mass. Earth has such a non-uniform gravity gradient field, inducing a torque on the spacecraft which is dependent on its orientation and moment of inertias. The gravity gradient torque is given in matrix notation as

$$\boldsymbol{\tau}_g = 3\frac{\mu_E}{r^3}\mathbf{o}_2^{\times}\mathbf{I}\mathbf{o}_2 \tag{4.3}$$

with $\mu_E$ depicting Earth's gravitational parameter, $r$ the magnitude of the radial distance between Earth and the orbiting body, $\mathbf{o}_2$ the unit vector directed towards the center of Earth, and $\mathbf{I}$ the mass moment of inertia of the spacecraft. For the gravitational disturbance torque, the following simplification are made;

1. The masses in consideration are the planet Earth and the spacecraft. The other celestial bodies in the solar system influences the gravity field, however the effect of other bodies are negligible as SHAPE is contained within Earth's sphere of influence (Wakker 2015).

2. Earth is assumed to be spherical and the orbit of the spacecraft to be circular. In reality, Earth is not spherical which produces irregularities in the gravitational field. The orbit is also not circular but spirals towards Earth as SHAPE does not have thrusters to correct for perturbations caused by Earth's atmosphere or solar radiation. However for a first order approximation, both assumptions can be applied.

3. The radius of the orbit around the primary body, Earth, is assumed to be much greater than the size of the spacecraft. This is valid as the orbit is an order of 6 larger relative to the spacecraft. Therefore, the higher order terms in the Taylor expansion are neglected.

To quickly estimate the magnitude of the gravity gradient torque, the $\mathbf{o}_3^{\times}\mathbf{I}\mathbf{o}_3$ term can be substituted to the maximum difference in inertias, or $(I_2 - I_1)$. The worst case torque on the spacecraft is then approximated to be $3.4 \cdot 10^{-7}$ Nm and $3.6 \cdot 10^{-7}$ Nm at 380 km and 230 km, respectively.

### 4.2.2 Aerodynamic Disturbance

Although the boundary to space is by some considered at the Kármán line or 100 km in altitude, atmospheric particles extent beyond this boundary. Albeit in significantly lower mass density, these particles impart onto the spacecraft, producing a net force located at the center of pressure. If the center of pressure does not coincide with the center of mass, a torque is formed for which its equation is given as

$$\mathbf{F}_a = -\frac{1}{2}\rho C_D v^2 \bar{\mathbf{v}} S \tag{4.4}$$

$$\boldsymbol{\tau}_a = \mathbf{l}_{cp}^{\times}\mathbf{F}_a \tag{4.5}$$

In Equation 4.4 and 4.5, $C_D$ represents the drag coefficient, $\rho$ the total air mass density, $\bar{\mathbf{v}}$ the unit velocity vector, $v$ the magnitude of the velocity vector, $S$ the surface area normal to the incident flow and $\mathbf{l}_{cp}$ the position vector of the center of aerodynamic pressure relative to the center of gravity. For the estimation of the worst-case aerodynamic torque, several assumptions have been applied. These are given as follows

1. One of the assumptions made is that the free molecular flow is applicable. This is valid as the molecular mean free path is relatively large compared to the size of the spacecraft for even VLEO (Storch 2002). This path is defined as the average distance traveled by a molecule before colliding with another. Application of this model allows one to use transfer of momentum through the impingement of the atmospheric molecules against its collision with the spacecraft's surface. For the derivation of Equation 4.4, several additional assumptions has been applied in correspondence to the free molecular flow as given by Hughes (2004).

    a) The momentum of molecules are lost through its impingement with the surface.
    b) The mean thermal motion of the molecules are much slower than the orbital speed of the spacecraft. This assumptions allows one to take the atmosphere as a beam with a density and a velocity.
    c) Additional momentum transfer after impingement are neglected.
    d) The spacecraft is non-spinning. The effect of the spinning momentum wheel has been assumed to be negligible for first order approximation.

2. The velocity vector $\mathbf{v}$ is assumed to be equivalent and parallel to the circular orbital velocity. In practice, Earth's atmosphere rotates in inertial space. This has a consequence that the velocity $\mathbf{v}$ should be subtracted by the atmospheric rotational velocity $v_a$. Typically, the flow is assumed to be co-rotating with Earth's surface in a first-order approximation. Due to the sun-synchronous orbit of SHAPE (approximately 97° for LEO), the orbital plane is almost perpendicular to the Earth's rotational plane (<10°) resulting that taking the orbital velocity gives an error less than 1%.

3. A drag coefficient of 2.2 is taken which is a typical first order approximation for LEO satellites. Changes due to the rotation of the spacecraft relative to the velocity vector is assumed to be negligible as the angle of attack will be within a few degrees.
4. The surface $S$, also called the wetted surface, is taken as the projected surface normal to the velocity vector of the spacecraft. The momentum wheel's projected area has been set to be approximately 10% of the total.
5. To determine the magnitude of the worst-case scenario torque, the aerodynamic force is assumed to be perpendicular to the position $\mathbf{l}_{cp}$ which implies that the cross-product yields in a simple multiplication between the two magnitudes. Due to the symmetry of the spacecraft the center of pressure can be assumed to be located at the geometric center. However as the flow is not continuous and uniform, the center of pressure might shift during nominal operations. As well from the fact that rotation of the spacecraft might change this distributive behavior. The center of mass however changes based on the design limitations and requirements. For now, the maximum deviations of the center of mass relative to the geometric center is assumed to be 7 cm as given by the highest allowable deviation of the mass center as stated in *6U CubeSat Design Specification* (2016).

Using the stated assumptions, one is still required to estimate or predict the air density which is given in Section 4.3. The maximum disturbance torque are estimated at $1.3 \cdot 10^{-6}$ Nm and $1.7 \cdot 10^{-5}$ Nm for altitudes of 380 km and 230 km, respectively.

### 4.2.3 Magnetic Field Disturbance

As the spacecraft is orbiting around the Earth, it is subjected to the magnetic field of the Earth. Due to magnetic residue of electronic equipment, a torque is exhibited against the field. The equation for this disturbance is given as

$$\boldsymbol{\tau}_m = \mathbf{M}_M{}^{\times}\mathbf{B} \tag{4.6}$$

with $\mathbf{M}_M$ denoting the magnetic moment vector of the spacecraft and $\mathbf{B}$ the magnetic flux density vector of Earth. The assumption applied to the magnetic field disturbance torque are given below.

1. The magnetic field is modeled as a dipole which its axis located at the center of the (spherical) Earth and its south pole located at 72.6°W longitude and 80.3°N latitude in 2015 (NOAA 2015) with a magnetic dipole strength of $\|\mathbf{M}_E\| = 8 \cdot 10^{22}$ Am$^2$ (Merrill 2010). Although the dipole axis rotates with Earth, it has been assumed to be aligned within the plane of the orbital plane. This allows that the worst-case magnetic disturbance to occur at either of the poles.

2. The magnetic flux density $\mathbf{B}$ is derived from the magnetic potential

$$V = \frac{1}{4\pi r^3}\mathbf{M}_E \cdot \mathbf{r} \tag{4.7}$$

   The magnetic field is then given as the derivative of the magnetic potential as

$$\mathbf{B} = -\mu_0 \nabla V = \frac{-\mu_0 \|\mathbf{M}_M\|}{4\pi R^3} \begin{bmatrix} 2\cos\theta \\ \sin\theta \\ 0 \end{bmatrix} \tag{4.8}$$

   in spherical polar coordinates with $R$ expressing the radial distance to the center of the Earth, $\mu_0$ the vacuum magnetic permeability. The vector elements are given with respect to $r$, $\theta$ and $\phi$.

3. The magnetic moment $\mathbf{M}_M$ and the magnetic flux density $\mathbf{B}$ are constant throughout the spacecraft. Small deviations however cause a magnetic field gradient torque, similar to the gravity gradient torque.

4. The magnetic moment is estimated at a value of 0.002 Am$^2$ per axis which is 3.5 times the magnitude of the magnetic moment assumed by Reijneveld (2011) for the Delfi-n3xt 3U CubeSat.

The worst case disturbance torque due to the magnetic field of Earth can be estimated by assuming the magnetic moment vector of the spacecraft to be perpendicular to the magnetic flux density at one of the poles ($\theta = 0$). This results in a value of $1.0 \cdot 10^{-7}$ Nm at 380 km and $1.1 \cdot 10^{-7}$ Nm at 230 km.

### 4.2.4 Eddy-Current Disturbance

Similar to the magnetic field disturbance, the magnetic field of the Earth affects rotating bodies due to incitement of eddy currents. This disturbance torque is given Hughes (2004) as

$$\boldsymbol{\tau}_{ec} = -k\mathbf{B}^{\times}(\boldsymbol{\omega}^{\times}\mathbf{B}) \tag{4.9}$$

with $k$ a constant which depends on the conductivity and geometry of the considered rotating body for which a compilation of special cases can be found in the technical report by Boyle et al. (1969). An example of a single-spinning CubeSat which is thought to have lost its minor axis spin due to eddy current torque was the nanosatellite Pico Satellite Solar Cell Testbed. By losing rotational energy over time, its cone angle has been estimated to increase from approximately 6° to 60° in a time span of a week (Janson & Hinkley 2009).

From the experimental studies performed by Boyle et al. (1969), the vertical closed cylinder formula given by Smythe (1950) agrees the best with the experimental values corresponding to high rotation speeds and with lower speeds with Hooper (1957). Their respective formula are given as

$$\tau_{ec,S} = \frac{4\pi\omega S r_b^3 l B^2}{4S^2 + \omega^2\mu_0^2 r_b^2} \tag{4.10}$$

$$\tau_{ec,H} = \frac{\pi(B^2 l^2 \omega\sigma_c)10^{-9}}{4(l + r_o + r_i)(r_o^4 - r_i^4)^{-1}} \tag{4.11}$$

with $S$ the surface resistivity, $r_b$ the radius of the cylinder, $l$ the height of the cylindrical body and $\mu_0$ vacuum magnetic permeability. The surface resistivity is defined as

$$S = \frac{1}{\sigma_c t} \tag{4.12}$$

with $\sigma_c$ denoting the conductivity and $t = r_o - r_i$ the thickness of the cylinder with $r_o$ and $r_i$ the outer and inner radii. The inputs of Hooper's formula are given in CGS units and the following conversion can be made from SI units;

$$1\text{ m} = 10^{-2}\text{ cm}, \quad 1\text{ Si/m} = 10^{-11}\text{ abmhos/cm}, \quad 1\text{ T} = 10^{4}\text{ Gauss} \tag{4.13}$$

Using the assumptions for $\mathbf{B}$ that the magnetic field is uniform and perpendicular to the spin axis, an aluminum 6061 body with a conductivity of $2.39 \cdot 10^7$ S/m as given by Boyle et al., thickness of 4 cm, outer radius of 6 cm, and $\omega_s$ = 7000 rpm = 733 rad/s yields in an eddy current torque of $1.8 \cdot 10^{-8}$ Nm and $0.7 \cdot 10^{-8}$ Nm for Smythe and Hooper, respectively. It should be emphasized that although the magnitude of the order is one lower than the gravity gradient torque, it still has significant impact on the momentum wheel design during the lifetime. For example, assuming a constant torque over 180 days, this results in an angular momentum reduction of 0.3 Nms. Material with low conductance and eddy current reduction methods are recommended.

## 4.3 Atmospheric Density

The density of Earth's atmosphere decreases exponentially over the altitude. Although the density reduces more than billion times from sea level to LEO, the effects of atmospheric particles are still very impactful to the design of LEO spacecraft. Besides the disturbance torque mentioned in the previous section, the atmosphere also induces an exponential decay in the orbit. Therefore, a precise estimation of the atmospheric density is needed. In contrast to the other parameters in Section 4.2.2, the total mass density of the atmosphere is more tedious to estimate. This is due to the variation of the density spatially in longitude, latitude and altitude, and also temporally (Doornbos 2012).

Density variations affected by time include many contributions, mainly attributed by the solar activity. One of such consist of changes in the number of sun spots cycling approximately every 11 years resulting in high and low solar activities. Furthermore, there are variations due to the Sun's rotation, diurnal and seasonally changes or due to geomagnetic activities. These all influence on the estimation of the density of Earth's atmosphere for which the design of the spacecraft should be made accordingly. One can estimate the density using the 2001 United States Naval Research Laboratory Mass Spectrometer and Incoherent Scatter Radar Exosphere (NRLMSISE00) model (Picone et al. 2002). The numerically implementation of this model called *atmosnrlmsise00* by Matlab has been used to determine

the total mass density. Next to this NRLMISE00 model there are several different models to estimate and predict the air density. One of these is the JB2008 model which estimates with a better accuracy and certainty (Bowman et al. 2008). However, the runtime increases with a factor of approximately 2.5 (*Space systems - Estimation of orbit lifetime* 2010). Due ease of application, availability of the code, small non-storm errors, and decent computation time, it has been opted to use the NRLMSISE00 model. For this model, additional input data such as the 10.7 cm solar flux data and the magnetic index are retrieved from the National Centers for Environmental Information (2017). The code for this retrieval and computations of the average can be found in Appendix E and Appendix F.

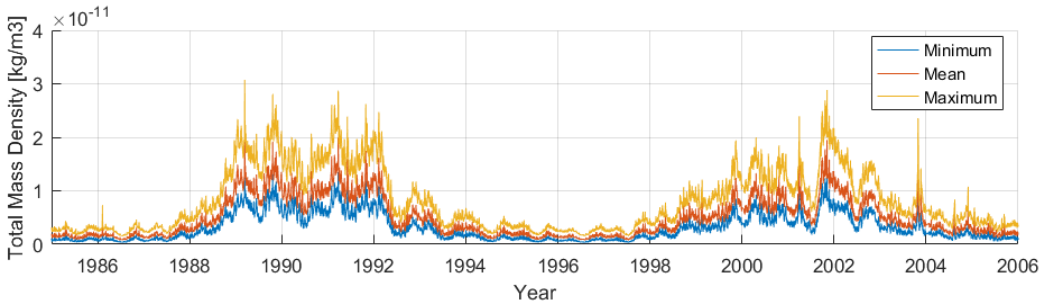


(a) Altitude of 380 km

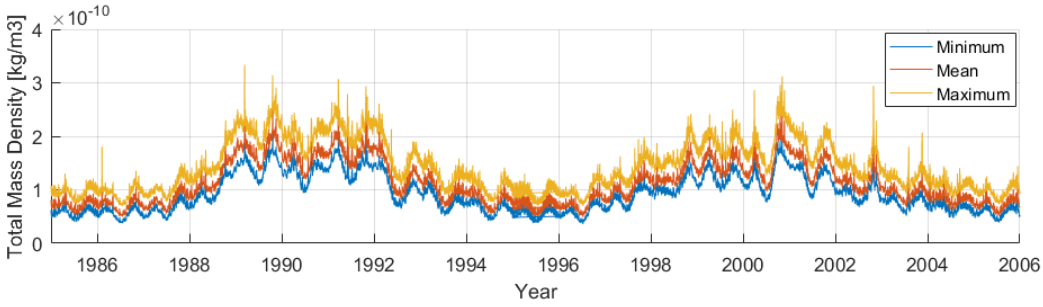


(b) Altitude of 230 km

Figure 4.2: Two 11-year Solar Cycles

In Figure 4.2, two cycles of the 11-year cycle can be observed from 1985 to 2006 at an altitude of 380 km and 230 km computed using the NRLMSISE00 model. In these figures, differentiations have been made between the minimum, mean and maximum which are defined over the whole range of longitude and latitude. The variations during periods with low solar activity fluctuates less than during high activity. For the current design, the launch window is not known and therefore the design will be based around the full 11-year cycle. One can design a much more optimal design using the period in which the solar activity is low if the launch window for the spacecraft allows. The angular momentum of the wheel will then be a magnitude lower. The disadvantage however is that an unexpected transition to a higher regime may yield in complete failure of the mission. This may also be caused by a short burst of solar activity which can even occur during periods with low activity.

### 4.3.1 Prediction

In general three types of prediction methods are used; precursor, regression, and model based techniques. Precursor methods utilize a solar or magnetic measure in a specific point in time to estimate the amplitude of the upcoming solar maximum. Regression methods are based on series of points in time to extrapolate the solar activity in the near future. The last of the three methods implements the dynamics of the solar dynamo for its prediction. The model based methods are still in development and due to the current lack of data is still not reliable (Hathaway et al. 1999, Petrovay 2010). The upcoming solar cycle which is numbered 25, has been analyzed by multiple studies and the maximum number of sunspots varies, ranging from 50±10 (Javaraiah 2015) to 132.1 (Rigozo et al. 2011) sunspots from studies within 10 years. Most predictions from 2007 and onwards show however a range between around 110 to 120 (Hiremath 2008, Pishkalo 2008, Helal & Galal 2013, Li et al. 2015). The current observed and predicted sunspots data by the

Space Weather Prediction Center (SWPC) and by NASA are shown in Figure 4.3.

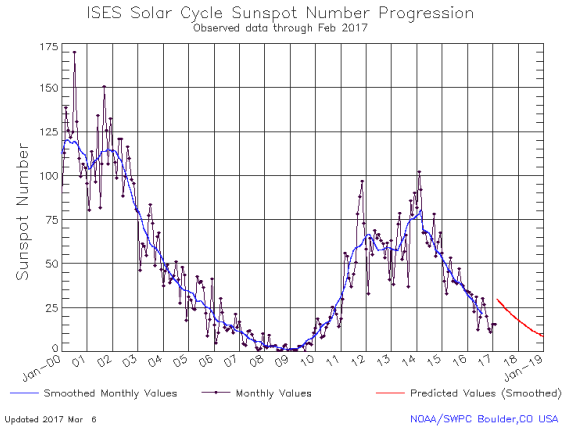


(a) Space Weather Prediction Center - National Oceanic and Atmospheric Administration (2017)

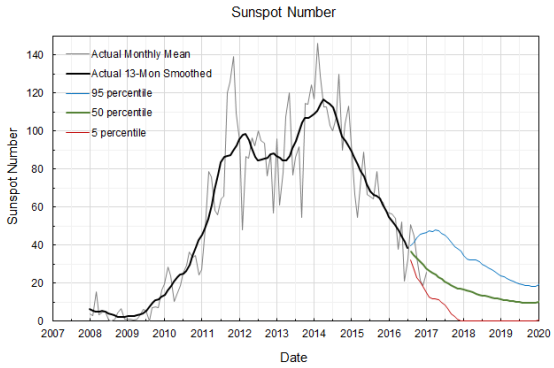


(b) Space Weather Prediction Center - National Oceanic and Atmospheric Administration (2017)

Figure 4.3: Observed and Predicted Sunspots

The study by Hathaway et al. (1994) showed that the accuracy of the sun spots prediction is within 30% at the start of the solar cycle, 20% 30 months into the cycle and the accuracy increases as it further progresses. At current time of this research, solar cycle 24 is advancing towards its end. The accuracy of the prediction for solar cycle 25 is therefore still wide open and a good estimation of the next solar cycle's amplitude is yet to be determined. For this case study, the estimation based on the upcoming solar cycle (#25) is still used. For a more reliable design, it is recommended to do at least one additional design iteration after 30 months into the cycle if the project time allows.

In a compilation study of more than 50 prediction methods done by Pesnell (2008), a large spread of predictions of the maximum sunspots is given for solar cycle 24. One can take a method out of the list with the best matching result. However, the small sample size, the undetermined probabilistic nature, and the type of prediction technique result that these predictions are still not reliable.

For this prediction, predicted results for the solar radio flux and magnetic indices from NASA - Marshall Space Flight Center (MSFC) are used to determine the upper and lower bounds of the density (Niehuss et al. 1996) due to immediate availability and its use in NASA engineering programs. This method implemented in the program Marshall Solar Activity Future Estimates Model (MSAFE), applies the modified McNish-Lincoln linear regression technique to extrapolate intermediate and long-range values (McNish & Lincoln 1949). Currently, only 23 data cycles are available which limits the upper and lower boundaries MSAFE can estimate. Although a slightly higher confidence estimation can be provided, the boundaries parsed by MSFC are given with 95% and 5% as it closely represent the normal distribution's 2-sigma values. Furthermore, taking the highest confidence estimation has shown that the boundaries are less smooth. These computed prediction data are shown in Figure 4.4 (NASA - Marshall Space Flight Center 2017).

These data are fed into the chosen atmospheric model to compute the densities. The predicted solar radio flux and magnetic index are given in monthly terms and to generate inputs suitable for *atmosnrlmsise00*, the data have been interpolated using spline interpolation at a daily rate. The model can output densities with respect to the longitude, latitude, altitude and time. In Figure 4.5, the predicted densities over solar cycle 25 are shown with the corresponding confidence intervals of 5%, 50% and 95% for altitudes of 380 and 230 km. The minimum, mean and maximum densities are defined over the longitude and latitude. At 230 km, the altitude is approximately an order higher than at 380 km. Furthermore, the spread between the 95% and the 50% differs substantially more at 380 km.

Besides the large deviations between the percentiles at the solar maximum, the time at which these are predicted has been found to vary as well. These temporal errors have been stated to induce density errors of up to more than 100% (*Space systems - Estimation of orbit lifetime* 2010). Although beneficial in time and mass at low solar activities, designing the spacecraft at these periods tend to have more risk associated with it, especially at the start or before the solar cycle.

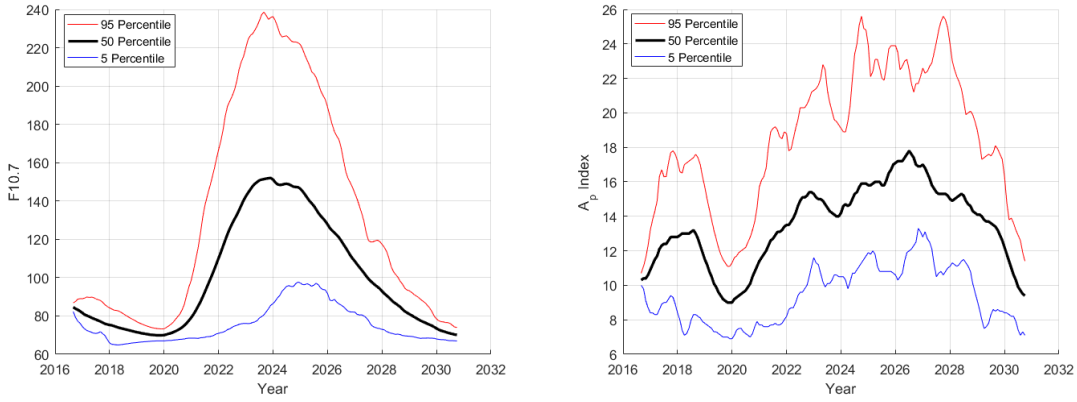


(a) Solar Radio Flux 10.7cm

(b) Magnetic Index

Figure 4.4: Predicted Values for Solar Cycle 25

## 4.4 Design Parameters

After evaluating the disturbances, the momentum wheel sizing can be traded off between a list of parameters which are related through Equation 3.51 or the angular momentum. Equation 3.51 is the main driver for the sizing as it directly relates to the key requirement of the mission; achieving a pointing accuracy of at least 1.0°. The variable $\mu$ represent the maximum allowable deviation from the desired attitude of the spacecraft. From this point, one can suggest to design the dual-spin spacecraft by having a large as possible momentum wheel. However, in addition to the constraints in terms of volume and mass, it also inhibits the ability to control. This inhibition can be interpret by viewing the equation from the point after it has exceeded the maximum allowable angular deviation. The system is then to be transitioned to the maintenance mode. During this mode, SHAPE is ordered to reposition back to its original orientation. The same equation for the angular deviation however cannot be applied to determine the required control torque as the previous worst-case scenario is for SHAPE's control now the best-case scenario.

The sizing of the momentum wheel requires a trade-off between multiple parameters and requirements such as the pointing accuracy $\mu$, the spinup torque, the nominal mission and maintenance times $t_n$ and $t_m$, and the control torques in pitch, roll and yaw direction. This requires a more in-depth analysis as the external disturbance torques and thus the required angular momentum changes throughout SHAPE's lifetime. In this section, some of these important parameters are discussed.

### 4.4.1 Change in Parameters over the Lifetime

The main contributor to the momentum wheel sizing is the aerodynamic disturbance. This disturbance torque increases over time and having a fixed momentum wheel with fixed rotational speed and size yields in either a decrease in pointing requirement or a reduction in nominal operation time over the lifetime. To cover as much of SHAPE's mission life with high pointing accuracy it is beneficial to know the orbit decay throughout the time. A simple computation of the semi-major axis decay due to the air density can be done by using the equation below after every orbit (Larson & Wertz 1999)

$$\Delta a_{2\pi} = -2\pi(C_D A/m)\rho a^2 \tag{4.14}$$

with $a$ the semi-major axis, $C_D$ the drag coefficient, $A$ the wetted surface and $\rho$ the total air density.

Using the same assumptions as applied for the aerodynamic disturbance given in Section 4.2.2, one can approximate the decay due to atmospheric particles over the spacecraft's life with the predicted density values. To fulfill the requirement regarding the lifetime, multiple simulations have been performed to give a launch window recommendation for the upcoming solar cycle. Note that for this analysis, the confidence interval values of 95% and 50% are adopted. The reasons for using these two values are to estimate its worst-case and mean lifetimes of the mission. For this analysis, an assumption is made regarding the spatial variation of density. The density of the latitude and longitude are averaged. This induces additional errors into the lifetime as some parts of the Earth are propagated more often

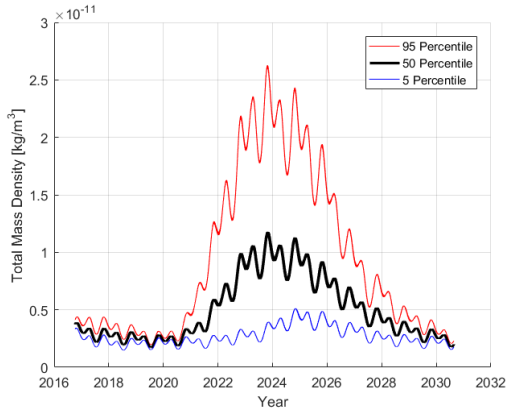


(a) Altitude of 380 km - Maximum

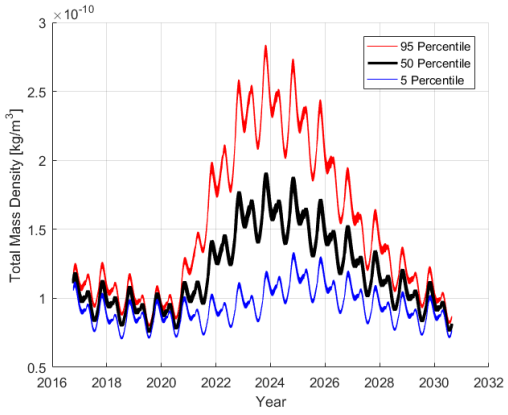


(b) Altitude of 230 km - Maximum

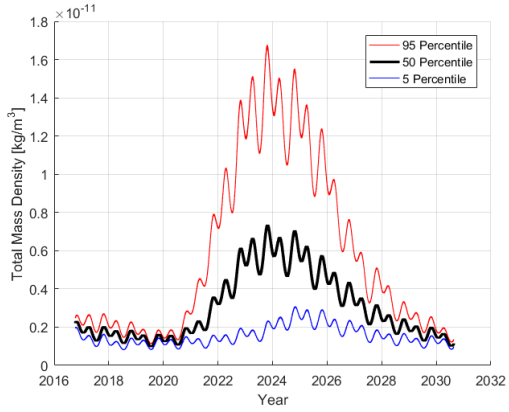


(c) Altitude of 380 km - Mean

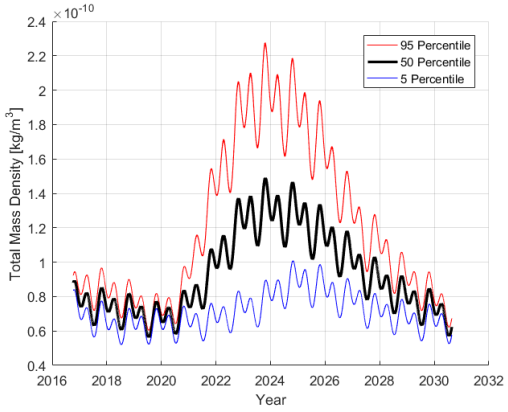


(d) Altitude of 230 km - Mean

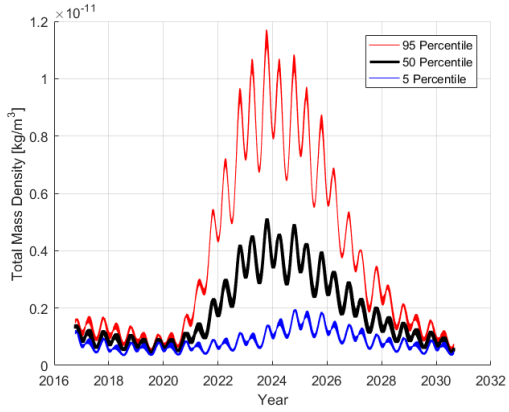


(e) Altitude of 380 km - Min

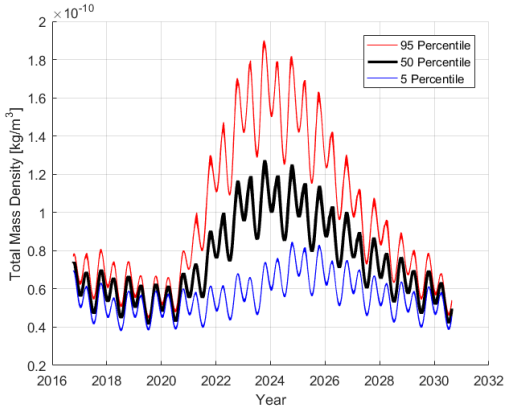


(f) Altitude of 230 km - Min

Figure 4.5: Predicted Densities for Solar Cycle 25

than other locations such as the areas near the poles due to an almost polar SSO. Assumptions made previously for the disturbance torques applied to the orbit decay such as the projected surface is an estimation and might induce a faster decay. An important phenomenon not modeled is the solar storm. Storms should produce peaks of densities in orbit which could speed up the process of orbit decay. An stochastic analysis in the form of Monte Carlo simulations can be performed to evaluate its effect on the orbit lifetime (*Space systems - Estimation of orbit lifetime* 2010). These simulations have been left for future work due to the amount of computation required for analysis. However, for an

estimation, current research should be sufficient.

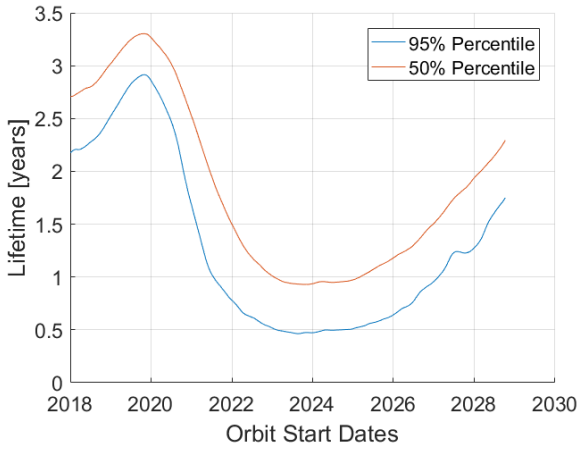


Figure 4.6: Mission Lifetime Estimation

In Figure 4.6, the lifetimes are shown with respect to the initial date of orbit, starting from the year 2018. The difference caused by the solar activity at VLEO altitudes are considerable with a maximum lifetime of around 3 years at low solar activity and half a year at the high activity. To have a minimum orbit life time of 6 months, the spacecraft should avoid a small launch window on the 67th day of the year 2023 to the 82th day of the year 2024 which still closely reach a lifetime of half a year. In the next solar cycle, the lifetime of SHAPE should reach approximately 6 months with 95% confidence. The 50% percentile's worst case lifetime is predicted to be 340 days with an orbit start date at 127th day of 2023, surpassing with a factor 2. Note that the cycle timing is imprecise and therefore an additional margin should be incorporated if one would plan at a starting date with a longer lifetime.

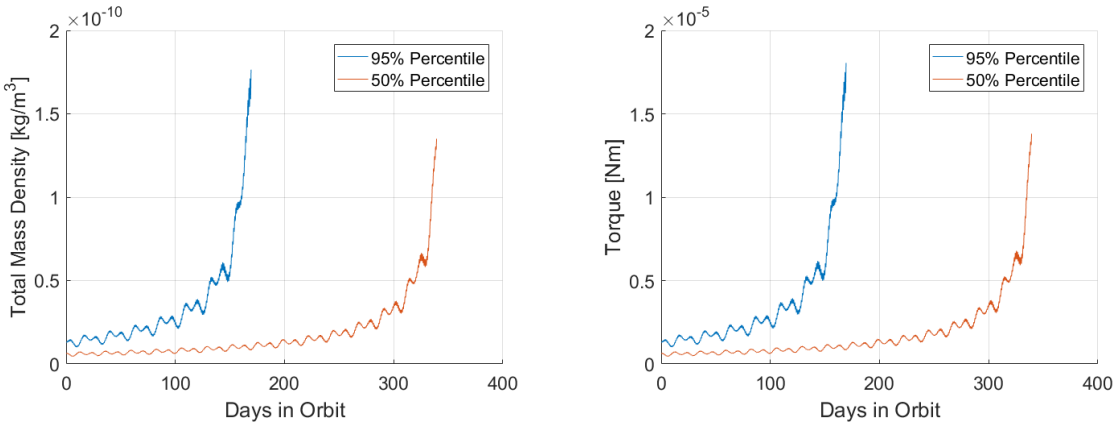


(a) Atmospheric Density

(b) Aerodynamic Torque

Figure 4.7: Worst-Case Disturbance Profiles

The basis of the momentum wheel's worst case design has thus taken on the datum with the lowest lifetime at 95% confidence. The date of this predicted occurrence is at the 237th day of the year 2023 and the spacecraft is expected to have a lifetime of 169. For this particular orbit propagation, the density and torque profiles are shown in Figure 4.7 colored blue. Akin to the 95%, the 50% worst case scenario is given in red and has an orbit start date at the 297th day of the year 2023. The torque profile can then be used in conjunction with Equation 3.51 to determine the required angular momentum of the wheel over time which is shown in Figure 4.8.

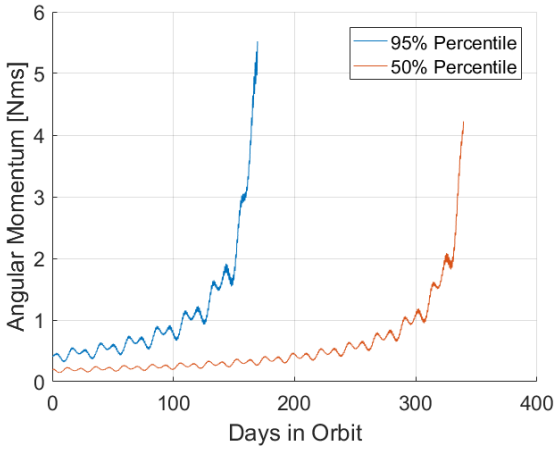


Figure 4.8: Required Angular Momentum to Sustain 1/2 Orbit of Continuous Mission Operation

### 4.4.2 Size, Mass and Spinup Time

Now that the angular momentum requirement over SHAPE's lifetime has been determined, directly related wheel parameters can be estimated; the size and mass of the wheel, and the spinup time. Following from the minimum rotation requirement of 5000 rpm, the angular momentum relates directly to the size and mass of the momentum wheel through

$$H_s = I_s \omega_s \tag{4.15}$$

Note that the application of this equation implies that all of the momentum is stored in the wheel and not on the spacecraft's main platform. This is reasonable as the mean motion at which the platform should be rotating is negligible compared to the total angular momentum. Assuming a constant torque from the thruster requirements, the spinup time can simply derived using

$$t_{\text{spin}} = \frac{H_s}{g_a} = \frac{H_s}{2F_T r} \tag{4.16}$$

with $g_a$ representing the torque applied by the two thrusters diagonal to each other, $r$ the moment arm, and $F_T$ the constant thrust level. If the momentum wheel is approximated as a solid disk, the mass moment of inertia can be computed as

$$I_s = \frac{1}{2}\rho_m \pi r^4 t \tag{4.17}$$

with $\rho_m$ the material density, $r$ the radius of the wheel and $t$ the thickness of the momentum wheel. The mass of the wheel is computed using Equation 4.18.

$$m = \rho_m \pi r^2 t \tag{4.18}$$

Using the minimum mission operation time of 1/2 orbit, one can determine the minimum required angular momentum depending on the aerodynamic torque. For the wheel sizing, the effect of other disturbance torque are not taken into account due to being a magnitude smaller, but more importantly as they are cyclic. Due to the high atmospheric density and thus the aerodynamic torque, the required angular momentum increases exponentially. Designing the momentum wheel over its complete lifetime is therefore not optimal. One can deduct a part of the lifetime with decreased performance to design the spacecraft with lower mass and costs. For example, either with a decreased continuous mission operation, pointing accuracy or a combination of both during the last 10% of the lifetime, an angular momentum which is approximately a factor 3 lower can be taken than its end-of-life value.

## 4.5 Controllers

During the nominal or maintenance phase, several actuators are available for keeping the platform focused to the nadir. These include such as reaction wheels, control moment gyros, magnetorquers or thrusters. Each having its own

benefits and disadvantages. To select the proper actuator and its qualities for the spacecraft, two differentiations should be made regarding the spacecraft axes for controllability. The angular momentum provided by the momentum wheel couples the roll and yaw axes and gives the system gyroscopic stiffness. To counteract this in the maintenance mode, the spacecraft requires to have strong actuators. The pitch axis is in contrast uncoupled from the angular momentum of the wheel. While it is still coupled through the cross terms exhibited by the transport theorem or the inertia tensor, these values are underwhelming with respect to the gyroscopic coupling. The pitch axis therefore requires continuous steering.

The selection of the actuator is thus based on the size of the angular momentum of the rotor, the control torque and its duration to be exerted. This still requires a more thorough analysis then a simple trade-off. Numerical simulations are needed to determine the control effort and the maximum torque to be exerted. A simple PD controller will not be sufficient without understanding the dynamics. Unlike the 3-axis stabilized spacecraft, applying an unpredicated torque to the system can cause a nutational motion.

To determine the required control and time for readjustment of the inertial angular momentum vector, two controller are considered; a Linear Quadratic Regulator (LQR) and a controller based on Lyapunov's Direct Method. The LQR is a linear controller for which its objective is to minimize its control effort. The latter, Lyapunov's Direct Method, uses a Lyapunov function to develop a controller which is globally (asymptotic) stable. For both controllers, the linearized equation is used with small angles approximation; $\boldsymbol{\omega} = (\dot{\alpha}_1, \dot{\alpha}_2, \dot{\alpha}_3)$ which should be valid during the nominal mode as angles larger than 10° is not expected to be exceeded. Applying linearization and small angles to Equation 3.66 gives

$$I_1\ddot{\alpha}_1 = u_1 \tag{4.19}$$

$$I_2\ddot{\alpha}_2 = -H_s\dot{\alpha}_3 + u_2 \tag{4.20}$$

$$I_3\ddot{\alpha}_3 = H_s\dot{\alpha}_2 + u_3 \tag{4.21}$$

here, $u_i$ are the control vector elements. The disturbance-free linearized equations for the pitch axis is completely decoupled. For the pitch control, a PD controller can be used to adjust against disturbances and to rotate the platform with a magnitude equal to the mean motion. The coupled roll and yaw equations can be written in matrix notation as

$$\dot{\mathbf{x}} = \mathbf{A}\mathbf{x} + \mathbf{B}\mathbf{u} \tag{4.22}$$

with

$$\mathbf{x} = \begin{bmatrix} \alpha_2 \\ \alpha_3 \\ \dot{\alpha}_2 \\ \dot{\alpha}_3 \end{bmatrix} \qquad \mathbf{A} = \begin{bmatrix} 0 & 0 & 1 & 0 \\ 0 & 0 & 0 & 1 \\ 0 & 0 & 0 & -\frac{h_s}{I_2} \\ 0 & 0 & \frac{h_s}{I_3} & 0 \end{bmatrix} \qquad \mathbf{B} = \begin{bmatrix} 0 & 0 \\ 0 & 0 \\ \frac{1}{I_2} & 0 \\ 0 & \frac{1}{I_3} \end{bmatrix} \qquad \mathbf{u} = \begin{bmatrix} u_2 \\ u_3 \end{bmatrix} \tag{4.23}$$

In this thesis, a separate pitch PD controller is not designed and it is included into the LQR using the following form;

$$\mathbf{x} = \begin{bmatrix} \alpha_1 \\ \alpha_2 \\ \alpha_3 \\ \dot{\alpha}_1 \\ \dot{\alpha}_2 \\ \dot{\alpha}_3 \end{bmatrix} \qquad \mathbf{A} = \begin{bmatrix} 0 & 0 & 0 & 1 & 0 & 0 \\ 0 & 0 & 0 & 0 & 1 & 0 \\ 0 & 0 & 0 & 0 & 0 & 1 \\ 0 & 0 & 0 & 0 & 0 & 0 \\ 0 & 0 & 0 & 0 & 0 & -\frac{h_s}{I_2} \\ 0 & 0 & 0 & 0 & \frac{h_s}{I_3} & 0 \end{bmatrix} \qquad \mathbf{B} = \begin{bmatrix} 0 & 0 & 0 \\ 0 & 0 & 0 \\ 0 & 0 & 0 \\ \frac{1}{I_1} & 0 & 0 \\ 0 & \frac{1}{I_2} & 0 \\ 0 & 0 & \frac{1}{I_3} \end{bmatrix} \qquad \mathbf{u} = \begin{bmatrix} u_1 \\ u_2 \\ u_3 \end{bmatrix} \tag{4.24}$$

To evaluate the effect of the angular momentum on the control capacity, a performance parameter is chosen in the form;

$$P_u = \int_0^{t_f} \mathbf{u}^T\mathbf{u}\,\mathrm{d}t \tag{4.25}$$

which is the control effort. Additionally, the time itself is an important characteristic as a faster response is preferred.

### 4.5.1 Linear Quadratic Regulator

LQR is a controller under the branch of optimal control which minimizes the control effort for the system as given in Equation 4.22. Here, a brief summary is given of the LQR derived from the textbook by Lavretsky & Wise (2013). To analyze the effect of the angular momentum of the wheel on the control effort of the spacecraft, an infinite horizon

($T = \infty$) method is taken. The finite horizon LQR could allow the system to achieve the desired state within a given time, however it requires a gain scheduler and hence has not been taken. The corresponding cost objective to be minimized is given as

$$J = \int_0^\infty (\mathbf{x}^T\mathbf{Q}\mathbf{x} + \mathbf{u}^T\mathbf{R}\mathbf{u})d\tau \quad \text{with} \quad \mathbf{Q} = \mathbf{Q}^T \geq 0 \qquad \mathbf{R} = \mathbf{R}^T \geq 0 \tag{4.26}$$

The matrices $\mathbf{Q}$ and $\mathbf{R}$ are cost weight matrices and are defined to be positive semidefinite. By selecting these matrices correctly one can prioritize the minimization process. Additionally, the system has to be checked on its controllability and ($\mathbf{A}$,$\mathbf{Q}^{1/2}$) on the detectability or observability. These conditions are stated by Bubnicki (2005) as

$$\text{rank}([A^{n-1}B\ A^{n-2}B\ ...\ AB\ B]) = n \tag{4.27}$$

with $n$ the size of matrix $\mathbf{A}$. The condition for observability is given as

$$\text{rank}\left(\begin{bmatrix} C \\ CA \\ CA^2 \\ \vdots \\ CA^{n-1} \end{bmatrix}\right) = n \tag{4.28}$$

with $C = \mathbf{Q}^{1/2}$ and $A^i$ defined as the submatrices of $\mathbf{A}$. Both are verified for SHAPE's parameters and a weighting matrix $\mathbf{Q}$ of

$$\mathbf{Q} = \bar{\mathbf{1}}_4 \tag{4.29}$$

The LQR controller has been given to have the following from

$$\mathbf{u} = -\mathbf{R}^{-1}\mathbf{B}^T\mathbf{P}\mathbf{x} = -\mathbf{K}\mathbf{x} \tag{4.30}$$

which is derived by solving the Algebraic Riccati Equation (ARE):

$$\mathbf{P}\mathbf{A} + \mathbf{A}^T\mathbf{P} - \mathbf{P}\mathbf{B}\mathbf{R}^{-1}\mathbf{B}^T\mathbf{P} + \mathbf{Q} = 0 \tag{4.31}$$

The ARE is solved with the MATLAB command *lqr*. To account for control saturation, the following method is considered for the pitch axis;

$$\text{sat}(u_1) = \min(\max(u_1, -u_{\max}), u_{\max}) \tag{4.32}$$

and for the transverse axes;

$$\text{sat}(\mathbf{u}_{2,3}) = \begin{cases} \mathbf{u}_{2,3}/\beta, & \text{if } \beta > 1. \\ \mathbf{u}_{2,3}, & \text{otherwise.} \end{cases} \tag{4.33}$$

with $\beta = \max(|\mathbf{u}_i|/u_{\max})$ with $i = 2, 3$. This saturation function does not utilize the full control available for every axis, but integrates its direction by scaling with factor $\beta$ if one of the axes is saturated. A LQR controller accommodating saturation effects are given by Saberi et al. (1996). The design process is given in three steps; the synthesis of low and high gain controllers and their integration into a single controller. The design of the low gain controller is given in Equation 4.30 with $\mathbf{R}$ as the low gain parameter. Similarly, the high gain controller is given with a high gain parameter $\rho_c$;

$$\mathbf{u}_H = \rho_c\mathbf{u}_L \tag{4.34}$$

with $\mathbf{u}_L$ denoting the low gain controller. Adding the controllers gives a composite controller in the form of

$$\mathbf{u}_{LH} = (1 + \rho_c)\mathbf{u}_L \tag{4.35}$$

The addition of the high gain controller allows a faster response to its steady-state. By increasing the value of $\rho_c$ the system approaches a bang-bang control which increases power consumption. Limitation of the power during SHAPE's nominal mode disallows the use of its actuators and therefore the high gain parameter is set to zero. However, the high gain can be activated when the system has unexpected reduced performance or in contingency mode.

### 4.5.2 Lyapunov's Direct Method

Ruiter (2012) provides several controllers for bias momentum and dual-spin spacecraft using magnetorquers for reorienting the spin axis in inertial space also accommodating saturation implemented for magnetorquers. Ruiter uses infinitesimal linearized equations to develop the controller for which Lyapunov's direct method is applied. The controller accommodates besides the roll and yaw axes, the pitch motion through the notion that the momentum wheel can be controlled. For SHAPE, this is not a possibility and the controller derivation are here verified for this condition using a similar Lyapunov function. Ruiter suggests a transformation of variables of the linearized Equation;

$$\hat{\mathbf{x}} = \mathbf{T}\mathbf{x} \tag{4.36}$$

where $\mathbf{T}$ and its inverse are given as

$$\mathbf{T} = \begin{bmatrix} 1 & 0 & 0 & -\frac{I_3}{h_s} \\ 0 & 1 & \frac{I_2}{h_s} & 0 \\ 0 & 0 & \frac{1}{\sqrt{I_3}} & 0 \\ 0 & 0 & 0 & \frac{1}{\sqrt{I_2}} \end{bmatrix} \qquad \mathbf{T}^{-1} = \begin{bmatrix} 1 & 0 & 0 & \frac{I_3\sqrt{I_2}}{h_s} \\ 0 & 1 & -\frac{I_2\sqrt{I_3}}{h_s} & 0 \\ 0 & 0 & \sqrt{I_3} & 0 \\ 0 & 0 & 0 & \sqrt{I_2} \end{bmatrix} \tag{4.37}$$

and

$$\hat{\mathbf{A}} = \mathbf{T}\mathbf{A}\mathbf{T}^{-1} = \begin{bmatrix} 0 & 0 & 0 & 0 \\ 0 & 0 & 0 & 0 \\ 0 & 0 & 0 & -\frac{h_s}{\sqrt{I_2 I_3}} \\ 0 & 0 & \frac{h_s}{\sqrt{I_2 I_3}} & 0 \end{bmatrix} \tag{4.38}$$

Applying the transformation to Equation 4.22 yields in

$$\dot{\hat{\mathbf{x}}} = \hat{\mathbf{A}}\hat{\mathbf{x}} + \mathbf{T}\mathbf{G}\mathbf{u} \tag{4.39}$$

A Lyapunov function of the from is suggested;

$$V(\hat{\mathbf{x}}) = \frac{1}{2}\hat{\mathbf{x}}^T\mathbf{P}\hat{\mathbf{x}} \tag{4.40}$$

where

$$\mathbf{P} = \begin{bmatrix} 1 & 0 & 0 & 0 \\ 0 & 1 & 0 & 0 \\ 0 & 0 & k & 0 \\ 0 & 0 & 0 & k \end{bmatrix} \quad \text{with} \quad k > 0 \tag{4.41}$$

The Lyapunov function $V(\hat{\mathbf{x}})$ can be verified easily on its positive definiteness for $\hat{\mathbf{x}} \neq 0$ and the condition V(0) = 0. For the system to be globally asymptotically converging, the derivative of the Lyapunov function derivative should be negative definite

$$\dot{V} = \nabla V \cdot \dot{\hat{\mathbf{x}}} = \left(\frac{\partial V}{\partial \dot{\hat{x}}_1}, \frac{\partial V}{\partial \dot{\hat{x}}_2}\right) \cdot \dot{\hat{\mathbf{x}}} \tag{4.42}$$

with the $\nabla$ operator depicting the gradient. Continuing the derivation yields

$$\dot{V} = \nabla V \cdot \dot{\hat{\mathbf{x}}} = \hat{\mathbf{x}}^T\mathbf{P}(\hat{\mathbf{A}}\hat{\mathbf{x}} + \mathbf{T}\mathbf{G}\mathbf{u}) \tag{4.43}$$

As the first term is equivalent to zero, Equation 4.42 reduces to

$$\dot{V} = \hat{\mathbf{x}}^T\mathbf{P}\mathbf{T}\mathbf{G}\mathbf{u} \tag{4.44}$$

with a control method without any limitations given as

$$\mathbf{u} = -K\left(\mathbf{G}^T\mathbf{T}^T\mathbf{P}\hat{\mathbf{x}}\right) \tag{4.45}$$

Note that $\mathbf{P} = \mathbf{P}^T$ and $K > 0$. Substituting into the derivative of the Lyapunov function yields

$$\dot{V} = -\frac{1}{2}\mathbf{u}^T\mathbf{u} \tag{4.46}$$

The Lyapunov function $V(x)$ goes to infinity as $\|\hat{\mathbf{x}}\| \to \infty$ and Equation 4.46 is negative definite as long as $\hat{\mathbf{x}}$ is non zero. So that the point $\hat{\mathbf{x}} = 0$ is a globally asymptotic point. Note that this is valid for the linearized equation and not for its nonlinear version. Therefore the global property might not be valid at large angles from the equilibrium. The feedback controller is then given for the roll and yaw as

$$\mathbf{u} = \begin{bmatrix} -K\left(\frac{\alpha_3}{h_s} + \left(\frac{I_2}{h_s^2} + \frac{k}{I_2 I_3}\right)\dot{\alpha}_2\right) \\ -K\left(-\frac{\alpha_2}{h_s} + \left(\frac{I_3}{h_s^2} + \frac{k}{I_2 I_3}\right)\dot{\alpha}_3\right) \end{bmatrix} \tag{4.47}$$

where $K > 0$ and $k > 0$. Hereby, it should be underlined that the system assumes no actuator constraints.

## 4.6 Nutation Damping

During the nominal mission mode, nutation and precession might be induced by either the external disturbances or by the actuators which can invalidate requirement (S-NM.5). To minimize these motions, one can employ nutation dampers. These can be categorized into two divisions; active and passive components. Active dampers require power from the system but can provide a more accurate damping as the attitude measurement are used to determine the needed control torque.

Passive dampers however do not need any form of power, but are more limited in the frequencies it can damp. Adding damping to the system has been proven to give the torque-free system asymptotic stability (Section 3.5). In Section 3.5, the parameter $\Omega$ was given to assess the spacecraft's precession frequency against the stability. The parameter is defined as a ratio of the precession frequency over the platform rate. As the platform's rotation rate is set to be equal to the mean motion, the value of $\Omega$ far exceeds 1 with an order of magnitude 3 which stabilizes the system asymptotically and directionally.

Passive damper types compose of various models which can be chosen depending on mission requirements and constraints. For analytical purposes two types are often considered; the viscous ring and more often the ball-in-tube dampers. Cochran Jr & Thompson (1980) studied two configuration which they defined as precession and nutation dampers. The precession type had its damper mass movement in the direction parallel to the spin axis and perpendicular for the nutation type. Using a energy sink analysis, they found that the nutation damper was more suited for large nutation angles. During the mission, the pointing performance is expected to be smaller than 1 degree and therefore for analysis, the precession damper is selected. The equations of motion of a gyrostat with a ball-in-tube damper is given by Hughes (2004) as

$$\frac{\mathrm{d}\mathbf{p}}{\mathrm{d}t} = -\boldsymbol{\omega}^{\times}\mathbf{p} + \mathbf{f} \tag{4.48}$$

$$\frac{\mathrm{d}\mathbf{H}}{\mathrm{d}t} = -\boldsymbol{\omega}^{\times}\mathbf{H} - \mathbf{v}^{\times}\mathbf{p} + \boldsymbol{\tau} \tag{4.49}$$

$$\frac{\mathrm{d}p_n}{\mathrm{d}t} = m_d\boldsymbol{\omega}^T\mathbf{n}^{\times}\left(\mathbf{v} - \mathbf{r}_d^{\times}\boldsymbol{\omega}\right) - c_d\dot{\xi} - k_d\xi \tag{4.50}$$

and the momenta as

$$\mathbf{p} = m\mathbf{v} - \mathbf{c}^{\times}\boldsymbol{\omega} + m_d\dot{\xi}\boldsymbol{n} \tag{4.51}$$

$$\mathbf{H} = \mathbf{c}^{\times}\mathbf{v} + \mathbf{J}\boldsymbol{\omega} + m_d\dot{\xi}\mathbf{b}^{\times}\mathbf{n} + \mathbf{H}_s \tag{4.52}$$

$$p_n = m_d\left(\mathbf{n}^T\mathbf{v} - \mathbf{n}^T\mathbf{b}^{\times}\boldsymbol{\omega} + \dot{\xi}\right) \tag{4.53}$$

$$H_a = I_s\mathbf{a}^T\boldsymbol{\omega} + H_s \tag{4.54}$$

where $\mathbf{p}$ is the linear momentum vector, $\mathbf{f}$ the external force vector, $\mathbf{v}$ the absolute velocity of the spacecraft, $m_d$ the damper mass, $\mathbf{n}$ the direction of damper mass point in the body frame, $\mathbf{r}_D$ the distance of the damper mass point with respect to the origin of body reference frame, $c_d$ the damper coefficient, $k_d$ the spring coefficient, $\xi$ the displacement of the damper mass in the direction of $\mathbf{n}$, $m$ the total mass of the spacecraft, $\mathbf{J}$ total inertia matrix including the damper mass defined as

$$\mathbf{J} = \mathbf{I}_P + \mathbf{I}_W + m_d\left(r_D^2\bar{\mathbf{I}}_3 - \mathbf{r}_D\mathbf{r}_D^T\right) \tag{4.55}$$

and **b** the distance of the mass damper from its initial position to the origin of the body reference frame. The first moment of inertia **c** is defined as the summation of the inertias of the platform $\mathcal{P}$, wheel $\mathcal{W}$ and damper $\mathcal{D}$;

$$\mathbf{c} = \mathbf{c}_P + \mathbf{c}_R + m_d \mathbf{r}_D \tag{4.56}$$

Several assumptions have been made to simplify the problem. First, zero external forces ($\mathbf{f} = 0$) and linear momentum ($\mathbf{p} = 0$) are assumed. This results that the number of differential equation reduces from 8 to 5 considerably lowering the computational effort. Additionally, the mass displacement is chosen to be aligned to the spin axis ($\vec{n} = \vec{a}$). The full derivation to the differential equations are given in Appendix B.

### 4.6.1 Passive Damper Tuning

Selecting the damper's damping stiffness and coefficient are important parameters to select for optimizing its performance. An often used method is called *tuning* (Hughes 2004). Optimal damper tuning for the ball-in-tube type dampers are limited for a single frequency. In this study, only the addition of a damper's utility is analyzed and in reality various other dampers are used to accommodate a range of frequencies and should be preferred over a ball-in-tube design.

As the damper's design will be mainly prioritized to the nominal mission mode, the damper is to be tuned on the precession frequency during the nominal mode. Tuning is done by matching the natural frequency of the damper system to the precession frequency of the spacecraft. By doing so, one can determine the spring constant. The precession frequency of a non-spinning platform and the natural undamped frequency of the damper are given as

$$\Omega_p \triangleq h_s \sqrt{\frac{I_a}{I_1 I_2 I_3}} \tag{4.57}$$

$$\omega_d = \sqrt{\frac{k_d}{m_d}} \tag{4.58}$$

with $I_a$ representing the moment of inertia of both the rotor and platform in the direction of the spin axis, $k_d$ the spring constant, and $m_d$ the point damper mass. To determine the values for $k_d$ and $m_d$, one should consider also the maximum distance the damper mass can travel. By simply reducing the damper's mass will not yield in a mass optimal system as the increased spring stiffness will increase the mass. To design a damper, material selection and maximum damper displacement are also important characteristics.

### 4.6.2 Damping Criteria

Before continuing on the sizing, there is one consideration to be made about the damper design. Energy dissipation in the momentum wheel can destabilize the directional stability of the spacecraft if the following condition is not met;

$$I_a > \sqrt{I_2 I_3} \tag{4.59}$$

where $I_a$ is the axial inertia of the wheel. This is one of the conditions derived from an energy sink analysis which a gyrostat should satisfy to be directionally asymptotically stable (Cherchas & Hughes 1973, Hughes 2004). For SHAPE this is clearly not the case as the wheel has smaller inertia than its platform. If this condition is not satisfied, the gyrostat is still stable if

$$|\dot{T}_p| > \frac{I_a}{\sqrt{I_2 I_3} - I_a} |\dot{T}_w| \tag{4.60}$$

where $T_p$ is the energy of the platform and $T_w$ the energy of the wheel. For the design of the damper, the energy dissipation rate of the wheel is thus an important characteristic to be estimated.

## 4.7 Trade-off and Performance

Several simulations have been performed for a range of angular momentum values from 0.4 to 2.8 Nms at 60% to 100% design points in SHAPE's lifetime. To evaluate the control effort defined in Equation 4.25, a common angular threshold has been set to 2% of the initial condition (0.02°). From the $t_0$ to this threshold, the maintenance time is defined. The

Table 4.2: Control Effort and Maintenance Times for Rotor Angular Momenta with $u_{\max} = 10^{-5}$ Nm

| % **Lifetime** | $H_s$ [Nms] | $h$ [km] | $\tau_a$ [$\mu$Nms] | $P_u$ (mean,max) [$10^{-7}$Nm$^2$ s] | $t_m$. (mean,max) [Orbits] |
|---|---|---|---|---|---|
| 60% | 0.4 | 332 | 2.9 | 0.8 , 1.1 | 0.12 , 0.17 |
| 70% | 0.6 | 319 | 3.8 | 1.3 , 1.7 | 0.19 , 0.26 |
| 80% | 0.8 | 302 | 5.3 | 1.9 , 2.7 | 0.28 , 0.39 |
| 90% | 1.0 | 280 | 6.7 | 2.6 , 3.8 | 0.38 , 0.52 |
| 100% | 2.8 | 230 | 18.1 | N.A. | N.A. |

Table 4.3: Control Effort and Maintenance Times for Rotor Angular Momenta with $u_{\max} = 10^{-3}$ Nm

| % **Lifetime** - | $H_s$ [Nms] | $h$ [km] | $\tau_a$ [$\mu$Nms] | $P_u$ (mean,max) [$10^{-7}$Nm$^2$ s] | $t_m$. (mean,max) [Orbits] |
|---|---|---|---|---|---|
| 60% | 0.4 | 332 | 2.9 | 12 , 13 | 0.01 , 0.02 |
| 70% | 0.6 | 319 | 3.8 | 18 , 19 | 0.02 , 0.03 |
| 80% | 0.8 | 302 | 5.3 | 24 , 25 | 0.03 , 0.04 |
| 90% | 1.0 | 280 | 6.7 | 31 , 32 | 0.04 , 0.06 |
| 100% | 2.8 | 230 | 18.1 | N.A. | N.A. |

external disturbance torques as given in Section 4.2 are applied to all the simulations. It should be highlighted that the aerodynamic torque acts on the second body axis of the spacecraft only. The pitch axis is left out intentionally as the purpose of the analysis is to estimate the control effort in the transverse direction of the spin axis. Note that the third body axis component of the aerodynamic torque has been assumed to be negligible. Furthermore, saturation limits of the actuators are set to a value of $10^{-5}$ Nms and $10^{-3}$ Nms to mimic magnetorquer and reaction wheel performances, respectively.

The simulations are performed using the dynamics in Equation 3.66 and kinematics in terms of quaternions as given in Section 3.3 while the controllers are based on Euler angles using the quaternions to Euler angles conversion (Section 3.3.5). To accommodate the orbital rotation, a platform angular momentum is required in the pitch axis equivalent to

$$H_1 = -nI_p \tag{4.61}$$

An offset of 1 degree constitutes of a domain of initial conditions with respect to the pitch and roll axis. To derive the performance, the set is approximated as a circle with a radius of 1 degree divided into 32 equal pieces. Due to computational limitations, smaller divisions could not be made.

The initial conditions of the transverse angular momenta have been taken as zero. In Table 4.2, the results of the control effort $P_u$ and the maintenance time $t_m$ are given with the mean and maximum values for a minimal continuous mission time of half an orbit. For each entry in the table, a different gain has been set up for the LQR controller due to the difference in the rotor angular momentum which are found in Appendix D. The corresponding weights are also found in the appendix. The Lyapunov controller has not been further pursued. The gains for the LQR shows that the control scheme between the two are alike and thus the LQR has been opted due to its optimal control property. Increasing the number of initial points for numerical simulation is to be performed in the future. The control effort and the maintenance time for 100% lifetime are not available as the maximum control effort of $10^{-5}$ Nm cannot exceed the maximum disturbance torque of $1.8 \cdot 10^{-5}$ Nm. In Table 4.3, the results are shown for $10^{-3}$ Nm saturation limit. The control effort is a magnitude higher while the maintenance time has reduced to a tenth of to the $10^{-5}$ Nm case.

### 4.7.1 Actuator Trade-off

The selection of the control actuators depends on a lot of factors and requirements. Performance-wise, the difference between the use of reaction wheels and magnetorquers are of a magnitude higher as listed in Table 4.2 and 4.3. Although having an increased maintenance time, reaction wheels require approximately 10 times more control effort.

Table 4.4: Actuator Trade-off

| Criteria | Weight | CMG | RW + MT | MT | RW + T |
|---|---|---|---|---|---|
| Performance | 3 | +1 | +1 | 0 | +1 |
| Mass | 5 | -1 | -1 | +1 | -1 |
| Volume | 2 | -1 | -1 | +1 | -1 |
| Power | 5 | -1 | -1 | 0 | 0 |
| Cost | 3 | -1 | 0 | +1 | 0 |
| Complexity | 3 | -1 | -1 | +1 | -1 |
| Reliability | 5 | -1 | 0 | +1 | -1 |
| **Total** | **26** | **-20** | **-10** | **18** | **-9** |
| **Normalized Total** | | **-0.77** | **-0.38** | **0.82** | **-0.41** |

To utilize reaction wheels however, the system must have additional actuators for momentum desaturation such as magnetorquers or thrusters, adding mass, complexity, and risk to the system. The benefits therefore seem not to outweigh the disadvantages. For affirmative purposes, the trade-off is given between 4 possible concepts in Table 4.4; control moment gyros (CMG), reaction wheels and magnetorquers (RW + MT), magnetorquers (MT), and reaction wheels and thrusters (RW + T). The weights are ordered from 1 to 5 with 1 being of least concern. The focus is given on whether the system is expected to be within the constraints given with +1 for over, 0 for on-par and -1 for under fulfillment. As shown, the MT concept is clearly the best option as it is the only one with a positive net score.

As shown in the table, the trade-off criteria are the performance, mass, volume, power, cost, complexity, and reliability. The performance criterion is judged based on the magnitude of the control torque available and also the maintenance time. This criterion is given a weight of 3 as the control torque can give additional maneuverability. The maintenance time is only of importance when the value exceeds the half orbit value as decreasing the maintenance time does not give additional benefits. The mass and power are the two most important criteria as these are critical to be within the expected mass and power constraints. A weight of 2 has been given to the volume to be fit into the CubeSat design. The cost dictates to stay within the relative low cost budget and has been given a weight of 3. The complexity regards to the dynamics and uncertainty which make the control less tractable and inducing additional problems. An example is the use of reaction wheels, due to mechanical parts, unwanted vibrations induce jitter to the system reducing imaging capabilities. Damping these make the use of the reaction wheels complex. The reliability is also of primary importance as one of the main mission objective is to demonstrate high pointing capabilities of CubeSats over its intended lifetime. Note that although the thruster performance has not been analyzed (saturation torque value of $10^{-4}$ Nm), it has been assumed that the performance will lie in between. Similar in that regard, the control moment gyro has been given highest performance value.

### 4.7.2 Momentum Wheel Optimization

From the radius and angular velocity requirements (S.7 & S-AQ.3), one can determine the maximum required angular momentum of the rotor. Assuming the rotor as a disk with a radius of 14 cm, thickness of 1 cm and aluminum as material, one obtains a maximum of 8.9 Nms using Equation 4.17. This value far surpasses the end of life 1 degree performance of 5.5 Nms and therefore does not constrain the momentum wheel sizing. Similarly, the minimum sizing is determined using the cyclic disturbances. Adding the maximum cyclic disturbance torques at 230 km gives a value of 0.47 $\mu$Nm. The momentum wheel should be able to be within the 1 degree pointing requirement over half an orbital period at 230 km of 2670 seconds. Using Equation 3.51, one obtains a minimum angular momentum of 0.07 Nms. Both boundaries are outside the range determined in Section 4.4.

To determine the appropriate size of the momentum wheel and the relevant control actuators, a trade-off is required between several performance parameters. Given in the previous sections, these consist of the time within 1 degree pointing performance, the mass and volume of the wheel, the control effort, the maintenance time, and the spinup time. The main performance of the mission is dictated by the lifetime as it will provide crucial earth observation data. By increasing the angular momentum, the maintenance time of the mission will increase due to the increased control effort. This leads to a reduced 'effective' mission lifetime if the maintenance time surpasses half an orbit. The sizing of the

momentum wheel is therefore a balance between two complementary parameters; the nominal and maintenance time. The payload requirement (S.5) states that the spacecraft will be in a noon/midnight SSO. Thus, approximately half the orbit the system will be in noon and half in midnight. To find an optimized momentum wheel, the system should be continuously observing the Earth during noon and adjust its pointing error during the midnight period. Resulting in the following optimization constraints;

$$t_n \geq 0.5 \cdot T_O(h) \tag{4.62}$$

$$t_m \leq 0.5 \cdot T_O(h) \tag{4.63}$$

with $T_O$ the period of one orbit. The optimization problem of finding the smallest angular momentum $H_s$ which fit above optimization conditions is a complex task. The changes throughout SHAPE's lifetime with respect to the atmospheric density as described in Section 4.4.1 are exponential. Taking a naive worst-case approach of an end-of-life design yields in inefficiency during the early stages of the mission. An earlier point within the lifetime provides a reduction in other parameters such as the spinup time, mass and volume with however a loss in performance after this point. Thus, the exponential decrease in atmospheric density is crucial in the selection of a design point. This yields in both an exponential decline in altitude and lifetime. As such the atmospheric torque acting on the spacecraft increases exponentially. The combined effect makes the end-of-life design an unattractive point.

A question one can ask is then to what extent one can reduce mission observation time to profit from the diminishing reduction of mass and volume. The optimization objective is to minimize the angular momentum of the wheel and therefore the mass, radius and the spinup time while maximizing the observation time. One can apply weights to the optimization process to find a balance between these two parameters resulting from a cost analysis. However as SHAPE is a demonstration satellite, the importance of mission lifetime can be considered of lesser magnitude. For this study, a reduction of 10% is taken from the lifetime, reducing the angular momentum by approximately 60%. After this point the radius and mass decline as at slower rate as shown in Figure 4.9. The angular momentum over the lifetime curve has been obtained using an exponential fit function;

$$H = 0.1802 \cdot 10^{0.008774t} + 8.735 \cdot 10^{-7} \cdot 10^{0.08633t} \tag{4.64}$$

which has been converted to percentages. Note that the spin time slightly deviates from the angular momentum. This is due to the decreasing torque caused by the reducing moment arm (the radius of the rotor).

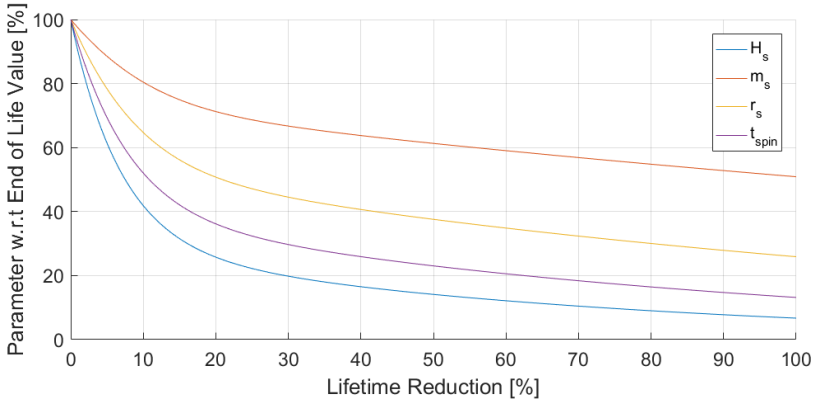


Figure 4.9: Effect of Reduction of Lifetimes on Wheel Parameters

A second reason for the 10% mark is that before this value, the maintenance time exceeds the half an orbit condition. As a result, the observation time is negatively affected. To verify whether the condition given in Equation 4.63 is indeed valid for the angular momentum at 90% of the lifetime, control simulations have been performed to see whether the maintenance time exceeds half an orbit. The required mass moment of inertia can be determined using Equation 4.15 and requirement (S-AQ.3) yielding in $1.9 \cdot 10^{-3}$ kg m$^2$. To quickly verify whether the system satisfies requirement (S.11), the rotor is assumed to be a disk made out of solid aluminum of 1 cm thick with a density of 2830 kg/m$^3$. An angular momentum of 1.0 Nms yields in a radius of 8 cm and a mass of 0.57 kg which is a reduction of 2 cm and 0.4 kg compared to the end-of-life design. This mass exceeds the requirement, however it should be noted that a disk-like structure is not mass optimal with respect to the inertia. The final wheel inertia is equivalent to $1.8 \cdot 10^{-3}$ kg m$^2$.

### 4.7.3 Nominal and Maintenance Performance without Damping

Before finalizing the momentum wheel sizing, the system has been checked on its performance during the nominal mode. The nominal mission time determined previously are based on Equation 3.51 which is the worst-case scenario whereby the angular momentum vector is displaced with a constant tangential torque. To simulate a more realistic scenario, the system is simulated with the assumed disturbance torques initialized with the values listed in Table 4.5. The simulation results for the nominal mode are shown in Figure 4.10. It should be added that the simulation is halted

Table 4.5: Initial Conditions for Nominal (N) and Maintenance (M) Performance without Damping

| **Variables** | **Values** |
|---|---|
| $\boldsymbol{\theta}_0$ (N) | $[0, 0, 0]^T$ deg |
| $\boldsymbol{\theta}_0$ (M) | $[0, 1, 0]^T$ deg |
| $\mathbf{H}$ | $[1, 0, 0]^T$ Nms |
| $h$ | 280 km |
| $\vec{\tau}_a$ | Only on the $\vec{b}_2$ axis |

after the pointing error has surpassed the 1 degree requirement. The system shows remarkable performance as the duration of the nominal mode exceed more than 13 orbits. The transverse angular velocities reaches approximately a value of around 1 $\mu$rad/s two orders of magnitude beneath requirement (S-NM.5). This has an equivalent MTF value of 99.99996% which is virtually no image quality degradation. The need for a damping is therefore questionable.

In Figure 4.11, the maintenance mode performance is shown. Wherein Figure 4.10b and 4.11b, the transverse angular momenta are given. During the maintenance mode, the control actuators are commanded to damp angular velocities due to the nonzero gains of the LQR controller. These final values are within requirement (S-NM.5) which shows that the LQR controller is also suitable for active damping. The maintenance has been simulated to stop after an angular offset less than 0.02 degree is detected.

To see how the system behaves after the actuators are deactivated, a simulation has been performed from the maintenance to the nominal mode using the initial conditions of the maintenance mode in Table 4.5. After the nominal mode sets in and the actuators are deactivated, oscillations due to disturbances arise immediately. Concurrently, the system's angular rates oscillates to a steady value. In the beginning of the nominal mode, the oscillation seem to converge, but diverges after the 13 orbits mark. This might be due to the direction of the aerodynamic disturbance torque to be initially opposing to the motion for which after the 13 orbits this effect reverses and amplifies. The 0.02 degree requirement is not strict as the oscillating motion arises instantly. A more suitable point for termination is a point within the first oscillation instead of reducing the yaw and roll angles to within 0.02 degree.

### 4.7.4 Damping and Pitch Performance

The results in the previous section were conducted under zero initial transverse angular velocities and without any form of damping for the nominal mode. Hereby, it was found that a form of damping is not necessary as the system did comply requirement (S-NM.5). These simulations however lacked uncertainties in disturbances, sensor noise, inertia errors, spin axis offset and perfect pitch control was assumed. In reality, control dynamics such as hysteresis of magnetorquers or jitter caused by reaction wheels can lead to higher angular rates and reduction in pointing performance.

A more substantial problem is the gyroscopic coupling between the three axes. For the design of the LQR controller, linear dynamics had been assumed, leaving the pitch axis uncoupled from the two other axes. This has important implications to the nonlinear dynamical system, even though the angles are relatively small. Coupling in the Euler's rotational motion of equations in the principal axis frame (Equation 3.66) may limit the effect of the pitch actuator.

A simple calculation can provide the magnitude to determine to what extent this can affect the system. Take the gyroscopic term of Equation 3.66 as

$$\max\left(\tau_g\right)_1 = |(I_2 - I_3)\omega_2\omega_3| \tag{4.65}$$

If the maximum gyroscopic torque $\max\left(\tau_g\right)_1$ reaches a value of $10^{-5}$Nm, the system loses its pitch axis control as the control torque is negated. Note that this also does not consider the effects of disturbance torques or the torque required to rotate the platform with the mean motion. Simplifying that $\omega_{\max} \triangleq \omega_2 = \omega_3$ yields in an angular rate of

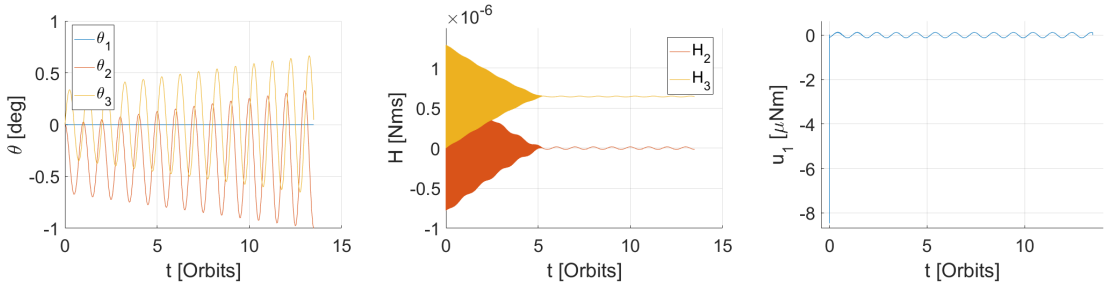


(a) Euler Angles (b) Transverse Angular Momenta (c) Pitch Control

Figure 4.10: SHAPE Nominal Mode Performance with $H_s = 1.0$ Nms

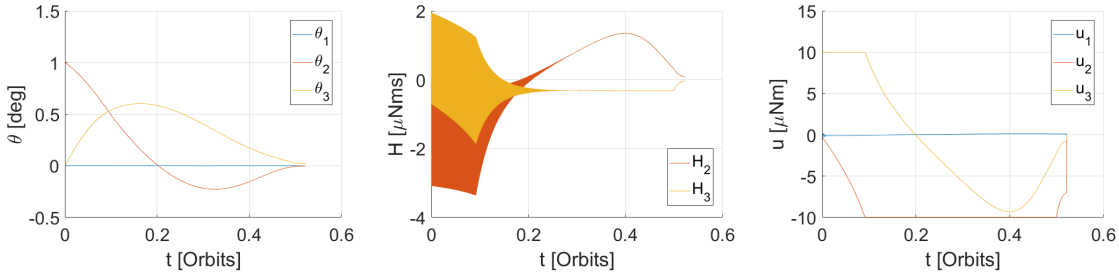


(a) Euler Angles (b) Transverse Angular Momenta (c) Control Torque

Figure 4.11: SHAPE Maintenance Mode Performance with $H_s = 1.0$ Nms

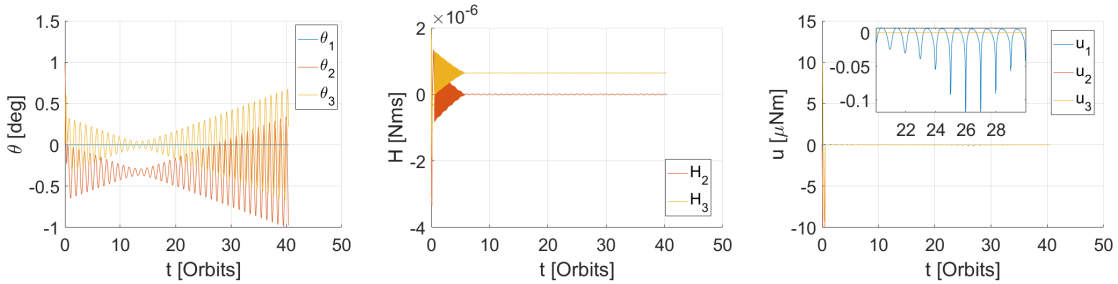


(a) Euler Angles (b) Transverse Angular Momenta (c) Control Torque

Figure 4.12: SHAPE Sequential Performance with $H_s = 1.0$ Nms

14 mrad/s. Past this value, the system loses partially its controllability. This partial loss is only temporarily at that specific combination of angular body rates. The spacecraft precesses and there will be intervals for which either of the angular velocities drops to a value where it can regain control. As the transverse momenta increases, this interval will decline.

The gyroscopic coupling can be further amplified if the system has nonzero products of inertia. These add additional terms to the system. This can be simply derived by expanding the term; $\boldsymbol{\omega}^{\times}\mathbf{I}\boldsymbol{\omega}$. The first entry of this column vector is equivalent to

$$\max\left(\tau_g\right)_2 = |\omega_1(\omega_2 I_{zx} - \omega_3 I_{yx}) + \omega_2(\omega_2 I_{zy} - \omega_3 I_{yy}) + \omega_3(\omega_2 I_{zz} - \omega_3 I_{yz})| \tag{4.66}$$

In similar fashion as the previous however with the notion that $\omega_{\max} \triangleq \omega_2 = -\omega_3$ and 10% product of inertia errors yields in a value of 6 mrad/s. This concludes that the pitch controllability is lost at a half the value. This effect cannot be neglected and these errors should be mitigated by moving the subsystems in the CubeSat. Small mass offsets are however inevitable which cause the spacecraft to precess. The products of inertia might be further minimized by adding non-functional counterweight to the system. This is superfluous. By adding a form of damping, the system can provide alleviation for the pitch control as the transverse momenta are damped and thus the gyroscopic torques are minimized.

Is a passive damper justifiable? While the limit for the pitch uncontrollability has been determined, the more strict

requirement (S.NM-5) causes a larger strain to the pitch control. Unlike the transverse axes, the pitch axis does not benefit as much from the gyroscopic stiffness and disturbances impact the pitch axis more heavily. Some analyses are performed for a more in-depth evaluation.

**Ball-in-Tube Damper Design**

For the design of a ball-in-tube damper consisting of a spring and a dashpot as given in Section 4.6, five parameters are relevant; the damper mass $m_d$, the perpendicular distance $b$ from the origin of the body frame to the undamped location of the damper mass, the spring coefficient $k_d$, the damping coefficient $c_d$, and the maximum absolute displacement of the damper mass $|\xi|_{\max}$. The selection of $k_d$ is based on the precession frequency and the damper mass. Assuming that the damper will be 10 g and using the equations given in Section 4.6.1, a precession frequency of 8.4 rad/s is computed and thus a spring constant of 0.71 kg/m is required. The parameters $b$ and $c_d$ has been determined manually.

To differentiate the levels of transverse momenta, the nutation angle $\eta$ is used which for the torque-free scenario defined as;

$$\mathbf{H}_0 = \begin{bmatrix} cH & \sqrt{(H^2 - (cH)^2)} & 0 \end{bmatrix}^T \tag{4.67}$$

where $c = \cos(\eta)$ and $H$ the magnitude of the angular momentum. Some values of $\eta$ are given with the corresponding $H_2$ values in Table 4.8. Furthermore, an initial angular position of $\boldsymbol{\theta} = (0, 0, 0)$ is taken with the external disturbances given for the conditions at 280 km, $H_s = 1$ Nms, $\xi_0 = 0$, $p_{n,0} = 0$, and $b$ aligned to $\vec{b}_3$. At approximately a nutation angle of 0.4°, the pitch controllability. In Table 4.6, the effect of $b$ is listed against the time at which requirement (S-NM.5) is met $T_{\text{req}}$, the transverse momentum after 2 orbits $H_T$, and the maximum displacement $|\xi|_{\max}$. Here, initial conditions for the nominal conditions given in Table 4.5 are used with $\mathbf{H}$ determined using Equation 4.67 and a $c_d = 0.01$ kg s/m.

The damping for every case reaches a steady state transverse momenta of $6 \cdot 10^{-7}$ Nms. The differences are shown in the other parameters. The requirement time decreases for increasing $b$ and the effect lessens similarly to the control effort. The maximum displacement in contrast increases almost linearly. For the following damping simulations, $b$ of 0.15 m equivalent to the maximum dimension of SHAPE has been taken. Although the maximum displacement is relatively high for $\eta = 1°$, the system should not reach past 0.1° for which the maximum displacement is tenth of the $\eta = 1°$ value.

In Table 4.7, several values of the damping coefficient are listed. As shown, the four values of $c_d$ gives satisfying solutions to the requirement and the differences lie primarily on the speed of the transient behavior and the maximum deflection. All cases except the $c_d = 1$ kg s/m case show identical final angular momenta. This exception is due to the very slow damping which results that the final value is attained after 2.7 orbits. For $c_d = 1$, the long transient time makes this choice undesirable. The parameters $T_{\text{req}}$ and $|\xi|_{\max}$ then remains to be traded-off. The first increases for increasing damping coefficient while the latter decreases. As fast damping is preferred to regain high image quality, priority is put on parameter $T_{\text{req}}$ and thus the damping coefficient $c_d = 0.01$ kg s/m is selected. A damping coefficient of $c_d = 0.001$ provides a slightly higher speed, the deflection however increases by a factor 4. It is emphasized that the design of this damper are not considered within engineering perspective and has been left for future work.

**Damping and Pitch Analysis**

As said previously, the spacecraft should lose its pitch controllability at nutation angles above 0.4°. To see whether the pitch control is alleviated effectively, simulations have been performed. For comparison, the nominal mode performance without damping are shown for $\eta = 0°$ and $\eta = 1°$ in Figure 4.13 and 4.14, respectively. Hereby, the pitch aerodynamic disturbance torque has been added.

As seen in Figure 4.13b, the system without a damper is still able to damp the transverse angular momenta, although at a very slow rate. The pitch LQR controller is commanded to rotate at the mean motion and to do this as close to this rate as possible, the system has to compensate for the gyroscopic torques. While doing so, the transverse cross coupling reduces the transverse angular momenta, basically acting like an active damper. In Figure 4.14, the system is subjected to high transverse momenta and although the pitch is able to stabilize, a bang-bang control is required. The difference between with and without a damping system is rather insignificant at low transverse momenta values as seen in Figure 4.15. Additionally, small oscillatory differences can be noticed in the pitch control torque. The control torque is mostly used to counter the external disturbances having a value of $6.7 \cdot 10^7$ Nm which is equivalent to the aerodynamic torque. The oscillating behavior is induced by the cyclic disturbance torques. For $\eta = 1°$, the difference is clear. The angular momentum converges within the requirement value in approximately 100 seconds.

Table 4.6: Effect of $b$ on the Damping Performance with $c_d = 0.01$

| $b$ [m] | $\eta$ [deg] | $T_{\text{req}}$ [Orbits] | $H_T$ after 2 Orbits [Nms] | $\lvert\xi\rvert_{\max}$ [mm] | $P_u$ [Nm$^2$ s] |
|---|---|---|---|---|---|
| 0.05 | 0 | 0 | $6 \cdot 10^{-7}$ | $3 \cdot 10^{-3}$ | $2 \cdot 10^{-15}$ |
| | 1 | 0.15 | $6 \cdot 10^{-7}$ | 6 | $7 \cdot 10^{-11}$ |
| 0.10 | 0 | 0 | $6 \cdot 10^{-7}$ | $5 \cdot 10^{-4}$ | $2 \cdot 10^{-15}$ |
| | 1 | 0.04 | $6 \cdot 10^{-7}$ | 11 | $5 \cdot 10^{-11}$ |
| 0.15 | 0 | 0 | $6 \cdot 10^{-7}$ | $7 \cdot 10^{-4}$ | $2 \cdot 10^{-15}$ |
| | 1 | 0.02 | $6 \cdot 10^{-7}$ | 15 | $6 \cdot 10^{-10}$ |

Table 4.7: Effect of $c_d$ on the Damping Performance with $b = 0.15$

| $c_d$ [N s/m] | $\eta$ [deg] | $T_{\text{req}}$ [Orbits] | $H_T$ after 2 Orbits [Nms] | $\lvert\xi\rvert_{\max}$ [mm] | $P_u$ [Nm$^2$ s] |
|---|---|---|---|---|---|
| 0.001 | 0 | 0 | $6 \cdot 10^{-7}$ | $2 \cdot 10^{-3}$ | $2 \cdot 10^{-15}$ |
| | 1 | 0.03 | $6 \cdot 10^{-7}$ | 44 | $4 \cdot 10^{-11}$ |
| 0.01 | 0 | 0 | $6 \cdot 10^{-7}$ | $5 \cdot 10^{-4}$ | $2 \cdot 10^{-15}$ |
| | 1 | 0.04 | $6 \cdot 10^{-7}$ | 11 | $5 \cdot 10^{-11}$ |
| 0.1 | 0 | 0 | $6 \cdot 10^{-7}$ | $8 \cdot 10^{-5}$ | $2 \cdot 10^{-15}$ |
| | 1 | 0.17 | $6 \cdot 10^{-7}$ | 1.8 | $6 \cdot 10^{-11}$ |
| 1 | 0 | 0 | $9 \cdot 10^{-6}$ | $7 \cdot 10^{-4}$ | $2 \cdot 10^{-15}$ |
| | 1 | 1.72 | $4 \cdot 10^{-5}$ | 0.2 | $4 \cdot 10^{-11}$ |

Table 4.8: Passive Damping Cases

| **Case** | $\eta$ [deg] | $H_{2,0}$ [mNms] |
|---|---|---|
| 1 | 0 | 0 |
| 2 | 0.5 | 8.7 |
| 3 | 1.0 | 17.5 |
| 4 | 2.0 | 34.9 |

Table 4.9: Passive Damper Parameters

| **Parameter** | **Value** |
|---|---|
| $m_d$ | 10 g |
| $b$ | 0.15 m |
| $k_d$ | 0.71 kg/m |
| $c_d$ | 0.01 kg s/m |
| $\lvert\xi\rvert_{\max}$ | 15 mm |

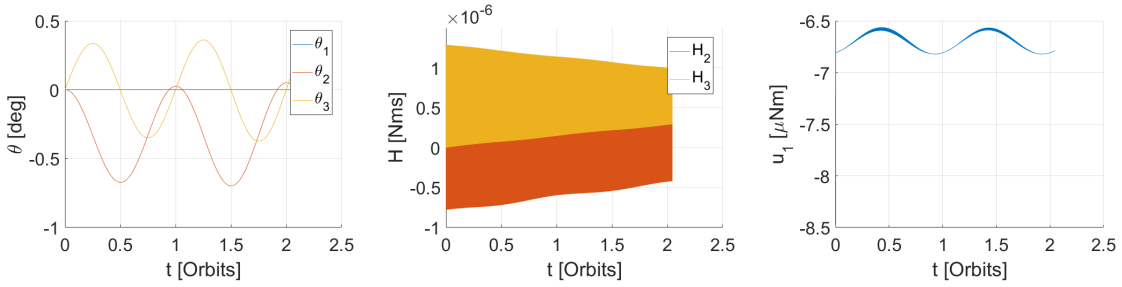


(a) Euler Angles (b) Transverse Angular Momenta (c) Pitch Control Torque

Figure 4.13: Nominal Mode without Damping for $\eta = 0°$

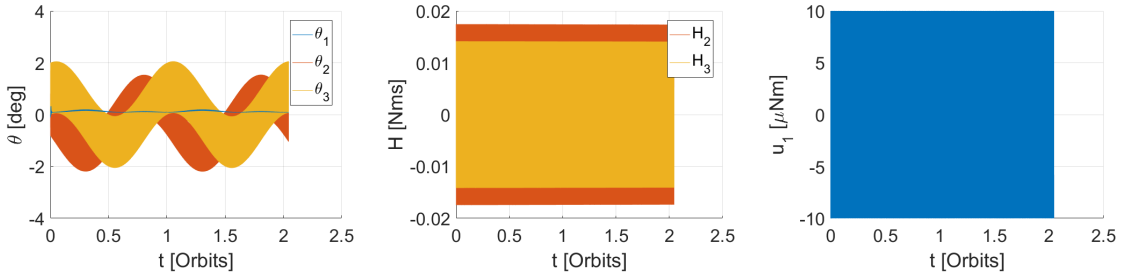


(a) Euler Angles (b) Transverse Angular Momenta (c) Pitch Control Torque

Figure 4.14: Nominal Mode without Damping for $\eta = 1°$

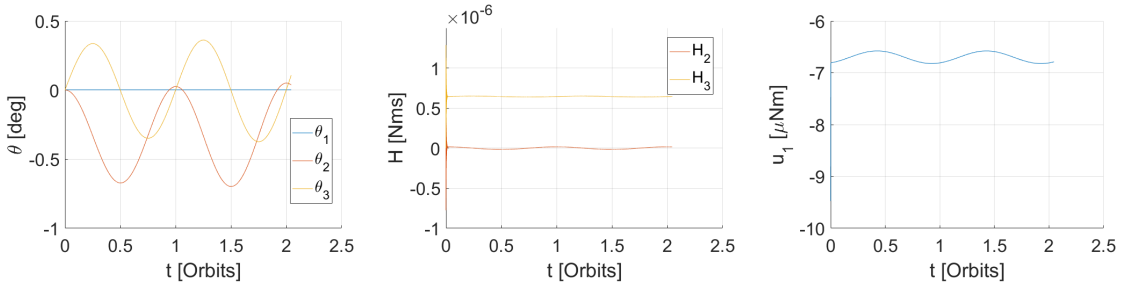


(a) Euler Angles (b) Transverse Angular Momenta (c) Pitch Control Torque

Figure 4.15: Nominal Mode with Passive Damping for $\eta = 0°$

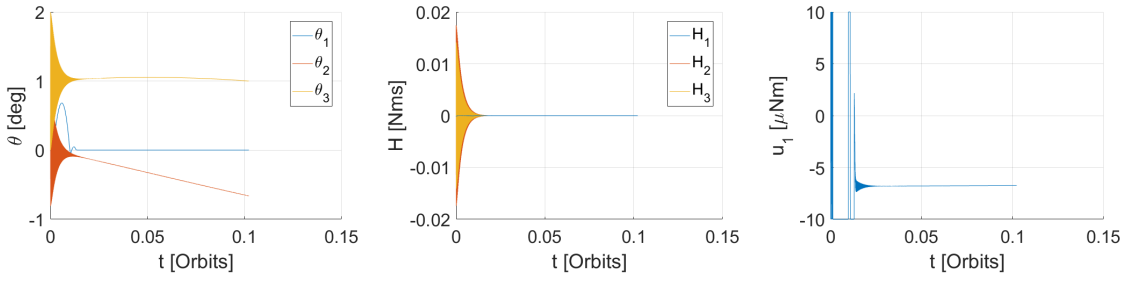


(a) Euler Angles (b) Transverse Angular Momenta (c) Pitch Control Torque

Figure 4.16: Nominal Mode with Passive Damping for $\eta = 1°$

**Effect of Product of Inertia**

A form of damping still seems to be not necessary as nutation angles of 1 degree or more is not expected to occur under nominal circumstances. However for the previous simulations, it had been assumed that no products of inertia is present. This implies that the spin axis is aligned to the first principal axis. In reality, spin axis offset, misalignment and unequal mass distribution yield in nonzero product of inertia terms. As a result, the spacecraft will precess with a larger nutation angle and thus has higher transverse angular body rates. Assuming that the products of inertia is approximately 10% of the principal inertias, one can obtain the following inertia matrix;

$$\mathbf{I} = \begin{bmatrix} 0.064 & 0.006 & 0.015 \\ 0.006 & 0.146 & 0.010 \\ 0.015 & 0.010 & 0.096 \end{bmatrix} \text{ kg m}^2 \tag{4.68}$$

Figure 4.17 shows the simulation with product of inertia with a nutation angle of 0 degree and initial conditions as the previous simulation. The transverse momenta have increased by around a factor of 10. The resulting transverse momenta are still within the requirement values. Damping the transverse momenta at $\eta = 0°$ does not improve the situation (Figure 4.19), but at higher values such as at an angle of 0.1 degree (Figure 4.20) major improvements can be noticed. The system without damping takes 0.32 orbits to be within the requirement values, whereas damping can attain it within 0.01 orbits. The difference in control effort is staggering with a value of $3.5 \cdot 10^{-7}$ Nm$^2$s and for the system without damping of $4.7 \cdot 10^{-11}$ Nm$^2$s.

**Active Damping**

Active damping in the form of magnetorquers can use sensory measurements to reduce the transverse angular momenta. Using the LQR controller, this can be attained while also readjusting the pointing offset. This requires however additional constraint on the power supply and continuous dependence is therefore demanding. A passive system might therefore provide an adequate solution at the expense of increased mass. Besides that it does not require power, a passive system is able to provide additional benefits as given in the next chapter. The active control system selected as magnetorquers can still provide unaccounted changes in the body rates. This should be reserved as a contingency procedure for body rates yielding in pitch uncontrollability or if a faster convergence is needed.

## 4.8 Summary

To summarize this chapter, the momentum wheel design has been based on a prediction made for solar cycle #25 with a 95% confidence interval at the time of minimum lifetime. At this condition, the aerodynamic torque profile over SHAPE's lifetime and altitude has been used to size the momentum wheel. Due to the exponential decrease of the atmospheric density, it has been concluded that an end-of-life design was not efficient. By forfeiting a part of the pointing performance at 10% of SHAPE's lifetime, 41% of the mass (400 g) and 20% of the radius (2 cm) have been reduced. Appropriate actuators have been chosen based on several criteria and a maintenance time requirement of less than half orbit. Hereby, magnetorquers have been found to be sufficient. Additionally, a passive damping is recommended as the presence of gyroscopic coupling and products of inertia can cause the system to exceed the maximum angular velocity requirement (S-NM.5). To minimize power consumption, active damping with the use of magnetorquers have been considered only for contingency. In Table 4.10, the momentum wheel parameters are summarized. For further design, one should consider the structure, material and thruster configurations more carefully. The momentum wheel has been assumed to be disk-like and a more improved wheel with more mass at the edge can make the system more compact and lighter.

Table 4.10: Momentum Wheel Parameters

| Parameter | Value |
|---|---|
| Angular Momentum $H_s$ | 1.0 Nms |
| Mass $m_s$ | 570 g |

| Parameter | Value |
|---|---|
| Radius $r$ , Thickness $t$ | 8 cm , 1 cm |
| Spinup Time $t_{spin}$ | 1.13 Orbits |

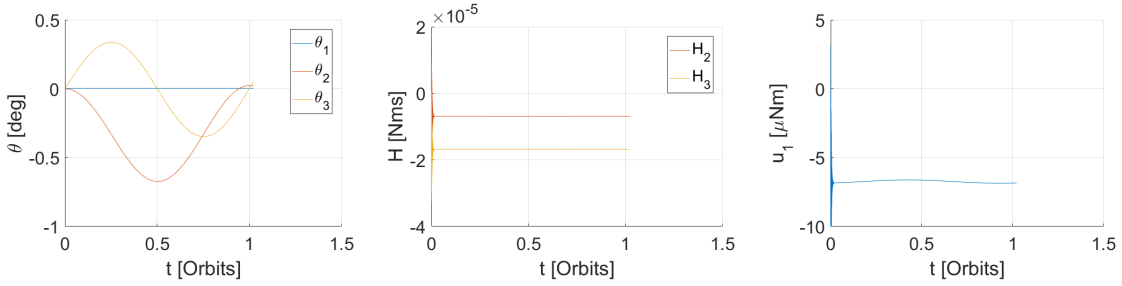


(a) Euler Angles (b) Transverse Angular Momenta (c) Pitch Control Torque

Figure 4.17: Nominal Mode with Product of Inertia without Damping for $\eta = 0°$

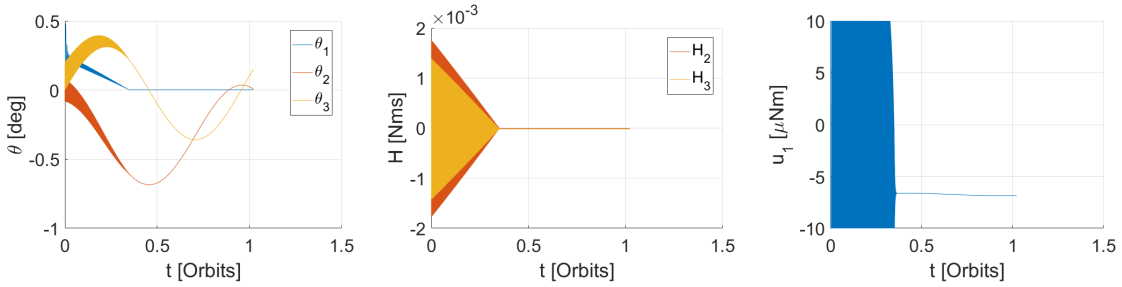


(a) Euler Angles (b) Transverse Angular Momenta (c) Pitch Control Torque

Figure 4.18: Nominal Mode with Product of Inertia without Damping for $\eta = 0.1°$

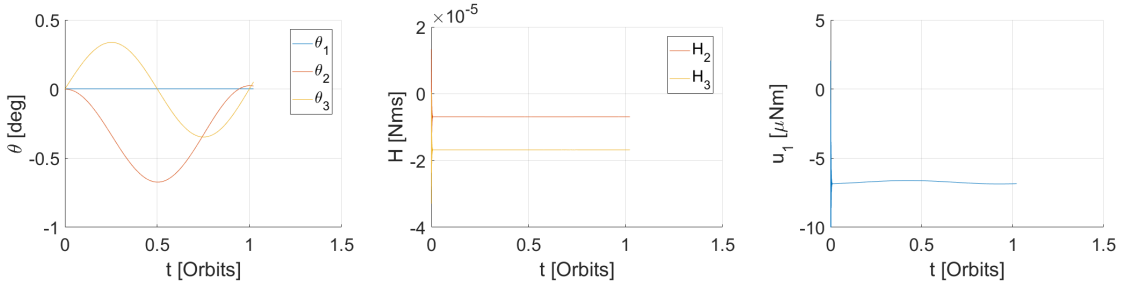


(a) Euler Angles (b) Transverse Angular Momenta (c) Pitch Control Torque

Figure 4.19: Nominal Mode with Product of Inertia with Damping for $\eta = 0°$

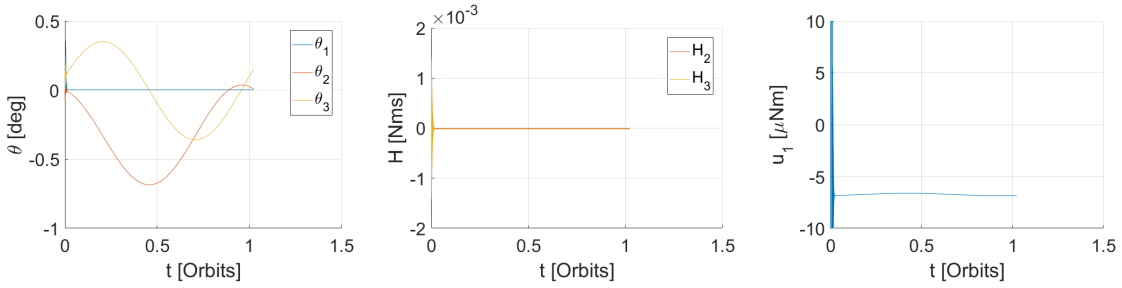


(a) Euler Angles (b) Transverse Angular Momenta (c) Pitch Control Torque

Figure 4.20: Nominal Mode with Product of Inertia with Damping for $\eta = 0.1°$

# Chapter 5

# Acquisition Mode

In the previous chapter, the momentum wheel design has been discussed and established. To realize the nominal state, a maneuver is required to spin the momentum wheel to its required value. This chapter is devoted to the acquisition phase and how one could achieve to the nominal mode in an effective manner. The first section covers the objective of the spinup. In Section 5.2, the considered spinup strategies are presented. This is followed with the spinup dynamics of one of the two main branches of the discussed spinup processes in Section 5.3. Section 5.4 presents possible states during the spinup for which the spacecraft can deviate from its desired final configuration. Then, the spinup procedure is analyzed including a passive damping system. In Section 5.6, the other main branch of the spinup concepts is analyzed. This chapter closes of with a trade-off of several main spinup concepts in Section 5.7.

## 5.1 Objective

The main goal of the acquisition mode is to spin the momentum wheel such that the spacecraft is gyrically stabilized for its nominal mission phase. This goal is accompanied with the realization of the nominal orientation mentioned in the previous chapter. These two objectives are the minimal requirements to lead to the mission objective defined in the nominal mode. If the spacecraft does not reach the correct orientation closely, the energy required to adjust the misalignment might become too costly. Therefore, choosing a spinup strategy which is able to reach these conditions are of utmost importance.

To define what is more "suited" for the mission, some parameters can be analyzed which might bottleneck or even fail the mission. The biggest hurdle during the spinup process is the power. Due to the possibility of initially limited capabilities of solar pointing and stability, power is expected to be constrained and to be reliant by the batteries. Especially as the acquisition mode is followed after the detumbling mode. Even though one can think of spinup strategies where power can be established. Aversion of risk involved in the complete maneouvre is prioritized. Besides the power, the time the maneuver takes is also an important aspect. Although power limits the use of actuators and subsystems, the duration of the acquisition phase determines the total energy needed for the battery. The energy capacity of the spacecraft should also include the energy needed for the detumbling phase.

## 5.2 Conceptual Strategies

To conceptualize the available spinup strategies, one can start from the nominal conditions given in Section 4.1 as this is the final result to be achieved by the acquisition phase. The initial conditions should be derived from the conditions after detumbling. However, these can vary depending on the spinup mode itself. One can achieve full 3-axis control or maintain a spin through one of its axis. The first option might provide better communication with the ground and deployment of solar panels for power. The latter can utilize the "undesired" angular momentum resultant from the deployment of the launcher's upper stage and provide a means of passive stabilization to prepare for the spinup process, reducing the power consumption.

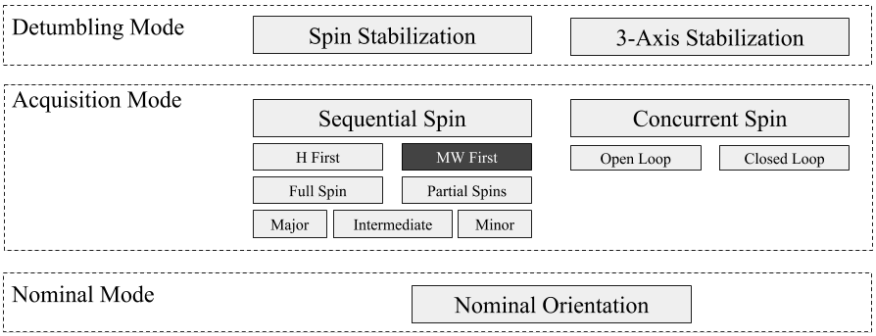


Figure 5.1: Conceptual Spinup Strategies

For the spinup phase itself, there are few options to be explored which is branched into two options as shown in Figure 5.1. One branch focuses on attaining the angular momentum before the momentum wheel spinup (or vice versa) and the other relates to achieving both concurrently denoted with "Sequential Spin" and "Concurrent Spin", respectively. The naming of these two has been given based on the procedure itself. The first requires a setup of an initial spin of the spacecraft. In the latter, both the spacecraft and the momentum can be initialized for the process. The difference in these two types are extensive in terms of dynamics. The mathematical model *gyrostat* mentioned in Chapter 3 can be applied in the sequential spin but not in the latter which is rather complex and numerical simulations have to be performed for its analysis.

The *sequential* spinup strategies can be divided into three subsets. The first division is based on whether the angular momentum is attained before or after the momentum wheel spinup. "MW First" can already be eliminated from the possible concepts as shown in black in the figure. This is due to the fact that if no gyroscopic stability is achieved, the momentum wheel will react as a reaction wheel. In combination with large disturbance torques, this will lead to a complex motion of the spacecraft for the 3-axis stabilized configuration after detumbling. Without compensation through the use of active control elements, the spacecraft will lead to an undesired state which is hard to control. If spin stabilization is obtained beforehand, the "MW First" subconcept will be ambiguous as the differentiation is then made when the detumbling mode ends. Therefore, it will be concluded that by choosing the 3-axis stabilization concept, the concurrent spin option in the acquisition phase will be followed.

The second subset is when the concepts are differentiated based on the number of sequential spins. One can do this in a single step, meaning that the desired angular momentum is obtained completely followed by the spinup of the momentum wheel. For partial spin types, the final configuration is attained by dividing this process in two or more steps i.e. the iteration of first spinning the spacecraft to a partial value and then spinning the momentum wheel until the platform has reached a steady state and repeating this until the desired angular momentum has been reached.

The last subdivision is made depending on the rotation axis. Mathematically, an infinite number of axis can be taken for analysis. It is more practical and efficient to divide it into three axes depending on the inertias of the system while analyzing the surrounding regions. The axis from highest to lowest inertia are defined as the major, intermediate and minor axis which influences the rotational dynamics considerably as discussed in the next section. An example of a sequential spinup type is shown in Figure 5.2a.

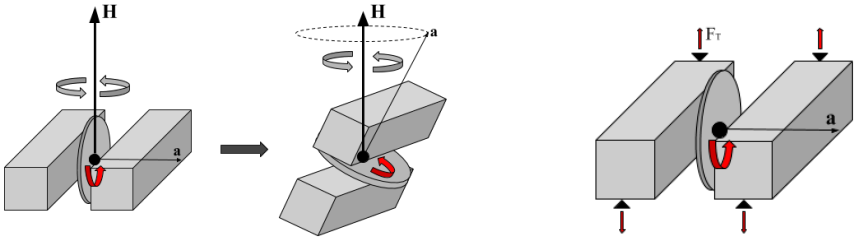


(a) Sequential Type (b) Concurrent Type

Figure 5.2: Examples of Spinup Strategies

The *concurrent* spin types are subdivided into just one category consisting of open or closed loop control. Open loop strategies are used to analyze the effect of using control actuators without any sensory feedback. The corresponding open loop controllers is expected to be very elementary and will be used to compare with closed loop types. Closed loop will use a more elaborated control schemes with feedback for analysis. An example of a concurrent spinup type is shown in Figure 5.2b.

One could argue to spin the momentum wheel in the upper stage. The use of thrusters for the momentum wheel spinup however might result in contamination of other spacecraft in the upper stage vehicle and put additional design strains on the separation system. Another concept which has not been mentioned is a method suggested by Doroshin (2014). Doroshin concludes that chaos, a recurring motion which is aperiodic and sensitive to initial conditions, is inherent to the spinup procedure. By adding a second conjugate rotor rotating in the opposite direction with equal torque, the chaotic regions during the spinup can be bypassed by suddenly braking one of the two rotors when the desired angular momentum has reached. This system albeit looking promising theoretically, requires a momentum wheel equivalent to the other. Although one could argue that this adds a redundancy to the design, the mass, volume, and complexity are not enough valued to be used just for the spinup procedure. Therefore, these options have been put aside from the conceptual spinup strategies.

## 5.3 Spinup Dynamics

Following from the spinup concepts, several methods are available for analysis. A major distinction between the models and methods are defined by the sequential and concurrent spins as mentioned in the previous section. For the sequential spin strategies, the torque-free gyrostat model will be used for analysis. There are two methods considered for the gyrostat; the momentum sphere method and the method proposed by Hall & Rand (1994) which will be referred shortly as Hall and Rand's method. The momentum sphere method by Barba & Aubrun (1976) uses a series of momentum sphere as given in Section 3.6 to graphically represent the changing behavior in the dynamics by using a series of different values of the rotor momentum pseudo-statically. Hall and Rand's method continues on this approach by reducing the number of equations from 4 to 3 using a transformation of energy for the axial gyrostat. This transformation allows the system's energy to be represented in a two-dimensional plane instead of a three-dimensional surface on the momentum sphere. Furthermore, they investigate the averaged solutions for this system using the method of averaging giving an approximate solution at a given energy level.

A more general approach which does not assume an axial rotor is given by Hall (1995). Euler's rotational motion for the torque-free case is expressed in a non-canonical Hamiltonian system of equations to represent a similar two-dimensional representation between the rotor angular momentum and the energy. As a result of generalization, Hall was not able to give the averaged solutions as it was deemed to be too complex. However, the use of this Hamiltonian system is recommended by Hall for its use in graphical representations. This is done by numerically projecting the exact solutions unto the two-dimensional energy plane. The same approach has been given for a dual-spin spacecraft with two rotors by Hall (1996) and has been used to study the escape of trap states by Hall (1998). Additionally, a torque-free gyrostat with a discrete damper has been studied (Hall 1997). Hall defines in this study stability conditions for values of the platform inertia and the spring stiffness, derived for an axial gyrostat with the discrete damper aligned parallel to the rotor's spin axis. For SHAPE's case, the axial gyrostat is assumed and therefore the solution given by Hall & Rand (1994) will be used for torque-free analysis as the averaged solutions are also provided in contrast to the more general case by Hall (1995).

### 5.3.1 Zero-momentum Spacecraft Dynamics

A seemingly unimportant aspect of spinup dynamics is the motion of the torque-free gyrostat induced by the rotor without any absolute momentum. Although this might seem trivial for spinning spacecraft, it does correspond to the conditions of the spinup motion of a rotor in the 3-axis stabilized spacecraft configuration. This type of spacecraft is also known as the zero-momentum spacecraft and has been studied by Kane (1970) and Chen & Kane (1979). Kane provides the solution to the spinup motion of the axisymmetric spacecraft. The more general case is given in the work of Chen and Kane. They inverse the problem and provide a method to find the orientation of the rotor axis and its magnitude for a required platform rotation.

The rotational motion of the platform with zero-momentum is derived using Equation 3.63 and the fact that $\mathbf{H} = 0$.

For a spacecraft for which the spin axis is aligned to the first principal body axis, $\mathbf{a} = (1, 0, 0)^T$, the following holds

$$\omega_1 = -\frac{I_s}{I_1}\omega_s \tag{5.1}$$

$$\omega_2 = \omega_3 = 0 \tag{5.2}$$

A simple rotation of the rotor therefore induces a rotation opposite to the platform with a factor equivalent to rotor with respect to the total. While the other two body axes do not lead to any changes in rotational velocities. The infinitesimal analysis is given for the zero-momentum gyrostat by Hughes (2004) for which Hughes concludes that no axes are stable and neither directionally.

### 5.3.2 Gyrostat Dynamics

In contrast to a constant angular momentum during the nominal mode, the momentum wheel is spun up in the acquisition mode and the angular momentum of the wheel is gradually increasing over time. This has important implications in the dynamics. One convenient way to represent the dynamics is in terms of angular momenta as applied by Hall & Rand (1994). Substitution of Equation 3.63 into Equation 3.62 gives

$$\frac{\mathrm{d}H_1}{\mathrm{d}t} = \frac{I_2 - I_3}{I_2 I_3} H_2 H_3 \tag{5.3}$$

$$\frac{\mathrm{d}H_2}{\mathrm{d}t} = \left(\frac{I_3 - I_p}{I_3 I_p} H_1 - \frac{H_a}{I_p}\right) H_3 \tag{5.4}$$

$$\frac{\mathrm{d}H_3}{\mathrm{d}t} = \left(\frac{I_p - I_2}{I_2 I_p} H_1 + \frac{H_a}{I_p}\right) H_2 \tag{5.5}$$

$$\frac{\mathrm{d}H_a}{\mathrm{d}t} = g_a \tag{5.6}$$

and in dimensionless units (Guelman 1989)

$$\dot{x}_1 = (i_2 - i_3) x_2 x_3 \tag{5.7}$$

$$\dot{x}_2 = (i_3 x_1 - \mu) x_3 \tag{5.8}$$

$$\dot{x}_3 = -(i_2 x_1 - \mu) x_2 \tag{5.9}$$

$$\dot{\mu} = \epsilon \tag{5.10}$$

using the following substitution

$$x_1 = \frac{H_1}{H}, \qquad x_2 = \frac{H_2}{H}, \qquad x_3 = \frac{H_3}{H}, \qquad \mu = \frac{H_a}{H}, \qquad \hat{t} = \frac{Ht}{I_p}, \qquad \epsilon = \frac{\tau_a I_p}{H^2} \tag{5.11}$$

and

$$i_j = 1 - \frac{I_p}{I_j}, \qquad j = 1, 2, 3 \tag{5.12}$$

### 5.3.3 Equilibrium Points

In the context of differential equations, there are special points which dictates the behavior of the system. These are called equilibrium or critical points. To obtain them, one is should find the roots of Equations 5.7 to 5.9. The issue regarding setting Equation 5.10 equal to zero is that the resulting system will be a trivial solution. This corresponds then to the specific situation when $\epsilon = 0$. Note that this condition is irrelevant for this analysis except for the cases of initial and final conditions. Instead one can adjust the differential equations to a non-autonomous system as given by Hall (1991) by substitution of $\mu(t) = \mu_0 + \epsilon t$.

$$x_2 = 0 \qquad \vee \qquad x_3 = 0 \tag{5.13}$$

$$x_1 = \frac{\mu(t)}{i_3} \qquad \vee \qquad x_3 = 0 \tag{5.14}$$

$$x_1 = \frac{\mu(t)}{i_2} \qquad \vee \qquad x_2 = 0 \tag{5.15}$$

If one assumes that for Equation 5.13, $x_2 = 0$ and for Equation 5.13 $x_3 = 0$, then the point $x_1$ can be determined by using the momentum conservation, $x_1^2 + x_2^2 + x_3^2 = 1$ and thus $x_1 = \pm 1$. The other possibility when $x_2 = 0$ is when $x_1 = \mu(t)/i_3$. Using again the momentum conservation equation, one gets $x_3 = \pm\sqrt{1 - (\mu(t)/i_3)^2}$. In the same fashion, if one assumes $x_3 = 0$ and $x_1 = \mu(t)/i_2$, $x_2 = \pm\sqrt{1 - (\mu(t)/i_2)^2}$. The results with their corresponding names are listed in Table 5.1. Note that there are two points in time when the equilibrium points merges. This occurs at when

Table 5.1: Equilibrium Points

| **Equilibrium Point** | **Coordinates** |
|---|---|
| Prolate, $P_{+/-}$ | (±1,0,0) |
| Intermediate, $I_{+/-}$ | $(\mu(t)/i_3,0,\pm\sqrt{1 - (\mu(t)/i_3)^2})$ |
| Oblate, $O_{+/-}$ | $(\mu(t)/i_2,\pm\sqrt{1 - (\mu(t)/i_2)^2},0)$ |

the intermediate and the oblate equilibrium points reaches the time when $\mu = i_3$ and $\mu = i_2$, respectively. These points are called bifurcation points for which more information can be found in the textbook by Verhulst (2006). Bifurcation analysis of the spinup process are not pursued in this study and one is referred to Sandfry & Hall (2004).

### 5.3.4 Momentum Sphere Method

Akin to the momentum spheres given in Chapter 3 for the spinning spacecraft, the quasi-static momentum sphere method introduced by Barba & Aubrun (1976) utilizes the momentum sphere and the energy ellipsoid to graphically represent the attitude motion of the momentum wheel spinup process. For the analysis, they introduced a composite rigid body $C$ which consists of the platform $\mathcal{P}$ without the axial inertia component of the rotor $\mathcal{R}$. Assuming that the external disturbances are negligible, the momentum conservation holds which yields in the following relation

$$\vec{H}_C + \vec{H}_R = \vec{H} \tag{5.16}$$

with $H$ denoting the total angular momentum and the subscripts $C$ and $R$ the angular momentum of the composite body and rotor, respectively. One could argue that by increasing $\vec{H}_R$, the angular momentum vector of the composite body will disappear. However, due to the fact that the rotor is aligned at a single axis, this is unlikely. The kinetic energy of the system can be derived as

$$E_C = \frac{1}{2}\left[\frac{(H_1 - H_{R,1})^2}{I_1} + \frac{(H_2 - H_{R,2})^2}{I_2} + \frac{(H_3 - H_{R,3})^2}{I_3}\right] \tag{5.17}$$

with $H_i$ the angular momentum components of the total system of $\mathcal{P}$ and $\mathcal{R}$, $H_{R,i}$ components of the wheel $\mathcal{R}$ and $I_i$ the principal axes of the composite system $C$. For a given energy $E_C$, above equation represents an ellipsoid if one considers the inertias unequal, $I_1 \neq I_2 \neq I_3$. In reality, the changing wheel momentum is dynamic and the ellipse is therefore constantly changing. By taking multiple points in time, one can quasi-statically analyze the dynamics through time. With the equation for the conservation of angular momentum

$$H^2 = H_1^2 + H_2^2 + H_3^2 \tag{5.18}$$

one can obtain the possible attitude motion by intersecting this sphere with the energy ellipsoid resulting in either orbits or points. The points represent the roots defined earlier which has mathematically equivalence to the ellipsoid tangentially intersecting the momentum sphere. By increasing the momentum of the rotor, the relative position of the energy ellipsoid shifts with respect to the static momentum sphere. For the analysis done in this study, dimensionless units are used as the underlying dynamics are equivalent and can easily be scaled. The corresponding energy ellipsoid and momentum sphere are then given as

$$e_c = \frac{1}{2}\left((x_1 - \mu)^2 + (1 - i_2)x_2^2 + (1 - i_3)x_3^2\right) \tag{5.19}$$

and

$$x_1^2 + x_2^2 + x_3^2 = 1 \tag{5.20}$$

Note that the rotor axis has been aligned to the first principal inertia axis ($x_1$). The computation of the intersection points between the energy ellipsoid and the momentum sphere have been done numerically using a brute force method. First, the coordinate points of the energy ellipsoid are parsed using Matlab's *ellipsoid* command. These were then fed into the conditions for the angular momentum conservation (Equation 5.20) to obtain the required intersection points. Note that finding exact intersection points is numerically not possible as therefore non-strict inequality statements as given in the form below were implemented to find approximate values.

$$|x_e^2 + y_e^2 + z_e^2| \leq \epsilon_{err} \tag{5.21}$$

with $x_e$, $y_e$ and $z_e$ the coordinate of the ellipsoid and $\epsilon_{err}$ the detection error.

**Results & Discussion**

The results of the momentum sphere method using the inertia parameters of SHAPE as given in Chapter 2 are shown in Figure 5.3. Note again that SHAPE's major, intermediate and minor inertia axes are given on the $x_2$, $x_3$ and $x_1$ axes, respectively. Several values of the momentum sphere are given for the rotor's angular momentum from $\mu = 0$ to $\mu = 1$. No negative values of $\mu$ are shown as these are qualitatively similar symmetrically (Hall & Rand 1994). Increasing the dimensionless angular momentum past 1 has no qualitative use as the behavior will not change as no bifurcation occurs after the point $\mu = i_2$. Besides, above this value, the platform will start rotating in the opposite direction. For nadir pointing Earth-observation missions, a rotation value close to the orbital velocity is favorable for which $\mu = 1$ is an adequate value for qualitative analysis.

One important remark to make is that the energy curves on the momentum sphere are different for each separate subfigure. This is due to that the rotational energy is determined by the motion of $\mathcal{P}$ which changes depending on the value of $\mu$. The energy ranges from 0 to 2 given in dimensionless units for which the first is given for when $\mathcal{P}$ is not rotating. The latter arises on the conditions when the platform spins up to counterbalance the angular momentum of the wheel rotating opposite to the inertial angular momentum vector.

In Figure 5.3a, SHAPE's configuration is shown for which the momentum wheel is not rotating inertially. The configuration shown applies to the situation in which the spacecraft is spinning while the momentum wheel is inertially fixed. There is thus a relative spin between $\mathcal{P}$ and $\mathcal{R}$. In practice, the spacecraft is in a so-called *all-spun* condition. Here, the spacecraft is spinning while the relative angular velocity between the two components are zero. This results that initially $\mu \geq 0$. The $\mu = 0$ condition however closely approximate that situation. For example, an angular momentum of 1 Nms on the minor axis has a dimensionless rotor angular momentum $\mu$ of 0.0284. Observe also that this figure is the same as for a spinning body as given in Figure 3.6.

The orbits surrounding the centers located at the positive and negative $x_2$, and the two unstable equilibrium points move upwards towards the positive $x_1$ axis. The two stable centers which were initially aligned to the $x_2$ axis (depicted as $O_+$ and $O_-$ in Figure 5.3a) merges at $\mu = i_2$. Thus by spinning the spacecraft initially around the major axis, the spacecraft is expected to move towards its spin axis which should be beneficial. In contrast, a transverse spinning body is initially unstable (see Chapter 3) and in practice a spacecraft spinning initially on this axis yields in a motion away from this point. Therefore, describing a motion around these roots ($I_+$ and $I_-$) is ambiguous. Depending on the initial deviation around the transverse axis, a motion around $I_+$ or $I_-$ is rather described as a motion around one of the other axes with a somewhat large angle. The unstable roots $I_+$ and $I_-$ coalesce with the initially stable $P_+$ root. The resulting point at $\mu = i_3$ becomes unstable between $i_3 < \mu < i_2$ which affects the positive minor axis spin. The merger of the roots results that an initial orbit around the $P_+$ sets towards either one of the two centers $O_+$ or $O_-$.

An essential point which cannot be derived from these momentum spheres is the phase which has been emphasized by Barba & Aubrun (1976). While the spacecraft orbits on a particular energy level, the exact motion of the spacecraft cannot be tracked. This can be observed especially in the positive minor axis spin. The motion crosses a so-called *instantaneous separatrix*, a line dividing regions with different behavior, around $\mu = i_3$ (Hall & Rand 1994). The added term "instantaneous" is explained in the next section. The exact location of intersection with the separatrix however differs for different initial conditions yielding in a large range of final orientations.

### 5.3.5 Hall and Rand's Method

The momentum sphere method by Barba & Aubrun (1976) aids as a visualisation tool for rotational motions. A similar method by Hall & Rand (1994) expands this into a two dimensional plane by reducing the number of equations from 4 to 3 using the three integrals of motion; kinetic energy, angular momentum and axial momentum of the rotor. Their

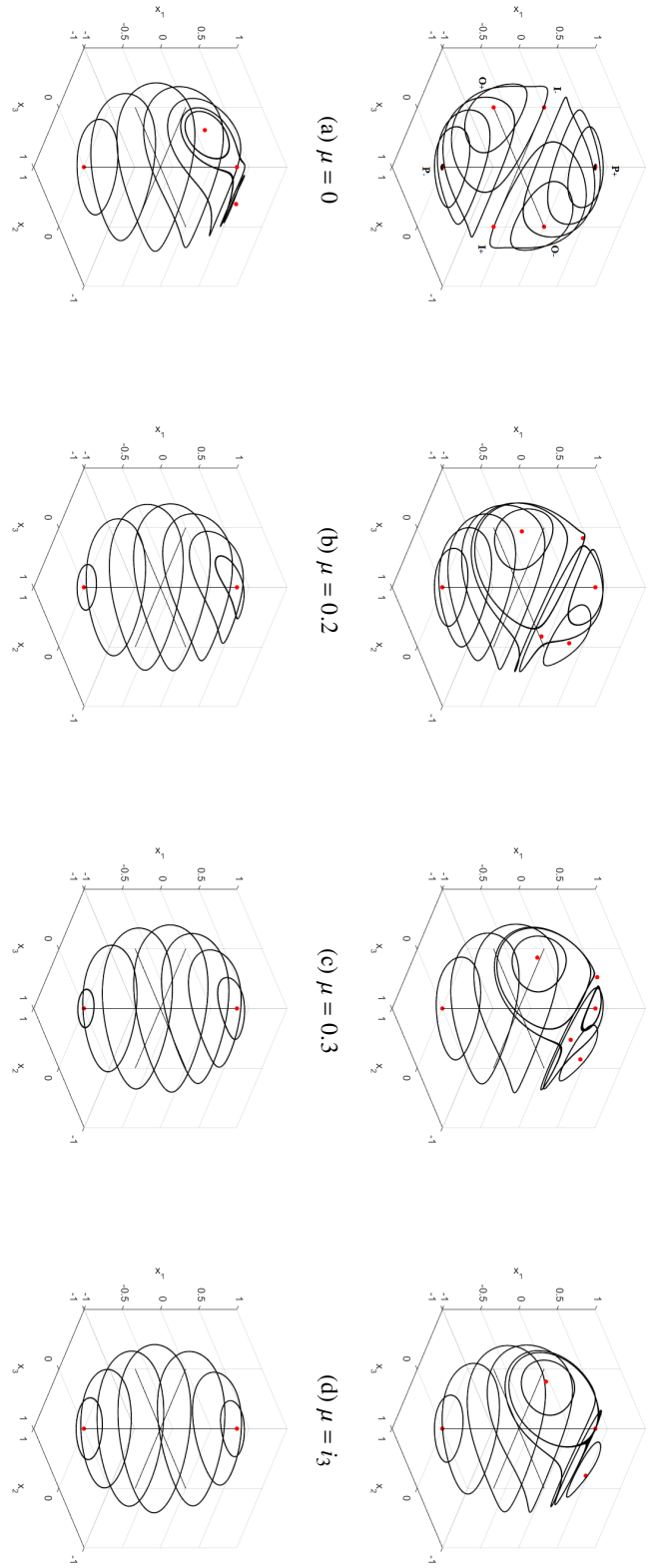

(a) $\mu = 0$ (b) $\mu = 0.2$ (c) $\mu = 0.3$ (d) $\mu = i_3$

(e) $\mu = 0.45$ (f) $\mu = i_2$ (g) $\mu = 0.75$ (h) $\mu = 1$

Figure 5.3: Momentum Sphere Method Applied to SHAPE

method utilizes an adjusted energy form given as

$$y \triangleq -2\mu x_1 - i_2 x_2^2 - i_3 x_3^2 \tag{5.22}$$

which simplifies the equations and has as additional benefit that some of the boundary lines on the $\mu y$-plane are represented as straight lines as seen in Figure 5.5 (Hall 1991). The transverse angular momenta are then given as

$$x_2^2 = \frac{(y_2 - y)}{i_2 - i_3} \tag{5.23}$$

$$x_3^2 = \frac{(y - y_3)}{i_2 - i_3} \tag{5.24}$$

with $y_2$ and $y_3$ defined as

$$y_2 = i_3 x_1^2 - 2\mu x_1 - i_3 \tag{5.25}$$

$$y_3 = i_2 x_1^2 - 2\mu x_1 - i_2 \tag{5.26}$$

reducing the rotational equations of motion to

$$\dot{x}_1 = \pm\sqrt{y_2(x,\mu) - y}\sqrt{y - y_3(x,\mu)} \tag{5.27}$$

$$\dot{y} = -2\epsilon x \tag{5.28}$$

$$\dot{\mu} = \epsilon \tag{5.29}$$

These equations are difficult to integrate numerically as additional bookkeeping is required to track which branch of $\dot{x}_1$ (positive or negative) the integration is on. However, its importance is stated by Hall and Rand that the equations can be divided into a "slow" and "fast" part by assuming that $\epsilon$ is small with $\mu$ regarded as the slow time.

Because SHAPE's dimensionless inertia properties are $i_2 = 0.5704$ and $i_3 = 0.3455$, and therefore $i_2 > i_3$. This property in conjunction with the notion that $x_1$ is always real and positive, limits the possible energy levels as $y_3 \leq y \leq y_2$. The energy levels of the equilibrium points can be derived by substituting the points into Equation 5.22. The equilibrium point $P_+$, (1,0,0), has energy levels of $y_P \triangleq y_2 = y_3 = -2\mu$. Similarly $P_-$, (-1,0,0), has $y_2 = y_3 = 2\mu$. The equilibrium points $O_+$ and $O_-$ have an energy level located at the extremum of the parabola $y_3$;

$$y_O \triangleq -\frac{\mu^2}{i_2} - i_2 \tag{5.30}$$

and similarly for $I_+$ and $I_-$ at $y_2$;

$$y_I \triangleq -\frac{\mu^2}{i_3} - i_3 \tag{5.31}$$

The energy level $y_I$ also corresponds to the separatrices dividing the behavior around $O_+$, $O_-$, $I_+$ and $I_-$. In Figure 5.4, the $xy$-plane is given for four different values applied to SHAPE. The roots $O$ and $I$ account both for their positive and negative counterpart. The dashed lines depict separatrices. These disappear at $\mu = i_2$ when the equilibrium points coalesce also seen in Figure 5.3.

Hall and Rand then suggest the use of the $\mu y$-plane by slicing individual slices of $\mu$ together. Hereby, an important consequence is that "instantaneous" separatrices can be crossed viewed on this $\mu y$-plane, because the momentum wheel torque $\epsilon$ is zero for each individual "frame". They coin the terms *instantaneous separatrix* and *separatrix crossing* for these effects due to adding the slices together. In Figure 5.5, the equilibrium points are projected unto the $\mu y$-plane. Here, the dots represent the points in which the equilibrium points coalesce, located at $\mu = i_3$ and $\mu = i_2$.

The use of this $\mu y$-plane in first sight does not seem to provide a great benefit over the momentum sphere method besides its two-dimensional representation. However, the importance in this graph is the energy $y$. For the spinup process of the momentum wheel and despin process for the platform, one should approach the energy level corresponding the $P_+$ root. Although the final orientation of the spacecraft is not quantified directly, the energy level gives a relatable solution. One should realize that the final orientation of the spacecraft will be at a single energy level within the confines of the gyrostat model, meaning that the spacecraft will be precessing around the angular momentum vector if the energy level does not correspond to a stable equilibrium point. The spacecraft will spin at a certain angle from its inertial angular momentum defined as the nutation angle in Chapter 3.

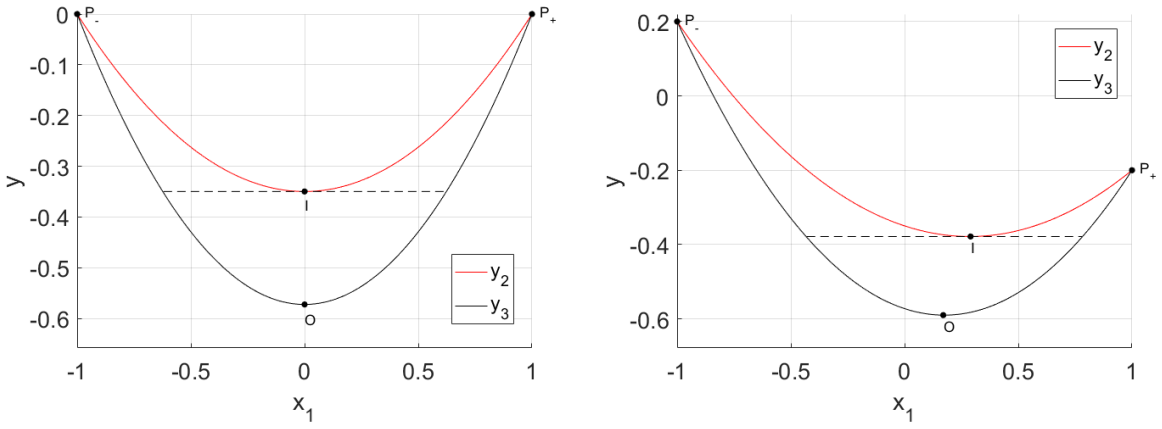


(a) $\mu = 0$




(b) $\mu = 0.1$

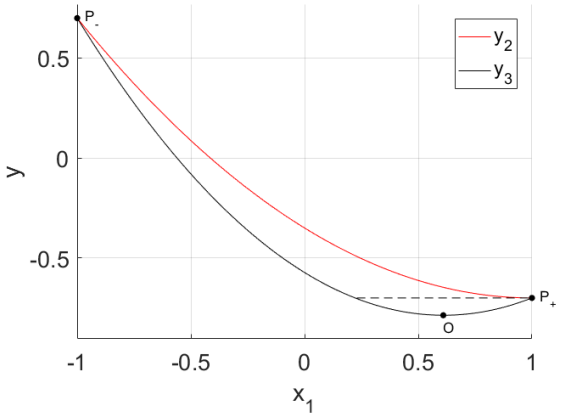


(c) $\mu = i_3$

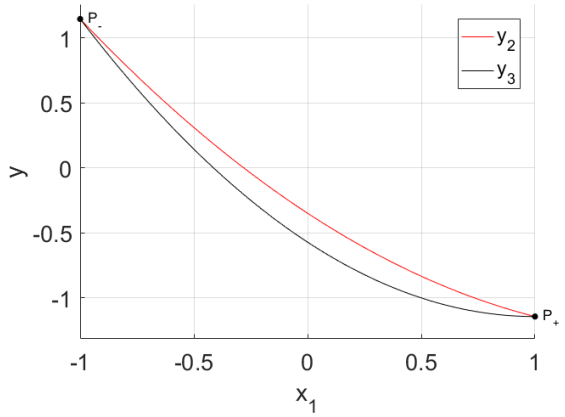


(d) $\mu = i_2$

Figure 5.4: xy-planes Applied to SHAPE's Inertia Properties

An important result given by Hall and Rand is the averaged solution. Averaging is a technique applied to differential equations which uses averaging of fast oscillating periodic terms to cancel these terms resulting in an approximate solution (Verhulst 2006). The averaging technique applied by Hall and Rand uses the cancellation of the faster oscillatory dynamics so that the approximation is given with respect to the slower.

The derivation and the conditions of the solution is complex and dependent on the region the trajectory is on. The regions are differentiated by the behavior of the dynamics and specify several parameters. The PhD thesis by Hall (1991) is recommended for the exact derivation and solutions. The following solution is given for an oblate spacecraft however using the symmetry transformation, $(x_1, x_2, x_3, i_2, i_3) \rightarrow (-x_1, x_3, -x_2, -i_3, -i_2)$, equivalent results for prolate spacecraft can be obtained. Averaging Equations 5.28 and 5.29 over one period, Hall and Rand obtain the following

$$\frac{\mathrm{d}\bar{y}}{\mathrm{d}t} = -2\epsilon\bar{x} \tag{5.32}$$

$$\frac{\mathrm{d}\mu}{\mathrm{d}t} = \epsilon \tag{5.33}$$

with an overbar denoting the averaged solution. The averaged solution for $x_1$ for Region 1 is given as

$$\bar{x} = \frac{\beta}{K}\left[K + \frac{\pi(\alpha^2 - \alpha_1^2)(1 - \Lambda_0(\psi, k))}{2\sqrt{\alpha^2(1-\alpha^2)(\alpha^2 - k^2)}}\right] \tag{5.34}$$

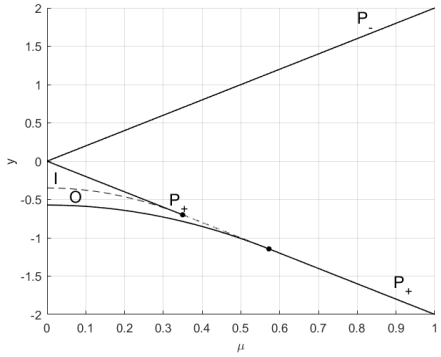


Figure 5.5: Trajectories of the Equilibrium Points on the $\mu y$-plane

with the parameters $\beta$, $\alpha$, $\alpha_1$, $u$ and $k$ dependent on subregions of Region 1 and the function $\Lambda_0(\psi, k)$ defined as

$$\Lambda_0(\psi, k) = \frac{2}{\pi} \left( EF(\psi, k') + KE(\psi, k') - KF(\psi, k') \right) \tag{5.35}$$

Here, $K$ and $E$ denote the complete elliptic integral of the first and second kind, respectively. The variables $F(\psi, k')$ and $E(\psi, k')$ represent the respective incomplete integrals with $k'^2 = 1 - k^2$. For Region 2, $\bar{x}$ is defined as

$$\bar{x} = \frac{\beta}{\alpha K} \left[ \alpha_1 K + \frac{\alpha - \alpha_1}{1 - \alpha^2} \Pi(\hat{\alpha}^2, k) \right] \tag{5.36}$$

with $\Pi(\hat{\alpha}^2, k)$ the complete integral of the third kind and $\hat{\alpha}^2 = \alpha^2/(\alpha^2 - 1)$. The accuracy of this solution has been given to be of $O(\epsilon)$. Hall and Rand state that near the separatrix crossing, this condition is invalid as the elliptic integral $K$ approaches infinity. At these locations, an additional error is induced which affect some of the spinup strategies considerably. The averaged cone angle can be derived similarly to the exact solutions.

$$\bar{\eta} = \cos^{-1}(-\bar{x}) \tag{5.37}$$

The negative sign is added to adjust for the symmetry transformation from oblate to prolate spacecraft.

**Results & Discussion**

Hall and Rand's method is used to analyze the sequential spin type strategies. First, the most basic type of spin is analyzed; the *full-spin* subtype. Here, the spacecraft as a whole is spun up to 1 Nms to acquire the momentum needed to transfer to its wheel. The analysis is then subdivided into either by spinning initially from the major or minor axis. The intermediate axis spin has already been ruled out as explained in Section 5.3.4.

In Figure 5.6, the exact and averaged solutions of using different wheel torques $\epsilon$ have been plotted for an initial energy value of -0.0569 which is equivalent to approximately 1° offset. The results show a similar conclusion to that of Hall (1991). By decreasing the wheel torque, the cone angle $\eta$ increases. The difference between the averaged and exact values are however large. Hall and Rand explain this effect due to the two separatrix crossings this maneuver undertakes, invalidating the averaging approximation at the crossings. This error can be seen both in the $\mu y$- and the $\mu\eta$-plane, varying from approximately 20 to 40 degrees. The energy levels of $\epsilon = 10^{-1}$ and $\epsilon = 5 \cdot 10^{-2}$ are indistinguishable in the "exact" graph. In the averaged plane, the deviations are clearly visible.

One additional consideration is that small variations in initial conditions might result in different final conditions especially for low rotor torque. A probability-theoretic approach for low torque has been provided by Neishtadt & Pivovarov (2000) to determine the chance for which an initial condition in either a region away from the prolate axis or close to it. The situation for which the spacecraft's spin axis turns away from the desired axis has been called an overturn of the spacecraft. This is visible in the exact $\mu\eta$-plane for $\eta = 0.001$ for which a clear overturn can be seen of over 40 degree. In short, a higher wheel torque is preferred for the minor axis spinup.

In Figure 5.7, the major axis spinup is shown on the $\mu y$- and the $\mu\eta$- planes with an initial offset of 1 degree and an energy level of -0.5722. In contrast to the minor axis spin, the major axis spin has inverse properties. The nutation angle decreases for decreasing momentum wheel torque. For the major axis spinup, a small torque is thus

preferred. With regard to the energy, it approaches the positive prolate equilibrium point $P^+$ as the torque decreases. The differences between the exact and averaged solutions also has similar properties to that of the minor axis spinup. SHAPE has a dimensionless torque of $10^{-5}$ for which the result are shown in Figure 5.8 initialized at a 1 degree offset. It shows clearly that the major axis spinup provides a better final result.

Using these results, it is possible to look at the effects of the *partial* subtypes. These types can either start from the minor or major axis spin. The follow-up spins sequential to it are minor spins as the major axis spin develops in a position around the minor axis. After a minor axis spin, a follow-up is only possible around the major axis spin by correcting the angular momentum with external means. Momentum exchange is not possible as the only internal type (the momentum wheel) is aligned to the pitch axis and not to any other axes.

It was already explained that prolate spinup are inefficient due to the overturn of the spacecraft for small wheel torques. Applying the spins in steps improves upon this types of spins. The dimensionless torque given in Equation 5.11 shows that the dimensionless torque is lower in value if the angular momentum is low and thus result in a smaller nutation angle after completing a spinup step. For example at $H = 0.01$ Nms, the dimensionless torque is equivalent to 0.1 yielding in a nutation angle smaller than 2 degrees. There are however two issues regarding partial spinup types.

First, the system still has to achieve an angular momentum of 1 Nms meaning that a small dimensionless torque is inevitable. This results that the chances of an overturn increases making prolate spinups unattractive. Besides, dividing the spinup in steps requires that the dynamics of this process will re-occur for which an increase in nutation angle is usually expected. Adjusting the nutation angle after each partial spin through damping further delays the spinup time. At large angles, damping might even become unfeasible as explained in the previous chapter. The effects of external disturbances cannot be visualized using the two mentioned methods and simulations have been performed for the major and minor axis spinup given in Appendix G.

The use of averaging of Hall and Rand's method has some negative consequences in terms of computational effort. First, it requires conditions to find in which region the current trajectory is on. Furthermore, the more complex Equations 5.34 and 5.36 contain the computation of complete and incomplete elliptical integrals. Although the number of equations to be solved has reduced, the added complexity to the system has increased the computational time for analysis. In addition, this is amplified due to the small wheel torque $\epsilon$ of SHAPE, resulting in evaluation of a large quantity of points. As a result, the computation time increases by a factor of 10 with respect to the "standard" numerical integration of Euler's rotational equations of motion.

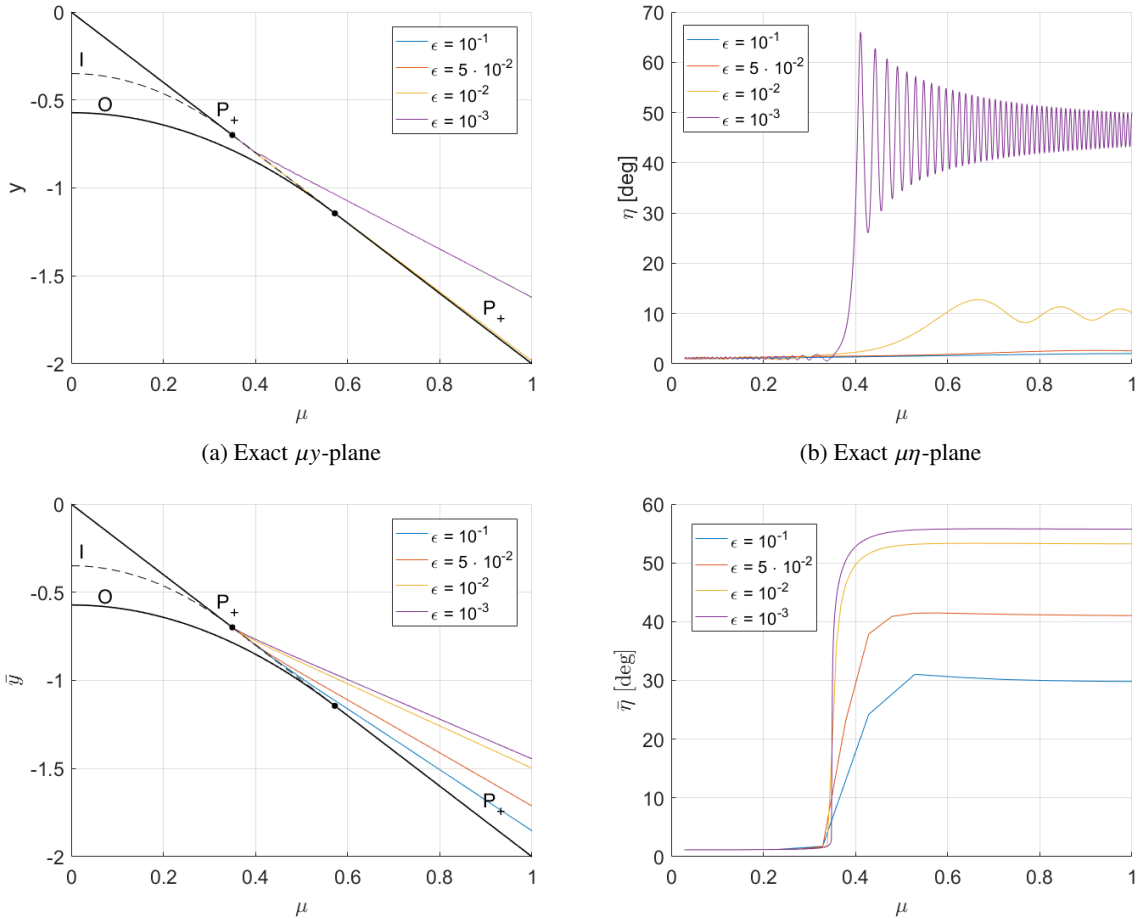


(a) Exact $\mu y$-plane

(b) Exact $\mu\eta$-plane

(c) Averaged $\mu y$-plane

(d) Averaged $\mu\eta$-plane

Figure 5.6: Exact and Averaged Solutions for the Minor Axis Spinup with Initial Energy of -0.0569

## 5.4 Trap States

An important aspect which has not been considered are trap states. Under specific conditions such as rotor asymmetry and mass imbalance, the gyrostat can enter certain states which are not possible to escape from under regular circumstances. These trap states also called capture phenomena are distinguished in two types; minimum energy trap and nutation resonance.

### 5.4.1 Minimum Energy Trap

Minimum energy trap has been first discovered by Scher & Farrenkopf (1974) and is characterized by the minimum energy state of a spinning spacecraft located at the principal axis of maximum inertia. After the rotor of the dual-spin spacecraft is spun-up and deactivated, viscous friction results eventually in a complete standstill of the rotor with respect to the platform. From an energy perspective, it has arrived to its minimum state as the rotational energy is dissipated. This trap state where the dual-spin spacecraft is spinning as a single body at its maximum inertia also known as a flat spin can be recovered. Scher and Farrenkopf have shown that torquing the wheel at the natural frequency can recover from this flat-spin. Hall (1998) provides a constant torquing method which can overcome this trap state even at the presence of any level of damping.

Note that this trap is applicable to SHAPE if the magnetic bearings are not activated due to a bearing failure or when the rotation rate does not reach its minimum requirement. If failure would occur, friction of the ball bearings may

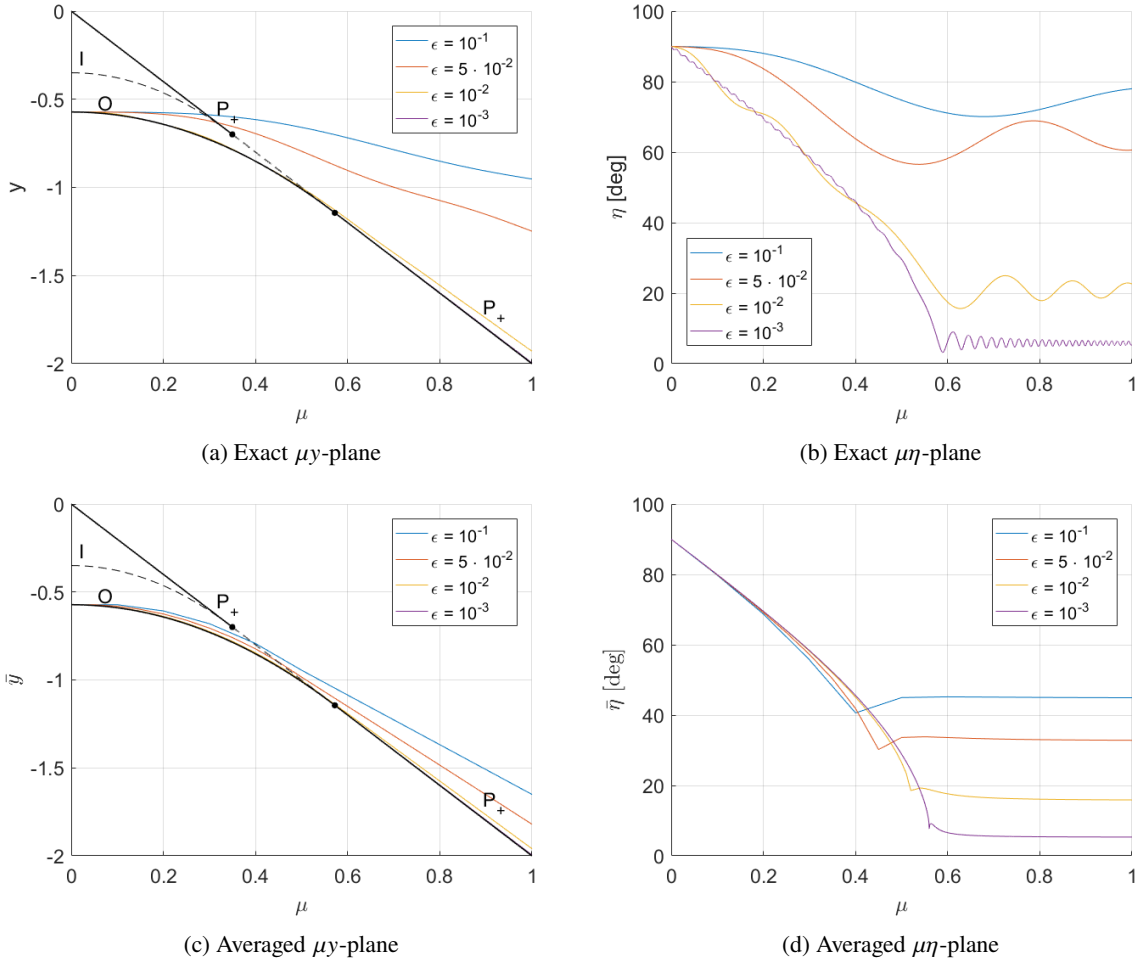


(a) Exact $\mu y$-plane

(b) Exact $\mu\eta$-plane

(c) Averaged $\mu y$-plane

(d) Averaged $\mu\eta$-plane

Figure 5.7: Exact and Averaged Solutions for the Major Axis Spinup with Initial Energy of -0.5722

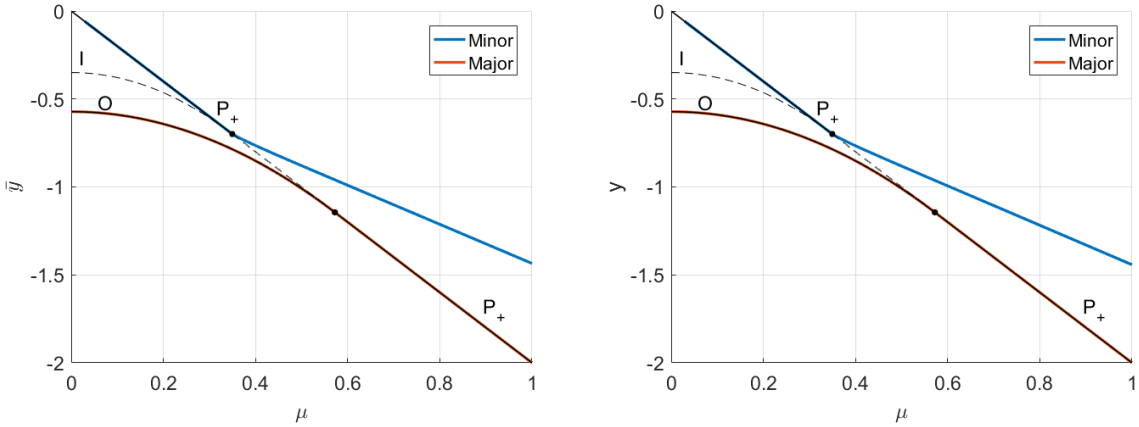


(a) Averaged $\mu y$-plane




(b) Exact $\mu\eta$-plane

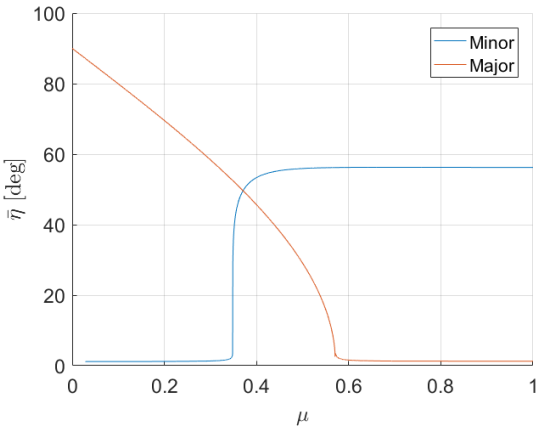


(c) Averaged $\mu\eta$-plane

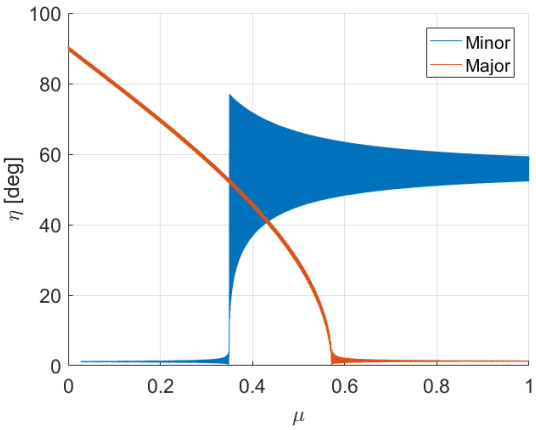


(d) Exact $\mu\eta$-plane

Figure 5.8: Averaged and Exact Solutions for the Minor and Major Axis Spinup with $\epsilon = 10^{-5}$

cause the momentum wheel to reduce to this energy trap. A secondary cause to the slowing down of the momentum wheel can be the aerodynamic drag or eddy current torques.

### 5.4.2 Nutation Resonance

Scher and Farrenkopf have also observed a different trap state which they called the resonance trap or nutation resonance. In contrast to the previous trap state, this state can occur during the spinup. The dual-spin spacecraft model analyzed by Scher and Farrenkopf had rotor asymmetry and its platform was unbalanced. During the spinup process, when the rotation rate is near a multiple of the nutation frequency, heavy oscillations occur with an increase in the nutation angle if the despin motor is not able to provide sufficient torque. Further increasing at an insufficient rate can cause to add more energy to the nutational motion. Scher and Farrenkopf concluded that this is eliminated as one of the two conditions (asymmetry or imbalance) is excluded or by increasing the motor torque so that the system can rapidly traverse this trap state. A third solution is given by periodically torquing at a lower frequency.

A similar trap state is found by Kinsey et al. (1992) in which the dual-spin spacecraft has only either the platform or the rotor dynamic imbalance which they named it Precession Phase Lock (PPL). Here, the trap state occurs when the rotor inertial spin rate is close to the precession rate of the spacecraft. Instead of periodic torquing, Kinsey et al. provide a feedback control method to escape from the resonance capture. Tsui & Hall (1995) performed analysis to determine the probability of capture and developed a tool to illustrate initial conditions resulting in capture.

To illustrate the effect of an unbalanced rotor more in detail, Tsui (1994) used the momentum sphere method and the method of Hall & Rand (1994). Here, the first method is used to analyze its effect. Tsui's gyrostat model assumed a special reference frame which Tsui termed a "pseudo-principal" reference frame. Hereby, the mathematical principal axis frame is adjusted to incorporate the inertia tensor of the rotor as this is not diagonal due to its imbalance while excluding the axial component. The resulting new inertia tensor is then defined as

$$\mathbf{J} \equiv \mathbf{Q}(\mathbf{I} - I_s \mathbf{a}\mathbf{a}^T)\mathbf{Q}^T \tag{5.38}$$

This approach can also differently obtained by applying Equation 3.47. The matrix $\mathbf{I} - I_s\mathbf{a}\mathbf{a}^T$ has then its diagonal entries $J_1$, $J_2$, and $J_3$ equivalent to the eigenvalues. The eigenvectors then results in this pseudo-principal reference frame with respect to the "real" principal reference frame. It should be noted that the eigenvectors' direction can be ambiguous (+ or -) and has to be adjusted corresponding to the rotation. It should also be emphasized that the concatenated eigenvectors (in column notation) as a 3 by 3 matrix is equivalent to the transpose of the rotation matrix.

The degree of rotor's imbalance is expressed by Tsui as

$$\mathbf{a} = \begin{bmatrix} a_1 \\ a_2 \\ a_3 \end{bmatrix} \tag{5.39}$$

given in the "real" principal reference frame. As the axis is farther away from the intended spin axis, the mass imbalance increases. For this model, the platform angular momentum has to be adjusted by multiplying with the rotation matrix;

$$\hat{\mathbf{H}} = \mathbf{Q}\mathbf{H} \qquad \boldsymbol{\alpha} = \mathbf{Q}\mathbf{a} \tag{5.40}$$

As no external torques are present, the angular momentum is still conserved. The energy ellipsoid is given as

$$T_0 = \frac{(H_1 - H_a\alpha_1)^2}{2J_1} + \frac{(H_2 - H_a\alpha_2)^2}{2J_2} + \frac{(H_1 - H_a\alpha_3)^2}{2J_3} \tag{5.41}$$

hereby the notation of $\hat{\mathbf{H}}$ has been dropped for $H$ in this section and $H_a$ represents the inertial angular momentum of the rotor. The numerical method given in Section 5.3.4 has been used to produce Figure 5.10 and Figure 5.11 for a spin axis angle relative to principal axis of the platform at 1 and 30 degrees, respectively. The 1 degree offset shows no explicit difference between the result given in Section 5.3.4. The difference is more evident in Figure 5.9. In Figure 5.9a, the inner right polhode has the same energy level as the left and as a result the system can be captured in the larger polhode resulting in larger nutational motion in contrast to the one at the left. It should be noted that the increased line thickness near the inner side of these polhodes are due to computational inaccuracies of a too large detection error. The difference in imbalance is more visible in the 30 degree offset. Figure 5.9b and Figure 5.11 display the effect

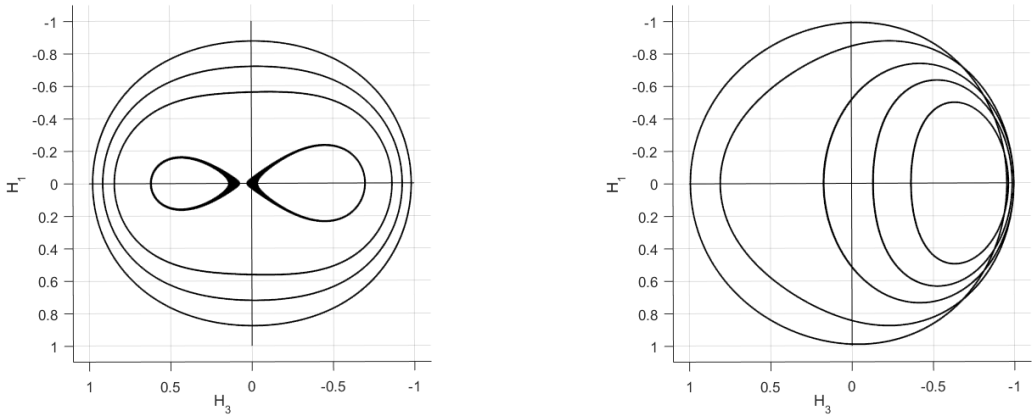


(a) $\alpha_1 = 0.99985$ and $\alpha_3 = -0.01707$

(b) $\alpha_1 = 0.87076$ and $\alpha_3 = -0.49171$

Figure 5.9: Top View of the Momentum Sphere with $H_a = 0.5$ Nms

more clearly. At $H_a = 0.3$ Nms, the system has already a clear distinction between the area of capture and escape. Minimization of the rotor imbalance therefore is an important engineering objective.

Imbalance and asymmetry of the rotor thus have important consequences in the design of the spinup process. For the remainder of the study these conditions have not been taken into account, albeit this conditions can yield in failure. Some solutions have been suggested in the form of a high torque motor and feedback control or by determining initial conditions for which the system is not captured (phase and energy level) as shown by Tsui and Hall.

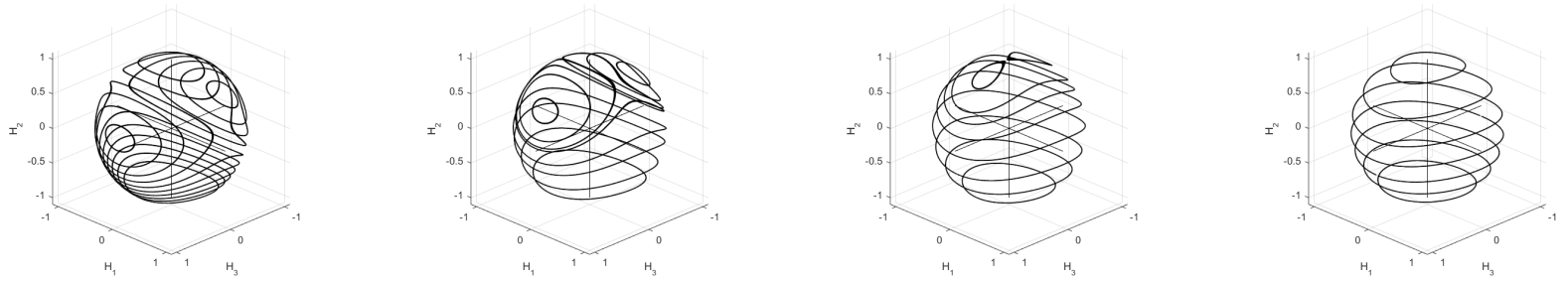


(a) $H_a = 0.1$ Nms (b) $H_a = 0.3$ Nms (c) $H_a = 0.5$ Nms (d) $H_a = 0.9$ Nms

Figure 5.10: Momentum Sphere Method for Unbalanced Rotor with $\alpha_1 = 0.99985$ and $\alpha_3 = -0.01707$

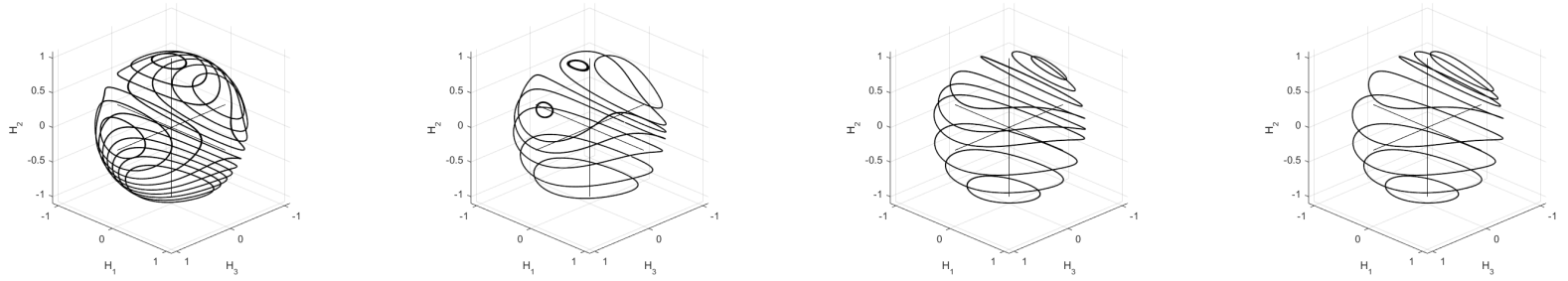


(a) $H_a = 0.1$ Nms (b) $H_a = 0.3$ Nms (c) $H_a = 0.5$ Nms (d) $H_a = 0.9$ Nms

Figure 5.11: Momentum Sphere Method for Unbalanced Rotor with $\alpha_1 = 0.87076$ and $\alpha_3 = -0.49171$

## 5.5 Spinup with Passive Nutation Damping

In Section 4.6, the passive nutation damper had been designed for the nominal mode. To see whether this has positive influence on the spinup procedure of the momentum wheel, an analysis is performed using the equations given in the previous chapter. For convenience the equations are restated below

$$\dot{\mathbf{H}} = -\boldsymbol{\omega}^{\times}\mathbf{H} - \mathbf{v}^{\times}\mathbf{p} + \boldsymbol{\tau} \tag{5.42}$$

$$\dot{p}_n = m_d\boldsymbol{\omega}^T\mathbf{n}^{\times}\left(\mathbf{v} - \mathbf{r}_d^{\times}\boldsymbol{\omega}\right) - c_d\dot{\xi} - k_d\xi \tag{5.43}$$

$$\dot{H}_a = g_a \tag{5.44}$$

and the momenta as

$$\mathbf{p} = m\mathbf{v} - \mathbf{c}^{\times}\boldsymbol{\omega} + m_d\dot{\xi}\boldsymbol{n} \tag{5.45}$$

$$\mathbf{H} = \mathbf{c}^{\times}\mathbf{v} + \mathbf{J}\boldsymbol{\omega} + m_d\dot{\xi}\mathbf{b}^{\times}\mathbf{n} + \mathbf{H}_s \tag{5.46}$$

$$p_n = m_d\left(\mathbf{n}^T\mathbf{v} - \mathbf{n}^T\mathbf{b}^{\times}\boldsymbol{\omega} + \dot{\xi}\right) \tag{5.47}$$

$$H_a = I_a\mathbf{a}^T\boldsymbol{\omega} + H_s \tag{5.48}$$

These equations can be reduced similarly by applying the same assumption in Section 4.6 as done in Appendix B. Due to the spinup motion of the momentum wheel, the system has an additional equation (Equation 5.44).

Spinup dynamics with dampers have been studied by Sandfry & Hall (2004) for axisymmetric and near-axisymmetric dual-spin spacecraft for which the equilibria of the axisymmetric spacecraft were found to be on the principal planes. They found that a slight offset in the transverse inertia causes additional equilibrium branches to arise. Additionally, Sandfry and Hall concluded that nearly axisymmetric spacecraft with a tuned damper have branches placed primarily around the principal planes that are continuous. The addition of an undertuned damper produced high oscillatory behavior and jump phenomena of the equilibria points were observed. These conclusions are however only valid for near-axisymmetric dual-spin spacecraft. SHAPE is asymmetric and the branches of equilibria including a damper have yet to be analyzed.

From the results of the momentum sphere diagrams in Section 5.3.4, it can be predicted that energy dissipation would have a positive influence on the major axis spinup maneuver for the asymmetric gyrostat. As the energy of the system is getting reduced while the angular momentum is conserved, the polhodes will move towards the direction of the equilibrium point associated with the lowest energy $O_{+/-}$. The dynamics of the spinup procedure ensues that this equilibrium conjoins to that of the prolate axis, asymptotically reducing the nutation angle.

In contrast, the energy dissipation during the prolate spinup might destabilize the process. Before the merger between the prolate and the oblate equilibrium points, the system has its lowest energy throughout the spinup procedure at its oblate equilibrium point. By dissipating energy, the system is expected to attempt to diverge to the $O_{+/-}$ equilibrium point. Afterwards, the system should recover as the oblate equilibrium points merge with the prolate point. A locking mechanism for the damper can prevent this initial destabilizing effect.

**Result & Discussion**

To verify if damping is indeed effective, numerical analyses are conducted. For analysis, the nominal mode damper parameters are used as given in Section 4.7.4. Before analyzing the system including damping, the exact results are given for comparison which have been computed using the Equations 5.3 to 5.6. The results of the minor and major axis spinups are shown in Figure 5.12 with a nutation angle of 0.1 degree. Figure 5.12d and Figure 5.12b are the projections of the angular momenta through time on a single momentum sphere using the method by Barba & Aubrun (1976) of Section 5.3.4.

First, the external torque-free case is studied without any restriction on the length of the damper displacement. In Figure 5.13, the results of the simulation for the minor axis spinup is shown with an initial nutation angle of 0.1° with $t_{end}$ depicting the end of the spinup. After this point, the system stops the spinup process and performs a nominal spin. As expected due to energy dissipation, the system degenerates to an oblate spinup in less than 2 minutes as shown in Figure 5.13b. To dissipate this energy in this short time, a length of approximately 3 meters is required which is unrealistic as SHAPE has a maximum length of 30 cm. The procedure is also projected onto a single momentum sphere in Figure 5.13c and Figure 5.13d. In the first, the initial part is shown for which due to energy dissipation the

system degrades from a minor to major axis spin. From the position (1,0,0), the system traverse to an orbit around the negative $H_2$ axis. Afterwards, as seen in Figure 5.13d the system exhibits the typical major axis spinup behavior as given in Figure 5.12 with $H_2$ starting negative instead of positive.

Figure 5.14 shows the major axis spinup including passive damping without damper restriction. The maximum damper displacement surpasses 20 cm which although still possible to fit into the spacecraft, it is relatively very long compared to the approximately 3 cm required for the nominal mode. On the momentum sphere a clear straight arc is shown from the positive $H_2$ axis to the positive $H_1$ axis. In Figure 5.14a, small oscillations can be observed around the 0.57 orbit mark. These are likely excited due to the merger of the equilibrium points. The transverse momenta are damped to marginal values near the end of the spinup process. Comparing to the case without damping, the final transverse momenta are damped to even smaller values from 0.5 to 0.02 degree.

More realistic results are plotted in Figure 5.15 and 5.17 where the damper has been restricted to a maximum value $|\xi_{\max}|$ of 2 cm. At these locations, boundary constraints have been applied. These consist of restricting any movement which promotes damper displacement past $|\xi_{\max}|$ or $\dot{\xi} = 0$. Furthermore, the time derivative of the linear momentum of the damper in the direction of $\vec{n}$ is set to zero for the same condition. This is done as the normal force to the end caps of the damper limits any further increase in linear momentum. The linear momentum of the damper mass however does not require to be zero as it might be induced due to the rotation of the spacecraft. In reality fluid and other dynamics influence the damper performance differently at the end points but have been here dismissed for simplification.

The results of the minor axis spinup are given up until around the first 2000 seconds in Figure 5.15 which corresponds to the moment of the first equilibrium point merger. In the angular momenta graph, a clear destabilizing effect is observed. In contrast to Figure 5.12a, the transverse angular momenta oscillates at a higher value. In the momentum sphere, the first 2000 seconds correspond to the trajectory from near point (0,0) to the red dot. The system then overturns yielding in a large almost-circular trajectory around the major axis equilibrium point. Note that the destabilizing effect stalls within the first 40 seconds as the maximum displacement has been reached locking the system from dissipating more energy. The simulation has not been performed past 2000 seconds as the precision required exceed to values of -12 in orders of magnitude, resulting in increased computational effort due to the very stiff rotational dynamics which causes a singularity to occur in the numerical integration. In Figure 5.16, the same simulation is performed using tolerances of order -6. The difference is clearly visible, as shown, the direction of the trajectory has changed from a down- to an upward motion.

The major axis spin as depicted in Figure 5.17 does not show nearly any difference. The system damps the transverse momenta to a similar value. One remarkable feature however is that the damper is locked during the initial period. This might be explained due to the high rotation rate the system undergoes for which the energy dissipation cannot chase the shift in the minimum energy equilibrium.

To prevent destabilization for the minor axis spinup, a locking mechanism for the damper can be implemented. After the first equilibrium conjoins, an energy dissipation device should have a stabilizing effect. The results are given in Figure 5.18. It is clear that for the minor axis spinup, a locking mechanism is preferred to suppress the negative effect of the passive damping. Although it is not necessary, the nutation angle reduces by approximately half a degree with respect to the case without locking.

Summed up, the passive damping to the spinup process deceases the final nutation angle. The relative effect to the minor axis spinup is found to be greater than that of the major axis. The absolute angle however is still an order of magnitude smaller and therefore the major axis damping type is preferred. The nutation angles are listed in Table 5.2.

Table 5.2: Final Nutation Angle After Spinup

| **Spin Type** | **Damping (Y/N)** | **Locking (Y/N)** | **Max. Nutation Angle [deg]** |
|---|---|---|---|
| Minor Axis | N | N | 59 |
| Minor Axis | Y | N | 5 |
| Minor Axis | Y | Y | 4.5 |
| Major Axis | N | N | 0.6 |
| Major Axis | Y | N | 0.005 |

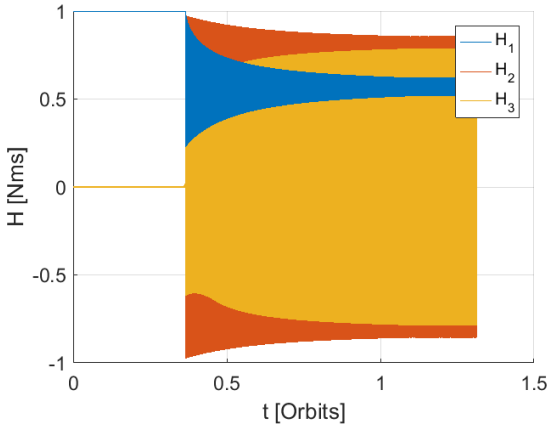


(a) Minor - Angular Momenta

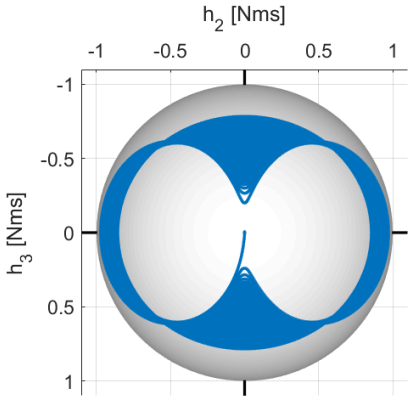


(b) Minor - Momentum Sphere (Top View)

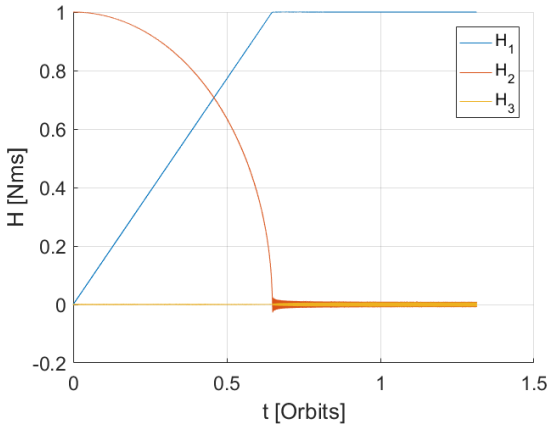


(c) Major - Angular Momenta

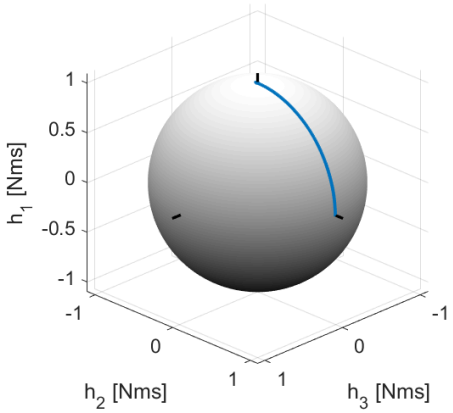


(d) Major - Momentum Sphere

Figure 5.12: Minor and Major Axis Spin without Passive Damping

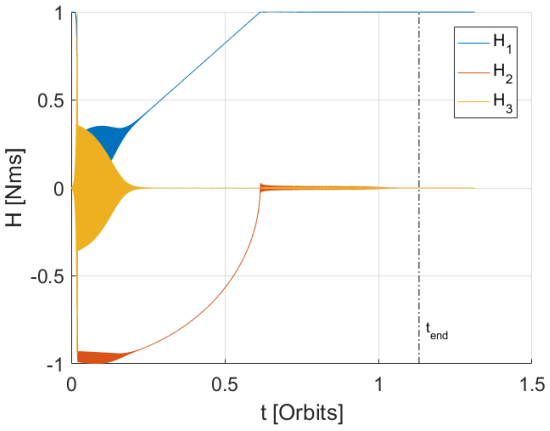


(a) Angular Momenta

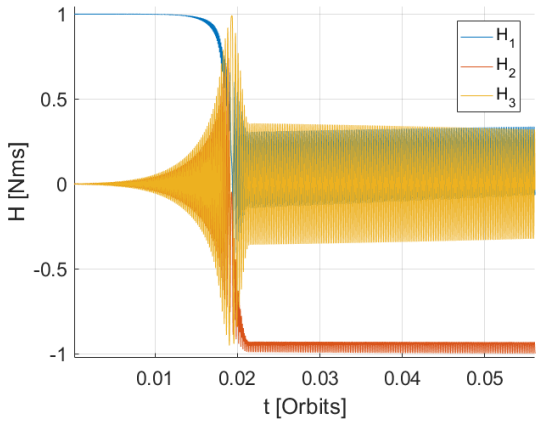


(b) Angular Momenta from 0 to 0.055 Orbits

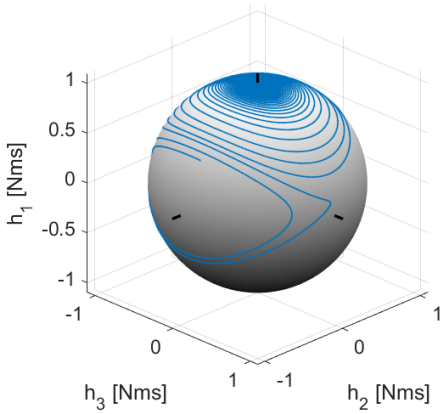


(c) Momentum Sphere at $t$ <= 0.02 Orbits

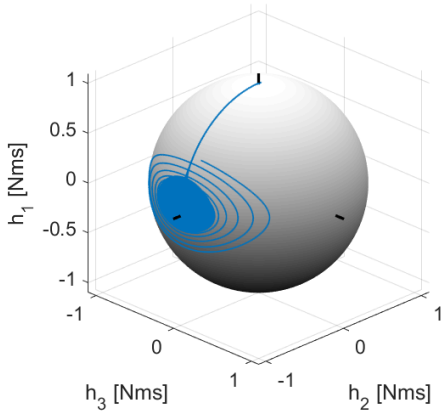


(d) Momentum Sphere at $t$ > 0.02 Orbits

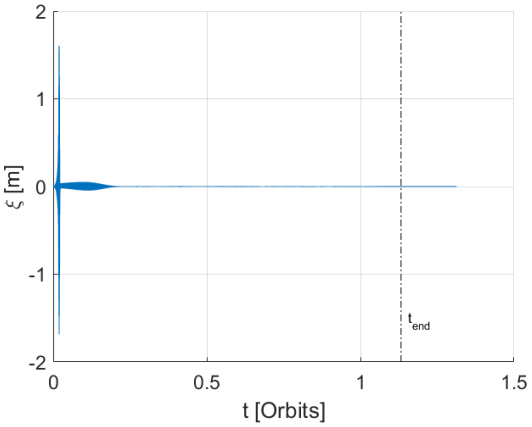


(e) Damper Displacement

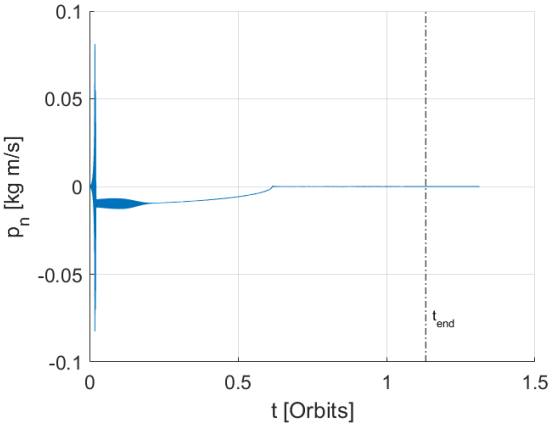


(f) Damper Linear Momentum

Figure 5.13: Minor Axis Spin with Passive Damping without Damper Displacement Restriction

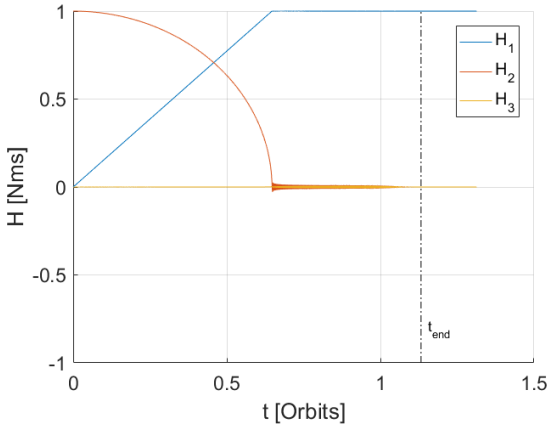


(a) Angular Momenta

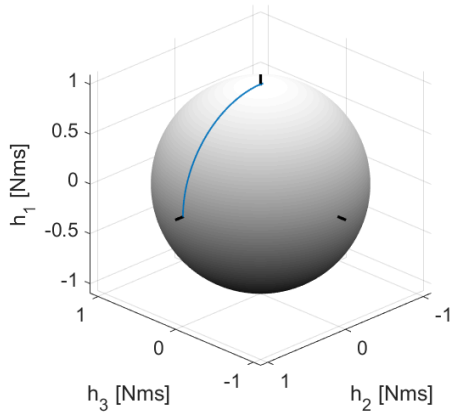


(b) Momentum Sphere

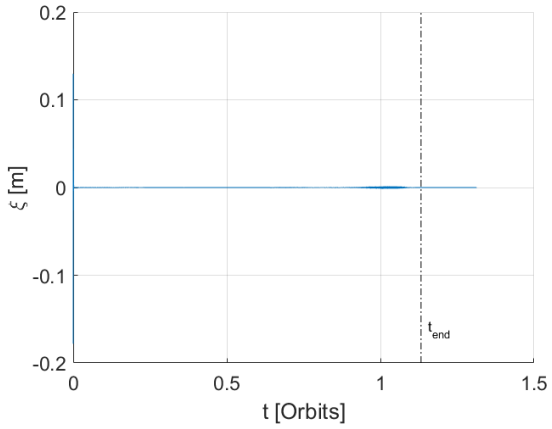


(c) Damper Displacement

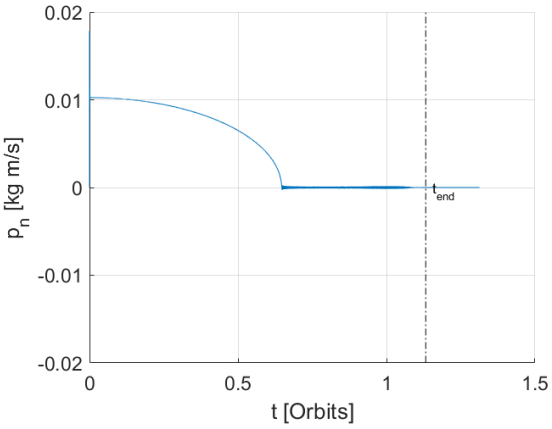


(d) Damper Linear Momentum

Figure 5.14: Major Axis Spin with Passive Damping without Damper Displacement Restriction

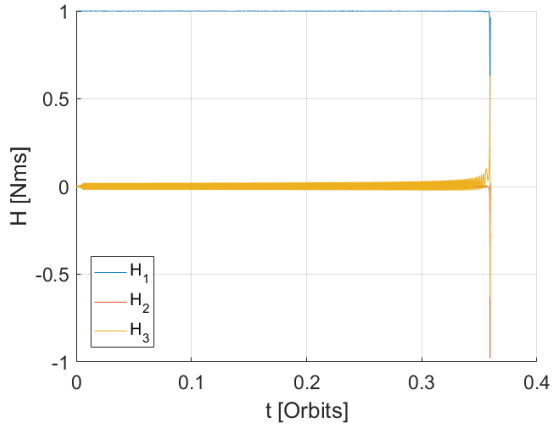


(a) Angular Momenta

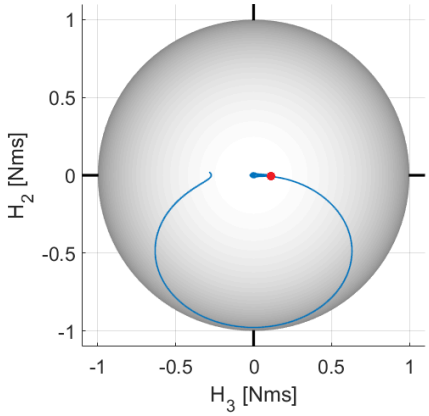


(b) Momentum Sphere (Top View)

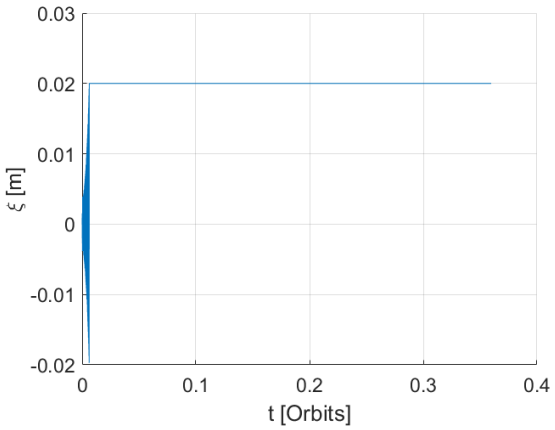


(c) Damper Displacement

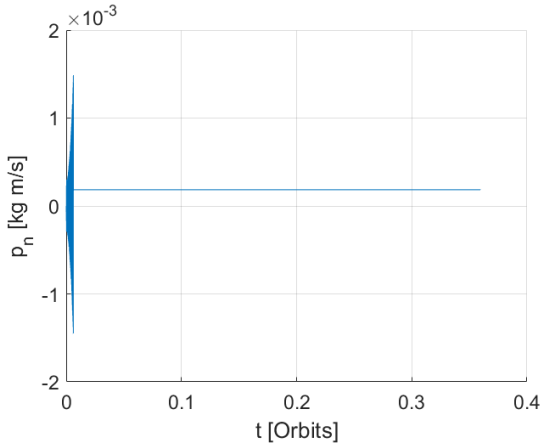


(d) Damper Linear Momentum

Figure 5.15: Minor Axis Spin with Passive Damping with Damper Displacement Restriction

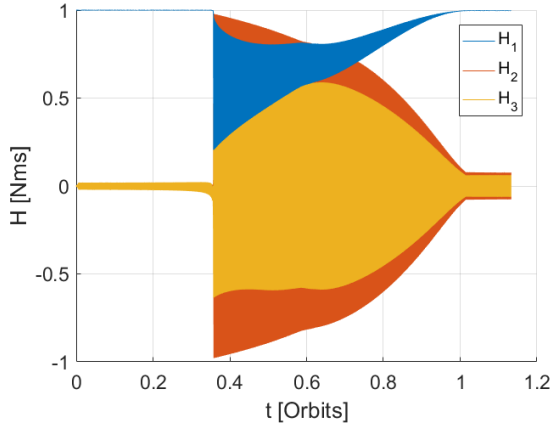


(a) Angular Momenta

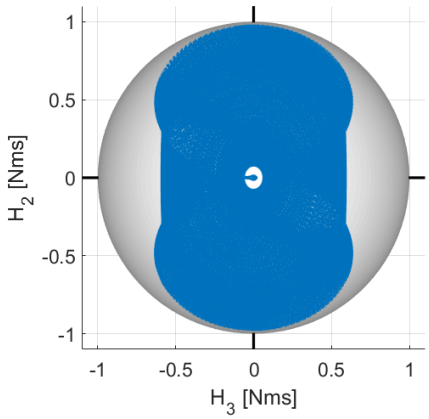


(b) Momentum Sphere (Top View)

Figure 5.16: Minor Axis Spin with Passive Damping with Damper Displacement Restriction using Low Tolerances

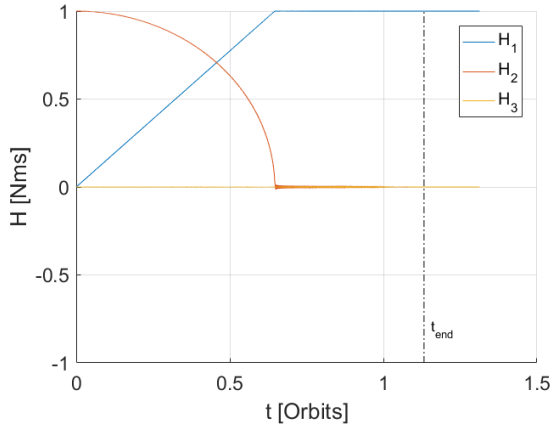


(a) Angular Momenta

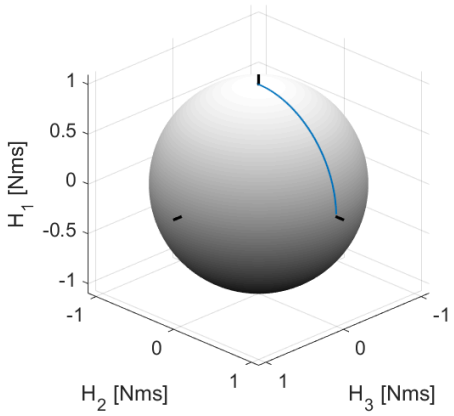


(b) Momentum Sphere

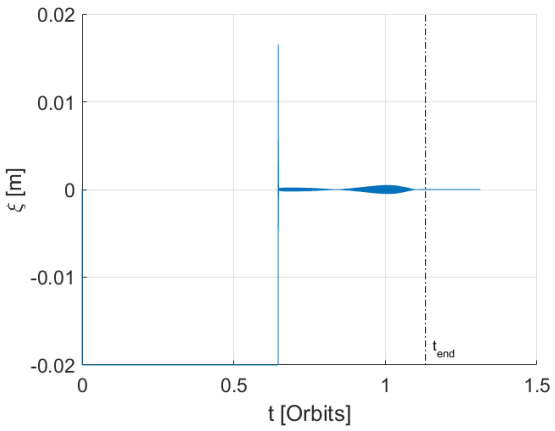


(c) Damper Displacement

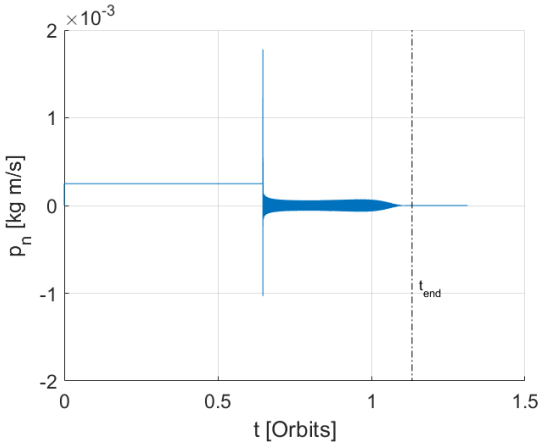


(d) Damper Linear Momentum

Figure 5.17: Major Axis Spin with Passive Damping with Damper Displacement Restriction

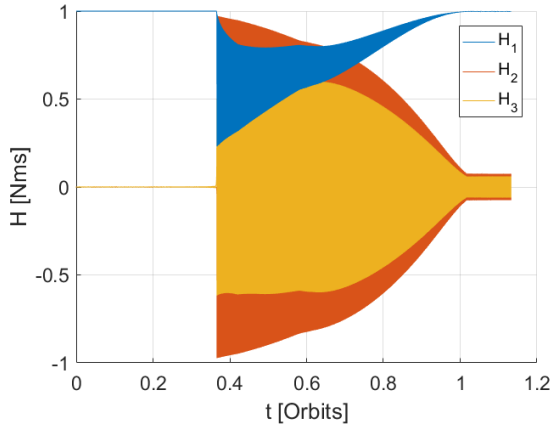


(a) Angular Momenta

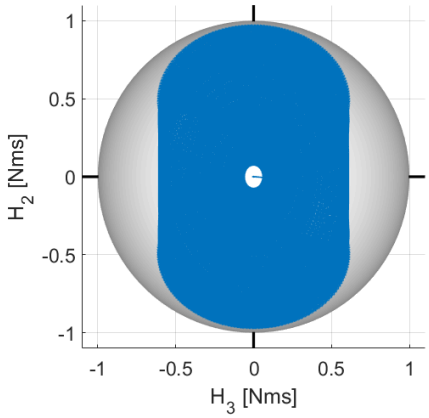


(b) Momentum Sphere

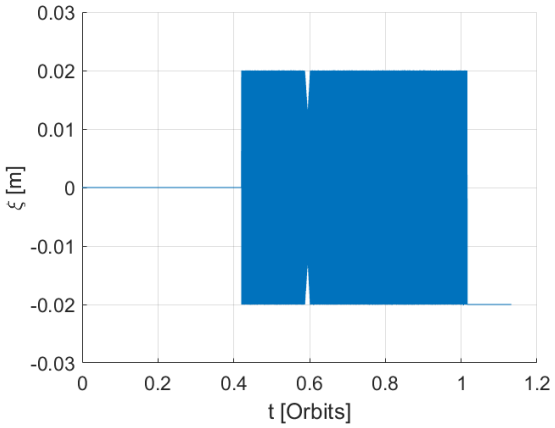


(c) Damper Displacement

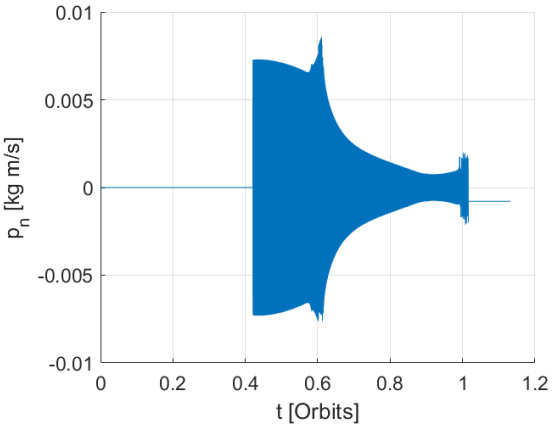


(d) Damper Linear Momentum

Figure 5.18: Major Axis Spin with Passive Damping with Damper Displacement Restriction and Locking

## 5.6 Controlled Spinup

Instead of a simple momentum wheel spinup after the all-spun configuration, an active control system might provide a better solution for the spinup procedure. In this section, the open loop control is first analyzed. Afterwards this control is improved upon adding active feedback elements. The torque-free assumption in the previous section is thus dropped and for this initial analysis perfect sensory feedback and actuator control are assumed. Here, the rotational dynamics are stated including the control torque $\mathbf{u}$;

$$\dot{\mathbf{H}} = -\boldsymbol{\omega}^{\times}\mathbf{H} + \mathbf{u} + \boldsymbol{\tau} \tag{5.49}$$

$$\dot{\mathbf{H}}_a = g_a \tag{5.50}$$

with

$$\mathbf{H} = \mathbf{I}\boldsymbol{\omega} + H_s\mathbf{a} \tag{5.51}$$

$$H_a = I_s(\mathbf{a}^T\boldsymbol{\omega} + \omega_s) \tag{5.52}$$

### 5.6.1 Open Loop

Open loop control or non-feedback control is a form of control in which the output is not fed back to the system to compare it with the desired condition. One could argue that the previously mentioned momentum wheel spinup is a form of open loop control as the wheel is spun without any sensory feedback. However as the system can only provide a constant torque for the momentum wheel, the open loop control is defined based on the system with actuators excluding the momentum wheel.

Analysis of open loop types for the acquisition mode are done naively by aligning the actuator to one of the principal axes of the spacecraft with a control torque equal to the spinup torque $g_a$. This is based on the zero-momentum dynamics (Section 5.3.1). By applying an opposing torque to the rotation of the platform equal to that of the momentum wheel, the platform is expected to be steady, assuming no external disturbance torques. For the remainder of this thesis, it will be termed as a *steady spinup maneuver*. The control torque is thus simply given as

$$\mathbf{u} = \begin{bmatrix} g_a \\ 0 \\ 0 \end{bmatrix} \tag{5.53}$$

**Results & Discussion**

The simulation results for the torque-free dynamics is given in Figure 5.19 under ideal initial conditions with $\mathbf{H}_0 = [0, 0, 0]^T$ Nms and $\boldsymbol{\theta}_0 = [0, 0, 0]^T$ degree. Note that these results are trivial as in reality mismatch of torque, existence of external disturbances and angular offset are present. The results however does show that the platform is steady making deployment of solar panels and directional instruments possible.

A more realistic simulation including a non-zero angular offset and body rates is provided in Figure 5.20 with the initial conditions given in Table 5.3. The angular momenta have been derived from initial body rates of 0.2 deg/s which are adequate levels of body rates after detumbling. The angular momentum in the $b_1$ axis exceeds the desired 1 Nms by approximately 1%. This value has been accumulated over time due to the external disturbances in the pitch axis. The excess momentum results in a rotation in the pitch axis as seen in Figure 5.20b. The roll and yaw axes show an oscillatory behavior with an amplitude of about 10 degrees. No growth in these transverse axes occurs as the wheel momentum provides stiffness to the system over time. The system's attitude can be corrected after this maneuver using an active control approach such as given in Section 4.5.1.

### 5.6.2 Closed Loop

By applying sensory feedback, one can use the measured states to adjust the orientation of the spacecraft accordingly. In this section, the steady spinup maneuver of the previous section is further improved upon. The sequential spinup type is not further analyzed due to its complexity in the rotational maneuver. One could argue to device a tracking type of controller to adjust the system's angular momentum and attitude for the ideal torque-free scenario. This however has

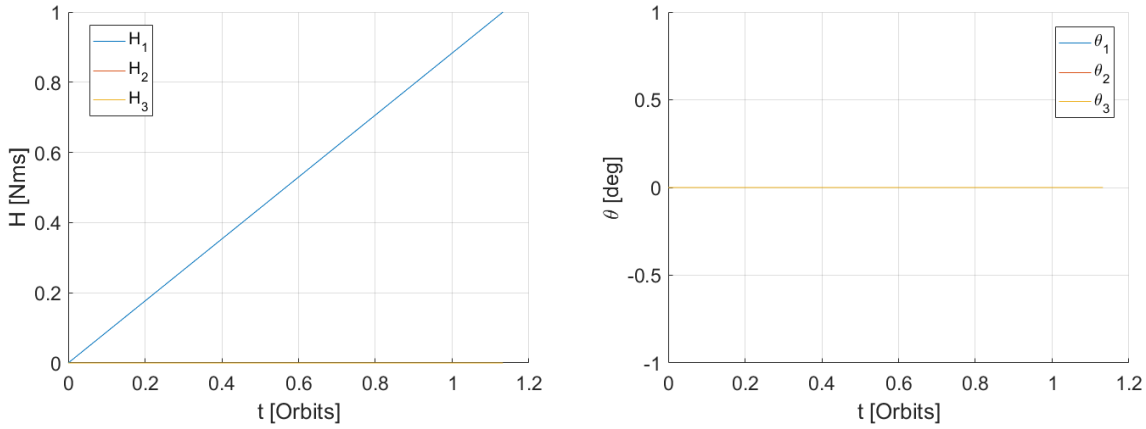


(a) Angular Momenta (b) Euler Angles

Figure 5.19: Open Loop Control without External Disturbances and Mean Motion

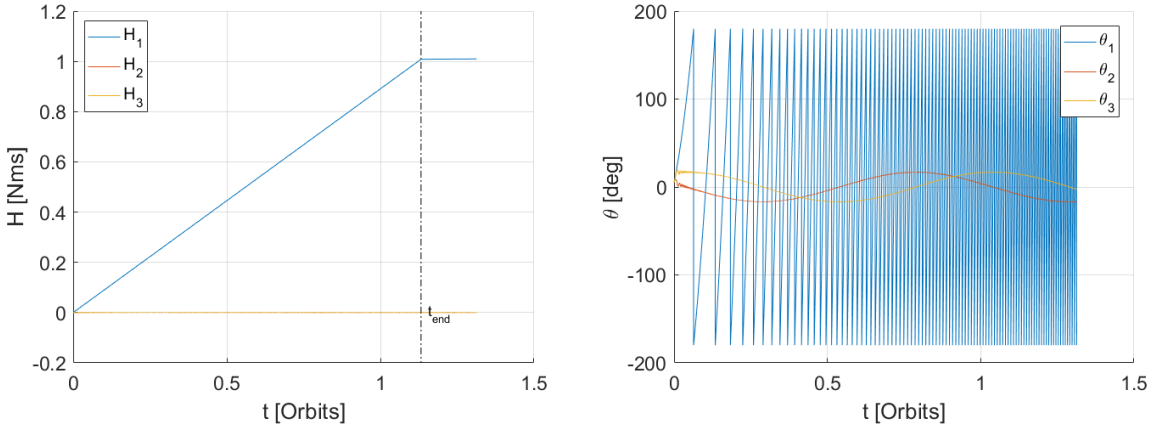


(a) Angular Momenta (b) Euler Angles

Figure 5.20: Open Loop Control with External Disturbances and Mean Motion

Table 5.3: Initial Conditions for the Open Loop Simulation

| **Variables** | **Values** |
|---|---|
| $\boldsymbol{\theta}_0$ | $[5, 5, 5]^T$ deg |
| $\mathbf{H}_0$ | $([0.2, 0.5, 0.3]^T$ mNms |
| $h$ | 380 km |
| $\vec{\tau}_a$ | $[1.3, 1.3, 0]^T$ $\mu$Nm |

harsh demands to the control system. Due to the relative high angular momentum with respect to its size, the system has high rotational velocity throughout the momentum transfer from the platform to the rotor. An initial small discrepancy in the attitude or the angular momentum will then yield in large attitude offsets over time. Therefore for these types, attitude adjustment should take place after the system has reduced its platform body rates. To avoid this problem, exclusive angular momentum control is also possible with high fidelity sensors, the final attitude is however required for adjustment at the end of the spinup. An example of such type is developed by Manchester (2016). This controller has been based on Lyapunov's direct method and uses three reaction wheels to adjust the momentum. For this thesis, only the steady spinup maneuver is researched as the momentum type control for sequential spinup is expected not to

provide much improvement while adding additional power.

**Sliding Mode Control**

In contrast to the maintenance mode controller, the momentum wheel spinup for the steady spinup maneuver requires a fast responsive controller. The LQR controller is a controller derived from optimal control theory which minimizes either the control effort or the state for a linear system. The linearized Euler's rotational dynamics given in Section 5.3.2 do not include the effects of the gyroscopic coupling and neither the effects of disturbances which are more impacting during the initial stage of the spinup when the angular momentum provided by the momentum wheel is of lower value. To include these effects, a nonlinear controller is preferred. For the following analysis, the sliding mode control (SMC) is applied for which the main theory and application are taken from Shtessel et al. (2014) and Liu (2017). Its main advantages are that the behavior of the system dynamics can be customized and is insensitive to uncertainties. The main shortcoming of this controller is that an undesirable phenomenon of oscillating behavior called chattering occurs as the system reaches its steady state. The sliding mode controller synthesis consists of 2 steps. First, the sliding surface is to be designed. This is the desired plane of the system's state to be steered (slided) unto. The second step is then to construct a feedback control law for the system to reach this sliding surface.

Consider a system of the form

$$\dot{\mathbf{x}} = f(\mathbf{x}) + g(\mathbf{x})\mathbf{u} + d \tag{5.54}$$

with the state vector $\mathbf{x} \in \mathbb{R}^N$ and the control vector $\mathbf{u} \in \mathbb{R}^M$. The sliding surface is then given as

$$\mathbf{s}(\mathbf{x}) = \mathbf{C}^T\mathbf{x} = \sum_{i=1}^{N} c_i x_i \tag{5.55}$$

where $\mathbf{C} = [c_1 ... c_{N-1} 1]$ and $x_i = x_i^{N-1}$. To guarantee that $x_i \to 0$ for $\mathbf{s}(\mathbf{x}) \to 0$ the vector $\mathbf{C}$ should be Hurwitz for the polynomial

$$P(c) = p^{N-1} + c_{N-1}p^{N-2} + ... + c_2 p + c_1$$

with $p$ the Laplace operator. This polynomial is Hurwitz if the roots of $P$ have zero or negative real parts (McName & Pan 2013). For the steady spin type, a sliding function of the following form is modeled

$$\mathbf{s} = \mathbf{H}_e + \mathbf{c}\boldsymbol{\theta}_e \tag{5.56}$$

with

$$\mathbf{H}_e = \mathbf{H}_d - \mathbf{H} \tag{5.57}$$

$$\boldsymbol{\theta}_e = \boldsymbol{\theta}_d - \boldsymbol{\theta} \tag{5.58}$$

here $\mathbf{c} > 0$ so that the polynomial is Hurwitz. The variables $\mathbf{H}_d$ and $\boldsymbol{\theta}_d$ represent the desired angular momentum and attitude in Euler angles, respectively. As the desired angular position of this maneuver is (0,0,0) degree, the sliding surface can be reformulated as

$$\mathbf{s} = \mathbf{H}_d - \mathbf{H} - \mathbf{c}\boldsymbol{\theta} \tag{5.59}$$

To reach this manifold, several classical reaching laws are available; constant, exponential, power rate laws (Hung et al. 1993). For a fast responsive system to the manifold, the exponential reaching law is selected. Although the power rate law provides a fast response far from the manifold as well, the rate reduces closer to the sliding surface. The exponential reaching law is given by Hung et al. as

$$\dot{\mathbf{s}} = -\boldsymbol{\epsilon}\,\mathrm{sgn}(\mathbf{s}) - \mathbf{k}\mathbf{s} \quad \text{with} \quad \boldsymbol{\epsilon} > 0, \quad \mathbf{k} > 0 \tag{5.60}$$

where sgn is the signum function.

Constructing the control law is done by taking the derivative of the sliding surface

$$\dot{\mathbf{s}} = \dot{\mathbf{H}}_d - \dot{\mathbf{H}} - c\dot{\boldsymbol{\theta}} \tag{5.61}$$

Substitution of Equation 5.49 into Equation 5.61 and setting it equal to the reaching law, gives

$$\dot{\mathbf{H}}_d + \boldsymbol{\omega}^{\times}\mathbf{H} - \mathbf{u} - \boldsymbol{\tau} - c\dot{\boldsymbol{\theta}} = -\boldsymbol{\epsilon}\,\mathrm{sgn}(\mathbf{s}) - \mathbf{k}\mathbf{s}$$

or

$$\mathbf{u} = \dot{\mathbf{H}}_d + \boldsymbol{\omega}^{\times}\mathbf{H} - \boldsymbol{\tau} - c\dot{\boldsymbol{\theta}} + \boldsymbol{\epsilon}\text{sgn}(\mathbf{s}) + \mathbf{k}\mathbf{s}$$

Because the disturbance $\boldsymbol{\tau}$ is not known, the control law cannot be established. Instead one can set up a control law as

$$\mathbf{u} = \dot{\mathbf{H}}_d + \boldsymbol{\omega}^{\times}\mathbf{H} + \mathbf{D}\text{sgn}(\mathbf{s}) - c\dot{\boldsymbol{\theta}} + \boldsymbol{\epsilon}\text{sgn}(\mathbf{s}) + \mathbf{k}\mathbf{s} \tag{5.62}$$

here $\mathbf{D}$ is the maximum expected disturbance torque. Note that this value has been multiplied with sgn($\mathbf{s}$). This has been done to make the surface globally asymptotically stable as shown in Appendix C. If the external disturbance exceed $\mathbf{D}$, the global asymptotic stability can be lost.

The desired value $\dot{\mathbf{H}}_d$ and $\mathbf{H}_d$ are derived from the results under perfect conditions from the open loop simulation in Section 5.6.1 and are as follows

$$\dot{\mathbf{H}}_d = \begin{cases} [g_a, 0, 0]^T, & \text{if } H_a < 1 - nI_p. \\ [0, 0, 0]^T, & \text{otherwise.} \end{cases}, \qquad \mathbf{H}_d = \begin{cases} [H_a, 0, 0]^T, & \text{if } H_a < 1 - nI_p. \\ [0, 0, 0]^T, & \text{otherwise.} \end{cases} \tag{5.63}$$

While the spinup process continues, the desired angular momentum rate is expected to be $g_a$ on the pitch axis as it is expected to increase with $\dot{H}_a = g_a$. This condition is given as $H_a < 1 - nI_p$, due to the angular momentum of the platform required to match the rotation rate of the orbital motion. If this is not the case, no increase in angular momentum is assumed. Similarly, the desired pitch angular momentum of the system is expected to be equivalent to the inertial angular momentum of the rotor under perfect conditions while the transverse angular momentum is desired to be zero.

The control torque on the pitch axis is limited with a saturation function in the form of

$$\text{sat}(u_1) = \min(\max(u_1, g_a - u_{\max}), g_a + u_{\max}) \tag{5.64}$$

which is set to deviate from the spinup torque $g_a$ by $\pm u_{\max}$ to allow to adjust for disturbances. The other two axes have been limited using Equation 4.33 or

$$\text{sat}(\mathbf{u}_{2,3}) = \begin{cases} \mathbf{u_{2,3}}/\beta, & \text{if } \beta > 1. \\ \mathbf{u_{2,3}}, & \text{otherwise.} \end{cases} \tag{5.65}$$

with $\beta = \max\left(|\mathbf{u}_{2,3}|/u_{\max}\right)$. Note that the torque induced by the thrusters is assumed to be constant and that the magnetorquers are used to adjust the torque to the required values. Adding a saturation limit to the actuators can invalidate the stability properties and it is expected that this property will only hold at low values of $H_a$ with a saturation torque of magnitude of $10^{-5}$ Nm (see Appendix C).

**Result & Discussion**

For the simulation, a saturation control torque of $10^{-5}$ Nm has been taken with initial conditions and SMC parameters given in Table 5.4 and Table 5.5, respectively with the disturbance torques acting at 380 km. The sliding mode controller parameters have been chosen after trial and error. The results are shown in Figure 5.21 and Figure 5.22 for a saturation control torque of $1 \cdot 10^{-5}$ and $2 \cdot 10^{-5}$ Nm, respectively. Figure 5.21e and Figure 5.21b show that the controller is only able to converge the pitch axis within reasonable values. The transverse axes in contrast oscillate with an amplitude of more than 10 degrees. During the initial phase of the spinup, the control torque is not sufficient for a fast transient response (Figure 5.21c).

After 100 seconds, the system seems to reach a critical value for which the system is not able to converge to the surface within the spinup time. The insufficiency of the control torque is seen in Figure 5.21d. The SMC behaves like a bang-bang controller and chattering does not occur as the system has not reached its sliding mode except for the pitch axis.

Using the same conditions with twice the saturation control torque, an increase in performance is achieved as shown in Figure 5.22. The system achieves in approximately 330 seconds its desired state. The controller still behaves like a bang-bang controller and is thus not energy efficient. To improve energy efficiency, one can switch to a different control scheme or by adjusting the gains. As a result, the performance is expected to have a slower settling time. One remarkable thing is that chattering does not occur due to the gyroscopic stiffness softening the impact of the control torque on the state variables, making chattering attenuation or elimination techniques unnecessary.

Table 5.4: Initial Conditions for the SMC Simulation

| Variables | Values |
|---|---|
| $\boldsymbol{\theta}_0$ | $[2, 2, 2]^T$ deg |
| $\mathbf{H}_0$ | $[0.2, 0.5, 0.3]^T$ mNms |
| $h$ | 380 km |
| $\vec{\tau}_a$ | $[1.3, 1.3, 0]$ $\mu$Nm |

Table 5.5: SMC Parameters for the SMC Simulation

| Variables | Values |
|---|---|
| $\boldsymbol{\epsilon}$ | $[10^{-3}, 10^{-3}, 10^{-3}]^T$ |
| $\mathbf{D}$ | $1.2\boldsymbol{\tau}_{\max}$ |
| $\mathbf{k}$ | $[10^{-1}, 10^{-2}, 10^{-2}]^T$ |
| $\mathbf{c}$ | $[10^{-2}, 10^{-2}, 10^{-2}]^T$ |

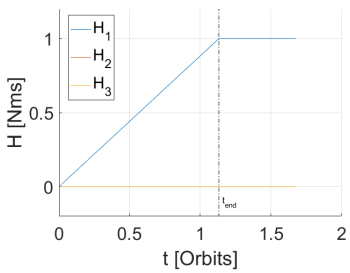


(a) Angular Momenta

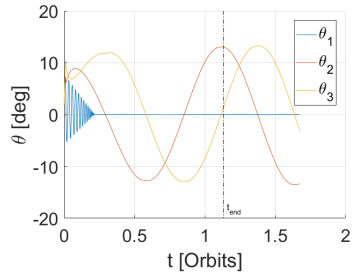


(b) Euler Angles

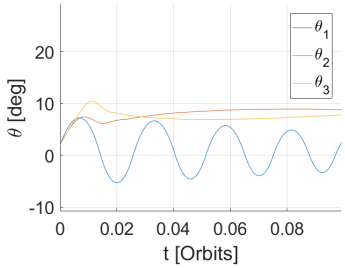


(c) Euler Angles from 0 to 0.075 Orbits

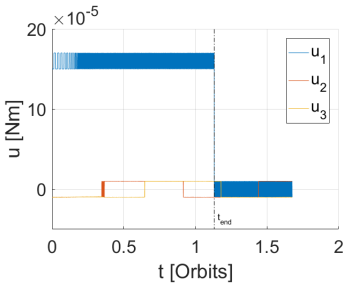


(d) Control Torque

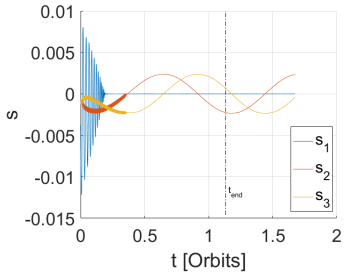


(e) Sliding Function

Figure 5.21: SMC Simulation with $u_{\max} = 1 \cdot 10^{-5}$ Nm

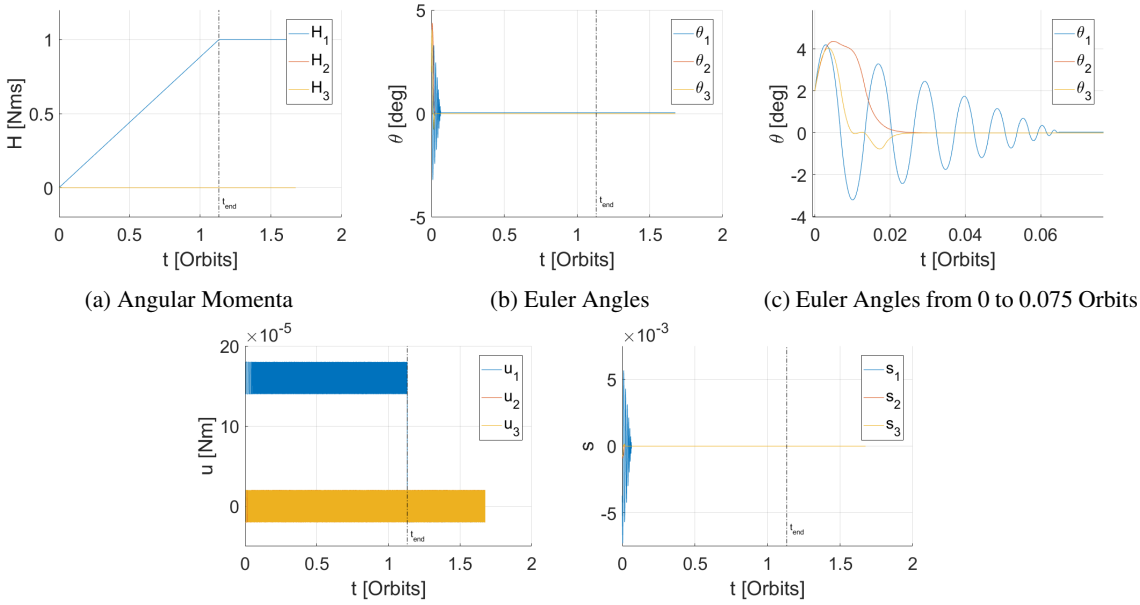


(a) Angular Momenta (b) Euler Angles (c) Euler Angles from 0 to 0.075 Orbits

(d) Control Torque (e) Sliding Function

Figure 5.22: SMC Simulation with $u_{\max} = 2 \cdot 10^{-5}$ Nm

## 5.7 Spinup Method Selection

In Section 5.2, the possible concepts were stated for which these were analyzed on performance. For the initially spin stabilized ones (sequential types), three concepts were analyzed; the full-major-spin type (FMS1), the full-minor-spin type (FMS2), and the partial-spin type (PS). For the controlled (concurrent) type, the SMC control spinup (SMCS) was considered. To select which spinup method is most suitable for SHAPE a trade-off is performed in this section. Hereby, it has been chosen that a passive damper and a locking mechanism are included for the sequential types. In Figure 5.23, the three spinup concepts are illustrated. The partial spin can be viewed as a combination of a series of FMS2 spinups with the initial either FMS1 or FMS2. Note that the nutation angles have been exaggerated.

### 5.7.1 Positive and Negative Effects of Spinup Types

The FMS1 and FMS2 types both provide a single-spin stabilized initialization which provides the system a passive method of stabilization. Under energy dissipation, the FS-minor type however suffers from instability over time. This effect should be minimal if the loss in rotational energy and thus the transition time to the spinup process is minimized. The major type is in contrary asymptotically stable. A major disadvantage of the major type is that it cannot generate power as the angular momentum vector is perpendicular to the sun synchronous orbital plane until the spinup is progressed close to its final orientation. In the case for the minor type, the spacecraft can provide marginal power generation for the body mounted solar panels due to the rotational motion. The PS type has been concluded to be inferior compared to the two other sequential types. The additional corrections to damp the transverse angular momenta between each maneuver makes this spinup with respect to power and time to be lesser than FMS1 or FMS2. It benefits only from the fact that after each procedure power can be generated using its body mounted solar panels. All these types also suffer from the added time required to be spun up to reach the all-spin configuration.

SMCS has two advantages over the previous mentioned types. First, the spinup is shorter as it can start from the 3-axis stabilized configuration and second is that the platform is steady over the spinup process. The latter can provide the system for communication and allows for solar panel deployment. This comes however at the price of added complexity in the control process and power consumption during its 3-axis stabilized configuration.

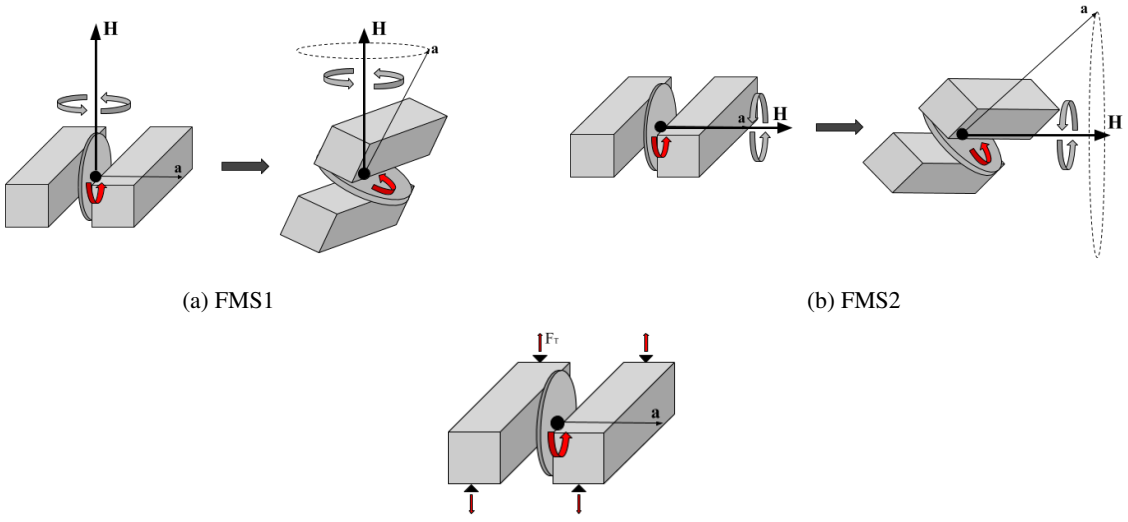


(a) FMS1

(b) FMS2

(c) SMCS

Figure 5.23: Schematic Spinup Concepts

### 5.7.2 Use of Thrusters

Sequential types of either the major or minor axis spin types require the system to achieve the all-spun configuration. At the higher ends of control torques of $10^{-5}$ Nm for CubeSat magnetorquers, this process can take more than 18 orbits or more than one day for completion. If the system is reliant on the battery during this duration and not to mention the detumbling process, a battery capacity of at least an order greater is expected. This is unfeasible and thus thrusters are required as magnetorquers with a control torque of $10^{-4}$ Nm will require volume not suitable for CubeSats.

The system with thrusters which matches the torque level of the spinup can be spun up within one orbit. This is an adequate solution for the FMS types. Note that for the SMCS, thrusters are a minimum requirement as it had been assumed that the torque will be based around the spinup torque. During this process magnetorquers will be required for active control to compensate for the disturbances. To eliminate single point of failure, SHAPE is required to posses at least two thrusters with enough fuel to allow the system to provide a spin with a single thruster.

### 5.7.3 Spinup Trade-off

Based on previous analysis in Chapter 4, the final condition after the spinup process has been deemed to be very important. If the transverse angular body rates are higher than 6 mrad/s, pitch control can be lost. The FMS2 spinup type yields in a final nutation angle of 4.5 degrees using a passive damper and a locking mechanism for the damper. These relate to very high transverse rates and correction will take substantial amount of time which can also prevent the deployment of solar panels. Therefore, the FMS2 and PS types have been rejected for trade-off candidates as both suffer from high nutation angles. An angle of 0.1 degree or smaller are required.

The mass are given for the two remaining options a weight of 3. The mass is an important factor especially as thrusters are required for both concepts. The volume has given a slightly lower value. The power criterium which considers also the energy required is an important measure to compare concepts. The SMCS type does not require additional energy from the battery as the platform and thus the solar panels are expected to be steady. Next, the complexity and reliability are given weights of 3 and 5. Currently, the SMCS type assumed perfect controllability, however the torque's direction and magnitude of the magnetorquers are dependent on the satellites position in space. This makes the use of magnetorquers very complex. The reliability has given a weight of 5 as the transition to the nominal orientation can yield in mission success or failure.

The trade-off is given in Table 5.6. Hereby, the FMS2 and PS types' criteria are given a cross as this concept is not feasible. The FMS1 type has a total point of 12 and thus chosen for the spinup process. It provides high reliability as the system's spinup dynamics is very dominant, requiring no additional actuators to be used during the process.

Table 5.6: Spinup Trade-off

| **Criteria** | **Weight** | **FMS1** | **FMS2** | **PS** | **SMCS** |
|---|---|---|---|---|---|
| **Performance** | 4 | +1 | -1 | -1 | +1 |
| Mass | 3 | 0 | × | × | 0 |
| Volume | 2 | 0 | × | × | -1 |
| Power | 5 | 0 | × | × | 1 |
| Complexity | 3 | 1 | × | × | -1 |
| Reliability | 5 | 1 | × | × | -1 |
| **Total** | **22** | **12** | × | × | **-1** |
| **Normalized Total** | | **0.55** | × | × | **-0.05** |

However, additional energy is needed to attain the all spun configuration.

# Chapter 6

# Detumbling Mode

As decided in the previous chapter, an all-spun configuration is required to execute the major axis spinup. Since the magnetorquer strength have been decided in Chapter 4, a detumbling simulation is performed to verify if the maximum magnetic dipole moment can provide sufficiently fast detumbling for the system. This chapter will first outline a more accurate magnetic field model and will also list the additional reference frames used. In Section 6.2, the control laws are given for detumbling and is followed in the subsequent section with the simulation results. This chapter is then finalized with a comment of an additional control mode in between the detumbling and acquisition mode.

## 6.1 Magnetic Field Model and Reference Frames

The simulations in the previous chapters applied a simple mathematical dipole model to represent the magnetic field. Additionally, it had been assumed that the satellite was orbiting around a plane on the magnetic poles. These assumptions have been applied to increase simulation speed as multiple simulations had to be performed to determine the momentum wheel and control actuators specifications. This computational constraint is lifted for the detumbling analysis as most of the spacecraft parameters have already been determined. Thus simulations can be focused on a specific set of initial conditions. In this section, a more accurate and higher resolution model of the Earth's magnetic field is discussed and followed with the set of new reference frames.

### 6.1.1 IGRF12 Model

The International Association of Geomagnetism and Aeronomy (IAGA) has developed a standardized model called the International Geomagnetic Reference Field 12th generation (IGRF12) to describe the Earth's magnetic field (Thébault et al. 2015). This model, a collaborative effort by multitudes of institutes and organizations, is able to estimate and predict the magnetic scalar potential and its annual rate of change from 1900 A.D. to the present. The magnetic field of the Earth is based on a scalar potential approximated with a finite series as

$$V(r,\theta,\phi,t) = a\sum_{n=1}^{N}\sum_{m=1}^{n}\left(\frac{a}{r}\right)^{n+1}\cdot\left[g_n^m(t)\cos(m\phi) + h_n^m(t)\sin(m\phi)P_n^m(\cos(\theta))\right] \tag{6.1}$$

here, $r$ denotes the radial distance to the geodetic center, $a$ the semi-major axis, $\theta$ the geocentric co-latitude, $\phi$ the east longitude, $P_n^m(\cos(\theta)$ the Schmidt quasi-normalized associated Legendre function of degree $n$ and order $m$ and, $g_n^m(t)$ and $h_n^m(t)$ are time-dependent Gauss coefficients computed as

$$g_n^m(t) = g_n^m(T_0) + g_n^m(T_0)(t - T_0) \tag{6.2}$$

$$h_n^m(t) = h_n^m(T_0) + h_n^m(T_0)(t - T_0) \tag{6.3}$$

with $T_0$ the epoch of exact multiples of 5 years. The coefficients can be found in the work by Thébault et al. (2015). The magnetic field vector is then computed by finding the negative gradient with respect to position coordinates. For this work, the Matlab command *igrfmagm* is used. It should be noted that the model is only valid up to the year 2020 and further predictions cannot be made. Therefore, the current date of research (06-09-2017) has been used for simulation.

### 6.1.2 Reference Frames

The use of Matlab's command *igrfmagm* is given with respect of the geodetic longitude, latitude and the semi-major axis. To correctly determine the magnetic field components, a new set of reference frames has to be set up. These are listed as follows

- **Earth-Centered Inertial Reference Frame** (see Chapter 3)
- **Earth-Centered, Earth Fixed Reference Frame** (ECEF) is a rotational reference frame for which the origin is centered at the geographic center and its axis fixed with the surface of the Earth. The X-axis is aligned to the equator and the prime meridian in Greenwich. From these two positions, the 0° latitude and 0° longitude are defined. The Z-axis is located from the origin to the direction of 90° latitude and 0° longitude. The Y-axis is determined from the right-hand rule.
- **Orbiting Reference Frame** (see Chapter 3)
- **North-East-Down Reference Frame** (NED) has its origin at the spacecraft center of mass with its X-axis located to the north as given in ECEF frame and is tangential to its longitudinal position. The Z-axis is located down, towards the geographic center of Earth and the Y-axis is directed eastward.
- **Spacecraft Principal Body Frame** (see Chapter 3)

To determine Earth's magnetic field using the *igrfmagm* command, the geodetic latitude and longitude are required as input. These are the angular positions in the geodetic reference frame which takes irregularities of the non-spherical Earth into account. For the detumbling analysis, it has been assumed that the Earth is spherical and that the latitude and longitude of the ECEF frame correspond to the geodetic counterparts. These can then be retrieved from the satellites position relative to its orbit.

The SSO of SHAPE is inclined at an angle of 97° with respect to the equator. For simplification, it is assumed that the orbit is initiated at the X-axis in the inertial frame. Furthermore, SHAPE's orbit is assumed to be circular and the argument of periapsis and the longitude of ascending node are taken to be zero. These assumptions allow for a simple transformation from the orbital frame to the ECI frame using an Euler rotation transformation around the X-axis with a magnitude equivalent to $90° - i$ degree with $i$ the inclination of the orbit. The position of the spacecraft in the orbital frame is given as

$$\mathbf{r}_o = \begin{bmatrix} a\cos(\theta_n) \\ 0 \\ a\sin(\theta_n) \end{bmatrix} \tag{6.4}$$

and in the ECI frame as

$$\mathbf{r}_N = \mathbf{C}_1(i)\mathbf{r}_o \tag{6.5}$$

The ECEF frame is rotating with respect to the inertial frame at an angular velocity of $\omega_E = 7.3 \cdot 10^{-05}$ rad/s on the Z-axis and thus the angular position is given against time as

$$\theta_E = \omega_E t \tag{6.6}$$

Applying the Euler rotation matrix around the Z-axis with a magnitude of $\theta_E$, the position of the spacecraft with respect to the ECEF frame can be computed, or equivalently

$$\mathbf{r}_E = \mathbf{C}_3(\theta_E)\mathbf{r}_N \tag{6.7}$$

for which the longitude and latitude can be derived respectively as

$$\lambda = \tan^{-1}\left(\frac{r_{E,1}}{r_{E,2}}\right) \qquad \phi = \tan^{-1}\left(\frac{r_{E,3}}{\sqrt{r_{E,1}^2 + r_{E,2}^2}}\right) \tag{6.8}$$

The magnetic field can be computed using the longitude, latitude, radius and the time which is given in the North-East-Down reference frame. Let $\mathbf{a} = [\vec{a}_1, \vec{a}_2, \vec{a}_3]^T$ be the axes of the ECEF reference frame and $\mathbf{b} = [\vec{b}_1, \vec{b}_2, \vec{b}_3]^T$ of the NED

reference frame, then the magnetic field vector can be represented in the ECEF frame by using two Euler rotations as follows

$$\mathbf{b} = \mathbf{C}_2(\phi)\mathbf{C}_3(\lambda)\mathbf{a} \quad \rightarrow \quad \mathbf{a} = [\mathbf{C}_2(\phi)\mathbf{C}_3(\lambda)]^T\mathbf{b} \tag{6.9}$$

The previous rotations can be inversed and multiplied to obtain the magnetic field components with respect to the orbital frame;

$$\mathbf{B}_o = \mathbf{C}_1(i)^T\mathbf{C}_3(\theta_E)^T[\mathbf{C}_2(\phi)\mathbf{C}_3(\lambda)]^T\mathbf{B}_{NED} \tag{6.10}$$

Finally, this vector can be given in the body frame using the direction cosine matrix in quaternions.

$$\mathbf{B}_b = \mathbf{C}(\mathbf{q})\mathbf{B}_o \tag{6.11}$$

## 6.2 B-dot Control

Detumbling of the spacecraft is composed of reducing the body rotational rates close to the mean motion. To do this, one can use a standard magnetic control scheme called the B-dot controller (Alfriendt 1976). This type of control uses measurements of Earth's magnetic field **B**;

$$\mathbf{M}_A = -\mathbf{K}\dot{\mathbf{B}} \quad \text{with} \quad \begin{bmatrix} K_1 & 0 & 0 \\ 0 & K_2 & 0 \\ 0 & 0 & K_3 \end{bmatrix} \tag{6.12}$$

with $\mathbf{M}_A$ the dipole moment of the magnetorquer, $K_i > 0$ the gain, and $\dot{B}$ the derivative of the measured magnetic field. This is usually done with the following differentiation scheme

$$\dot{\mathbf{B}} = \frac{B_i - B_{i-1}}{\Delta t} \tag{6.13}$$

with $\Delta t$ the sampling time of the sensor. The control torque is then computed as follows

$$\mathbf{u} = \mathbf{M}_A{}^{\times}\mathbf{B} \tag{6.14}$$

Note that this control scheme only uses measurements of the magnetic field to reduce the body rates to values in the order of magnitude of the mean motion. To add the saturation of the magnetorquer, a limit is set to the dipole moment of the magnetorquer as

$$\text{sat}(\mathbf{M}_A) = \begin{cases} \mathbf{M_A}/\beta, & \text{if } \beta > 1. \\ \mathbf{M_A}, & \text{otherwise.} \end{cases} \tag{6.15}$$

with $\beta = \max\left(|\mathbf{M}_A|\,/M_{A,\max}\right)$. A similar control scheme uses the maximum available dipole moment dependent on the sign of the derivative;

$$\mathbf{M}_A = -M_{A,\max}\text{sign}(\dot{B}) \tag{6.16}$$

This control scheme is also called a bang-bang controller as only either the maximum values are used.

## 6.3 Detumbling

In this section, the results of detumbling are discussed for initial conditions given in Table 6.1 for the static gain and bang-bang control law. The sampling frequency of the magnetometer has been taken at a value of 10 Hz. For the following simulations, it has been assumed that the sensors give perfect sensor feedback without the addition of noise or bias. Furthermore, the time delay caused by de-activating the magnetorquers have been neglected. The aerodynamic torque has been assumed to be acting constant in the orbital frame.

The first scheme uses a static gain $K_i = 4 \cdot 10^5$ for $i = 1, 2, 3$ over the duration of the whole detumbling procedure. The bang-bang controller is described in Section 6.2. The simulation results of both control laws are given in Appendix H. As seen in the figures, the difference between the two becomes noticeable at around 0.5 orbits. The $H_2$ body rate is damped slightly less than the bang-bang type. The distinction in the dipole moment becomes more evident as the static gain approach converges to the zero value.

Table 6.1: Initial Conditions for the Detumbling Simulation

| Variables | Values |
|---|---|
| $\boldsymbol{\theta}_0$ | $[10, 10, 10]^T$ deg |
| $\boldsymbol{\omega}_0$ | $[15, 15, 15]^T$ deg/s |
| $h$ | 380 km |
| $\vec{\tau}_a$ | $[1.3, 1.3, 0]$ $\mu$Nm |

In Figure 6.1, the magnitude of the body rates are compared between the two control laws with initial magnitude of 26 and 35 degrees per second. With an initial magnitude of 26 deg/s, the bang-bang controller is able to damp faster until it approaches an angular velocity of 14 mrad/s. The convergence within 10 mrad/s happens after 0.9 orbits into the detumbling process while the static gain controller is able to this in 0.75 orbits. The power consumption between the two are significant. Assuming that the magnetic dipole moment scales linearly with the power and defining the control effort as $P_A = \sum_{i=1}^{3} M_{A,i}(t) \cdot \Delta t$, the power consumption can be determined. The bang-bang controller is found to consume almost 3 times as much power over a single orbit. If one looks at the point the system reaches a body rate of 14 mrad/s, the bang-bang controller consumes 1.5 times as much while only being a fraction faster. For the higher magnitude of 35°/s, the system is still able to converge within 1 orbit for both controller types. The energy consumption has considerably increased for the static gain which is to be expected. The necessity of a fast convergence using the bang-bang controller therefore seem to be irrelevant under normal conditions. If the body rates are unexpectedly higher, the bang-bang controller can be applied to quickly cope up with extreme values.

The energy consumption has been estimated using Hyperion's MTQ400 magnetorquers (Hyperion Technologies 2017). These consume 0.35 W at a dipole moment of 0.5 Am$^2$. If the power scales linearly with the provided dipole moment, the energy consumed ($E_j$) can be estimated for each control scheme as shown in Table 6.2.

Table 6.2: Energy Consumption of the Static Gain and Bang-Bang Detumbling Control Laws

| Control Type | $\|\omega_0\|$ [deg/s] | $E_j$ over 1 Orbit [kJ] | $E_j$ to 14 mrad/s [kJ] |
|---|---|---|---|
| Bang-Bang | 26 | 5.8 kJ | 2.7 kJ |
| Bang-Bang | 35 | 5.8 kJ | 3.3 kJ |
| Static Gain | 26 | 2.0 kJ | 1.8 kJ |
| Static Gain | 35 | 2.6 kJ | 2.6 kJ |

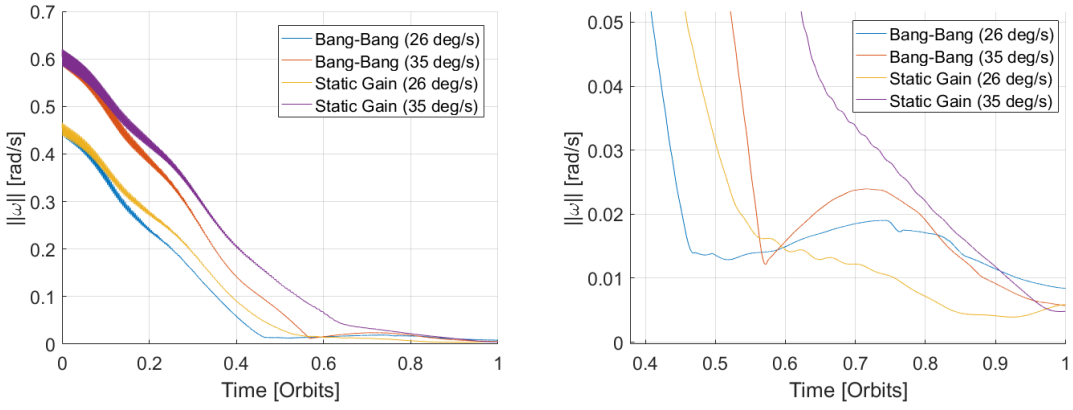


(a) Full View (b) Zoomed

Figure 6.1: Comparison between the bang-bang and the static gain controller

## 6.4 Pre-acquisition Mode

After the system has detumbled, there are additional tasks to be performed. Therefore, a supplementary control mode is added called the pre-acquisition mode. This can be considered to be part of the acquisition mode, but have been included to differentiate several tasks. One of these task consists of correcting the orientation after detumbling to the desired attitude set for the momentum wheel spinup procedure. Using coarse sensors (e.g. sun sensors and magnetometers), the system is to be oriented such that either the negative or positive major axis is aligned perpendicular to the orbital plane. The sign will be dependent on the direction of the momentum wheel's rotation axis and the worst-case magnitude of the rotation can be up to 180 degrees. This is a large angled maneuver to be performed with magnetorquers and the energy required should be accommodated in the battery design.

Next there are two options to be explored to attain the all-spun configuration. This can be done by immediately spinning up with the attitude thrusters or by applying a small spin using magnetorquers to initialize a passive spin stabilized configuration around the major axis. To what extent this has to be done is not pursued in this study and is recommended as future work.

# Chapter 7

# Design Specifications

In the previous chapters, the nominal, maintenance, acquisition, and detumbling control modes were analyzed for the system performance and constraints. Here, the design considerations, requirements and constraints will be given. This chapter starts with the impacts on the system structure in Section 7.1 which is followed with the momentum wheel, passive damper and sensors in Section 7.2, Section 7.3, and Section 7.5, respectively. The pointing and MTF budgets are given in the subsequent section. The chapter is finalized with the ADCS requirements and constraints in Section 7.8.

## 7.1 System Structure

The structure is one of the key importance in the design of spinning spacecraft. In this section, the system composed of the platform and rotor are discussed with relation to the design of the ADCS.

### 7.1.1 Structural Integrity and Imbalance

The structural integrity of the satellite is an important design factor. Besides the launch loads, the spacecraft has to undergo rotational forces during the acquisition mode as decided in Chapter 5. It was decided that the system should reach an angular momentum of 1 Nms before spinning up the momentum wheel. For the major axis spin, SHAPE has to achieve an angular velocity of approximately 6.8 rad/s or 390 deg/s. This results in a centripetal acceleration of 7.0 m/s$^2$ at a maximum distance of 15 cm. In combination with thermal shocks and external disturbances, various random and sinusoidal accelerations can impact the structures, the payload, and subsystems. These loads gradually change in magnitude and direction throughout the spacecraft's body as the spinup process continues.

From the nominal mode analysis in Section 4.7.4, it was found that the presence of product of inertia terms increases the nutation angle. Before, it had been assumed that SHAPE was composed of two boxes and a disk with uniform mass distribution leading to convenient principal moments of inertia for analysis. In practice, the mass distribution will not be uniform and products of inertia are likely to be present. The positioning of the subsystem will be complex and is expected to be constraining as one of the 3U boxes is reserved for the payload. A spinning spacecraft possessing products of inertia induces a wobbly movement and as a result can induce loads into the structure. Additionally, these movements can also impair the effectiveness of sensors, adding errors to the measurements.

The system consists of many subsystems with varying mass and volume. Positioning of these will therefore be an optimization process. As the payload has not yet been designed, the placement of lenses should be considered such that the payload positioning can be eased. If these are set, dynamical imbalance tests should be performed to validate analytical and numerical results with a spin balance machine as shown in Figure 7.1. The products of inertia determined from this test can then be used for calibrations of attitude sensors against offset motions. If products of inertia terms still exceeds expectations, non-functional mass can be added to the design. This measure however should be left as last if no other solutions can be found.

The imbalance of the spacecraft shows similar behavior as reaction wheels and is an important issue for non-axisymmetric platforms as the positioning is much more complex. There exist two types of imbalances; *static* and *dynamic* (Markley & Crassidis 2014). Static imbalance is the condition when the rotor's center of mass is shifted away

Figure 7.1: Spin Balance Machine (Space Electronics 2017)

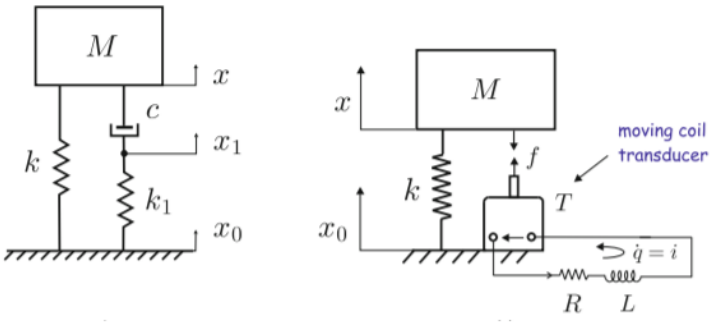


Figure 7.2: Schematic Views of a Passive (Left) and Active (Right) Isolators (Preumont 2011)

relative to the axis of rotation. This induces a radial force rotating in the platform body frame for which the bearing assembly must provide the centripetal force to maintain the rotation of the rotor. Besides a jittering motion, this force will also generate a sinusoidal torque if this force has an offset from the center of mass of the spacecraft. The force is given by Markley and Crassidis as

$$\mathbf{F}_s = -M_r \omega_r^2 \begin{bmatrix} x_1 \\ x_2 \\ 0 \end{bmatrix} \tag{7.1}$$

with $M_r$ and $\omega_r$ the mass and rotational velocity of the momentum wheel respectively. $x_i$ are the vector elements from the rotor's axis to its center of mass. The force changes direction as $x_i$ rotates with respect to the spin axis and this force is exhibited as a sinusoidal function. In a more general sense, this equation is given by its magnitude as follows;

$$F_s = U_s \omega_r^2 \quad \text{with} \quad U_s = M_r \sqrt{x_1^2 + x_2^2} \tag{7.2}$$

here $U_s$ is the magnitude of the static imbalance. This is usually in the order of g cm$^2$. For $U_s = 1$ g cm$^2$ and a rotational velocity of 733 rad/s, a force of 5.4 N is obtained. Depending on the spacecraft mass center offset from the spin axis, this torque can be in the order of tenths of Nm for centimeter offsets. Minimization of the distance of the spin axis with respect to the center of mass is therefore a high priority. By reducing this distance to mm values, the order of the torque are still in the orders of a few mNm. These are higher than external disturbance torques and should be mitigated as otherwise jittering motion will degrade the image quality significantly. Therefore, the momentum wheel suspension system should absorb these jittering with one or multiple dampers called isolators . A schematic view of a passive and active isolator are shown in Figure 7.2.

Dynamic imbalance is the case when the rotor's axis of rotation is not aligned to one of its principal axis. As a result, it induces a torque to the system. During the acquisition mode, a dynamically unbalanced rotor can cause resonance traps (Section 5.4) and during the nominal mode undesired transverse angular momentum. To estimate the maximum allowable products of inertia, one can iteratively (analytically or numerically) determine the conditions for which the rotational velocity is smaller than requirement (S-NM.5). Performing analyses for different conditions of dynamic imbalance are time-consuming. Instead, one can work from the parameter $\vec{a}$ as shown in Section 5.4 which represents the maximum allowable *degree of imbalance*. For example, an unbalanced rotor with an inertia tensor as

$$\mathbf{I}_{UR} = \begin{bmatrix} 0.0018 & 0 & 0.0002 \\ 0 & 0.009 & 0 \\ 0.0002 & 0 & 0.0009 \end{bmatrix} \tag{7.3}$$

has a degree of imbalance of $\vec{a} = (0.999980, 0, 0.00629)$. Hereby, the platform is assumed to be balanced and the rotor's spin axis is fixed in the platform body frame on the first axis. If one assumes that the rotor's product of inertia terms are small, then the spin axis $\vec{a}$ is located close to the spin axis given with respect to the pseudo-principal frame $\vec{\alpha}$.

A necessary condition for the degree of imbalance can be found from the best-case scenario. Assuming that angular momentum is conserved, the minimum energy point on the momentum sphere can be used to determine this condition.

Table 7.1: Necessary Rotor Product of Inertia Values

| **Max. Rotor Product of Inertia** | **Target** [g cm$^2$] | **Desired** [g cm$^2$] |
|---|---|---|
| $\lvert I_{12}\rvert = \lvert I_{21}\rvert$ | $< 2.4 \cdot 10^2$ | $< 1.7 \cdot 10^2$ |
| $\lvert I_{13}\rvert = \lvert I_{31}\rvert$ | $< 0.5 \cdot 10^2$ | $< 0.3 \cdot 10^2$ |

The point of minimum energy in the pseudo-principal frame is located at $\vec{H}_P = \vec{\alpha}$ when $H_a = 1$ which can be derived from Section 5.41. Because $\vec{\alpha} \approx \vec{a}$, the transverse momentum in the body frame can be estimated as $\vec{H} = \vec{\alpha}$. For the previous example with a degree of imbalance of $\vec{a} = (0.999980, 0, 0.00629)$, $\vec{\alpha} = (0.999982, 0, 0.00595)$. This is within 6% accuracy. To meet requirement (S-NM.5), the system should have a degree of imbalance better than $\vec{a} = (0.9999994, 0.00057, 0)$ or $\vec{a} = (0.9999994, 0, 0.00038)$, corresponding to the desired MTF goal. For the target goal, the values should be better than $\vec{a} = (0.9999994, 0.00082, 0)$ or $\vec{a} = (0.9999994, 0, 0.00054)$. Here, two values are given for both the desired and target goals, depending on transverse system inertia. The second value is more strict than the first as the room for adjustment in the inertia is less on the third axis than the second axis. In Table 7.1, the necessary requirements are given for the presence of only one set of products of inertia. The $I_{23}$ (and thus also $I_{32}$) are irrelevant as these do not produce angular offset between the spin and principal axis. Note again that these are the best-case solutions and in reality the expected values should be lower such that it does not exceed the MTF margin left for uncertainty.

Platform imbalance is only of importance during the acquisition mode. During the nominal mode, the platform has been despun and will therefore not induce forces or torques. The effects of products of inertia prevail mostly during the detumbling and the acquisition phases, assuming the rotor is balanced. Throughout these phases, dynamic imbalance of the platform will cause the spacecraft to wobble (=nutate) as the angular momentum vector and the spin axis are not aligned. The magnitude of this wobble or nutation angle can be found by transforming the system's frame to the principal axis frame and then finding the angle between the spin axes in the original body frame and the principal frame. Due to this offset, a nutation angle will always be present. The use of damping can elevate this situation, close to the averaged minimum angle.

### 7.1.2 Rigidity and Energy Dissipation

In Section 4.6.2, the damping criteria had been stated. The dual-spin system is expected to be stable if the energy dissipation rate of the damper is higher than a given ratio with respect to the energy dissipation of the spacecraft. If this is not the case, the system will lose its asymptotic stability and the spacecraft will become instable, resulting in an increasingly larger nutation angle over time. One can either design a passive damper which satisfies this condition or use magnetic control to damp the transverse momentum. Damper failure or the power usage of magnetorquers are no risk-free or possible performance degrading-free options. Failure to provide this energy damping can result in overturn and mission failure.

After exact analysis of energy dissipation, measures to increase or reduce the energy dissipation of either the platform or rotor should take place. On the momentum wheel, energy dissipation can be caused by friction, fuel sloshing and eddy currents (Section 4.2.4). In case of the platform, the dissipative contribution are elements such as the frame, electrical wiring, and the damper itself. An important aspect not analyzed in this thesis are the solar panels which have been neglected. These non-rigid structures will dissipate energy and has thus positive impact on the stability. However, these can induce flexure modes to the system.

### 7.1.3 Spin Axis Offset

An offset in the spin axis has clear consequences for the mission. If the spin-axis is off by 1 degree, the system points away with this offset from the nadir. Due to the rotational motion of the platform, additional smear is lost in the transverse direction. These effects on the MTF are however minimal as the effect of linear smear was already shown to be relative small in magnitude in contrast to the jitter (Chapter 2).

## 7.2 Momentum Wheel

The momentum wheel is the main ADCS component of SHAPE. Its relatively large inertia with respect to the total and its speed make this design a challenge such as the rotor imbalance discussed in the previous section. In this section, additional are presented.

### 7.2.1 Structure and Material

For the control mode analyses, it was assumed that the momentum wheel was a disk-like structure. This is convenient for analysis, but is not mass-optimal with respect to the inertia. A ring-like structure where the mass is located further from the center of mass can provide the system a more optimal design in mathematical sense. There are however structural and material constraints. The momentum wheel should provide space for the fuel tank, thrusters and a electrical power system. This last is required to heat up the liquid or solid propellant. The use of propellant can be harmful to the system as static and dynamic imbalance can be induced if it is not designed properly. If this cannot be circumvented, isolators should be designed such the disturbances can be absorbed. Additionally, due to the centripetal acceleration while the wheel spins, structural loads will be present equivalent to 43 km/s$^2$ at its maximum moment arm. These are a few magnitudes of order higher values than the radial acceleration of the total system described in the previous section and can thus constraint the thruster design on the momentum wheel. The resulting force produces radial and hoop stresses in the momentum wheel and should be designed accordingly. The maximum radial and hoop stresses occur at the center and can be computed as follows (Hearn 1997);

$$\sigma_r = \sigma_h = (3 + \nu)\frac{\rho\omega^2 R^2}{8} \tag{7.4}$$

Assuming a thin disk-like structure out of aluminum with a material density of 2700 kg/m$^3$, a Poisson's ratio $\nu$ of 0.33, and a maximum radius $R$ of 8 cm, yields in a stress of 4.8 MPa. These stresses should be incorporated especially for the thrusters and its related components.

Eddy current torques will act on a body if it is conductive and spinning in a magnetic field. Due to the rotational speed of the momentum wheel, a small torque is generated in the presence of Earth's magnetic field which slows down the momentum wheel over time. To limit this torque, one can implement non-conductive materials or laminated layers to reduce eddy currents.

### 7.2.2 Momentum Wheel Torquing Subsystem (MWTS)

From requirement (S.4), the spinup torque was decided to be imparted by TU-Delft thrusters. Currently, the propellants of these thrusters are expected to be either liquid or solid water (Cervone et al. 2017). Two resistojets at opposing sides of the momentum wheel are expected to be placed to minimize static and dynamic imbalance. To meet requirement (S.8), a single thruster should be able to provide the required rotor angular momentum. The spinup duration is then doubled and thus twice the fuel expenditure is expected. The choice for connecting valves and fuel lines have been rejected as this will induce rotor imbalance and a fuel pump will be required to act against centripetal forces.

From the study by Cervone et al., a thrust of 1.52 mN and a mass flow of 1.63 mg/s had been estimated for the performance of a liquid water resistojet and 1.14 mN and 1.32 mg/s for the free molecular type (sublimation of ice). Assuming that the mass flow scales linearly with the thrust, a single 1 mN spinup thruster requires a propellant mass of 6.7 g and 7.2 g for liquid and sublimation type resistojets, respectively. Taking the redundancy factor of 2 for single thruster failure and an additional margin of 20%, 16 g or 17 g of fuel is expected to be stored in the fuel tank. The (scaled) power requirement for these types of resistojets are 3.5 and 4.0 W, respectively. This yields in energy storage capacity requirements of 26 and 30 kJ per thruster which includes a 20% margin to include uncertainties and battery inefficiency.

The choice of thruster type (and propellant) is still left for future work. It should be noted that liquid types will affect the system's initial state as liquid sloshing can effect the spacecraft's controllability. This is expected to be lessened over time due to the centripetal force caused by the rotation of the wheel. It should also be considered that the placement and single thruster failure should be incorporated in the design to avoid forces and moments induced by static and dynamic imbalance.

### 7.2.3 Angular Velocity Sensor

Measuring the relative rotational velocity of the rotor (e.g. tachometers) with respect to the platform plays a significant role for the control system. At least two sensors are required for redundancy and systematic calibration. The range of the rotational velocity should be between 0 to 7000 rpm. An important rotational velocity is at 5000 rpm mark as the magnetic bearings will be deployed. The operational range is expected from approximately 5000 to 7000 rpm. At these ranges, the changes in rotational velocity are lesser in magnitude and an increased accuracy is required. The instrumental accuracy of this sensor affects the system's pointing capabilities due to its relation in the dynamics as given in Equation 3.63. To stay within the MTF requirement, a minimum rotation rate of at least 5.5 mrad/s (target) or 3.8 mrad/s (desired) is needed. A tenth of this value is taken to insure this requirement and to adjust for inertia uncertainty.

## 7.3 Passive Damper

In Section 4.6, a passive damper was designed to verify its effect on the dual-spin spacecraft's nominal and acquisition modes. Hereby, a simple point mass precession type damper was used as the spacecraft should operate within low nutation angle values during. A point mass damper is commonly used as mathematical implementation tool for energy dissipation analysis. In reality, a range of passive dampers are available depending on the design requirements and constraints. The need for a damper however was verified as it can provide the system asymptotic stability and elevation of active control.

The passive damper requires to be broadband due to the expected loss in angular momentum over its lifetime and as a result SHAPE's precession frequency will decline from approximately 11 to 8 rad/s. The damping time constant can be determined from the worst-case scenario. This time is defined as the time the system is able to damp an initial value to a factor of $1/e$ of it. For the passive damper, these values are defined as the time it takes to damp from pitch control loss (Section 4.7.4) to within requirement values. The damping time constant can be calculated using the following function

$$\omega_{T,\max}(t) = \omega_{T,\max}(0)e^{-t/\tau_d} \tag{7.5}$$

with $\omega_{T,\max}(t)$ the transverse angular velocity at time $t$, $\omega_{T,\max}(0)$ the initial maximum transverse angular velocity, and $\tau_d$ the damping time constant. To damp the system within half an orbit from 6 mrad/s to half the target requirement value, a damping time constant of 0.58 orbits is computed. For the target goal, this is equivalent to 0.39 orbits.

## 7.4 Actuators

There are two sets of actuators required for SHAPE; thrusters and magnetorquers. The thrusters have as its only goal to provide the system with the angular momentum of 1 Nms for the major-axis spinup. The magnetorquers are used to provide the system for detumbling, pitch control and inertial angular momentum vector re-alignment.

### 7.4.1 Attitude Thrusters Subsystem (ATS)

Similar to the thrusters used for the momentum wheel, a fuel tank and propellants are needed. Assuming the same thrust level, one can obtain the required propellant mass and energy. The spinup time for this process is shorter due to the longer moment arm available. Taking a distance of 15 cm, a torque of 0.15 mNm can be produced. Using two thrusters to achieve a momentum of 1 Nms, a spinup time of around 3300 seconds is needed. Using the same margins as for MWTS, the propellant mass and electrical energy capacity can be determined. The mass is required to be at least 8.6 and 9.2 g for the liquid water and free molecular flow resistojet, respectively with an energy capacity of 12 and 13 kJ.

Like for the momentum wheel torquing subsystem, an interconnecting line and a pump from one fuel tank to the other will be difficult and inefficient. Therefore, this option has been excluded and a redundant system at both sides is chosen. Thruster misalignment can cause the system to nutate. Although the system can damp the transverse momentum within requirement values using a damper, a too large offset can either increase the settling time or limit pitch controllability.

### 7.4.2 Magnetorquers

From Chapter 4, it was concluded that the magnetorquers should produce a dipole moment of around 0.5 $Am^2$. Due to the nature of the magnetic field, only 2 axes can be controlled. Three axis control is however still possible as the field changes with respect to the orbital reference frame. The control scheme is therefore highly nonlinear. SHAPE's near polar orbit makes the pitch axis advantageous for control. At the magnetic poles, the field strength is at VLEO approximately 50 000 nT and at the equator 25 000 nT producing $1.3 \cdot 10^{-5}$ and $2.5 \cdot 10^{-5}$ Nm of torque for a dipole moment of 0.5 $Am^2$. In reality, lower values occur as SSO has an offset to the magnetic poles.

After the system has reached 90% of its mission lifetime (95% confidence), pitch control will be lost partially. It is expected that the image quality and pointing capabilities will be reduced exponentially over time. For the 50%, this is only the last 4 days or 1% of the mission. These are adequate values if one takes into account that the dipole moment produced must be increased by a factor of around 1.7 to 1.4 times to sustain end-of-life for 95% and 50% confidence, respectively.

Other important aspects of magnetorquers such as the sensitivity, linearity and noise are to be determined after a more thorough investigation of control schemes, sensor dynamics and estimators. A maximum upper limit for the magnetorquers should be at most 2 $mAm^2$. A higher value will increase the magnetic torque acting on the spacecraft and thus enlarging the angular offset of the inertial momentum vector.

## 7.5 Sensors

There are various sensors to measure the attitude and angular velocities of the spacecraft. From Section 4.7.3, it was found that the spacecraft immediately starts to oscillate with an amplitude of 0.7 degree due to external disturbances. This is already a large portion of the pointing budget and the sensor determination error has to be minimal. As therefore, a maximum of 0.1° attitude determination error is set. The control error can be of higher magnitude as the system can affect the amplitude of the oscillation. The adjustment should be at least within half its amplitude at a minimum of 2-sigma certainty.

### 7.5.1 Sensors Selection

There are several sensors available for CubeSat application. Sun sensors are one of the more commonly used sensors as they provide accurate absolute measurement with respect to its size and mass. It requires however to be within the view of the sun and therefore a spacecraft in umbra cannot sense its attitude with only sun sensors. SHAPE's maintenance operation is to take place in the midnight part of its orbit and thus sun sensors alone are not applicable. One can use a combination of sun sensors with conjunction with gyros to measure its attitude by integration. The shortcoming of this is that gyros for CubeSat have high drift errors. These are usually microelectromechanical systems (MEMS). The error drift of high-end MEMS type gyros are around the values of $1°/h$ such as Honeywell's HG4930 (Honeywell 2017). After a quarter of orbit, this can be around 0.4 degree and is thus unsuitable. Another option is to use star trackers. Despite their large volume and mass, these instruments provide the highest accuracy in the orders of arcseconds. Earth horizon sensors can also be employed and are suitable for both daylight and umbra operations. They lack in accuracy but consume less power and are lighter than star trackers.

During the nominal and pre-acquisition phase, fine and course sun sensors can be used, respectively. Fine sun sensors have high accuracy with a small field of view and vice versa for the latter. For the maintenance mode, two Earth sensors can provide full attitude during sunlight and umbra. Out of the available Commercial Off the Shelf (COTS) components, the best available contender is Maryland Aerospace's horizon sensor with a value of $< 0.25°$ (Maryland Aerospace 2017). To correct the oscillating angular momentum in the transverse plane, the ADCS is required to point the spacecraft within 0.7° in magnitude. A determination error of 0.25° will be sufficient. However, a more in-depth analysis is required on how the magnetorquer control error affect the pointing. During the nominal mode, a more accurate sensor is needed as the oscillations will add 0.7° to the pointing knowledge error. The horizon sensors can add up to 0.25° allowing only a very small margin for uncertainties. Thus, during nominal mode a fine sun sensor can be used with an accuracy of 0.1°.

Besides sun and Earth horizon sensors, magnetometers are required to sense the magnetic field and to feed the measurements to the magnetorquers. The use of magnetorquers for pitch control is anticipated to introduce the biggest contribution in the MTF budget yielding in body rates approximately to few times the mean motion. To approach the

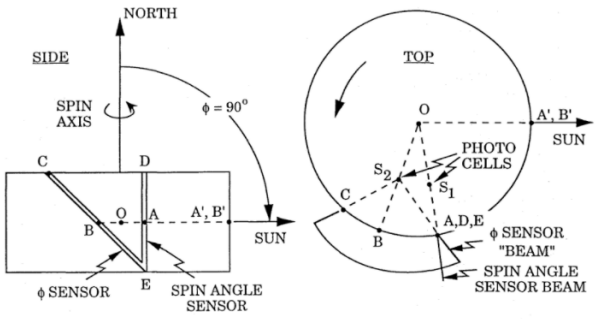


Figure 7.3: Schematic View on the Functioning of the V-beam Split Sensor (Bryson Jr 2015)

current accuracy of the IGRF model, a sensor sensitivity of 10 nT is required (Lowes 2010). For the body rates, gyros are commonly used. A necessary minimum condition for these measurements should be at most the tenth value from requirement (S-NM.5). From COTS components, these values tend to be magnitudes lower and thus image quality are expected to be virtually unaffected.

### 7.5.2 High Rotational Velocity Sensors

During the pre-acquisition, the spacecraft has to achieve its all-spun configuration. The spacecraft increases its rotation rate and centripetal accelerations can be measured. If the inertia of the spacecraft is known within high accuracy, accelerometers can be used to measure the rotational rate. Gyros are unsuitable as their range are limited. Assuming that no external disturbances affect the spacecraft and inertia are known with exact accuracy, the acceleration range can be determined as

$$a = r_a \omega^2 = r_a \left( \frac{H}{I_2} \right)^2 \tag{7.6}$$

with $r_a$ the radial distance from the spin axis to the accelerometer. Placing the accelerometer further away yields in better measurements of the angular velocity as the arm amplifies this value, assuming that the distance is exactly known. For $r_a = 15$ cm, an acceleration of 7.0 m/s$^2$ is expected. The range should therefore be between 0 to 8 m/s$^2$. Availability of accelerometer in all three axes allows also the measurement of transverse angular momenta. If these are to be measured for requirement (S-NM.5) values the accuracy of the accelerometers should be better than $2.5 \cdot 10^{-8}$ m/s$^2$. These values are too accurate for CubeSat applications (order of 1 mm/s$^2$) and uncertainties of internal and external disturbance forces will dominate over the measurement of the rotational rate. Accelerometers can however be used as a coarse measurement device. A more accurate sensor can be deployed after a certain threshold has been achieved to minimize power.

For a more accurate rotation rate sensor, inertial angular measurements have to be determined. One of such sensor is the V-beam split sensor (Bryson Jr 2015). This device consists of two photocells that are mounted on a slit which forms a V as shown in Figure 7.3. The temporal measurement between each split then determines the rotational rate of the spacecraft. Assuming that the spin axis is normal to the sun rays and are in the sunlight side of the orbit, two angled sun sensors can be used to achieve a similar function. For a rotational speed of 6.8 rad/s, the rotational time is equivalent to 0.23 s for a 90° offset of the sensors. For the nominal mode, the rotation rate is expected to match the mean motion. For the instrument to match this exact is difficult and angular offsets smaller than 0.01° can introduce larger errors. Therefore, ten times the mean motion is taken for the sensitivity. This is approximately 0.6 degree per second. After the momentum wheel spinup, the spacecraft might have a rotation rate of up to 0.6°/s which can easily be adjusted to the mean motion. The rotation time sensitivity then equals to 2.9 ms which is approximately the value to a 1 degree offset of the sensors (2.6 ms). If four sensors are used at each side of the spacecraft, a more accurate value can be estimated. If this value cannot be achieved due to the distance of each sun sensor, a V-beam split sensor should be designed.

## 7.6 Pointing Error and MTF Budget

In Table 7.2, the estimated pointing error budget is shown for the worst-case scenario at 95% confidence defined over the observation window of half an orbit (nominal mode). The pointing error budget achieves a value close to the 1 degree requirement value without considering the TBDs at the design point of 280 km. At higher altitudes, the external disturbances are expected to be lower and thus a lower oscillatory and drift motions of the inertial transverse angular vector are anticipated (Section 4.7.4). The TBDs are yet to be resolved after one obtains results from pitch magnetorquer control analysis. These are expected to be the dominant factors for the pitch error. If the control accuracy exceeds, another solution has to be found such as a pitch reaction wheel. Additionally, the design of the momentum wheel and the suspension system influence whether the induced jitters are damped effectively and are also principal to keep the pointing accuracy within 1 degree and image quality within 15% or 20% values.

In Table 7.3, the attitude stability budget is given using angular velocities. Similar to the pointing error budget, several TBDs are yet to be found to see whether the system can achieve either the target or desired MTF goals. In the pitch control, only the mean motion is plays a significant role. Dependent on the magnetorquer qualities, this can be mitigated.

Table 7.2: Worst-Case Pointing Error Budget

| **Contribution** | **Pitch Error** [deg] | **Transverse Error** [deg] |
|---|---|---|
| Attitude Determination | 0.1 | 0.1 |
| $\vec{H}$ Oscillatory Motion | ~0 | 0.7 @ 280 km |
| $\vec{H}$ Secular Drift | ~0 | 0.02 @ 280 km |
| Magnetometers | TBD | ~0 |
| Pitch Magnetorquer | TBD | ~0 |
| Spin Axis Angular Offset | 0 | 0.05 |
| MW Imbalance | TBD | TBD |
| Payload Offset | 0.05 | 0.05 |
| **Total** without TBD | 0.15 | 0.92 |

Table 7.3: Attitude Stability Budget

| **Contribution** | **Pitch Angular Rate** [mrad/s] | **Transverse Angular Rates** [mrad/s] |
|---|---|---|
| Nutation | ~0 | 0.02 @ 280 km |
| Mean Motion | 1.1 | ~0 |
| Gyroscopes | ~0 | ~0 |
| External Disturbances | ~0 | ~0 |
| Pitch Magnetorquer | TBD | ~0 |
| MW Imbalance | TBD | TBD |
| **Total** without TBD | 1.1 | 0.02 |
| target / desired | (20% / 28%) | (0.4% / 0.5%) |

## 7.7 Flow Block Diagram

In Figure 7.4, the diagram is shown for the procedure from the detumbling to the nominal mode. For each mode, the peak power consumption has been estimated using COTS components available on CubeSatShop (2017). Note that the power consumption is compliant with the requirements given in Section 2.3.1.

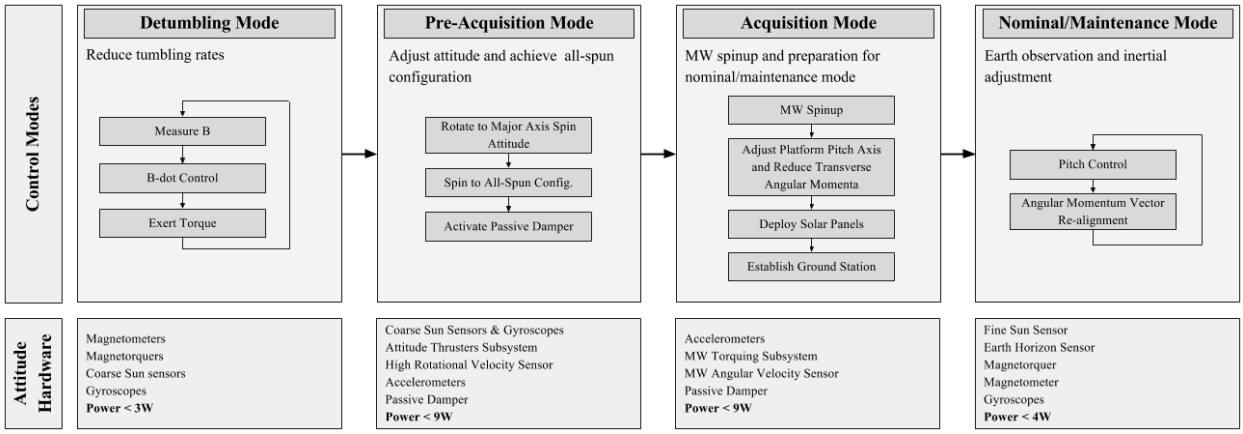


Figure 7.4: Flow Block Diagram from the Detumbling to Nominal Mode

## 7.8 ADCS Requirements

The ADCS components discussed in the previous sections are translated into requirements and are listed in Table 7.4 to Table 7.8. It should be noted that these are not definite and are only as a general line for the initial design.

Table 7.4: System Principal ADCS Requirements

| **Code** | **Requirements** | **Rationale/Note** |
|---|---|---|
| SS.1 | SHAPE's product of inertia shall be contained within <TBD> kg $m^2$. | TBD resolved after resonance capture analysis. |
| SS.2 | SHAPE's subsystems and components shall be able to withstands a load of at least 7.03 m $s^{-2}$ in the major-axis during the pre-acquisition and acquisition phases. | Centripetal acceleration |
| SS.3a | The momentum wheel shall have an energy dissipation rate of <TBD> W or lower. | TBD to be resolved after energy dissipation rate analysis of the momentum wheel. |
| SS.3b | The platform shall have an energy dissipation rate of more than 0.016 times the rotor's rate. | To be updated after inertia and flexible dynamics analyses & damping criteria (Section 4.6.2) |
| SS.4 | The momentum wheel suspension system shall be able to damp jitter forces of up to 5.4 N at a frequency of the wheel's rotational frequency. | Limit transverse body rates (Section 7.1.1) |
| SS.5a | The momentum wheel shall have a static imbalance of < 1 g cm. | Limit transverse body rates (Section 7.1.1) |
| SS.5b | The momentum wheel shall have a better dynamic imbalance than 30 g $cm^2$ (desired) / 50 g $cm^2$ (target). | Limit transverse body rates (Section 7.1.1) |
| SS.6 | The system's center of mass shall be located at a magnitude of less than 1 mm from the center of spin axis. | Limit transverse body rates (requirement (S-NM.5)) |
| SS.7 | The spin axis shall have a maximum angular offset of 0.05°. | Pointing budget |

Table 7.5: Momentum Wheel Requirements

| Code | Requirements | Rationale |
|---|---|---|
| MW-S.1 | The axial mass moment of inertia of the momentum wheel shall be $18 \cdot 10^3 \pm 30$ g cm$^2$. | Section 4.4 and imbalance |
| MW-S.2 | The torquing subsystem shall be integrated within the momentum wheel. | Section 7.2.2 and requirement (S.4) |
| MW-S.3 | The momentum wheel's subsystems and components shall be able to withstands a load of at least 43 km s$^{-2}$ in the $b_2$-axis during the pre-acquisition and acquisition phases. | Centripetal acceleration |
| MW-T.1a | The MWTS shall have two thrusters which can provide a torque of at least 0.16 mNm. | Requirement (within 1 orbit) and to be updated after thruster design. |
| MW-T.1b | A single thruster shall be able to complete the momentum wheel spinup procedure. | Section 4.4 and requirement (redundancy) |
| MW-T.2 | The MWTS' fuel tank shall contain a propellant mass of $17 \pm 1$ g. | Section 7.2.2 |
| MW-T.3a | The MWTS' electrical power subsystem shall have a power output of at least 4 W. | Section 7.2.2 and subjected to change dependent on thruster design. |
| MW-T.3b | The MWTS' electrical power subsystem shall have an energy storage capacity of at least 26 kJ | Section 7.2.2 and subjected to change dependent on thruster design. |
| MW-AS.1 | Two angular velocity sensors shall be mounted on the momentum wheel suspension system. | Redundancy and relative measurement |
| MW-AS.2 | The rotational rate sensors shall have a measurement range of 0 to 7000 rpm. | Section (7.2.3) |
| MW-AS.3 | The momentum wheel rotational rate sensor(s) shall have a sensitivity better than 0.6 mrad/s (target) / 0.4 mrad/s (desired). | MTF requirement and Section (7.2.3) |

Table 7.6: Passive Damper Requirements

| Code | Requirements | Rationale |
|---|---|---|
| PD.1 | The damper shall be able to damp frequencies from 8 to 11 rad/s. | Rotational energy loss cause change in precession frequency |
| PD.2 | The damper shall have a better damping time constant than 0.58 (desired) / 0.39 (target) orbits. | Section 7.3 |

Table 7.7: Actuator Requirements

| Code | Requirements | Rationale |
|---|---|---|
| A-T.1 | The ATS' thrusters shall deliver a thrust of at least 1 mN. | Minimize spin time for requirement ... |
| A-T.2 | The ATS' thrusters shall have a better alignment than 0.1° with respect to the principal major axis. | Avoid large nutation angles after spin. |
| A-T.3 | The ATS' fuel tank shall contain at least 8.6 g. | Assuming water as propellant (Section 7.4.1). |
| A-T.4a | The ATS shall receive a power output level of at least 4 W. | Same as above |
| A-T.4b | The ATS shall be able to deliver at least 26 kJ of heat. | Same as above |
| A-M.1 | The magnetorquers shall able to provide a nominal dipole moment of >0.5 $Am^2$ at all axes. | Torque |
| A-M.2 | The magnetorquers shall have a linearity better than <TBD>% on all axes. | TBD to be resolved after in-depth nominal mode control analysis. |
| A-M.3 | The magnetorquers shall have a resolution better than <TBD> $mAm^2$ on all axes. | TBD to be resolved after in-depth nominal mode control analysis. |
| A-M.4 | The magnetorquers shall have a residual magnetic moment lower than 2 $mAm^2$. | To be updated after in-depth control analysis. Note that this is the upper limit as this value had been assumed to be for the whole spacecraft. |

Table 7.8: Attitude Sensor Requirements

| Code | Requirements | Rationale |
|---|---|---|
| AS.S1 | The absolute measurement sensors should provide a better pointing accuracy than 0.1°. | |
| AS.A1 | The accelerometers should have a range of at least 0 to 8 $m/s^2$. | Coarse angular velocity measurement |
| AS.A2 | The gyros should have a better resolution than <TBD> $m/s^2$. | TBD to be resolved after power consumption analysis of the high rotational velocity sensor. |
| AS.G1 | The gyros should have a bias better than 0.003 deg/s. | Requirement (S-NM.5) |
| AS.G2 | The gyros should have a drift error better than 0.003 deg/s. | Requirement (S-NM.5) |
| AS.M1 | The magnetometers should have a range of -60 000 to 60 000 nT. | Maximum magnitude of the Earth's magnetic field at 50 000nT |
| AS.M2 | The magnetometers should have a sensitivity better than or equal to 10 nT. | IGRF Model has a root mean square error of 10 NT |

# Chapter 8

# Conclusion and Recommendation

In this chapter, an overview is given of the results and choices taken throughout the analyses as performed in the previous chapters and a conclusion is given based on the research objective in the introduction. Additionally, several recommendations are given for work to be done.

## 8.1 Conclusion

In this thesis, SHAPE's momentum wheel design has been revisited and redesigned based on worst-case predictions of the atmospheric density for the next solar cycle (# 25). As the next solar cycle is approaching at the time of this research and due to the limited availability of observed data points, an accurate prediction could not be made. The predicted atmospheric densities for the 95% and 50% confidence intervals showed a large deviation yielding in lifetime differences of more than half a year. Nevertheless, the design has been based on the 95% interval at the point of minimal lifetime to design the spacecraft on the worst-case scenario. At this point, the lifetime has been determined to be 10 days less than the required 6 months and it is concluded that the launch window between the year 2023 and 2024 should be avoided with the caution that this window has uncertainty in itself.

Based on this condition, the momentum wheel have been designed. Due to the exponential increase in aerodynamic disturbance torque over its lifetime, the design point located at 90% into the lifetime has been taken as it was found that the mass of the momentum wheel could be reduced by 400 g and the radius by 2 cm assuming a disk-like structure. The selection of this lifetime has been done in consideration of possible control actuators, mass constraint of the wheel, and the maximum and minimum of half orbit requirement for maintenance and nominal operations, respectively to optimize the Earth observation time. Assuming that the momentum wheel is made out of aluminum, it has been estimated to have a radius of 8 cm, a thickness of 1 cm and a mass of 570 g.

Furthermore, for the nominal and maintenance design phases, damping has been found to be necessary under the conditions that the nutation angle exceeds 0.1 degree and a product of inertia of 10% of the moments of inertia. This angle corresponds to a transverse momentum of 1.7 mrad/s which is a considerable part of the attitude stability margin and thus the use of a passive damping system has therefore found to be positive. Also, due to its asymptotic stability properties, transverse momenta of 1.5 mNms can be damped to minimal values in less than 0.1 orbits. This is especially significant if the momentum wheel is unbalanced, producing an undesired torque and undampable parasitic angular momenta. Damping allows to minimize the nutation angle and is therefore decided to be integrated into the ADCS design.

To reach the nominal state, several strategies have been surveyed on their performance. Out of the many strategies proposed, it was found out that only three candidate options were distinct and performing within reasonable bounds. Two of these options should first attain the all-spun condition at the desired angular momentum of the momentum wheel on either the major or the minor axis. From this point on, by spinning the rotor at a constant rate, the spacecraft's nominal orientation can be achieved. The major axis showed very low nutational angles after completion which is critical as otherwise the system loses its pitch controllability due to the effect of gyroscopic coupling. In contrast, the minor axis was found to lead to a large increase in nutation angle. The addition of passive damping improved the reduction of the nutation angle from 0.6 to 0.005 degrees. Similarly, the minor axis spinup showed a decrease from 59

to 5 degrees. The initial phase of the minor axis spinup was expected to destabilize as the point of lowest energy was located at the major axis equilibrium points. By adding an energy dissipative device, the system repelled itself from its initial position. These destabilizing effect although not detrimental was able to be bypassed by adding a locking mechanism, reducing the nutation angle to 4.5 degrees. During the spinup, an unbalanced momentum wheel can cause dynamic imbalance to the system for which it can be captured in a so-called resonance trap. If the system is captured, the nutation angle will increase violently. Solutions such as applying a periodic torque with a thruster is expected to be difficult and analysis of exact initial condition for escape can increase risk of failure due to non-torque-free conditions. Rather, minimizing the dynamic offset is a better approach to obtain satisfactory results by lessening the effect of resonance capture.

The third strategy was based on using additional active controllers to steer the system to the desired attitude. The spinup is expected to start from an initial zero-momentum condition. For this procedure, thrusters are implemented to provide a torque with the same magnitude as the momentum wheel thrusters to negate the platform spinup. Additionally, magnetorquers are integrated within the procedure to adjust for an offset in initial conditions and external disturbances. Hereby, a robust nonlinear control scheme called the sliding mode controller was chosen to correct for uncertainties. It was found that the initial part (approximately first quarter orbit) of the spinup was crucial for a successful spinup. As the gyroscopic stiffness is not yet developed, corrections with low torque can easily be executed. However, at larger angular offsets from the desired state and disturbance, an insufficiency of the control torque can cause the spacecraft to oscillate with large amplitude.

Depending on positive and negative characteristics of each spinup process, a trade-off had been taken to select an optimal solution for SHAPE. The minor axis spinup was found not able to provide the adequate transverse angular momentum levels, despite its capability to provide partial power through solar panels. In contrary, the major axis spin has the solar panels aligned perpendicular to the sun synchronous orbital plane and partial power generation can only be achieved near the end of the procedure. Its advantage over the minor axis spin is that the transverse momenta are within mNms values. For the third strategy, it was concluded that the dependence on the initial condition adds too much risk. Additionally, magnetorquers dynamics have not been included in the simulations making the control scheme even more complex. Although theoretically full power can be generated due to a steady platform, full deployment of all the solar panels are to be avoided until gyroscopic stiffness has established to moderate values as vibrations can induce loads to the system. Thus, the major axis spin has been taken. To achieve the all-spun configuration, thrusters has been added as the use of magnetorquers demands a spinup time of approximately 18 orbits.

From the results of the detumbling analysis, it was found that 0.5 $Am^2$ magnetorquers can provide reduction of body rates within 1 orbit to several mean motion values. The bang-bang B-dot type controller was found to be only slightly faster while consuming around 2 to 3 times more power over a single orbit. Furthermore, the static gain controller has found to be able to damp the tumbling rates with magnitude of 26 degree per second to mean motion magnitudes within 0.75 orbits in contrast to over 0.9 orbits with the bang-bang controller. The system can damp magnitudes of up to 35 deg/s in a single orbit.

In Chapter 7, the requirements for the ADCS system were specified. The majority of stringent requirements resulted from the effect of momentum wheel's static and dynamic imbalances causing high internal disturbances. To reduce these, the spacecraft requires very strict mass positioning of subsystems. The momentum wheel suspension subsystem is also required to have isolators to damp the high frequency disturbances induced by imbalance. Under the assumptions that these motions can be damped, SHAPE is expected that at the design point of 280 km altitude can achieve 1 degree pointing performance and fulfill the attitude stability (MTF) requirement values under worst-case conditions. These assumptions however cannot be simply made and a thorough analysis is required to verify the one pointing performance.

## 8.2 Recommendations

As mentioned in the previous section, the design has been set at the 95% confidence interval for the atmospheric density prediction which showed a large discrepancy between the 50% interval. It is recommended to do a re-iteration of the momentum wheel 30 months into the solar cycle. At this point, a more accurate prediction can be made of the atmospheric density for which a more optimized and certain design can be made yielding most likely in a lower angular momentum and thus a lower mass and less power consuming design. For future work, the other subsystem of SHAPE and its payload are yet to be designed. Within the framework of the ADCS, there are several analyses and designs to be performed in more detail as they can affect the pointing performance considerably. These are as follows;

- **Energy Dissipation Analysis**; due to eddy currents and aerodynamic friction, the momentum wheel dissipates its rotational energy into heat which can have destabilizing effect on the spacecraft. Further analysis is required to confirm whether this destabilizing effect is critical or not.
  **Passive Damper Design**; above analysis is to be paired with the passive damper design. If energy dissipation is found to be insufficient, a passive damper should incorporate additional dissipate capabilities. Additionally, a different damper design should be selected than the one used for the analysis, taking into account the requirements set up in Chapter 7 while considering the size and mass.

- **Resonance Capture Analysis**; static and dynamic imbalance can cause very high internal disturbances if no actions are undertaken. An in-depth analysis is to be performed, taking limitations in manufacturing into account and a feasibility analysis should be performed whether liquid or solid propellants on the MWTS is possible. If not, the MWTS is to be replaced with an electrical torquing subsystem.
  **Momentum Wheel Suspension Subsystem Design**; adding passive or active isolators is most likely due to the high rotational velocity of the momentum wheel, inducing high static imbalance for even accurate structural designs. These isolators can be implemented within the magnetic bearing of the suspension system. The design of this system is critical to allow a pointing performance within 1 degree accuracy and attitude stability.

- **Pitch Control Analysis using Magnetorquers**; in this work, full controllability of all three axes was assumed (except for detumbling). This has consequences for both the pointing performance and the image quality in the in-track direction as this assumption is not valid using magnetorquers. If a set of magnetorquers cannot provide sufficient control accuracy, the pointing and/or angular velocity budgets cannot be met. Instead a pitch reaction wheel and a set of magnetorquers can be implemented as a solution. The magnetic bearings and isolators can then absorb disturbances induced by this reaction wheel. Changing the system to a "hybrid" bias momentum spacecraft.

- **Pre-Acquisition Mode Analysis**; albeit not as significant as the other analyses, a partial spinup before attaining the all-spun configuration can improve the procedure. The expenditure of energy can however limit this process and further analysis is recommended.

# Bibliography


*6U CubeSat Design Specification* (2016), Technical Report X1, The CubeSat Program, Cal Poly SLO.

Alfriendt, K. (1976), 'Elementary magnetic attitude control system', *J. SPACECRAFT* **13**(5).

Barba, P. & Aubrun, J. (1976), 'Satellite attitude acquisition by momentum transfer', *AIAA Journal* **14**(10).

Bowman, B., Tobiska, W. K., Marcos, F., Huang, C., Lin, C. & Burke, W. (2008), A new empirical thermospheric density model jb2008 using new solar and geomagnetic indices, *in* 'AIAA/AAS Astrodynamics specialist conference and exhibit', p. 6438.

Boyle, J., Greyerbiehl, J. & Mosher, E. (1969), 'Experimental determination of eddy-current torques on bodies rotating relative to a uniform magnetic field'.

Bracewell, R. N. & Garriott, O. K. (1958), 'Rotation of artificial earth satellites', *Nature* **182**(4638), 760–762.

Bryson Jr, A. E. (2015), *Control of spacecraft and aircraft*, Princeton university press.

Bubnicki, Z. (2005), *Modern control theory*, Springer Science & Business Media.

Cervone, A., Zandbergen, B., Guerrieri, D., e Silva, M. D. A. C., Krusharev, I. & van Zeijl, H. (2017), 'Green micro-resistojet research at delft university of technology: new options for cubesat propulsion', *CEAS Space Journal* **9**(1), 111–125.

Chen, J. & Kane, T. (1979), 'Reorientation of a gyrostat', *Journal of the Astronautical Sciences* **27**, 85–90.

Cherchas, D. & Hughes, P. (1973), 'Attitude stability of a dual-spin satellite with a large flexible solar array', *Journal of Spacecraft and Rockets* **10**(2), 126–132.

Cochran Jr, J. & Thompson, J. (1980), 'Nutation dampers vs precession dampers for asymmetric spacecraft', *Journal of Guidance, Control, and Dynamics* .

CubeSatShop (2017), 'One-stop webshop', `https://www.cubesatshop.com/`. Accessed: 2017-09-23.

Doornbos, E. (2012), *Thermospheric density and wind determination from satellite dynamics*, Springer Science & Business Media.

Doroshin, A. V. (2014), 'Chaos and its avoidance in spinup dynamics of an axial dual-spin spacecraft', *Acta Astronautica* **94**(2), 563–576.

Engberg, B., Ota, J. & Suchman, J. (1995), 'The opal satellite project: Continuing the next generation of small satellite development'.

GeoEye (2009), 'Geoeye-1 instrument/product desciption', `http://www.ugpti.org/smartse/research/citations/downloads/Digital%20Globe-GeoEye-1_Product_guide-2014.pdf`.

Guelman, M. (1989), 'On gyrostat dynamics and recovery', *Journal of the Astronautical Sciences* **37**(2), 109–119.

Hall, C. (1991), An Investigation of Spinup Dynamics of Axial Gyrostats Using Elliptic Integrals and the Method of Averaging, PhD thesis, Cornell University.

Hall, C. D. (1995), 'Spinup dynamics of gyrostats', *Journal of Guidance, Control, and Dynamics* **18**(5), 1177–1183.

Hall, C. D. (1996), 'Momentum transfer in two-rotor gyrostats', *Journal of Guidance, Control, and Dynamics* **19**(5), 1157–1161.

Hall, C. D. (1997), 'Momentum transfer dynamics of a gyrostat with a discrete damper', *Journal of Guidance Control and Dynamics* **20**, 1072–1075.

Hall, C. D. (1998), 'Escape from gyrostat trap states', *Journal of guidance, control, and dynamics* **21**(3), 421–426.

Hall, C. & Rand, R. (1994), 'Spinup dynamics of axial dual-spin spacecraft', *Journal of Guidance, Control and Dynamics* **17**(1).

Hathaway, D. H., Wilson, R. M. & Reichmann, E. J. (1994), 'The shape of the sunspot cycle', *Solar Physics* **151**(1), 177–190.

Hathaway, D. H., Wilson, R. M. & Reichmann, E. J. (1999), 'A synthesis of solar cycle prediction techniques'.

Hearn, E. J. (1997), *Mechanics of Materials 2: The mechanics of elastic and plastic deformation of solids and structural materials*, Butterworth-Heinemann.

Heidt, H., Puig-Suari, J., Moore, A., Nakasuka, S. & Twiggs, R. (2000), 'Cubesat: A new generation of picosatellite for education and industry low-cost space experimentation'.

Helal, H. R. & Galal, A. (2013), 'An early prediction of the maximum amplitude of the solar cycle 25', *Journal of advanced research* **4**(3), 275–278.

Hiremath, K. M. (2008), 'Prediction of solar cycle 24 and beyond', *Astrophysics and Space Science* **314**(1), 45–49.

Honeywell (2017), 'Non-itar micro electro mechanical system (mems) inertial measurement units (imus)âĂŃâĂŃ', `https://aerospace.honeywell.com/en/products/navigation-and-sensors/non-itar-micro-electro-mechanical-system-inertial-measurement-units?gclid=EAIaIQobChMI6JXT25Kj1gIVGouyCh20xwwPEAAYASAAEgKABPD_BwE`. Accessed: 2017-09-13.

Hooper, J. W. (1957), 'The damping of metallic cylindrical and spherical bodies rotating in a uniform magnetic field', *Army Ballistic Missile Agency, Technical Report DG* .

Hughes, P. (2004), *Spacecraft Attitude Dynamics*, Dover Publications.

Hung, J. Y., Gao, W. & Hung, J. C. (1993), 'Variable structure control: A survey', *IEEE transactions on industrial electronics* **40**(1), 2–22.

Hyperion Technologies (2017), 'Mtq400 product description', `http://hyperiontechnologies.nl/products/mtq400/`. Accessed: 2017-09-18.

Janson, S. & Hinkley, D. (2009), 'Spin dynamics of the pico satellite solar cell testbed spacecraft'.

Javaraiah, J. (2015), 'Long-term variations in the north–south asymmetry of solar activity and solar cycle prediction, iii: Prediction for the amplitude of solar cycle 25', *New Astronomy* **34**, 54–64.

Joseph, G. (2015), *Building earth observation cameras*, CRC Press.

Kane, T. R. (1970), 'Solution of the equations of rotational motion for a class of torque-free gyrostats', *AIAA Journal* **8**(6), 1141–1143.

Kinsey, R., Mingori, D. & Rand, R. (1992), Nonlinear controller to reduce resonance effects during despin of a dual-spin spacecraft through precession phase lock, *in* 'Decision and Control, 1992., Proceedings of the 31st IEEE Conference on', IEEE, pp. 3025–3030.

Kuiper, J. & Dolkens, D. (2016), Advanced earth observation systems with high spatial resolution, *in* 'The 4S Symposium'.

Larson, W. J. & Wertz, J. R. (1999), *Space mission analysis and design*, Kluwer Academic Publishers.

Lavretsky, E. & Wise, K. A. (2013), Optimal control and the linear quadratic regulator, *in* 'Robust and Adaptive Control', Springer, pp. 27–50.

Li, K., Feng, W. & Li, F. (2015), 'Predicting the maximum amplitude of solar cycle 25 and its timing', *Journal of Atmospheric and Solar-Terrestrial Physics* **135**, 72–76.

Likins, P. (1986), 'Spacecraft attitude dynamics and control-a personal perspective on early developments', *Journal of Guidance, Control, and Dynamics* **9**(2), 129–134.

Liu, J. (2017), *Sliding Mode Control Using MATLAB*, Academic Press.

Lowes, F. (2010), 'The international geomagnetic reference field: A "health" warning', `https://www.ngdc.noaa.gov/IAGA/vmod/igrfhw.html`. Accessed: 2017-09-17.

Manchester, Z. R. (2016), Lyapunov-based control for flat-spin recovery and spin inversion of spin-stabilized spacecraft, *in* 'AIAA/AAS Astrodynamics Specialist Conference', p. 5644.

Markley, F. L. & Crassidis, J. L. (2014), *Fundamentals of spacecraft attitude determination and control*, Vol. 33, Springer.

Maryland Aerospace (2017), 'Static earth sensor product specification', `http://maiaero.com/datasheets/MAI-SES-Specifications-20150827.pdf`. Accessed: 2017-09-17.

McName, J. & Pan, V. (2013), *Numerical Methods for Roots of Polynomials - Part II*, Elsevier Science.

McNish, A. & Lincoln, J. (1949), 'Prediction of sunspot numbers', *Eos, Transactions American Geophysical Union* **30**(5), 673–685.

Merrill, R. T. (2010), *Our magnetic earth: the science of geomagnetism*, University of Chicago Press.

Mingori, D. (1969), 'Effects of energy dissipation on the attitude stability of dual-spinsatellites.', *AIAA Journal* **7**(1), 20–27.

NASA - Marshall Space Flight Center (2017), 'Solar cycle progression & forecast', `https://sail.msfc.nasa.gov/`. [Online; accessed 09-March-2017].

Neishtadt, A. & Pivovarov, M. (2000), 'Separatrix crossing in the dynamics of a dual-spin satellite', *Journal of Applied Mathematics and Mechanics* **64**(5), 709–714.

Nelson, N. R. & Barry, P. (2001), Measurement of hyperion mtf from on-orbit scenes, *in* 'Geoscience and Remote Sensing Symposium, 2001. IGARSS'01. IEEE 2001 International', Vol. 7, IEEE, pp. 2967–2969.

Niehuss, K., Euler Jr, H. & Vaughan, W. W. (1996), Statistical technique for intermediate and long-range estimation of 13-month smoothed solar flux and geomagnetic index, Technical report, DTIC Document.

NOAA (2015), 'Wandering of the geomagnetic poles', `https://www.ngdc.noaa.gov/geomag/GeomagneticPoles.shtml`. Accessed: 2017-06-07.

Pesnell, W. D. (2008), 'Predictions of solar cycle 24', *Solar Physics* **252**(1), 209–220.

Petrovay, K. (2010), 'Solar cycle prediction', *Living Reviews in Solar Physics* **7**(1), 6.

Picone, J., Hedin, A., Drob, D. P. & Aikin, A. (2002), 'NRLMSISE-00 empirical model of the atmosphere: Statistical comparisons and scientific issues', *Journal of Geophysical Research: Space Physics* **107**(A12).

Pishkalo, M. (2008), 'Preliminary prediction of solar cycles 24 and 25 based on the correlation between cycle parameters', *Kinematics and Physics of Celestial Bodies* **24**(5), 242.

Preumont, A. (2011), *Vibration control of active structures: an introduction*, Vol. 179, Springer Science & Business Media.

Reijneveld, J. (2011), Dnx-tud-tn-0143, Technical Report 1.5, Delft University of Technology.

Rigozo, N., Echer, M. S., Evangelista, H., Nordemann, D. & Echer, E. (2011), 'Prediction of sunspot number amplitude and solar cycle length for cycles 24 and 25', *Journal of Atmospheric and Solar-Terrestrial Physics* **73**(11), 1294–1299.

Riki Munakata (2009), Cubesat design specification, Technical Report 12, California Polytechnic State University.

Ruiter, A. D. (2012), 'Magnetic control of dual-spin and bias-momentum spacecraft', *Journal of Guidance, Control, and Dynamics* **35**(4), 1158–1168.

Saberi, A., Lin, Z. & Teel, A. R. (1996), 'Control of linear systems with saturating actuators', *IEEE Transactions on Automatic Control* **41**(3), 368–378.

Sandau, R. (2009), *Digital airborne camera: introduction and technology*, Springer Science & Business Media.

Sandfry, R. A. & Hall, C. D. (2004), 'Steady spins and spinup dynamics of axisymmetric dual-spin satellites with dampers', *Journal of spacecraft and rockets* **41**(6), 948–955.

Scher, M. & Farrenkopf, R. (1974), 'Dynamic trap states of dual-spin spacecraft', *AIAA Journal* **12**(12), 1721–1725.

Shtessel, Y., Edwards, C., Fridman, L. & Levant, A. (2014), *Sliding mode control and observation*, Springer.

Smythe, W. B. (1950), 'Static and dynamic electricity'.

Space Electronics (2017), 'POI spin balance series', `https://www.space-electronics.com/Products/poi-spin-balance-series`. Accessed: 2017-09-10.

Space Weather Prediction Center - National Oceanic and Atmospheric Administration (2017), 'Solar cycle progression', `http://www.swpc.noaa.gov/products/solar-cycle-progression`. [Online; accessed 07-March-2017].

*Space systems - Estimation of orbit lifetime* (2010), Technical report, International Organization for Standardization.

Storch, J. (2002), Aerodynamic disturbances on spacecraft in free-molecular flow, Technical report, DTIC Document.

the National Centers for Environmental Information (2017), 'Solar-terrestrial physics (stp)', `https://www.ngdc.noaa.gov/stp/stp.html`. Accessed: 2017-06-07.

Thébault, E., Finlay, C. C., Beggan, C. D., Alken, P., Aubert, J., Barrois, O., Bertrand, F., Bondar, T., Boness, A., Brocco, L. et al. (2015), 'International geomagnetic reference field: the 12th generation', *Earth, Planets and Space* **67**(1), 79.

Tsui, R. (1994), Resonance capture in unbalanced dual-spin spacecraft, PhD thesis, U.S. Air Force Institute of Technology.

Tsui, R. & Hall, C. D. (1995), 'Resonance capture in unbalanced dual-spin spacecraft', *Journal of Guidance, Control, and Dynamics* **18**(6), 1329–1335.

Verhulst, F. (2006), *Nonlinear differential equations and dynamical systems*, Springer Science & Business Media.

Wakker, K. F. (2015), *Fundamentals of astrodynamics*, TU Delft Library.

Wie, B. (1998), *Space Vehicle Dynamics and Control*, AIAA Education Series.

# Appendix A

# Infinitesimal Analysis

To analyze nonlinear systems, a technique called infinitesimal or linear stability analysis is used (Hughes 2004). This method approximates the nonlinear system by linearization using Taylor series and neglecting the higher order terms. Assume a linearized autonomous system as

$$\dot{\mathbf{x}} = \mathbf{A}\mathbf{x} \tag{A.1}$$

The eigenvalues of the matrix $\mathbf{A}$ then determines the system's stability which can be computed using the following

$$\det\left(\mathbf{A} - \boldsymbol{\lambda}\bar{\mathbf{I}}_k\right) = 0 \tag{A.2}$$

with $\boldsymbol{\lambda}$ the eigenvalues. If the real parts of $\lambda_k$ are smaller or equal to zero for $k = 0, \ldots, n$ and the real part of of the eigenvalues which are equal to zero are distinct, then the solution $\mathbf{x} = 0$ of the system described in Equation A.1 is said to be Lyapunov stable. The system is asymptotically stable if all the real parts of $\boldsymbol{\lambda}$ are smaller than zero and unstable for the condition if there exists an eigenvalue which has a real part larger than zero.

To check whether the real parts of eigenvalues of systems of order $n = 4, \ldots, 8$ are larger than zero, one can use the Routh-Hurwitz criterion (Hughes 2004). This is based on the coefficients of the characteristic polynomial defined as

$$p_k(\boldsymbol{\lambda}) \triangleq \det\left(\mathbf{A} - \boldsymbol{\lambda}\bar{\mathbf{I}}_k\right) \tag{A.3}$$

which can be expanded for system with order 4 to 8 as

$$p_k(\boldsymbol{\lambda}) \triangleq \lambda^k + a_1\lambda^{k-1} + \cdots + a_{k-1}\lambda + a_k \tag{A.4}$$

If one of the coefficients $a_k$ is negative, then the system is unstable. For asymptotic stability, the Hurwitz matrix is used;

$$\mathbf{H}_m \triangleq \begin{bmatrix} a_1 & a_3 & a_5 & \cdots & 0 \\ 1 & a_2 & a_4 & \cdots & 0 \\ 0 & a_1 & a_3 & \cdots & 0 \\ \vdots & \vdots & \vdots & \ddots & \vdots \\ 0 & 0 & 0 & \cdots & 0 \\ 0 & 0 & 0 & \cdots & a_k \end{bmatrix} \tag{A.5}$$

or $a_i = 0$ for $i > n$. The following sub-matrices are defined as

$$\begin{aligned} \Delta_1 &\triangleq a_1 \\ \Delta_2 &\triangleq \det\begin{bmatrix} a_1 & a_3 \\ 1 & a_2 \end{bmatrix} \\ &\vdots \\ \Delta_k &\triangleq \det \mathbf{H}_m \end{aligned}$$

The system is asymptotically stable if $\Delta_i$ is larger than zero for $i = 1, \ldots, k$. The previous statement however only considered the linearized system. The nonlinear system does not always behave as the linearized system dictates. However, the following have been proven (see Verhulst (2006) for formal definitions and proof).

- If the linearized system is uniformly asymptotically stable for the point $\mathbf{x} = 0$, then the nonlinear system is also asymptotically stable.
- Similarly, if the linearized system is unstable, so is the nonlinear system.
- Lyapunov stability of the nonlinear system is not guaranteed.

# Appendix B

# Derivation: Passive Damping Equations

Here, the derivation of the passive damping are given to be suitable for numerical integration. The equations defined by Hughes (2004) which includes a ball-in-tube damper is given as

$$\frac{\mathrm{d}\mathbf{p}}{\mathrm{d}t} = -\boldsymbol{\omega}^{\times}\mathbf{p} + \mathbf{f} \tag{B.1}$$

$$\frac{\mathrm{d}\mathbf{H}}{\mathrm{d}t} = -\boldsymbol{\omega}^{\times}\mathbf{H} - \mathbf{v}^{\times}\mathbf{p} + \boldsymbol{\tau} \tag{B.2}$$

$$\frac{\mathrm{d}p_n}{\mathrm{d}t} = m_d\boldsymbol{\omega}^T\mathbf{n}^{\times}\left(\mathbf{v} - \mathbf{r}_d^{\times}\boldsymbol{\omega}\right) - c_d\dot{\xi} - k_d\xi \tag{B.3}$$

and the momenta as

$$\mathbf{p} = m\mathbf{v} - \mathbf{c}^{\times}\boldsymbol{\omega} + m_d\dot{\xi}\boldsymbol{n} \tag{B.4}$$

$$\mathbf{H} = \mathbf{c}^{\times}\mathbf{v} + \mathbf{J}\boldsymbol{\omega} + m_d\dot{\xi}\mathbf{b}^{\times}\mathbf{n} + \mathbf{H}_s \tag{B.5}$$

$$p_n = m_d\left(\mathbf{n}^T\mathbf{v} - \mathbf{n}^T\mathbf{b}^{\times}\boldsymbol{\omega} + \dot{\xi}\right) \tag{B.6}$$

$$H_a = I_s\mathbf{a}^T\boldsymbol{\omega} + H_s \tag{B.7}$$

The following assumptions have been applied to simplify the equations.

- No linear momentum, $\mathbf{p} = 0$
- No external forces, $\mathbf{f} = 0$

First, the first moment of inertia $\mathbf{c}$ is simplified. By setting the origin of the body frame $B$ to coincide with the mass center of the composite body or when $\xi = 0$, $\mathbf{c}$ can be re-stated as

$$\mathbf{c} = \mathbf{c}_P + \mathbf{c}_R + m_d\mathbf{r}_D \tag{B.8}$$

with $\mathbf{r}_D = \mathbf{b} + \xi\mathbf{n}$ and at $\xi = 0$;

$$\mathbf{c}_0 = \mathbf{c}_P + \mathbf{c}_R + m_d\mathbf{b} = 0 \quad \rightarrow \quad \mathbf{c}_P + \mathbf{c}_R = -m_d\mathbf{b}$$

Substituting into Equation B.8 gives

$$\mathbf{c} = m_d\xi\mathbf{n} \tag{B.9}$$

With the first assumption Equation B.4 can be simplified to

$$\mathbf{v} = \frac{1}{m}\mathbf{c}^{\times}\boldsymbol{\omega} - \frac{m_d}{m}\dot{\xi}\mathbf{n} \tag{B.10}$$

which can be substituted into Equation B.5

$$\begin{aligned}\mathbf{H} =& \mathbf{c}^{\times}\left(\frac{1}{m}\mathbf{c}^{\times}\boldsymbol{\omega} - \frac{m_d}{m}\dot{\xi}\mathbf{n}\right) + \mathbf{J}\boldsymbol{\omega} + m_d\dot{\xi}\mathbf{b}^{\times}\mathbf{n} + \mathbf{H}_s \\ =& \frac{1}{m}\mathbf{c}^{\times}\mathbf{c}^{\times}\boldsymbol{\omega} - \frac{m_d}{m}\dot{\xi}\mathbf{c}^{\times}\mathbf{n} + \mathbf{J}\boldsymbol{\omega} + m_d\dot{\xi}\mathbf{b}^{\times}\mathbf{n} + \mathbf{H}_s\end{aligned}$$

Note that the second term on the right-hand side is zero as the vector $\mathbf{v}$ is parallel to $\mathbf{c}$. Given that $\mathbf{H}_s = H_s\mathbf{a}$, substitute Equation B.7 into above equation yields

$$\mathbf{H} = \frac{1}{m}\mathbf{c}^{\times}\mathbf{c}^{\times}\boldsymbol{\omega} + \mathbf{J}\boldsymbol{\omega} + m_d\dot{\xi}\mathbf{b}^{\times}\mathbf{n} + H_a\mathbf{a} - I_s\mathbf{a}\mathbf{a}^T\boldsymbol{\omega}$$

Collecting the $\boldsymbol{\omega}$ values in the form of

$$\mathbf{y} = \mathbf{K}\boldsymbol{\omega}$$

where

$$\mathbf{K} = \frac{\mathbf{c}^{\times}\mathbf{c}^{\times}}{m} + \mathbf{J} - I_s\mathbf{a}^T\mathbf{a} \tag{B.11}$$

$$\mathbf{y} = \mathbf{H} - H_a\mathbf{a} - m_d\dot{\xi}\mathbf{b}^{\times}\mathbf{n} \tag{B.12}$$

To compute the body rates, a simple matrix inversion can be used

$$\boldsymbol{\omega} = \mathbf{K}^{-1}\mathbf{y} \tag{B.13}$$

However $\dot{\xi}$ is still required. This can be derived from Equation B.6.

$$\dot{\xi} = \frac{p_n}{m_d} - \mathbf{n}^T\mathbf{v} + \mathbf{n}^T\mathbf{b}^{\times}\boldsymbol{\omega}$$

Substituting Equation B.10 gives

$$\dot{\xi} = \frac{p_n}{m_d} - \frac{1}{m}\mathbf{n}^T\mathbf{c}^{\times}\boldsymbol{\omega} + \frac{m_d}{m}\mathbf{n}^T\mathbf{n}\dot{\xi} + \mathbf{n}^T\mathbf{b}^{\times}\boldsymbol{\omega}$$

Here, the second term of the right-hand side is zero, simplifying to

$$\dot{\xi} = \frac{p_n}{m_d} + \frac{m_d}{m}\mathbf{n}^T\mathbf{n}\dot{\xi} + \mathbf{n}^T\mathbf{b}^{\times}\boldsymbol{\omega}$$

Substituting Equation B.12 and B.13, results in

$$\dot{\xi} = \frac{p_n}{m_d} + \frac{m_d}{m}\mathbf{n}^T\mathbf{n}\dot{\xi} + \mathbf{n}^T\mathbf{b}^{\times}\mathbf{K}^{-1}(\mathbf{H} - H_a\mathbf{a} - m_d\dot{\xi}\mathbf{b}^{\times}\mathbf{n})$$

Collecting $\dot{\xi}$ terms

$$\left(1 - \mathbf{n}^T\mathbf{n}\frac{m_d}{m} + \mathbf{n}^T\mathbf{b}^{\times}\mathbf{K}^{-1}m_d\mathbf{b}^{\times}\mathbf{n}\right)\dot{\xi} = \frac{p_n}{m_d} + \mathbf{n}^T\mathbf{b}^{\times}\mathbf{K}^{-1}(\mathbf{H} - H_a\mathbf{a})$$

$$\dot{\xi} = \frac{\frac{p_n}{m_d} + \mathbf{n}^T\mathbf{b}^{\times}\mathbf{K}^{-1}(\mathbf{H} - H_a\mathbf{a})}{\left(1 - \mathbf{n}^T\mathbf{n}\frac{m_d}{m} + \mathbf{n}^T\mathbf{b}^{\times}\mathbf{K}^{-1}m_d\mathbf{b}^{\times}\mathbf{n}\right)} \tag{B.14}$$

which can be substituted into Equation B.12 to compute Equation B.13. The derivation of the spinup procedure is equivalent. However with the added equation

$$\frac{\mathrm{d}H_a}{\mathrm{d}t} = g_a \tag{B.15}$$

# Appendix C

# Derivation: Proof Sliding Surface Stability

In this appendix, the proof for the stability of the SMC sliding surface is given using Lyapunuv's direct method. The proof has been slightly adjusted to the variables used and one can find this in the textbook by Shtessel et al. (2014). The sliding surface is given as

$$\mathbf{s} = \mathbf{H}_d - \mathbf{H} - \mathbf{c}\boldsymbol{\theta} \tag{C.1}$$

and its derivativex

$$\dot{\mathbf{s}} = \dot{\mathbf{H}}_d - \dot{\mathbf{H}} - c\dot{\boldsymbol{\theta}} \tag{C.2}$$

Substitution of the dynamics (Equation 5.49) yields in

$$\dot{\mathbf{s}} = \dot{\mathbf{H}}_d + \boldsymbol{\omega}^{\times}\mathbf{H} - \mathbf{u} - \boldsymbol{\tau} - c\dot{\boldsymbol{\theta}} \tag{C.3}$$

The control law had been derived to be

$$\mathbf{u} = \dot{\mathbf{H}}_d + \boldsymbol{\omega}^{\times}\mathbf{H} + \mathbf{D}\text{sgn}(\mathbf{s}) - c\dot{\boldsymbol{\theta}} + \boldsymbol{\epsilon}\text{sgn}(\mathbf{s}) + \mathbf{ks} \tag{C.4}$$

Substitute Equation C.4 into Equation C.3

$$\dot{\mathbf{s}} = -\boldsymbol{\tau} - \mathbf{D}\text{sgn}(\mathbf{s}) - \boldsymbol{\epsilon}\text{sgn}(\mathbf{s}) - \mathbf{ks} \tag{C.5}$$

Multiplying it with $\mathbf{s}$ gives

$$\mathbf{s}\dot{\mathbf{s}} = \mathbf{s}(-\boldsymbol{\tau} - \mathbf{D}\text{sgn}(\mathbf{s}) - \boldsymbol{\epsilon}\text{sgn}(\mathbf{s}) - \mathbf{ks})$$

Applying the definition of the signum function;

$$\text{sgn}(\mathbf{s}) = \frac{|\mathbf{s}|}{\mathbf{s}} \tag{C.6}$$

simplifies the equation to

$$\mathbf{s}\dot{\mathbf{s}} = -\mathbf{k}\mathbf{s}^2 - \mathbf{D}|\mathbf{s}| - \boldsymbol{\tau}\mathbf{s} - \boldsymbol{\epsilon}|\mathbf{s}|$$

Assume a Lyapunov function in the form of

$$\mathbf{V}(\mathbf{s}) = \frac{1}{2}\mathbf{s}^2 \tag{C.7}$$

Its derivative is equal to

$$\dot{\mathbf{V}}(\mathbf{s}) = \mathbf{s}\dot{\mathbf{s}} = -\mathbf{k}\mathbf{s}^2 - \mathbf{D}|\mathbf{s}| - \boldsymbol{\tau}\mathbf{s} - \boldsymbol{\epsilon}|\mathbf{s}| \tag{C.8}$$

For the candidate function to be a Lyapunov function and to be globally asymptotically stable, the following should hold

- $\dot{\mathbf{V}}(\mathbf{s}) < 0$ for $\mathbf{s} \neq 0$
- $\mathbf{V}(\mathbf{s}) > 0$ for $\mathbf{s} \neq 0$
- $\mathbf{V}(0) = 0$

It is immediate that the last two conditions are easily satisfied. The first condition can be reasoned as follows. The first term on the right hand side is smaller than zero due to the squared negative term. The second and last terms are also always negative. The third term however can be positive, but it is always smaller than zero as **D** is the maximum value for the disturbance torque or

$$\mathbf{D} \geq |\boldsymbol{\tau}|$$

and thus

$$-\mathbf{D}|\mathbf{s}| - \boldsymbol{\tau}\mathbf{s} \leq 0$$

This proves that the sliding surface is indeed globally asymptotically stable. This does not take into account actuator saturation. In a similar method, this can be proven. If the actuator has a saturation limit, this is not valid anymore. To have the same properties of stability, the saturation torque must hold

$$|\mathbf{u}_{\text{sat}}| > \left|\dot{\mathbf{H}}_D + \boldsymbol{\omega}^{\times}\mathbf{H}\right| \tag{C.9}$$

This is only valid for below a certain value of $H_a$ given a saturation torque due to the increase in the cross product value throughout the spinup process as shown by the Equation 5.51. A more exact condition is here not further pursued.

# Appendix D

# LQR Gains

In this chapter, the weights of the objective function and gains $\mathbf{K}_H$ with the subscript $H$ denoting the corresponding wheel angular momentum for the LQR controller are given below.

$$\mathbf{Q} = \frac{1}{2500}\bar{\mathbf{1}}_6 \tag{D.1}$$

$$\mathbf{R} = \begin{bmatrix} \frac{1}{1000} & 0 & 0 \\ 0 & 1 & 0 \\ 0 & 0 & 1 \end{bmatrix} \tag{D.2}$$

$$\mathbf{K}_{0.4} = \begin{bmatrix} 0.2 & 0 & 0 & 0.25638 & 0 & 0 \\ 0 & 0.00134 & 0.01995 & 0 & 0.02814 & 0 \\ 0 & -0.01995 & 0.00134 & 0 & 0 & 0.02565 \end{bmatrix} \tag{D.3}$$

$$\mathbf{K}_{0.6} = \begin{bmatrix} 0.2 & 0 & 0 & 0.25638 & 0 & 0 \\ 0 & 0.00081 & 0.01998 & 0 & 0.02525 & 0 \\ 0 & -0.01998 & 0.00081 & 0 & 0 & 0.02359 \end{bmatrix} \tag{D.4}$$

$$\mathbf{K}_{0.8} = \begin{bmatrix} 0.2 & 0 & 0 & 0.25638 & 0 & 0 \\ 0 & 0.00058 & 0.01999 & 0 & 0.02387 & 0 \\ 0 & -0.01999 & 0.00058 & 0 & 0 & 0.02262 \end{bmatrix} \tag{D.5}$$

$$\mathbf{K}_{1} = \begin{bmatrix} 0.2 & 0 & 0 & 0.25638 & 0 & 0 \\ 0 & 0.00045 & 0.01999 & 0 & 0.02306 & 0 \\ 0 & -0.01999 & 0.00045 & 0 & 0 & 0.02206 \end{bmatrix} \tag{D.6}$$

$$\mathbf{K}_{2.8} = \begin{bmatrix} 0.2 & 0 & 0 & 0.25638 & 0 & 0 \\ 0 & 0.00015 & 0.02 & 0 & 0.02106 & 0 \\ 0 & -0.02 & 0.00015 & 0 & 0 & 0.0207 \end{bmatrix} \tag{D.7}$$

# Appendix E

# Matlab Code: getAPH.m

```
function[AP] = getAPH(year,dayofyear,UTseconds,update_files)
%% APH DATA RETRIEVAL FUNCTION
% -------------------------------------------------------------------------
% This functions retrieves APH data from the ftp server of the National
% Centers for Environmental Information (NCEI) to be implemented in the
% MATLAB function atmosnrlmsise00. This function should go in conjunction
% with getf107.m. FTP Server and corresponding directory can be found at
% ftp://ftp.ngdc.noaa.gov/STP/GEOMAGNETIC_DATA/INDICES/KP_AP/
% -------------------------------------------------------------------------
% Input:  - year         : Year [yr]
%         - dayofyear    : Day of Year [days]
%         - UTseconds    : Seconds as given in Universal Time [s]
%         - update_files : Boolean for File Update [true/false]
% -------------------------------------------------------------------------
% Output: - AP           : Contains APH info, see the MATLAB function
%                          atmosnrlmsise00 for exact information.
% -------------------------------------------------------------------------
% Developed by David Ju 09-02-17 Copyright (c)

%% Check Input Values
if (year < 1932 && dayofyear <= 2)
   disp('ERROR: No (complete) data exists before 1932/01/02')
elseif dayofyear < 0
   disp('ERROR: Please enter a positive day of year (real integer)')
elseif UTseconds < 0
   disp('ERROR: Please enter a positive UT seconds (real)')
end

%% Retrieve Magnetic Index Data
% Update Files
if update_files == true
   disp('Downloading takes a few minutes')
   ngdc = ftp('ftp.ngdc.noaa.gov');
   contents = '/STP/GEOMAGNETIC_DATA/INDICES/KP_AP/*';
   mget(ngdc,contents);
   close(ngdc);
   disp('Downloading Complete')
end
```

```
39
40 %% Convert Time to Serial Date Number
41 % Requested Times
42 date_n = datenum(year,1,dayofyear) + UTseconds/(24*3600);
43
44 %% Check Time 57H Before First Time
45 time_57h = date_n - 57/24;
46 [year_p,~,~,~,~] = datevec(time_57h);
47
48 if year_p < year
49    prev_year = true;
50    year = [year_p; year];
51 end
52
53 %% Get Data File(s)
54 % Convert Number to String
55 year_str = cellstr(num2str(year));
56
57 % Allocation Matrix
58 data_set = [];
59
60 % Start Data Selection
61 for i = 1:length(year)
62    file_name   = fullfile(pwd,'STP','GEOMAGNETIC_DATA','INDICES','KP_AP'...
63    ,year_str{i});
64    % Open File
65    fid         = fopen(file_name,'r'); % Open File
66    data        = fscanf(fid,'%c');     % Read File
67    fclose(fid);                        % Close File
68
69    % Reshape to Matrix Format
70    data = reshape(data,72,length(data)/72)';
71
72    % Take Last 3 Days of Previous Year
73    if (prev_year == true && i == 1)
74       data_set = data(end-2:end,:);
75    else
76       data_set = [data_set; data];
77    end
78 end
79
80 % Find Current 3H Interval
81 UTinterval = floor(UTseconds/(3*3600));
82 APinterval = 32:34; % Location in Folder
83
84 % Find Date
85 if prev_year == true
86    n_d = dayofyear +3;
87 else
88    n_d = dayofyear;
89 end
90
91 % Retrieve "Useful" Column Data
92 AP0 = str2num(data_set(n_d,56:58));
```

```
93  for i = 1:20
94     APi(i) = str2num(data_set(n_d,APinterval+3*UTinterval));
95     UTinterval = UTinterval -1;
96
97     if UTinterval < 0
98        UTinterval = 7;
99        n_d = n_d -1;
100    end
101 end
102
103 APmean1 = mean(APi(5:12));
104 APmean2 = mean(APi(13:end));
105
106 AP = [AP0,APi(1:4),APmean1,APmean2];
107 end
```

# Appendix F

# Matlab Code: getf107.m

```
function[f107a,f107d] = getf107(year,dayofyear,update_files)
%% 10.7cm SOLAR RADIO FLUX DATA RETRIEVAL FUNCTION
% ------------------------------------------------------------------------
% This functions retrieves 10.7 solar radio data from the ftp server of
% the National  Centers for Environmental Information (NCEI) to be
% implemented in the MATLAB function atmosnrlmsise00. This function
% should go in conjunction with getAPH.m. FTP Server and corresponding
% directory can be found at
% ftp://ftp.ngdc.noaa.gov/STP/space-weather/solar-data/solar-features/
% solar-radio/noontime-flux/penticton/penticton_observed/listings/
% Non existent data values will be discarded for averaging and a previous
% existing value will be taken for f107d.
% ------------------------------------------------------------------------
% Input:  - year         : Year [yr]
%         - dayofyear    : Day of Year [days]
%         - update_files : Boolean for File Update [true/false]
% ------------------------------------------------------------------------
% Output: - f107a        : Averaged Flux Data over 81 days
%         - f107d        : Previous Day Fulx Data
% ------------------------------------------------------------------------
% Developed by David Ju 09-02-17 Copyright (c)

%% Check Input Values
if (year < 1947 && dayofyear <= 44+40)
   disp('ERROR: No (complete) data exists before 1947/02/14')
elseif dayofyear < 0
   disp('ERROR: Please enter a positive day of year (real integer)')
end

%% Retrieve Magnetic Index Data
% Update Files
   if update_files == true
   disp('Download initiated...')
   ngdc = ftp('ftp.ngdc.noaa.gov');
   contents = '/STP/space-weather/solar-data/solar-features/solar-radio/
      noontime-flux/penticton/penticton_observed/listings/
      listing_drao_noontime-flux-observed_daily.txt';
   mget(ngdc,contents);
```

```
   close(ngdc);
   disp('Downloading Complete')
end

%% Retrieve Data File
% Start Data Selection
file_name  = fullfile(pwd,'STP','space-weather','solar-data', ...
'solar-features','solar-radio','noontime-flux','penticton',...
'penticton_observed','listings',...
'listing_drao_noontime-flux-observed_daily.txt');

% Open File
fid        = fopen(file_name,'r');           % Open File
data       = textscan(fid,'%4d %2d %2d %f','treatasempty','.'); % Read File
fclose(fid);                                 % Close File

%% Find Data Location
% Time Conversion
date_n = datenum(year,1,dayofyear); % Convert to Serial Date Number
[yy,mm,dd,~,~,~] = datevec(date_n); % Convert to Year, Month and Day.

% Find Date
idt = 0; % For error check
idty = find(yy == data{1});
idtm = find(mm == data{2});
idtd = find(dd == data{3});

idt1 = intersect(idty,idtm);
idt  = intersect(idt1,idtd);

if idt == 0
   disp('ERROR: No matching dates were found.')
   return
end

%% Parse Values
% Averaged 81 Days Value
f107a = nanmean(data{4}((idt-40):(idt+40)));

if isnan(f107a)
   disp('ERROR: No data available for 81 consecutive days.')
end

% f107 Previous Day Value
f107d = data{4}(idt-1);

% Take Closest Point if NaN
if isnan(f107d)
   disp('Data incomplete, the closes previous value will be taken.')
end

while isnan(f107d)
   idt = idt -1;
   f107a = (idt-1);
```

```
91 end
92 end
```

# Appendix G

# Spinup with External Disturbances

In this chapter, the spinup simulation is performed for the gyrostat which takes into account effects of disturbances and mean motion into the dynamics. The results are very similar as given in Chapter 5. One remarkable difference is shown in Figure G.1d, due to external disturbance torques acting on the pitch axis, the final attitude position is deviated from the desired 0 degree on the pitch axis. Some control adjustment is required for correction.

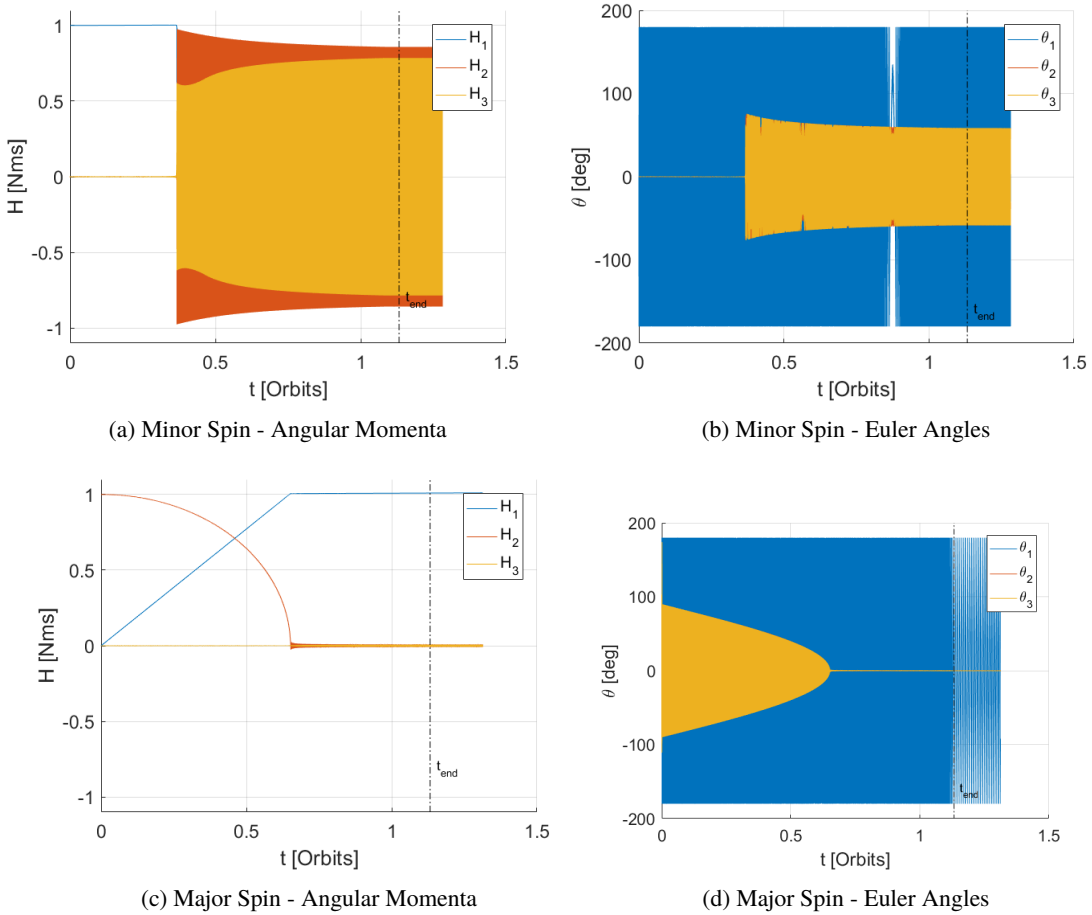


(a) Minor Spin - Angular Momenta

(b) Minor Spin - Euler Angles

(c) Major Spin - Angular Momenta

(d) Major Spin - Euler Angles

Figure G.1: Spinup Simulation Including External Disturbances

# Appendix H

# Detumbling Results

In this chapter, the results of the two detumbling control laws are shown in Figure H.1 and Figure H.2

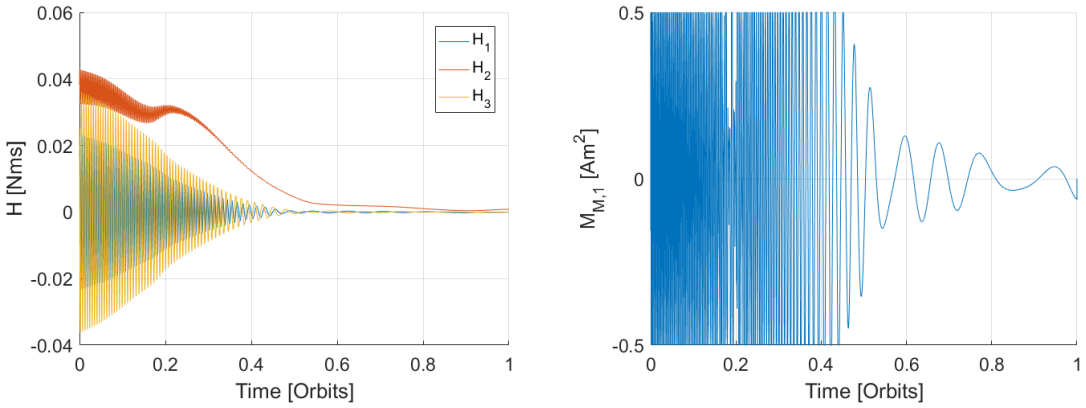


(a) Angular Momentum

(b) $M_{A,1}$

(c) $M_{A,2}$

(d) $M_{A,3}$

Figure H.1: Detumbling - Static Gain Control

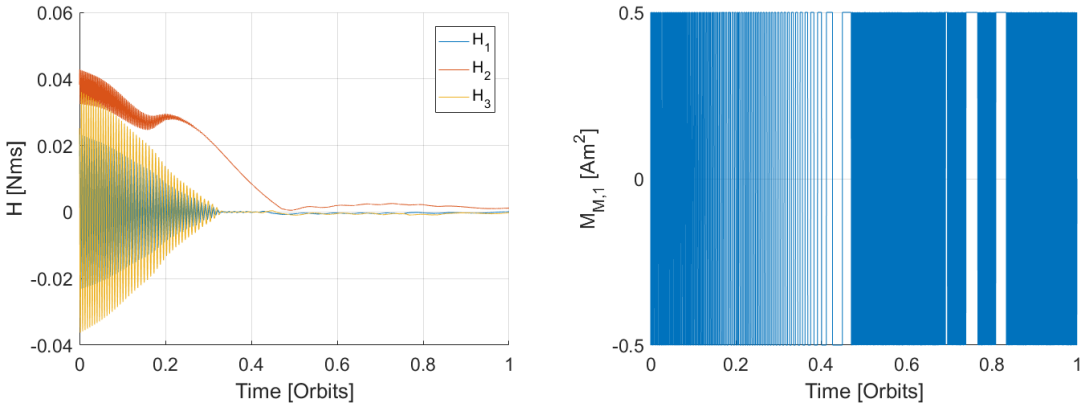


(a) Angular Momentum




(b) $M_{A,1}$

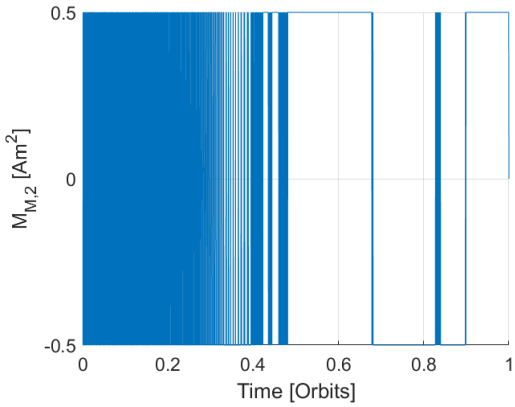


(c) $M_{A,2}$

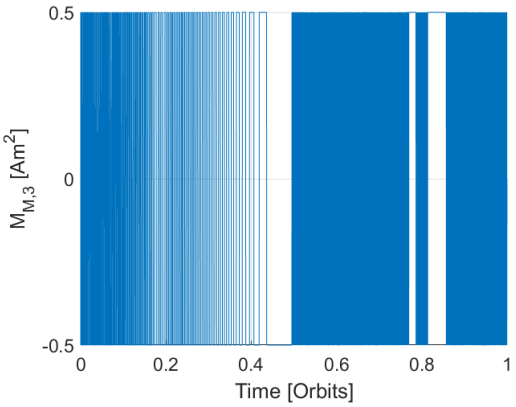


(d) $M_{A,3}$

Figure H.2: Detumbling - Bang-Bang Control